An Experimental Study of Non-Coaxial Soil Behaviour Using Hollow Cylinder Testing

by

Yanyan Cai, BEng, MSc

Thesis submitted to The University of Nottingham

for the degree of Doctor of Philosophy

March 2010

Abstract

Non-coaxiality of the principal stress direction and principal strain increment direction has been observed in both numerical modelling and experimental studies. The importance of non-coaxiality has been widely recognised in the geomechnical engineering. Without considering the non-coaxiality in the design may lead to an unsafe soil structure. Therefore, it is essential to understand the non-coaxial soil behaviour better and take it into account in the numerical modelling.

A new Hollow Cylinder Apparatus in Nottingham Centre of Geomechanics (NCG) has been employed in this study. A series of preliminary tests have been carried out to validate the reliability and repeatability of the testing results.

Three series of tests, including 24 tests on Portaway sand and 2 tests on Leighton Buzzard sand, were conducted to study the non-coaxial soil behaviour of granular materials. The three stress paths followed were monotonic loading along fixed principal stress direction, pure rotation of the principal stress axes with constant deviator stress and combined rotation of principal stress axes with increasing deviator stress. Portaway sand was chosen because it has been used in NCG to investigate granular soil behaviour. Therefore, stress-strain behaviour including non-coaxial behaviour can be observed and used by the other researchers in NCG to develop or verify numerical models.

The evidence of non-coaxiality has been obtained from the tests. In general, the non-coaxiality is relatively small in monotonic loading tests, but is more significant in the pure rotation tests and combined loading tests. The degree of non-coaxiality is affected by the density of the specimen, the stress path followed, the stress level and the material particle properties.

Acknowledgements

The work presented in this thesis was carried out during the author's doctoral study in the Nottingham Centre for Geomechanics from January 2006 to December 2009. The financial support provided by the Department of Civil Engineering and the University of Nottingham is gratefully acknowledged.

I would first and foremost like to thank my supervisor, Prof. Hai-Sui Yu, for his supervision, guidance and financial support throughout this research. Prof. Yu is also the person who introduced this topic to me, and gave me the opportunity to carry out this study.

Special and sincere thanks are due to my second supervisor, Dr. Dariusz Wanatowski, for providing me meticulous guidance and assistance in the experimental work and proof reading. Without his circumspection and patience, it would not be possible to complete this work.

I would like to thank all the technicians in the Department of Civil Engineering for their help and advice with the experimentation, in particular Ian Richardson. I would like to thank Amanullah Marri for his help in the triaxial test. Thanks were extended to Caroline Dolby for her kindly help in the four years.

I would also like to thank all my friends in NCG for their friendship and support.

Last, but by no means least, I would like to thank my parents, brother, sister and the other family members. Without their immense and endless support and love I would not be able to endure the challenging years.

Thank you, I love you all.

Contents

List of Tables

List of Figures

List of Symbols

A_{im} , A_{om} = Surface areas of the specimen covered by the inner and outer membranes

A_{MP} = Surface area of membrane

$b=(\sigma_2-\sigma_3)/(\sigma_1-\sigma_3)$ = Parameter that measurers the relative magnitude of the intermediate principal stress

C_{MP} = Parameter that depends on specimen size and density for membrane penetration correction

C_u = Uniformity coefficient (D_{60}/D_{10})

D_r = Relative density

D_{50} = Mean grain size

D_{10} = Effective grain size

e = Void ratio

e_c = Void ratio after consolidation

$e_{\max}$ = Maximum void ratio

$e_{\min}$ = Minimum void ratio

E_m = Young's modulus of membrane

G_S = Specific gravity

H = Height of apparatus

M_T = Torque

n = Inner and outer cell radius ratio $n=r_i/r_o$

$O.D$ = Outer diameter of apparatus

$I.D$ = Inner diameter of apparatus

P_i = Internal cell pressure

P_o = Outer cell pressure

$P=(\sigma_1+\sigma_2+\sigma_3)/3$ = Mean total stress

$P'=(\sigma'_1+\sigma'_2+\sigma'_3)/3$ = Mean effective stress

P_c = Mean stress at final consolidation state

$q=\sigma_1-\sigma_3$ = Deviator stress

r_i, r_o = Inner and outer cell radius

R = Stress ratio, $R= \sigma_1' / \sigma_3'$

R_{max} , R_{min} =Maximum and minimum stress ratios

t_m = Thickness of membrane

v_{MP} = Unit membrane penetration

V_{soil} = Volume of soil sample

W = Axial load

α = Inclination of the major principal stress

α_ε = Inclination of the major principal strain

$\alpha_{d\varepsilon}$ = Inclination of the major principal strain increment

β_1 = Normalized parameter

β_3 = Parameter to quantify the level of stresses non-uniformity

β_R =Stress non-uniformity coefficient

$\gamma_{\theta z}$, ε_z, ε_r and ε_θ = Shear, axial, radial and circumferential strains

ε_m = The unit membrane penetration

ε_1, ε_2 and ε_3 = Major, intermediate and minor principal strains

$\varepsilon_v=\varepsilon_1+\varepsilon_2+\varepsilon_3$ = Volumetric strain

σ_1, σ_2 and σ_3 = Major, intermediate and minor total principal stresses

σ'_1, σ'_2 and σ'_3 = Major, intermediate and minor effective principal stresses

σ_z, σ_θ, σ_r = Axial, circumferential and radial stress

$\tau_{\theta z}$, $\tau_{z\theta}$ = Shear stress

ΔV_{sr} , ΔV_{ir} = Measured volume changes of the inner chamber and the specimen

Chapter 1

Introduction

1.1 BACKGROUND

In geotechnical engineering, the non-coaxiality is defined as the non-coincidence of the principal stress direction and the principal strain increment direction. It has been widely recognized as an important feature in engineering practice which has been observed and recognized in soil tests using both simple shear and hollow cylinder apparatuses. Numerical analysis carried out by Yu and Yuan (2005, 2006), Yang and Yu (2006) showed that the non-coaxiality of a granular soil has very important consequences in geotechnical design. They concluded that the design of shallow foundations without considering the effects of the non-coaxiality might be unsafe. The importance of introducing non-coaxiality into the design of geotechnical

structures has been approbated for a more secure project (Yu and Yuan, 2005). Models with the consideration of non-coaxiality have been built to simulate the soil behaviour by several researchers (Yatomi *et al.,* 1989; Gutierrez *et al.,* 1993; Li and Dafalias, 2004; Lashkari and Latifi, 2007; Jiang *et al.*, 2005a and b; Yang and Yu, 2006a and b; Yu and Yuan, 2006; Yu, 2006)

The evidence of the non-coaxial behaviour in granular materials has been observed in both numerical and experimental studies. In simple shear tests, Roscoe *et al.* (1967) and Roscoe (1970) reported the non-coincidence between principal stress direction and principal strain rate direction. Based on the experimental micro-mechanical study using a photoelastic disc assembly as a two-dimensional analogue of granular media, Drescher and de Josselin de Jong (1972) reported further evidence of non-coaxiality. Using direct shear testing, Wong and Arthur (1986) showed that the deviation between the principal stress and the principal strain incremental directions can be larger than 30° in sand specimens subjected to continuous rotation of the principal stresses axes. Tests using a hollow cylinder apparatus have shown the fact that the behaviour of granular materials is non-coaxial when specimens were subjected to the rotation of principal stress axes (Symes *et al.* 1982; Ishihara and Towhata, 1983; Miura *et al*., 1986; Pradel *et al.*, 1990; Gutierrez *et al*., 1991). Non-coaxiality was observed by Alonso-Marroqu ń *et al.* (2005) from their 2D simulations with a model consisting of randomly generated convex polygons. Thornton and Zhang (2006) have reported non-coaxial behaviour similar to the results of Roscoe's study (1970) by a 2D numerical simulation using the discrete element

method. More recently, Li and Yu (2009) carried out 2D DEM experiments to investigate the directional dependence of the behaviour of granular material under monotonic loading. The non-coaxiality was found to be dependent on the material anisotropy, as well as the loading history.

Figure 1-1 shows an anisotropic specimen. In Figure 1-1(a), if the loading direction is normal to the bedding plane, then the directions of principal stress and principals strain increment will be coaxial even if the specimen fabric is anisotropic. However, as shown in Figure 1-1(b), when the loading direction and bedding plane is not normal to each other, the strain increment axis will deviate from the principal stress axis, thus non-coaxiality is induced.

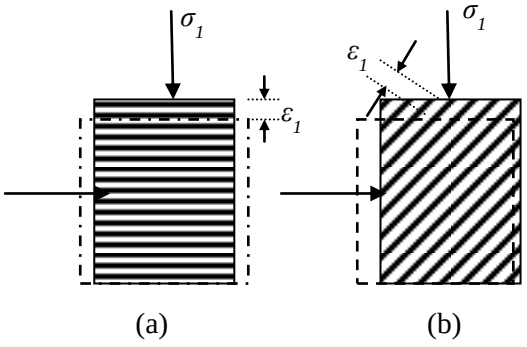

Figure 1-1 The interrelation of anisotropy and non-coaxiality

The theoretical origin of non-coaxiality can be found in the kinematic models for the flow of granular materials developed by de Josselin de Jong (1958). The so-called ‘double sliding, free rotating model’ for planar flow was based on the assumption of shear flow occurring along two surfaces where the available shear resistance has been exhausted. Spencer (1964) used the same

concept of double sliding to establish a set of kinematic equations termed the ‘double shearing model’ with a different rotation term from the de Josselin de Jong model. A similar model was also proposed independently by Mandel (1966). Further analysis of the double sliding model was made by Mandel and Fernandez (1970) with further justification for the non-coaxiality of principal stress and principal strain rate directions. These ‘double-sliding free rotation’ and ‘double-shearing’ models were developed for non-dilatant, rigid-plastic and post-peak flow of granular materials. Several researchers have extended them to account for dilatant, elasto-plastic and pre-peak strain hardening response (Mehrabadi and Cowin, 1978; Anand, 1983; de Josselin de Jong, 1988; Teunissen and Vermeer, 1988; Yu and Yuan, 2006). Rudnicki and Rice (1975) also reported that non-coaxial behaviour plays an important role in shear band formation in sands. In some pre-failure plasticity models that have been proposed for granular materials, such as a hypoplastic model (Wang *et al*. 1990; Kolymbas, 1991) and a multi-laminate model (Iai *et al.* 1992), non-coaxiality was also evident..

1.2 RESEARCH OBJECTIVES

A new hollow cylinder apparatus commissioned from GDS Instrument Ltd. was being used in this project. The ultimate goal of this project is to provide an understanding of non-coaxial soil behaviour using HCA testing. The aims of this project can be stated as:

- To evaluate the new HCA system in Nottingham Centre of Geomechanics and design possible testing stress paths;
- To gain a good understanding of the soil behaviour under various stress paths by testing on Portaway sand.
- To analyze the stress-strain response from the tests and study the non-coaxial soil behaviour.
- To study the factors that affect the degree of non-coaxiality by employing various stress paths, different specimen void ratios and different materials, which were Portaway sand and Leighton Buzzard sand.

The following specific objectives are required to achieve these aims:

- A literature review on the non-coaxial soil behaviour and HCA testing methods.
- Determination of physical characteristics of the Portaway sand and Leighton Buzzard sand.
- Experimental tests to understand the equipment well and to use the control software confidently, as well as for the validation of the testing program.
- Design stress paths for the HCA experiments
- Analysis of the experimental results to obtain the relationship between principal stresses directions and principal strain increments directions.

1.3 OUTLINE OF THE THESIS

This thesis is composed of seven chapters. The organization of the thesis is introduced below:

Chapter 1 gives a brief introduction of this research study and the thesis.

In **Chapter 2,** a literature review is given based on the non-coaxiality of the directions of principal stresses and principal strain increments, and the background of hollow cylinder apparatus. Previous studies on non-coaxial soil behaviour are presented including both numerical and experimental work. Particular attention is focused on the investigation of non-coaxiality using a hollow cylinder apparatus. The principles of the hollow cylinder apparatus and the effect of specimen geometry is discussed in this chapter as well.

Chapter 3 introduces the details of the testing system, including the hollow cylinder apparatus and control software, followed by the physical properties of the tested materials. The specimen preparation and test procedures are also described. Then validation experimentation to checking the test equipment and speicmen repeatability are presented.

Chapter 4 focuses on the results of monotonic loading tests on Portaway sand. Fourteen tests are designed on two densities following various stress paths to study the non-coaxiality of soil behaviour when specimen subjected to monotonic loading in a fixed principal stress direction. The effect of relative

density is also discussed.

Chapter 5 describes the test results of pure rotation tests on Portaway sand and Leighton Buzzard sand. Ten tests are presented in this chapter. The general soil behaviour is described first, followed by discussion of the non-coaxial soil behaviour. Results are compared between densities and different materials to study the influence of density and specimen anisotropy.

Chapter 6 contains the results of two tests subjected to the combined loading. The effect of stress path on non-coaxiality is discussed in this chapter.

Chapter 7 summarises the main outcome of the research and gives some suggestions for future work.

Chapter 2

Literature Review

2.1 INTRODUCTION

This chapter presents a literature review on the two main topics related to this study, which are the non-coaxiality of soil behaviour and a hollow cylinder apparatus. The chapter is organized in the following structure. Section 2.2 deals with the non-coincidence between the axes of principal stress and principal strain increment in granular materials, including the definition of non-coaxiality and a general introduction of the previous studies using both numerical simulations and laboratory experiments. Section 2.3 introduces the hollow cylinder apparatus, which can be used to investigate the effect of principal stress rotation as well as the influence of anisotropy. The fundamental principles to interpret the state of stress and strains, as well as stress distribution, specimen geometry selection, boundary effects and membrane errors are presented. A review of the development of the hollow cylinder

apparatus is also given in this section. Section 2.4 presents the studies on non-coaxial soil behaviour particularly by using the hollow cylinder apparatus. Finally, Section 2.5 summarizes this chapter.

2.2 NON-COAXIALITY OF SOIL BEHAVIOUR

In geomechanics, non-coaxiality is defined as the non-coincidence between the principal stress axis and the principal strain rates axis. In contrast, the assumption of coaxiality was postulated by Saint Venant when he applied Tresca's yield criterion to a problem in metal plasticity (de Saint Venant, 1870). Therefore it has also been termed Saint Venant's postulate. However it has long been recognized that coaxiality cannot be satisfied in the case of anisotropy.

2.2.1 Definition of non-coaxiality

As the non-coaxiality is between principal stress and principal strain increment directions, tensors σ_{ij} and $d\varepsilon_{ij}$, which describe the state of stress and strain rate at a point, are considered to define the non-coaxiality. The two tensors use the same reference axis $x_i = x, y, z$ which can be easily chosen.

$$\sigma_{ij} = \begin{bmatrix} \sigma_{xx} & \sigma_{xy} & \sigma_{xz} \\ \sigma_{xy} & \sigma_{yy} & \sigma_{yz} \\ \sigma_{xz} & \sigma_{yz} & \sigma_{zz} \end{bmatrix} \tag{2.1}$$

$$d\varepsilon_{ij} = \begin{bmatrix} d\varepsilon_{xx} & d\varepsilon_{xy} & d\varepsilon_{xz} \\ d\varepsilon_{xy} & d\varepsilon_{yy} & d\varepsilon_{ya} \\ d\varepsilon_{xz} & d\varepsilon_{yz} & d\varepsilon_{zz} \end{bmatrix} \tag{2.2}$$

If the principal stress and principal strain increment are used, the tensors σ_{ij} and $d\varepsilon_{ij}$ contain only the principal components and have zero off-diagonal components, then:

$$\bar{\sigma}_{ij} = \begin{bmatrix} \sigma_1 & 0 & 0 \\ 0 & \sigma_2 & 0 \\ 0 & 0 & \sigma_3 \end{bmatrix} \tag{2.3}$$

$$d\bar{\varepsilon}_{ij} = \begin{bmatrix} d\varepsilon_1 & 0 & 0 \\ 0 & d\varepsilon_2 & 0 \\ 0 & 0 & d\varepsilon_3 \end{bmatrix} \tag{2.4}$$

Tensors σ_{ij} and $\bar{\sigma}_{ij}$, $d\varepsilon_{ij}$ and $d\bar{\varepsilon}_{ij}$ together with their respective reference axes are equivalent representations of the state of stress and strain increment at a point in a continuum.

The tensor $\bar{\sigma}_{ij}$ and $d\bar{\varepsilon}_{ij}$ can be obtained from σ_{ij} and $d\varepsilon_{ij}$ by suitable transformations:

$$\bar{\sigma}_{ij} = A_{ik}\,\sigma_{kl}\,A_{lj} \tag{2.5}$$

$$d\bar{\varepsilon}_{ij} = B_{ik}\,d\varepsilon_{kl}\,B_{lj} \tag{2.6}$$

Where A_{ij} and B_{ij} are transformation tensors giving the directions of the principal stresses and principal strain increments from the reference axis x_i to which the tensors σ_{ij} and $d\varepsilon_{ij}$ are referred. If x_i^{σ} is denoted as the principal stress axis, then A_{ij} may be expressed as $A_{ij} = \cos(x_i^{\sigma}, x_j)$. If $A_{ij} \neq B_{ij}$, the non-coaxiality of $\bar{\sigma}_{ij}$ and $d\bar{\varepsilon}_{ij}$ is obtained

2.2.2 Previous studies on non-coaxiality

From numerous studies on granular materials, it was found that the coaxiality assumption is only valid for isotropic media. When the strain rate depends not only on the principal stress but also on other vectors and tensors, for the requirement of anisotropic behaviour, new theories have been developed and applied to represent the non-coaxiality for granular material behaviour.

The theoretical origin of non-coaxiality can be found in some pre-failure plasticity models that have been proposed for granular materials, such as hypoplastic models (Wang *et al*., 1990; Kolymbas, 1991) and multi-laminate models (Iai *et al*., 1992). Rudnicki and Rice (1975) focused on the strain localization of materials and reported that non-coaxiality plays an important role in shear band formation in sands. Moreover, by introducing vertices into the yield surface, in contrast to a smooth and continuous yield surface, the flow becomes dependent on the directions of the stress and stress increment, and then the flow becomes non-coaxial for non-straight ahead loading. As obtained in experiments, this may facilitate strain localization in the strain hardening region (Vardoulakis, 1980).

Non-coaxiality has been a feature of a number of physically established plasticity models that describe ‘fully developed’ plane plastic flow of granular materials by means of kinematic theories. The earliest kinematic models for granular material flow were developed by de Josselin de Jong (1958) with graphical methods. The so-called ‘double sliding, free rotating model’ for

planar flow was based on the assumption of shear flow occurring along two surfaces where the available shear resistance had been exhausted. Then Spencer (1964) used the same concept of double sliding to establish a set of kinematic equations termed as the ‘double shearing model’ with a different rotation term from the de Josselin de Jong model. A similar model was also proposed independently by Mandel (1966). Further analysis of the double sliding model was made by Mandel and Fernandez (1970) with further justifications for the non-coaxiality between principal stress and principal strain increment directions. These original ‘double-sliding free rotation’ and ‘double-shearing’ models were developed for non-dilatant, rigid-plastic and post-peak flow of granular materials. Several researchers have extended those models to account additionally for dilatant, elasto-plastic and pre-peak strain hardening response (Mehrabadi and Cowin, 1978; Anand, 1983; de Josselin de Jong, 1988; Teunissen and Vermeer, 1988; Harris, 1993; Joer *et al*., 1998). Therefore the models become determinate, but they have not been shown to be able to reproduce the non-coaxial behaviour as observed in Roscoe’s simple shear tests (Roscoe, 1970).

Figure 2-1 shows the experimental results reported by Roscoe (1970). Before this, Roscoe *et al*. (1967) had shown that the principal axis of strain rate and of stress were not coincident before reaching peak shear stress during a simple shear test of sand. From Figure 2-1, the rotations of the principal stress and the principal plastic strain are non-coaxial, particularly at the early stage of loading. Then the axes tend to become coincident at large shear strains.

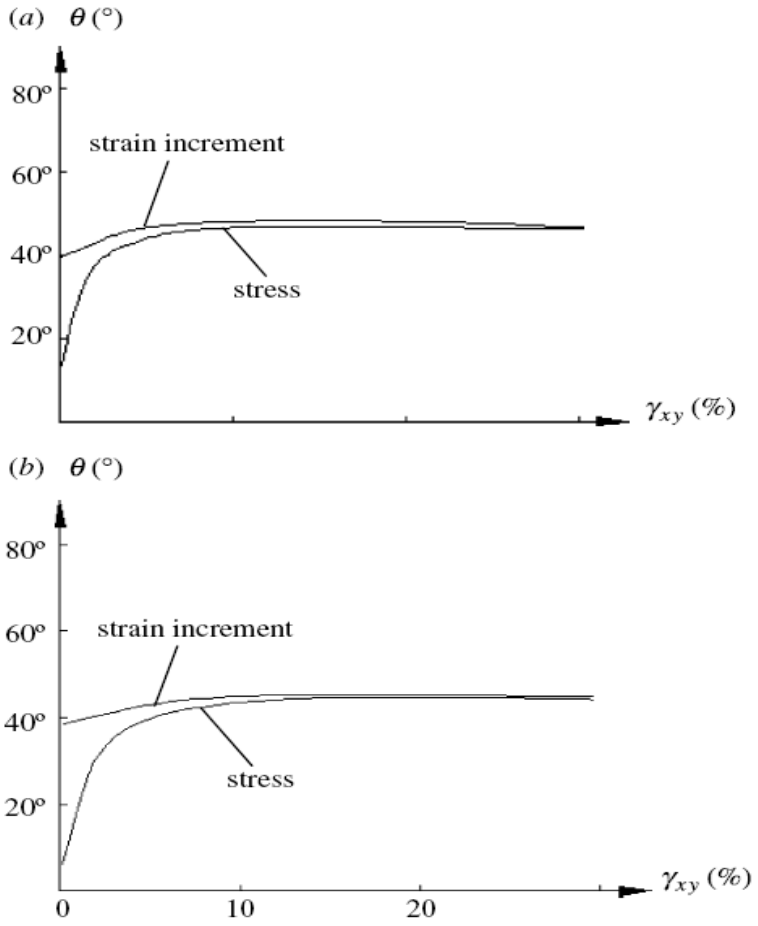

Figure 2-1 Experimental curves showing principal stress and strain increment rotations against shear strain during simple shear tests. (a) σ_{yy}=135kPa; (b) σ_{yy}=396kPa (after Roscoe, 1970).

One of the first evidences for non-coaxiality was reported by Drescher and de Josselin de Jong (1972) on the base of the experimental micro-mechanical study of a photoelastic disc assembly as a two-dimensional analogue of granular media. Besides, non-coaxiality has been observed in experimental studies on sands using the hollow cylinder apparatus (HCA), which allows full rotation of the principal stresses (Ishihara and Towhata, 1983; Symes *et al.*, 1982, 1984, 1988; Miura *et al.*, 1986; Pradel *et al.*, 1990; Gutierrez *et al.*, 1991, 1993; Gutierrez and Ishihara, 2000; Lade *et al.*, 2009). The studies included drained and undrained tests using different types of sand. Deviation between principal stress direction and principal strain increment direction was noticed

when specimens were subjected to monotonic shearing at a fixed principal stress direction or subjected to pure rotation of principal stress axis at constant deviator stress. These experimental studies using HCA will be introduced in detail in section 2.4. Similar experimental evidence has also been shown by Wong and Arthur (1986) in both dense and loose sands during cyclic rotation of principal stresses using the directional shear cell apparatus. These studies showed that the deviation between the principal stress and the principal strain incremental directions could be more than $30°$ in sand during continuous rotation of the principal stress axes.

2.2.3 Previous numerical studies on non-coaxiality

Due to the limitation of laboratory method to explore the underlying mechanisms and particle scale information, numerical techniques like discrete element method (DEM) can be a useful method of study of soil behaviour. DEM is a numerical method proposed by Cundall (1971) for computing the motion of a large number of particles like molecules or grains of sand. Alonso-Marroquń *et al.* (2005) combined the continuous and the discrete method to investigate the effect of the induced anisotropy on the elastoplastic response of a two dimensional model. The 2-D discrete element model consisted of randomly generated convex polygons which had adjusted shapes and no voids between particles. The authors concluded that the incremental response of the plastic response was unidirectional. Thornton and Zhang (2006) carried out a series of two dimensional numerical simulations to study the shear banding and simple shear non-coaxial flow rules. 5000 elastic spheres with seven different sizes were simulated using DEM. From Figure 2-2 we can see

that the non-coaxial behaviour agrees with the results of Roscoe's study in Figure 2-1 (Roscoe, 1970). When the specimens have approached critical state, the directions of principal and principal strain increment were coaxial.

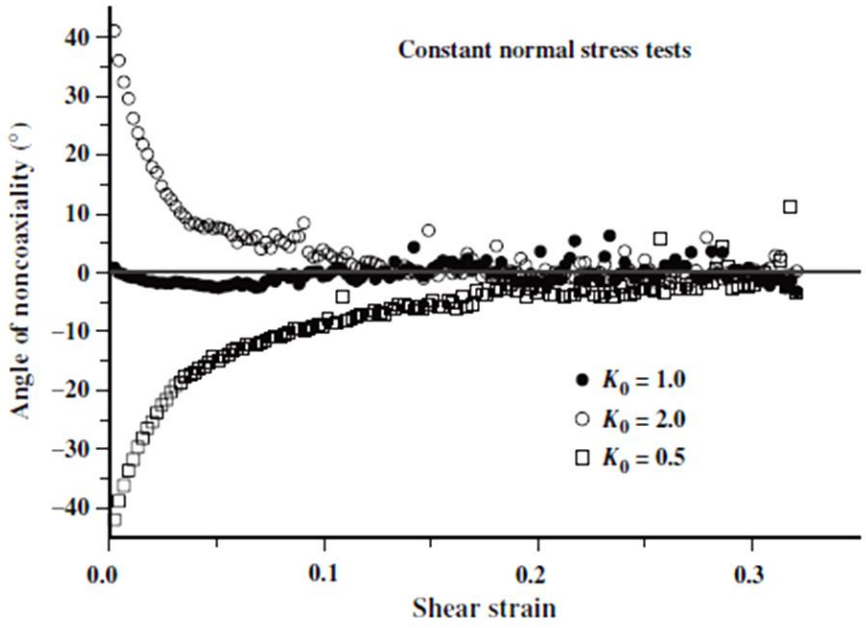

Figure 2-2 Evolutions of the angle of non-coaxiality (after Thornton and Zhang, 2006).

Li and Yu (2009) used a two dimensional DEM model to simulate granular material behaviour under monotonic loading at fixed strain increment directions. The study was focused on the effect of anisotropy on non-coaxiality. To investigate the initial anisotropy produced during specimen preparation, a specimen was generated using a controlled deposition method. Another specimen was prepared by preloading the initial anisotropic specimen along the deposition direction and then unloading it to an isotropic stress state. The specimens were tested in a number of loading directions varying from vertical to horizontal at 15 ° intervals. Figure 2-3 shows the curves of the directions of principal strain increments and principal stress versus the stress ratio. In Figure 2-3(a), very limited deviation angles were observed between the calculated

principal stress directions and the principal strain increments directions, the greatest value was under 5°. In this case the soil behaviour could be approximately considered as coaxial. This conclusion agrees well with the result of Miura *et al*. (1986) and Gutierrez *et al*. (1991). In Figure 2-3(b), much more significant non-coincidence between the axes of principal stress and strain increment was observed. The deviations were especially significant when the loading direction was close to the normal direction of the previous loading, with the exception of α=0°, where the symmetrical axis of the specimen coincides with the loading direction. The deviation between directions of principal stress and strain increment diminished gradually as shearing progressed to higher shear strain and larger stress ratio.

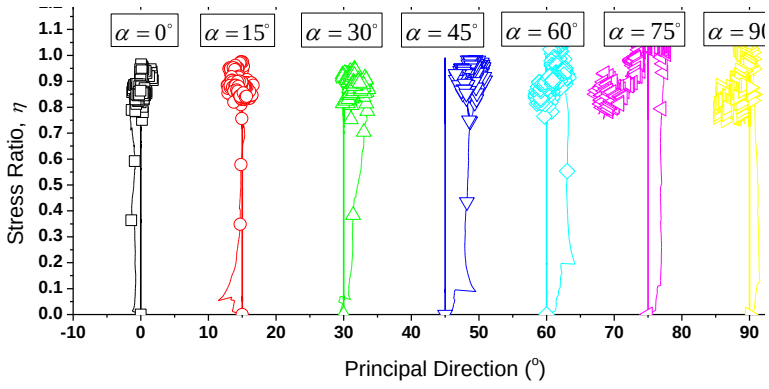

(a) Initially anisotropic specimen

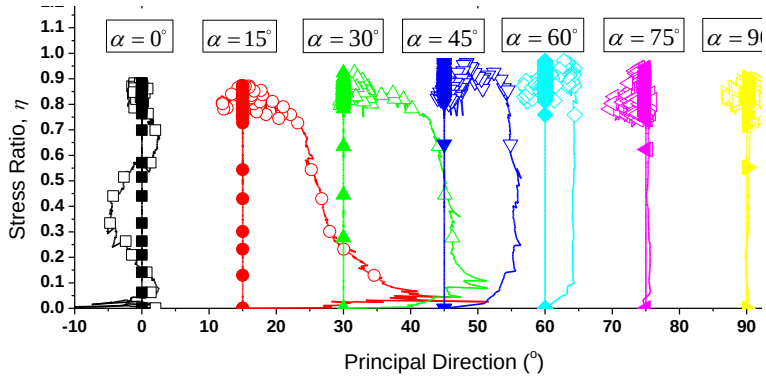

(b) Preloaded specimens

Figure 2-3 Stress and strain increment directions: (a) initially anisotropic specimens; (b) preloaded specimens (after Li and Yu, 2009).

For a safer geotechnical design, a precise prediction of magnitude and direction of deformation in soil is required. Although the effects of non-coaxiality have been studied widely by a number of researchers, the theory should be efficiently used to develop advanced plasticity models by introducing non-coaxial flow rules into analytical models. Yu and Yuan (2005) published their opinion of the importance of accounting for non-coaxial behaviour in modeling soil-structure interaction. Design might be unreliable due to the lack of consideration of non-coaxiality. Non-coaxiality has been applied into new models in geotechnical engineering. Yatomi *et al.* (1989) used a non-coaxial cam-clay model to simulate the formation of localized shear bands. Based on experimental studies, Gutierrez *et al.* (1993) proposed an elastoplastic constitutive model for the deformation of sand during rotational loading. In their model, the plastic principal strain increment direction was defined based on the current stress and the effects of inherent fabric anisotropy on non-coaxiality. Motivated by the observations of non-coaxial behaviour, Li and Dafalias (2004) introduced an extended platform model for anisotropic sand. The model treated the tangent loading as additional loading, called the rotational loading, which produced the non-coaxial and volumetric deformation components. Recently, Lashkari and Latifi (2007) focused on the simulation of non-coaxiality and presented a constitutive model to predict the anisotropic behaviour of granular soils under different stress paths. Yu and his co-workers have been doing lots of work on the non-coaxiality of granular materials. (Jiang *et al.*, 2005a and b; Yang and Yu, 2006a and b; Yu and Yuan, 2006; Yu, 2006). This project is part of the research study in the Nottingham Centre of Geomechanics (NCG) to gain experimental support for the numerical models.

2.3 HOLLOW CYLINDER APPARATUS

2.3.1 Introduction

It has been widely recognized that soil behaviour depends on the stress path. Therefore, the stress path method or a generalized model for behaviour which incorporates the dependence on stress path should be used to predict the performance of soil or soil-supported structure (Lambe, 1967). In order to study generalized mechanical characteristics of granular materials, a device with the ability to monitor and independently control the principal stresses and the direction of the major principal stress is urgently required. The conventional laboratory testing devices (e.g. triaxial cell, direct shear box, plane-shearing apparatus) are not capable of rotating the major principal stress direction and controlling the relative magnitude of the intermediate principal stress.

In this situation, a hollow cylindrical apparatus (HCA) is an extremely valuable tool for studying constitutive behaviour under generalized stress conditions. The HCA allows independent control of the magnitudes of the three principal stresses and rotation of the major-minor principal stress axes while recording the specimen deformational and pore pressure responses. When each of these boundary stresses can be controlled independently, both the principal stress direction, α, and the relative magnitude of the intermediate principal stress, b, can be controlled, thus the HCA can facilitate more generalized stress path testing than the conventional test apparatus. It is also possible to control

(or measure) the pore water pressure and apply back pressure, so that drainage conditions can be controlled and both drained and undrained tests can be performed. As a result, the HCA offers an opportunity of extending the stress path approach to include simulation of both principal stress rotation and variation in intermediate principal stress, as well as conducting fundamental research into the effect of principal stress rotation under a reasonably generalized stress state. Moreover, laboratory tests normally performed in the other devices, such as in triaxial compression and extension or simple shear tests can be simulated with the HCA.

2.3.2 Principles of hollow cylinder testing

Figure 2-3 illustrates idealized stress conditions in a hollow cylindrical element subjected to axial load, W, torque, M_T, internal pressure, P_i, and external pressure, P_o.

During shearing, the torque, M_T, develops shear stresses, $\tau_{\theta z}$ and $\tau_{z\theta}$ ($\tau_{\theta z} = \tau_{z\theta}$) in vertical and horizontal planes，the axial load, W, contributes to a vertical stress, σ_z. P_i and P_o determine σ_r, σ_θ. The relationship between σ_r and σ_θ, is established by the differences between P_i and P_o.

$$\sigma_\theta = \sigma_r + r\frac{d\sigma_r}{dr} \tag{2.7}$$

where r is the radial distance to a point in the hollow cylinder, and $d\sigma_r$ and $d\sigma_\theta$ are the radial and circumferential stress increments respectively. When $P_i = P_o$, σ_r becomes identical to σ_θ.

The state of stress in a hollow cylinder test is defined with reference to cylindrical coordinates, in terms of the stress components shown in Figure 2-4.

$$[\sigma]=\begin{bmatrix}\sigma_r & 0 & 0\\ 0 & \sigma_\theta & \tau_{\theta z}\\ 0 & \tau_{z\theta} & \sigma_z\end{bmatrix} \tag{2.8}$$

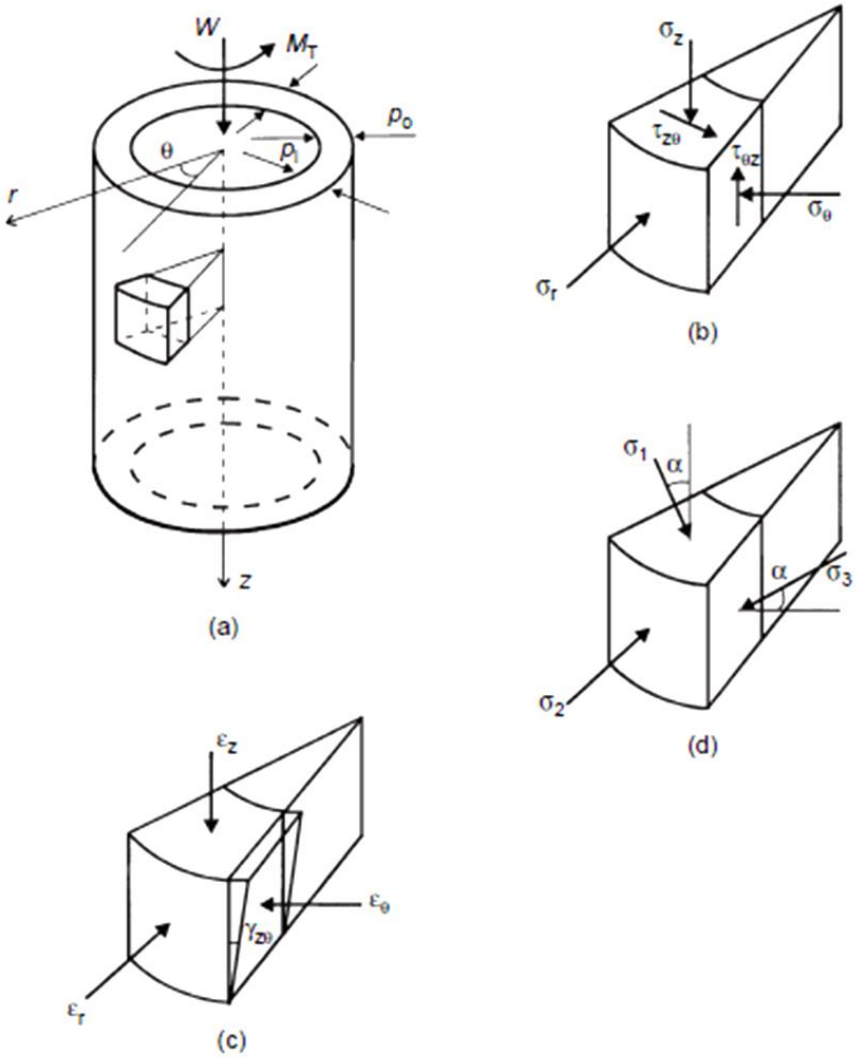

Figure 2-4 Idealized stress and strain components within the HCA subjected to axial load, *W*, torque, M_T, internal pressure, P_i, and external pressure, P_o: (a) hollow cylinder coordinates; (b) element component stresses; (c) element component strains; (d) element principal stresses (after Zdravkovic and Jardine, 2001).

Since the stresses will not be uniform across the wall of the cylinder for various loading conditions, to consider the hollow cylinder as an element, it becomes necessary to calculate average stresses, $\bar{\sigma}_z, \bar{\sigma}_r, \bar{\sigma}_\theta, \bar{\tau}_{\theta z}$. Hight *et al.* (1983) used the following expressions:

Average vertical stress $$\bar{\sigma}_z = \frac{W}{\pi(r_o^{\,2} - r_i^{\,2})} + \frac{P_0 r_o^{\,2} - P_i r_i^{\,2}}{r_o^{\,2} - r_i^{\,2}} \tag{2.9}$$

Average radial stress $$\bar{\sigma}_r = \frac{P_o r_o + P_i r_i}{r_o + r_i} \tag{2.10}$$

Average circumferential stress $$\bar{\sigma}_\theta = \frac{P_o r_o - P_i r_i}{r_o - r_i} \tag{2.11}$$

Average shear stress $$\bar{\tau}_{\theta z} = \frac{3M_T}{2\pi(r_o^{\,3} - r_i^{\,3})} \tag{2.12}$$

In hollow cylinder tests, the radial stress, $\bar{\sigma}_r$, is usually equal to the intermediate principal stress (σ_2). The major and minor principal stresses, σ_1 and σ_3, are observed from the average stress components $\bar{\sigma}_\theta$, $\bar{\sigma}_z$ and $\overline{\tau_{z\theta}}$ as following:

$$\sigma_1 = \frac{\bar{\sigma}_z + \bar{\sigma}_\theta}{2} + \sqrt{\left(\frac{\bar{\sigma}_z - \bar{\sigma}_\theta}{2}\right)^2 + \overline{\tau_{\theta z}}^{\,2}} \tag{2.13}$$

$$\sigma_2 = \bar{\sigma}_r \tag{2.14}$$

$$\sigma_3 = \frac{\bar{\sigma}_z + \bar{\sigma}_\theta}{2} - \sqrt{\left(\frac{\bar{\sigma}_z - \bar{\sigma}_\theta}{2}\right)^2 + \overline{\tau_{\theta z}}^{\,2}} \tag{2.15}$$

By regarding the specimen as a single element, the state of strain is

presented in cylindrical coordinates in terms of the following components:

$$[\varepsilon]=\begin{bmatrix} \varepsilon_r & 0 & 0 \\ 0 & \varepsilon_\theta & \frac{\gamma_{\theta z}}{2} \\ 0 & \frac{\gamma_{z\theta}}{2} & \varepsilon_z \end{bmatrix} \tag{2.16}$$

Also, it is necessary to calculate the average strains. According to the paper of Hight *et al.* (1983), the average strains are calculated using the following equations:

Average axial strain $$\bar{\varepsilon}_z = \frac{w}{H} \tag{2.17}$$

Average radial strain $$\bar{\varepsilon}_r = -\frac{u_0 - u_i}{r_o - r_i} \tag{2.18}$$

Average circumferential strain $$\bar{\varepsilon}_\theta = -\frac{u_0 + u_i}{r_o + r_i} \tag{2.19}$$

Average shear strain $$\bar{\gamma}_{\theta z} = \frac{2\theta(r_o^3 - r_i^3)}{3H(r_o^2 - r_i^2)} \tag{2.20}$$

Where the definitions of average stresses and strains are shown in Figure 2-5.

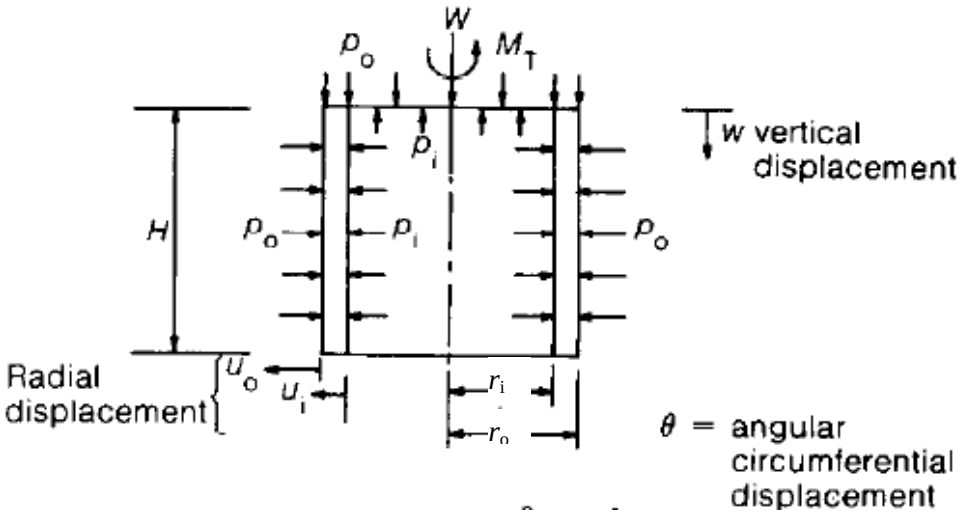

Figure 2-5 Definitions of average stresses and strains (after Hight *et al.*, 1983)

Since the average values of ε_z and $\gamma_{\theta z}$ are based on strain compatibility only, the expressions for the average strains are valid and independent of the constitutive law of the material. The average values of ε_r and ε_θ are based on a linear variation of radial displacement across the wall of the specimen. In the hollow cylinder test, the radial strain (ε_r) is usually the intermediate principal strain, ε_2. The major and minor principal strains can be observed from the average strain components:

$$\varepsilon_1 = \frac{\overline{\varepsilon_z} + \overline{\varepsilon_\theta}}{2} + \sqrt{\left(\frac{\overline{\varepsilon_z} - \overline{\varepsilon_\theta}}{2}\right)^2 + \left(\frac{\overline{\gamma_{\theta z}}}{2}\right)^2} \tag{2.21}$$

$$\varepsilon_2 = \overline{\varepsilon_r} \tag{2.22}$$

$$\varepsilon_3 = \frac{\overline{\varepsilon_z} + \overline{\varepsilon_\theta}}{2} - \sqrt{\left(\frac{\overline{\varepsilon_z} - \overline{\varepsilon_\theta}}{2}\right)^2 + \left(\frac{\overline{\gamma_{\theta z}}}{2}\right)^2} \tag{2.23}$$

Parameters α and b are two variables of stress path to describe fundamentally different aspects in the applied state of state of stress. α (as shown in Figure 2-4(d)), is the inclination of major principal stress direction with respect to the vertical axis, which can be varied from 0 to 90°. It can be computed from the known average stress components

$$\tan 2\alpha = \frac{2\overline{\tau_{\theta z}}}{\overline{\sigma_z} - \overline{\sigma_\theta}} \tag{2.24}$$

b is defined as the relative magnitude of the intermediate principal stress, which can be varied from 0 to 1:

$$b = \frac{(\sigma_2 - \sigma_3)}{(\sigma_1 - \sigma_3)} \tag{2.25a}$$

For the particular case of equal internal and external pressure, $P_i=P_o=P$, σ_r and σ_θ are usually assumed to be equal to P. From equation (2.10) σ_2 is equal to P as well. Therefore, changes in the α angle are accompanied by changes in magnitude of b. When $P_i=P_o$

$$b = \sin^2 \alpha \quad \text{(Hight. } et\ al.\text{, 1983)} \tag{2.25b}$$

The direction of strain increment $\alpha_{d\varepsilon}$ can be calculated from the incremental strain components

$$\tan 2\alpha_{d\varepsilon} = \frac{d\gamma_{\theta z}}{d\varepsilon_z - d\varepsilon_\theta} \tag{2.26}$$

The amount of non-coaxiality was defined as the difference between the directions of principal stress and of principal strain increments as, $\alpha_{d\varepsilon} - \alpha$.

2.3.3 Stress distribution in hollow cylinder specimens

Even though hollow cylinder devices offer highly promising capabilities for the study of soil behaviour, their use has been subjected of criticism. These objections arise principally due to the non-uniform distribution of stresses and strains within the specimens. Stress non-uniformities occur across the wall of a hollow cylinder due to the specimen geometry, end restraint, the application of torque or different internal and external pressures. The tested specimen size affects significantly the stress non-uniformity level. When the wall thickness is reduced or the inner radius is increased, the stress distribution becomes more uniform (Sayao and Vaid, 1991).

Because it is not easy to measure either the stresses or the strains across

the wall of the hollow cylinder directly, it becomes essential to set bounds to the differences between the calculated and real averages and the magnitude of deviations from the real averages. By using the finite element method and assuming that material behaves as either isotropic or elasto-plastic (modified Cam-clay), Hight *et al*. (1983) defined the non-uniformity coefficients β_1 and β_3 for individual stress components, as shown in Figure 2-6. The magnitude of the difference between calculated and real stress average can be characterized by normalized parameter β_1:

$$\beta_1 = \frac{\left|\overline{\sigma}^{*} - \overline{\sigma}\right|}{\sigma_L} \tag{2.27}$$

where $\overline{\sigma}^{*}$ is the real average, $\overline{\sigma}$ is the calculated average and σ_L, which is defined as $(\left|\overline{\sigma}_\theta\right| + \left|\overline{\sigma}_r\right|)/2$), is a measure of the stress level. Therefore β_1 is inversely related to accuracy. β_3 is the parameter to quantify the level of non-uniformity of stresses:

$$\beta_3 = \frac{\int_a^b \left|\sigma(r) - \overline{\sigma}^{*}\right| dr}{(r_o - r_i)\sigma_L} \tag{2.28}$$

where $\sigma(r)$is the distribution of the particular stress, σ_z, σ_θ or $\tau_{\theta z}$ under consideration across the hollow cylinder specimen. β_3 may be used to minimize the difference between the actual stress distribution and the real average.

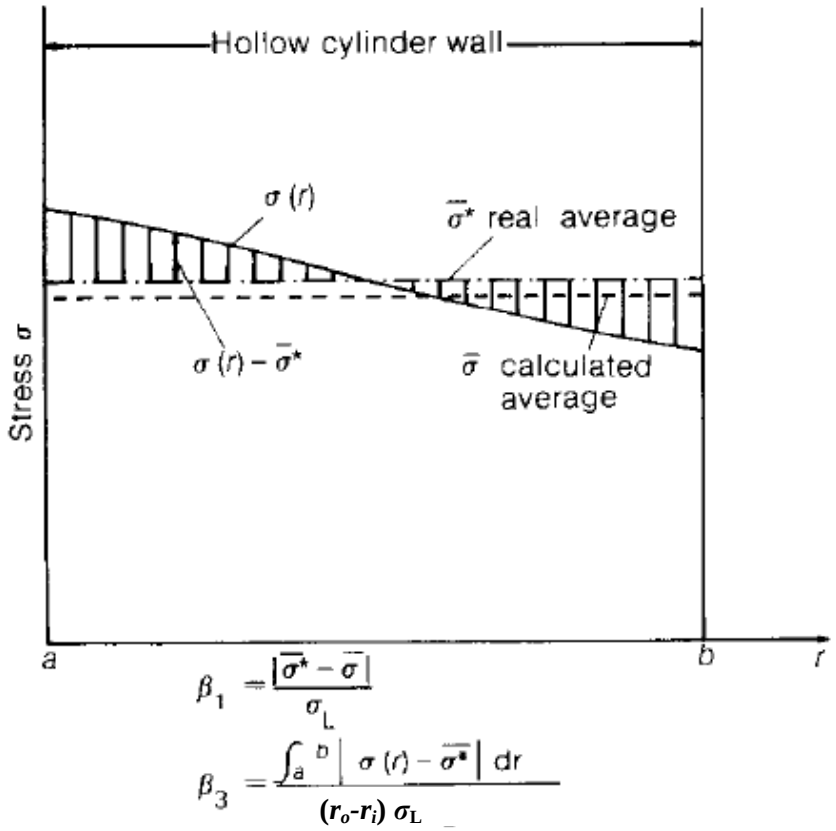

Figure 2-6 Definitions used for stress non-uniformity and accuracy (after Hight *et al.*, 1983).

For differences in strain averages and strain non-uniformities, similar definitions for β_1 and β_3 are used. According to Hight *et al.* (1983), the magnitudes of β_1 and β_3 are dependent on stress state, specimen geometry and the constitutive law of the specimen's material. The authors recommended keeping stresses within a limit where the ratio of outer to inner cell pressures is $0.9<P_o/P_i<1.2$, and β_3 should be kept below 11%.

Vaid *et al.* (1990) analyzed non-uniformities in hollow cylinder specimens by using a linear elastic model. By comparing the results with those of a finite element method, they argued that the use of the parameter β_3 defined by Hight *et al.* (1983) could lead to an underestimation of the HCA non-uniformities and

proposed a different stress non-uniformity parameter across the wall of the specimen in terms of the stress ratio R ($R= \sigma_1' / \sigma_3'$):

$$\beta_R = \frac{R_{max} - R_{\min}}{\overline{R}} \tag{2.29}$$

where R_{max} and R_{min} are the maximum and minimum stress ratios and $\overline{R}$ is the average value.

Figure 2-7 shows a comparison of the two definitions of non-uniformities for two stress states. The specimens had an outer radius of 7.1cm and an inner radius of 5.1cm. The result shows that the level of stress non-uniformities increases with the increase of R. The authors suggested that the stress non-uniformities were considered acceptable if the maximum difference between R_{max} and R_{av} was below 10%, which corresponds to a value $\beta_R \leq 0.2$. In order to keep the non-uniformities levels acceptable, they also recommend keeping the stress ratio R below 2.5. The authors also pointed out the assumptions used to define the non-uniformities of Hight *et al.* (1983) were inconsistent as an elastic constitutive law was used for the stress component of $\tau_{\theta z}$ while a plastic law was used for the other components. By applying the elastic law to $\tau_{\theta z}$, the idea that keeping outer and inner cell pressures constant would help to minimize the stress non-uniformities, would not be suitable.

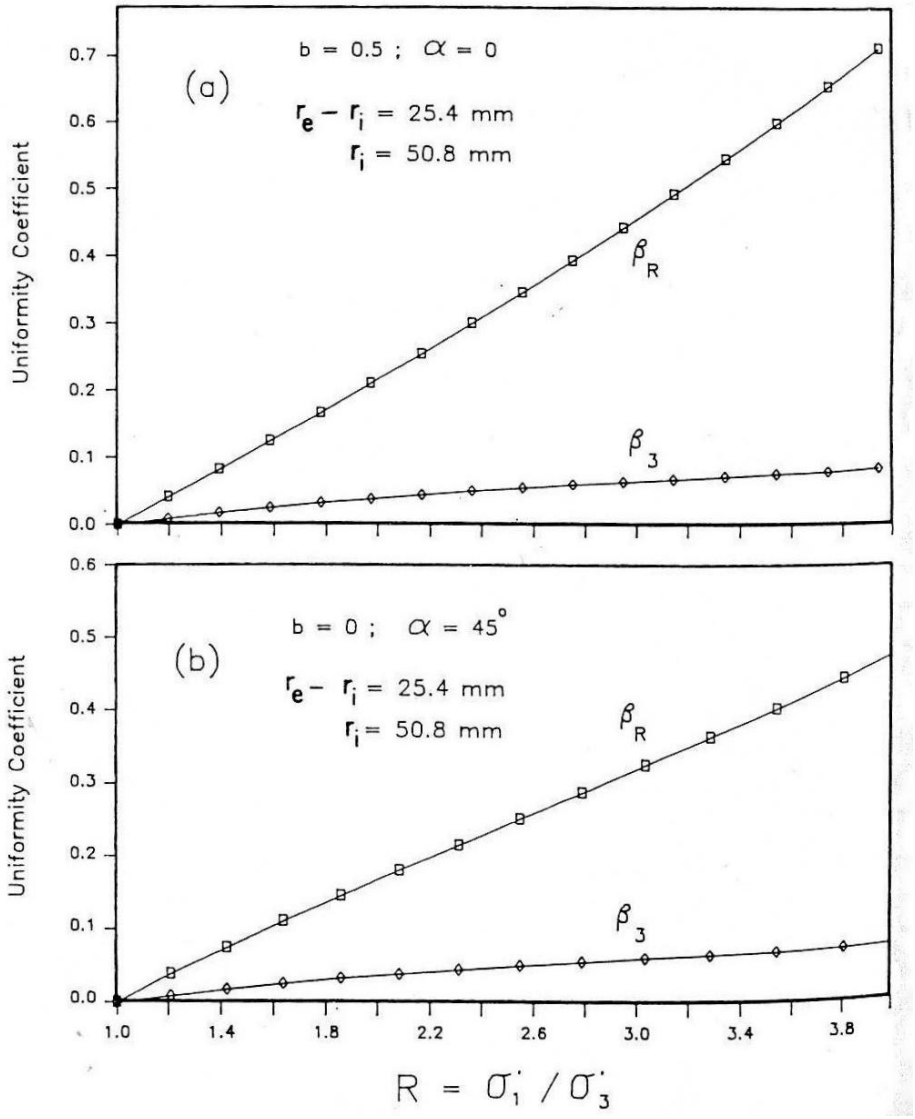

Figure 2-7 Effect of stress ratio level on non-uniformity coefficients (after Vaid *et al.*, 1990)

Wijewickreme and Vaid (1991) indicated that relatively large stress and strain non-uniformities could arise in hollow cylinder specimens, particularly in the small stress/strain (near elastic) region, for certain loading conditions. On the other hand, when large differences between P_o and P_i occurred, the stress non-uniformity across the wall became very large. According to their study with non-linear elastic soil, the stress non-uniformity coefficient β_R only increased continuously with the stress ratio R at lower values of R. β_R reached a

peak point or even started to decrease when *R* was higher.

Menkiti (1995) and Porovic (1995) found that in cases free from end restraint, the equations defined by Hight *et al.* (1983) to calculate average stresses and strain were sufficiently accurate for interpreting hollow cylinder tests. Furthermore, very good agreement was observed between the stress-strain and strength response of hollow cylinder simulations and a uniform single element.

Rolo (2003) used a classical elasto-plastic non-linear, modified Cam-clay soil model with a finite element method to analyze most of the features that were thought to influence the development and magnitude of non-uniformities. The non-uniformity increased as the specimen approached the failure surface, which agreed with the observations by Hight *et al.* (1983) on specimens with fixed ends. The specimen with free-ends resulted in more uniform conditions. The results revealed that non-uniformities could result in either over or underestimation of certain stress and strain parameters.

Naughton and O'Kelly (2007) studied the stress distribution in smaller sand specimens with the dimension of $I.D$=71mm, $O.D$=100mm, H=200mm. The stress non-uniformity levels were found to be acceptable with the ratio of outer and inner cell pressure P_o/P_i kept between 0.9~1.2, as well as the stress ratio R kept under 2.0

2.3.4 Specimen geometry

The uniformity of the stress distribution across the wall of hollow cylinder specimens is affected by the specimen geometry, both the curvature and end restraint. This result came from the detailed study of stress distributions using both isotropic linear elastic and plastic formulations to represent the soil in specimens of different geometries under different load combinations. A suitable height of the specimen can engender reasonably uniform distributions of stress (Hight *et al.*, 1983). The differences between real and calculated averages of stress and strain were attributed to the selected specimen geometry and the stress path. As the ratio of inner to outer radii, r_i/r_o, approaches unity, both β_1 and β_3 reduce. Figure 2-8 was produced by Porovic (1995) by assuming a linear variation of applied shear stresses, $\tau_{\theta z}$, and a linear elastic constitutive law, to display the ratio of maximum and minimum shear stresses to average shear stress for three different specimen dimensions. As the diagram shows, the level of non-uniformity for a fixed wall thickness would reduce with the increase of specimen diameter. Therefore, the degree of the stress difference between the calculated and real average was minimized as the inner radius of specimen increased. The selection of a suitable geometry for the hollow cylinder specimen would reduce stress non-uniformities to an acceptable level. Saada (1988) also quoted that selecting particular specimen geometry played a major role in reducing non-uniformity of stress distribution.

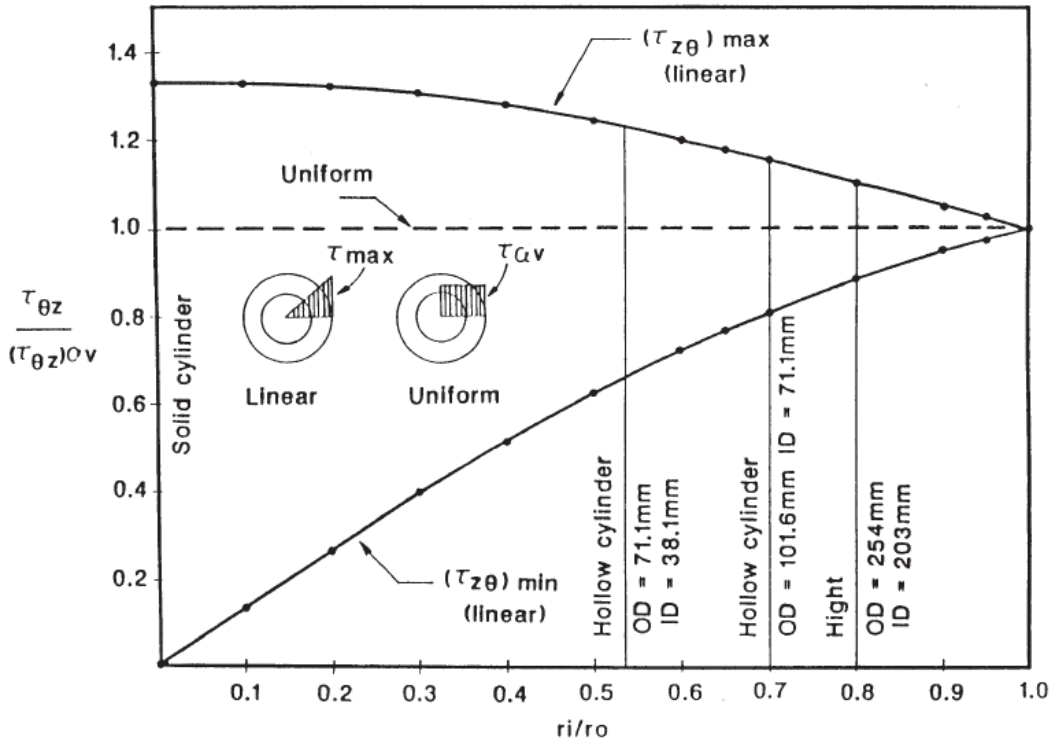

Figure 2-8 Shear stress distribution in Hollow cylinder torsional shear test specimens (after Porovic, 1995).

Firstly, for sand specimens, an appropriate wall thickness should be applied to meet the following criteria:

a) A wall thickness sufficiently large enough relative to the maximum grain size of the tested specimen so the failure mechanisms would not be constrained.

b) A specimen volume sufficiently large in relation to the potential volume change resulting from membrane penetration.

c) A uniform density across the wall.

In order to determine a reasonable specimen geometry, based on elasticity theory and the assumption that the central zone, free from end effects should be the same length as the zone influenced by the platens, Saada and Townsend (1981) suggested the following criteria for the specimen geometry:

a) Height: $H \geq 5.44\sqrt{r_o - r_i}$

b) Inner radius r_i: $n = \frac{r_i}{r_o} \geq 0.65$

where H is the height, r_i and r_o are the inner and outer radii of the specimen, and n is the ratio of inner and outer radii.

The criteria proposed by Sayao and Vaid (1991) were as follows:

a) Wall thickness r_o-r_i=20 to 60 mm

b) Inner radius: $0.65 \leq \frac{r_i}{r_o} \leq 0.82$

c) Height: $1.8 \leq \frac{H}{2r_o} \leq 2.2$

2.3.5 Membrane penetration errors

In the hollow cylinder test, rubber membranes are used to enclose the specimens. The effect of membrane penetration on the external measurement of volumetric deformations is attributed to the flexible membrane penetrating into or withdrawing out of the external voids of the soil specimen. The membrane penetration (MP) may influence the computed specimen's volume change in a drained test, and the magnitude of the pore water pressure measured in an undrained test. Therefore this effect should be accounted for to make a confident assessment of actual stress-strain behaviour of saturated granular

materials in a test. For materials of medium sand size having mean particle size of $D_{50} \geq$ 0.1mm, particularly for the large diameter specimens, correction for the membrane penetration is of great importance and should be applied (Molenkamp and Luger, 1981).

Studies of the effect of membrane penetration have been undertaken and the particle size of the material is identified to be the major factor to influence the membrane penetration (Frydman *et al*., 1973).

Theoretical expressions for the unit membrane penetration suggested by Baldi and Nova (1984) and Kramer and Sivaneswaran (1989) are as following:

$$A_{MP} \cdot v_{MP} = \frac{1}{2}\frac{d}{D} V_{soil} \left(\frac{\sigma_h^{'} d}{E_m t_m} \right)^{\frac{1}{3}} \tag{2.30}$$

$$v_{MP} = 0.395 d (1-\alpha) \left(\frac{1-\alpha}{5 + 64\alpha^2 + 80\alpha^4} \right)^{\frac{1}{3}} \left(\frac{\sigma_h^{'} d}{E_m t_m} \right)^{\frac{1}{3}} \tag{2.31}$$

where v_{MP}= unit membrane penetration (in mm); A_{MP}= surface area of membrane (in mm); d= mean particle size, D_{50} (in mm); D= Specimen diameter (in mm); V_{soil}= volume of soil specimen (in mm^3); E_m= Young's modulus of membrane (in kN/m^2); t_m= thickness of membrane (in mm); σ'_h= effective confining pressure (in kPa).

A new approach for the assessment of MP was obtained from the differences between measured volume strain of the specimen and the volume of the inner chamber using a single hollow cylindrical specimen under hydrostatic loading by Sivathayalan and Vaid (1998). The proposed expression for the unit

membrane penetration is:

$$\varepsilon_m = \frac{\Delta V_{sr} - \Delta V_{ir}(n^2 - 1)}{\chi(A_{im} + A_{om})} \tag{2.32}$$

where ε_m is the unit membrane penetration; ΔV_{sr} and ΔV_{ir} are the measured volume changes of the inner chamber and the specimen, respectively; n is the ratio of the outer to inner radii of the specimen, and A_{im} and A_{om} are the surface areas of the specimen covered by the inner and outer membranes, respectively.

Kuwano (1999) evaluated the apparent volumetric strains due to MP over the vertical sides of the specimens using Ham River Sand specimens with rough and lubricated ends. By comparing the measured volume deformations with a conventional volume gauge and with local instrumentation, she obtained the following relationship for v_{MP} based on isotropic loading/unloading/reloading tests:

$$v_{MP} = C_{MP} \cdot \Delta \log \sigma'_h = C_{MP} \cdot \log \frac{\sigma'_h}{\sigma'_{h0}} \tag{2.33}$$

where C_{MP} is a parameter that depends on specimen size and density, membrane thickness and elastic modulus, and on particle shape and size; σ'_h and σ'_{h0} are the current and initial effective confining pressures. From Kuwano's experiments, C_{MP} is 0.015mm for 100mm diameter specimens of Ham River Sand encased in a 0.5mm thick latex membrane. Kuwano (1999) found that Eq.2-32 matched the expressions suggested by Baldi and Nova (1984) and Kramer and Sivaneswaran (1989) very well.

2.3.6 Previous experimental studies using HCA

The HCA is becoming a popular testing device all around the world for geomechnical research. Hight *et al.* (1983) was one of the researchers who first introduced a hollow cylinder apparatus for investigating the effects of principal stress rotation in sands and clays. His colleagues then used it to investigate anisotropy and principal stress rotation in drained and undrained sand (Symes *et al.*, 1982, 1984, 1988). HCA has been widely used to study the anisotropy and non-coaxial behaviour of sand (Ishihara and Towhata, 1983; Symes *et al.*, 1984, 1988; Miura *et al.*, 1986; Pradel *et al.*, 1990; Vaid *et al.*, 1990； Gutierrez *et al.*, 1991, 1993; Gutierrez and Ishihara, 2000; Zdravkovic and Jardine, 2001; Li and Dafalias, 2004; Lade *et al.*, 2009). Vaid *et al.* (1990) presented a HCA with the following dimension: 15.2cm (*O.D*) × 10.2cm (*I.D*) × 30.2cm (*H*), including the design, performance and utility of the equipment. Sayao and Vaid (1996) then investigated the effect of intermediate principal stress on the deformation of Ottawa sand by using the same HCA. The tests were performed followed different stress paths varying the parameter *b*.

The HCA has also been used to study the characteristics of clay. Silvestri *et al.* (2005) used the HCA to study typical undrained extension behaviour of saturated clay. The HCA was modified from a hydraulic triaxial cell to permit testing of thick-walled cylindrical specimens of different dimensions. The specimens were prepared with the external diameter 100mm, internal diameter 50mm, with height of 100mm, and external diameter 127mm with internal diameter 38mm with the same height. Two different HCAs were employed by

Nishimura *et al.* (2007) to investigate the shear strength anisotropy of natural London Clay from Heathrow Terminal 5. One of the apparatus had a dimension of 70mm (*O.D*) × 38mm (*I.D*) × (170~190)mm (*H*), and the dimension for the other one was 100mm (*O.D*) × 60mm (*I.D*) × 200mm (*H*). Rolo (2003) used the HCA to study the stress-strain and strength anisotropy of a sand-clay mixture. The tests involved a range of fixed values of α and b.

2.4 PREVIOUS STUDIES ON NON-COAXIALITY OF SOIL BEHAVIOUR USING HCA

Symes *et al.* (1984) studied the anisotropy and the effects of principal stress rotation in medium-loose Ham River sand. The tests were carried out under an undrained condition using the hollow cylinder apparatus described by Hight *et al.* (1983), with the dimensions of 254mm/203mm/254mm (*O.D/I.D*/ height). While maintaining mean pressure, *P*, constant at 600kPa and *b* constant at 0.5, three tests were performed with the direction of the major principal stress α fixed at 0°, 24.5° and 45°, and the deviator pressure *q* was increased in small increments until failure. For test with α=0°, the major principal stress was vertical and coincident with the axis of symmetry of the specimen, therefore coaxiality of the principal stress and strain increment directions was obtained. For tests with α=24.5° and α=45°, as shown in Figure 2-9, directions for principal stress α and for strain increment $\alpha_{d\varepsilon}$, were not coincident. The maximum deviation reached as much as 20 degrees. The degree of non-coaxiality reduced as the specimen approached the failure point.

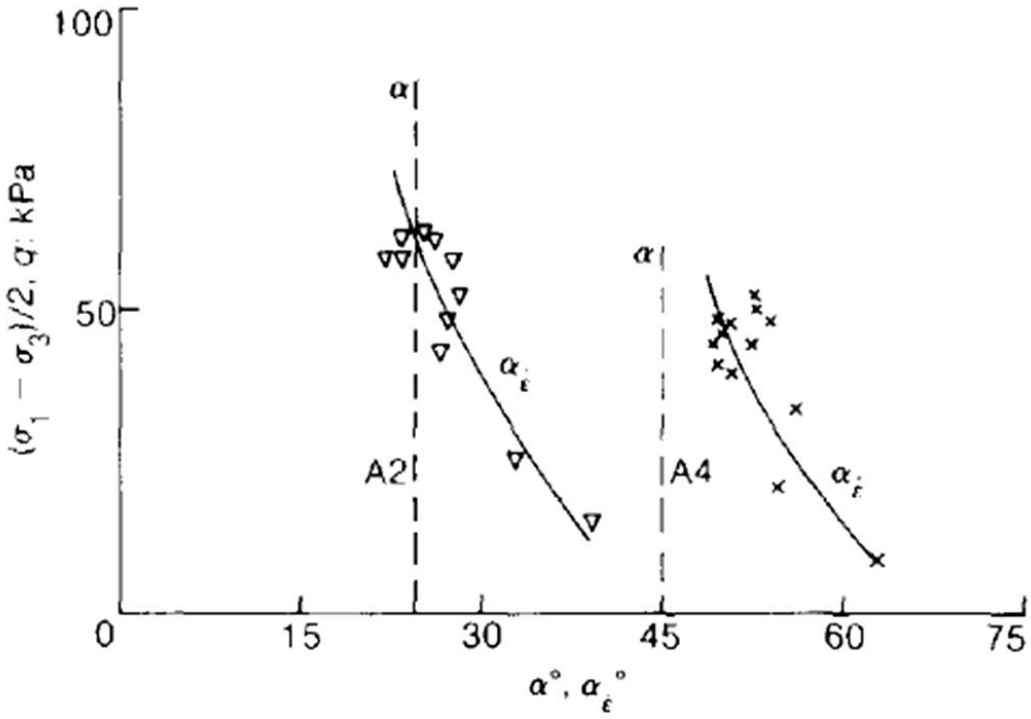

Figure 2-9 Principal strain increment directions in tests with α=24.5 ° and with α=45 ° for undrained tests (after Symes *et al.,* 1984) X axis: directions of principal stress and strain increment; Y axis: $(\sigma_i - \sigma_3)/2$.

Before the equipment was formally introduced in 1983 by Hight *et al.*, Symes *et al.* (1982) had published their research on the anisotropy and effects of intermediate principal stress and of the stress rotation using the HCA. Drained tests were conducted on Ham river sand with the effective stress held constant at 600kPa and back pressure at 400kPa.The study was focused on the influence of initial anisotropy (monotonic loading tests with α at 45 °, 67.5 ° and 90 °, and b=0.5), influence of b, and influence of continuous principal stress rotation (tests with constant b=0.5, constant q=110kPa, and α rotated from 0 ° towards 90 °). Figure 2-10 shows the results from monotonic loading and pure rotation tests. In Figure 2-10(a), the directions of principal strain increment were found to be larger than the stress direction. In Figure 2-10(b), non-coaxial

soil behaviour was obtained. The degree of non-coaxiality reduced with the rotation of α.

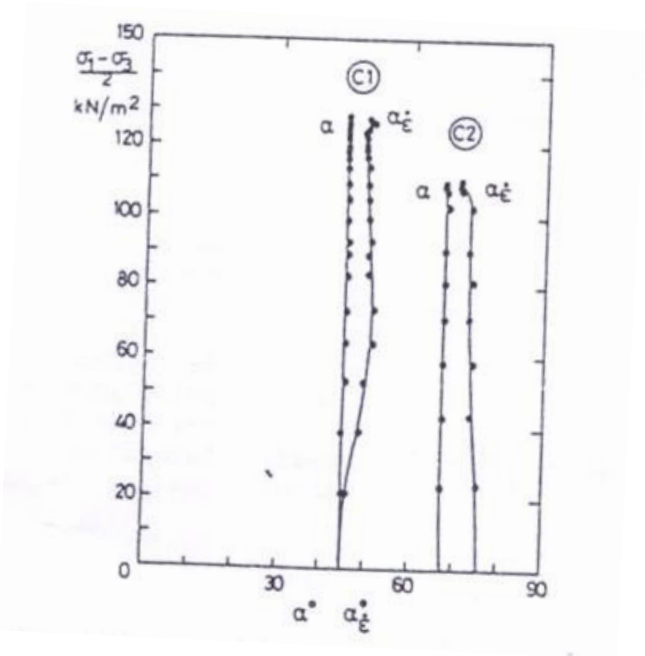

(a) monotonic loading tests with α=45 °and with α=67.5 °. X axis: directions of principal stress and strain increment; Y axis: $(\sigma_1 - \sigma_3)/2$

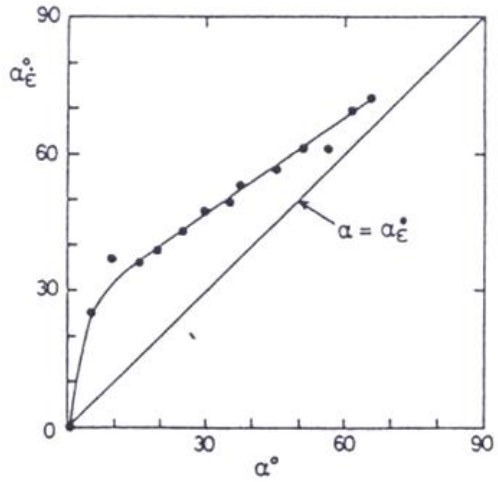

(b) pure rotation of α at constant q=110kPa

Figure 2-10 Results of drained tests: (a) monotonic loading tests with α=45 °and with α=67.5 °; (b) pure rotation of α at constant q=110kPa (after Symes *et al.*, 1982).

The authors carried out another investigation to study the effects of principal stress rotation on the behaviour of a drained saturated medium-loose

sand (Symes *et al.* 1988). The specimens were sheared along the same stress paths as in their previous work in 1984. All tests were conducted by keeping *b* constant at 0.5, the mean pressure *P* at 600kPa, and back pressure at 400kPa. Non-coaxiality between the axes of principal stresses and principal strain increment was obtained as shown in Figure 2-9. But again, similar to the results from undrained tests, when the major principal stress direction α=0 °, non-coaxiality was not obtained. For the other two tests, the non-coaxiality degree decreased with the increasing *q*, although for test α=24.5 °, the axes of principal stress and principal strain rate were coincident at some point at the early stage, as shown in Figure 2-11. A larger deviation of about 20 ° was obtained at the beginning of test when α=45 °.

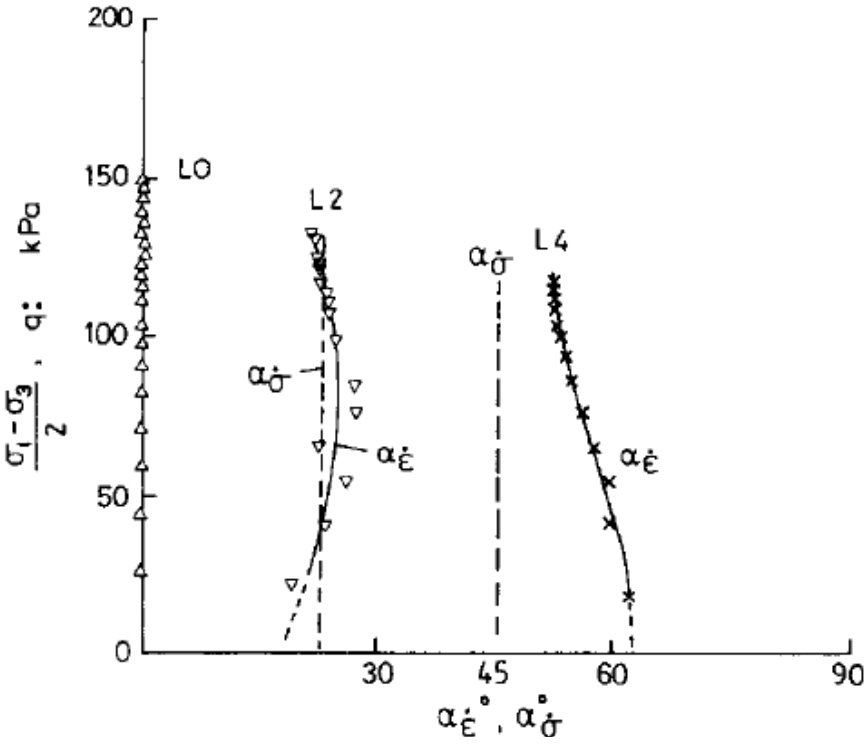

Figure 2-11 Principal strain increment directions in tests with α=24.5 °and with α=45 °for drained tests (after Symes *et al.*, 1988).

Several researchers in Japan have also worked on the behaviour of granular materials using the HCA for a long time, and have achieved prominence. As early as 1983, Ishihara and Towhata published a paper regarding to the response of sand under cyclic rotation of principal stress directions. In their study, a hollow cylindrical specimen with dimensions of 60mm×100mm×104mm (*I.D*×*O.D*×*H*) was prepared using Toyoura sand. Cyclic torsion was applied to the specimen. The result showed that directions of strain increments did not point to the same direction as the current principal stress directions or the stress increments directions. The principal strain increment directions were larger than the stress directions. At the beginning of the cyclic stage, the deviation was larger than that in the last stage, where the strain increment axis nearly coincided with the principal stress direction (see Figure 2-12). This was due to the elastic and plastic parts of the deformation that developed during the loading played different roles. Elastic component dominated at early stage and reduced with the shearing, and then the plastic part of deformation became dominant.

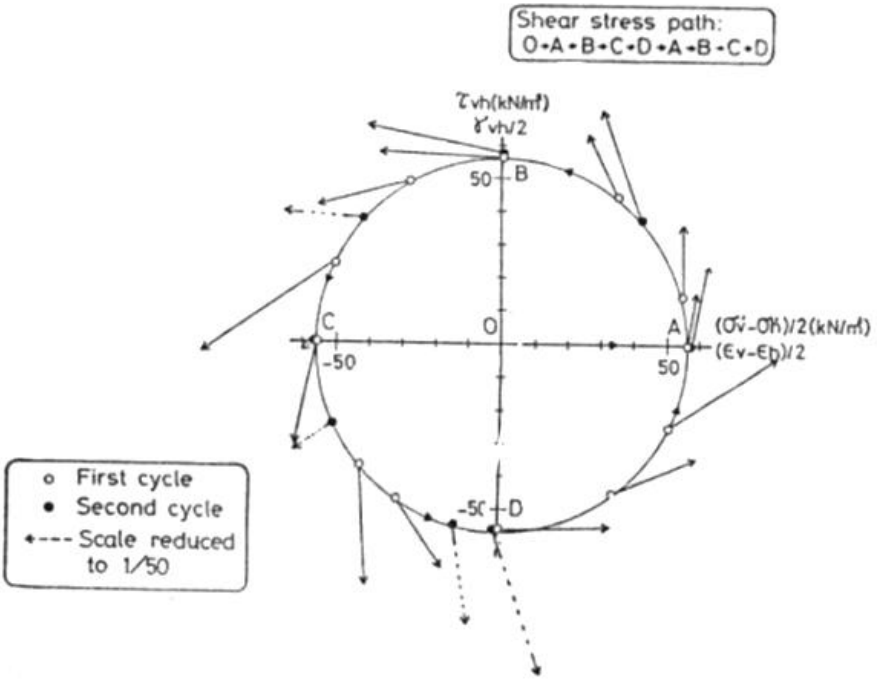

Figure 2-12 Plot of strain increment vectors superimposed on the stress space (after Ishihara and Towhata, 1983).

To investigate the fundamental deformation behaviour of anisotropic sand under more general stress condition involving the rotations of principal stress axes, Miura *et al.* (1986) carried out a series of drained tests on dense Toyoura sand specimens using a hollow cylinder apparatus. They used specimens of 60 mm (*I.D)* × 100 mm (*O.D*) × 200 mm height (*H)*. With the value of effective mean stress *p'* being held constant at 98kPa and the value of the intermediate principal stress ratio, *b,* also being kept constant at 0.5, two series of different tests were undertaken. The first one was the monotonic shear test. With a fixed major principal stress direction α, the stress ratio $(\sigma_i' - \sigma_3')/(\sigma_1' + \sigma_3')$ was increased until the specimen failed (F test). The principal stress direction α was fixed at 0 °, 15 °, 30 °, 45 °, 60 °, 75 °, 90 °. The second series had the stress ratio $(\sigma_i' - \sigma_3')/(\sigma_1' + \sigma_3')$ held constant, and the major principal stress axis rotated clockwise (R test). As shown in Figure 2-13(a), in the F test, the directions of

principal strain increment deviated slightly from the current principal stress axes. Unlike the results from the study of Symes *et al.* (1984), the maximum deviation was as small as 7 °, and towards the direction of $\alpha_{d\varepsilon}$=45 °. For F 0 °and F 180 °, the principal strain increment axis coincides with one of the principal stress axes, which agreed with the study of Symes *et al.* (1984). The strain increment vectors were plotted in Figure 2-13(b) to show the non-coaxial behaviour of sand under rotation of principal stress axes. The authors pointed out that in the R-tests, the strain increment direction was between the directions of major principal stress and principal stress increment. At larger strains, the deviation between principal strain increment axis and principal stress axis was smaller. Miura *et al.* (1986) concluded that the deviation of strain increment direction was caused by the initial anisotropic fabric of sand, and the effects was rather large even after 7 or 8 cycles of rotation of the major principal stress direction.

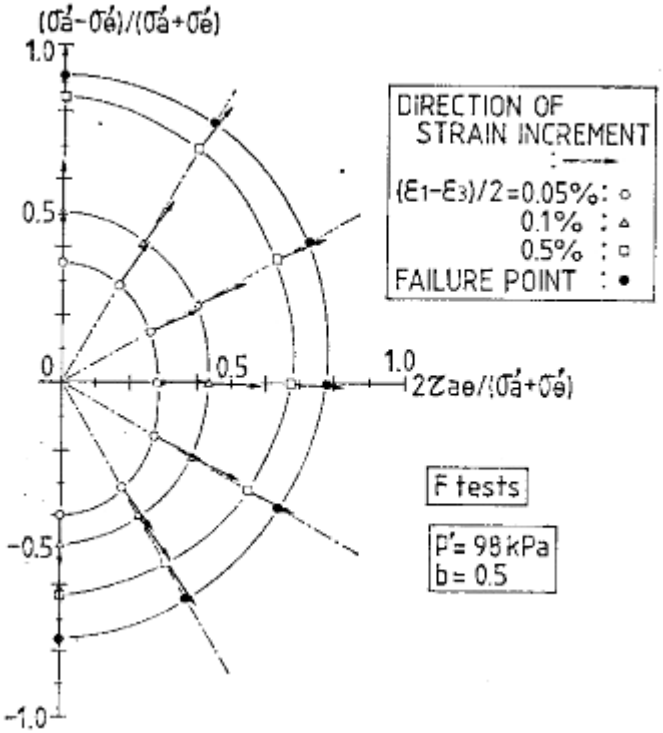

Figure 2-13 (a) Under the stress condition without principal stress rotation

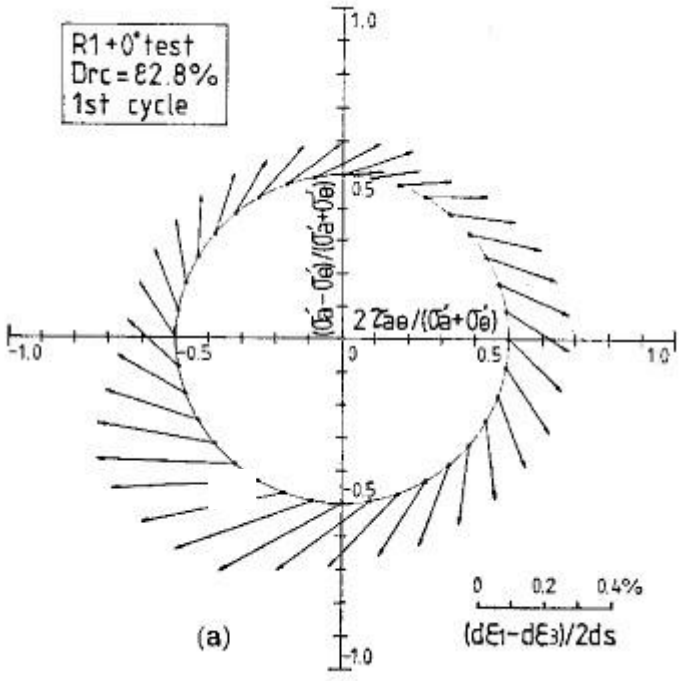

Figure 2-13 (b) Strain increment vectors due to the rotation of principal stress axes (R1+0 °)

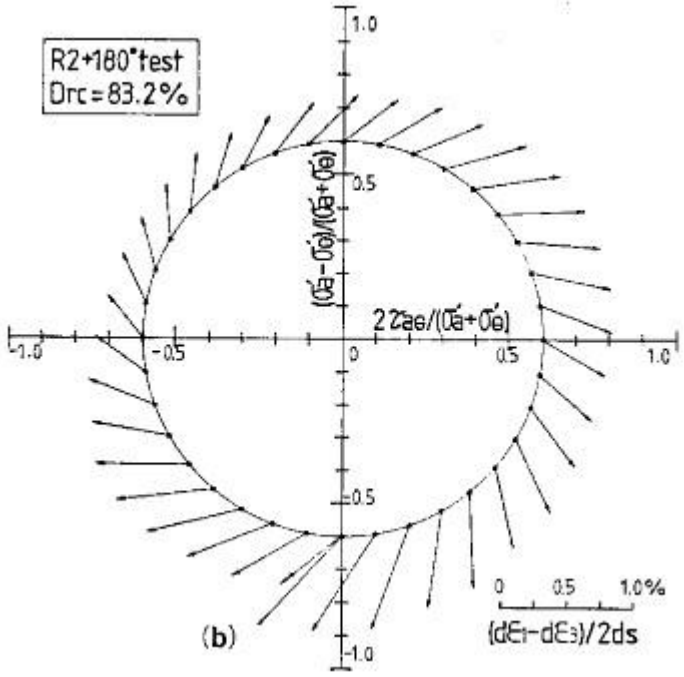

(c) Strain increment vectors due to the rotation of principal stress axes (R2+180 °)

Figure 2-13 Non-coincidence between principal strain increment axes and principal stress axes: (a) under the stress condition without principal stress; (b) Strain increment vectors due to the rotation of principal stress axes(R1+0 °) ; (c) Strain increment vectors due to the rotation of principal stress axes (R2+180 °)(after Miura *et al.* 1986).

Pradel *et al.* (1990) used the improved version of the HCA employed by Ishihara and Towhata (1983) to study the plastic flow of granular material. Dense Toyoura sand specimens with a relative density of D_r = 70% were sheared along the same stress path to a certain stage, and then a cycle of loading and unloading was applied with small stress increment. The test results showed that the direction of principal plastic strain increment was strongly dependent on the stress increment.

Gutierrez *et al.* (1991) proposed a plastic potential theory capable of representing the dependency of the flow of sand on the stress increment direction. The theory was guided by the results from the HCA tests, which

established the feature of sand behaviour named non-uniqueness of flow or the dependency of the plastic strain increment direction on the stress increment direction. Another experimental observation made by Gutierrez *et al.* (1991) indicated the non-coaxiality of the principal stress and principal plastic strain increment directions. The geometry of specimens was 100mm in outer diameter, 60mm in inner diameter, and 104mm in height, the same as Ishihara and Towhata (1983). Three different stress paths were followed in the study: (1) monotonic loading tests at different fixed principal stress directions, (2) pure rotation of principal stress directions at constant mobilized angles of friction of φ=20, 25, 30, 35, 40 and 45°, and (3) combined loading paths involving simultaneous increase in shear stress level and rotation of principal stress principal stress direction. The flow characteristics of the sand during the tests can be seen in Figures 2-14(a) to (c). In Figure 2-14(a), the deviations between axes of principal stress and axes of principal strain increment are obtained, but are very small and may be neglected. As shown in Figures 2-14(b) and (c), for both the pure rotation and the combined loading tests, the degree of non-coincidence between the principal plastic strain increment direction and the principal stress direction were more pronounced. The direction of plastic principal strain increment was getting close to the direction of principal stress at higher shear stress levels. For different stress paths, the strain increments directions were different even when the current stress states were the same. The results were used to build an elastoplastic constitutive model to simulate the behaviour of sand under rotational shear (Gutierrez *et al.*, 1993).

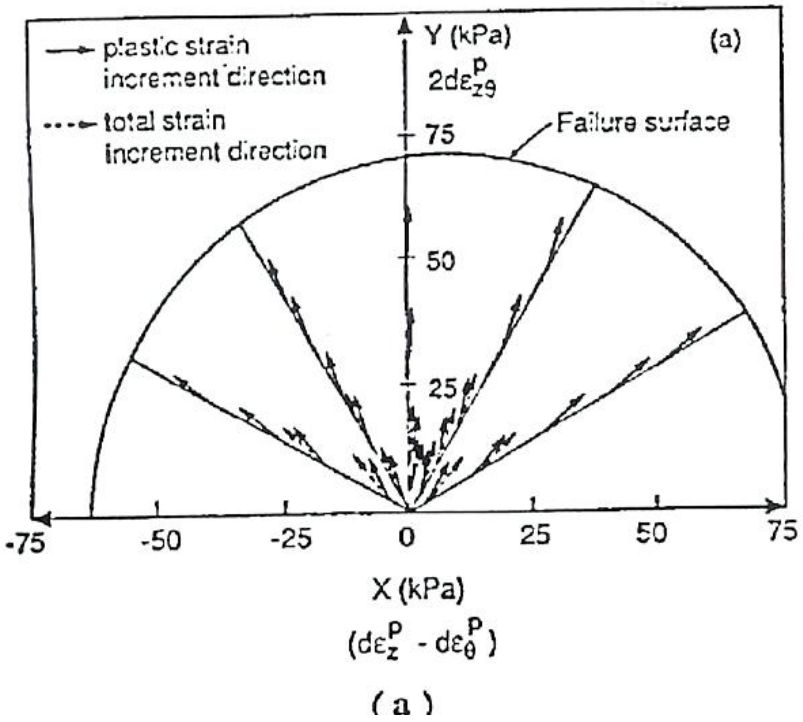

Figure 2-14 (a) Unit plastic strain increment vectors superimposed on the stress path for: (a) monotonic loading

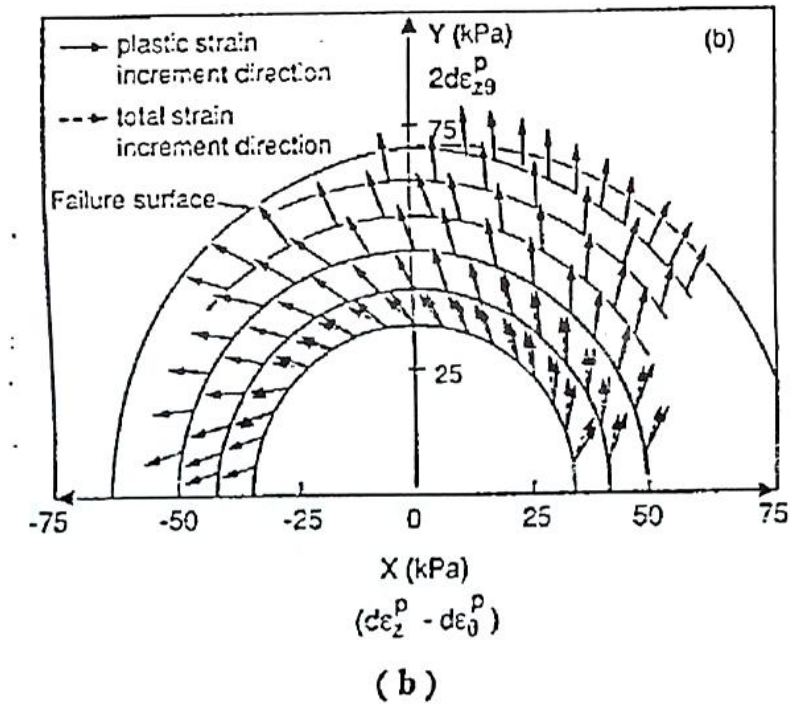

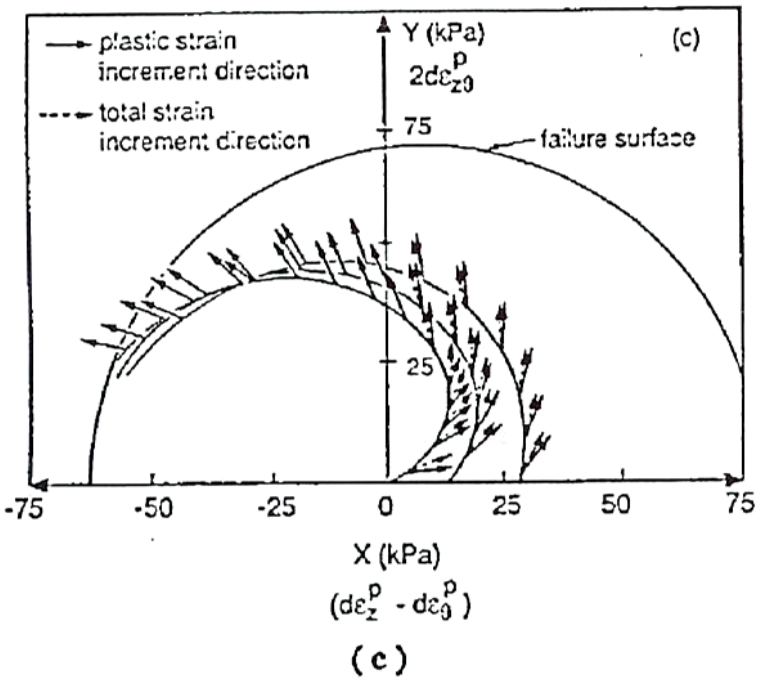

Figure 2-14 Unit plastic strain increment vectors superimposed on the stress path for: (a) monotonic loading, (b) pure rotation and (c) combined loading (after Gutierrez *et al.*, 1991).

Gutierrez and Ishihara (2000) presented a comprehensive analysis of the effects of non-coaxiality on the energy dissipation of sand with the experimental results from hollow cylindrical tests on sand by Gutierrez *et al.*. (1993). A non-coaxiality factor was given to correct the expressions for energy dissipation calculation, as using the strain increment invariants or stress increments would lead to an over-estimated result.

Recently, Lade *et al.* (2009) conducted a series of tests on a HCA with the specimen geometry 22cmn (*O.D*) × 18cm (*I.D*) × 40/25cm (*H*) using Santa Monica Beach sand. Non-coaxiality was reported as in Figure 2-15, showing that the axes of principal stress and principal strain increment were coincident at failure. The authors concluded that the sand behaved as an isotropic material when specimens approached failure.

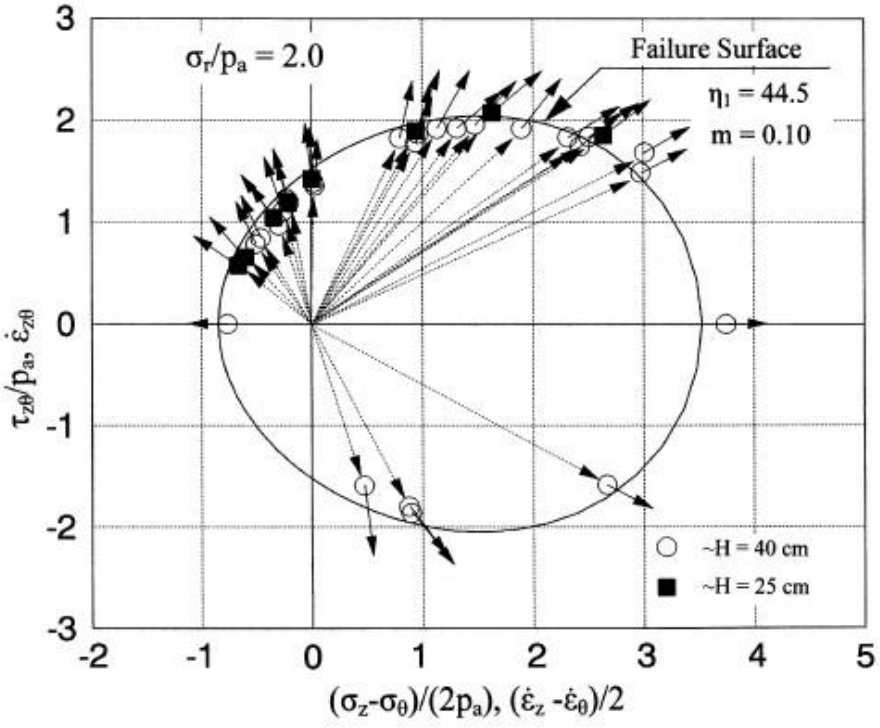

Figure 2-15 Comparison of directions of principal stress with directions of principal plastic strain increments at failure in physical space during rotation of principal stresses in torsion shear tests on Santa Monica Beach sand (after Lade *et al.*, 2009).

2.5 SUMMARY

In this chapter, theoretical studies of non-coaxiality, hollow cylinder apparatus testing techniques and previous studies on the non-coaxiality between the axes of principal stress and that of principal strain increments, using hollow cylindrical specimens on sand, have been reviewed. Experimental evidences of the non-coaxiality from previous experimental studies using both simple shear and HCA testing have been presented.

The theoretical background on hollow cylinder testing was given in this

chapter. It has been recognized that a hollow cylinder apparatus can generate many of the stress paths that are needed for independent control of the magnitudes of the three principal stresses and rotation of the major-minor principal stress axes. Non-uniformity of stress distribution across the wall of the hollow cylindrical specimen can be minimized by choosing particular specimen geometry and by using the same internal and external pressure.

Previous studies using HCA on sand have shown the deviation of principal plastic strain increments from the principal stress directions while rotating the major principal stress axes.

Although there have been several experimental studies showing the evidences of the non-coaxiality between the principal stresses directions and principal strains increments directions, most of the studies were focused on the other issues (e.g. stress-strain behaviour, effect of anisotropy). Only Gutierrez and Ishihara (2000) carried out a particular study on the non-coaxiality and energy dissipation in a granular material. More experimental evidence is still needed to provide a better understanding of non-coaxial soil behaviour.

Chapter 3

Experimental Methodology

3.1 INTRODUCTION

The purpose of this chapter is to describe the testing equipment and materials as well as the testing procedures used in the research work. The testing equipment, i.e. the Hollow Cylinder Apparatus (HCA) is introduced firstly, followed by the basic properties of Portaway sand and Leighton Buzzard sand, which were used in this study. Thirdly, the testing procedures, including specimen preparation, saturation and consolidation stages, are presented. A series of preliminary tests were carried out to evaluate the testing system, including the control system, the accuracy of the new equipment and the repeatability and reliability of the test results, which are described and discussed in Section 3.5. Finally, Section 3.6 is the summary for this chapter.

3.2 NCG HOLLOW CYLINDER APPARATUS

3.2.1 Introduction

Most sedimentary soils are inherently anisotropic. Consequently, ground deformations can occur due to changes in both the magnitude and the direction of the principal stresses. The hollow cylinder apparatus is an extremely valuable tool for studying soil constitutive behaviour of soil under generalized stress conditions including the principal stress rotation.

In this project, a new testing system, the Hollow Cylinder Apparatus (HCA), developed by GDS Instruments Ltd, is used throughout. The HCA allows the application of rotational displacement and torque to a hollow cylindrical specimen of soil. Using this equipment, an independent control of the magnitudes of the three principal stresses and rotation of the major-minor principal stress axes is possible. Therefore, a wide range of stress paths can be applied.

3.2.2 Equipment setup

The arrangement of the HCA is shown in Figure 3-1，and the general layout of the testing system is shown in Figure 3-2. A desktop computer is connected to a hollow cylinder hydraulic triaxial cell via three microprocessor-controlled hydraulic actuators described by Menzies (1984,

1988), which are called Digital Pressure/Volume Controllers (DPVC). The DPVCs precisely regulate and measure pressures and volume changes of water supplied to the outer and inner cell chambers, as well as the back pressure in the soil. The system can measure axial deformation indirectly by volume change into the lower chamber or directly using a digital indicator mounted in the actuator unit. Pore pressure may be measured by the back pressure controller (locked for the undrained condition so there is no volume change) or by a pressure transducer plumbed directly into the base pedestal. The transducer can resolve pore pressure to ±0.2kPa over a range of 2000kPa. The DPVCs, pore pressure transducer and actuator unit are connected by interface bus cables to the IEEE 488 standard parallel interface of the computer.

Figure 3-1(b) shows the picture of the HCA cell with the specimen preparation mould. In the base of the cell, there are three valves connected to the three DPVCs and two connected to the specimen for the flushing of deaired water. Another one is used for the pore pressure transducer. The cell can accommodate specimens with dimensions of 100/60/200mm (*O.D/I.D*/*H*). The loading capacities for the HCA are 12kN of axial load and 200Nm of torque.

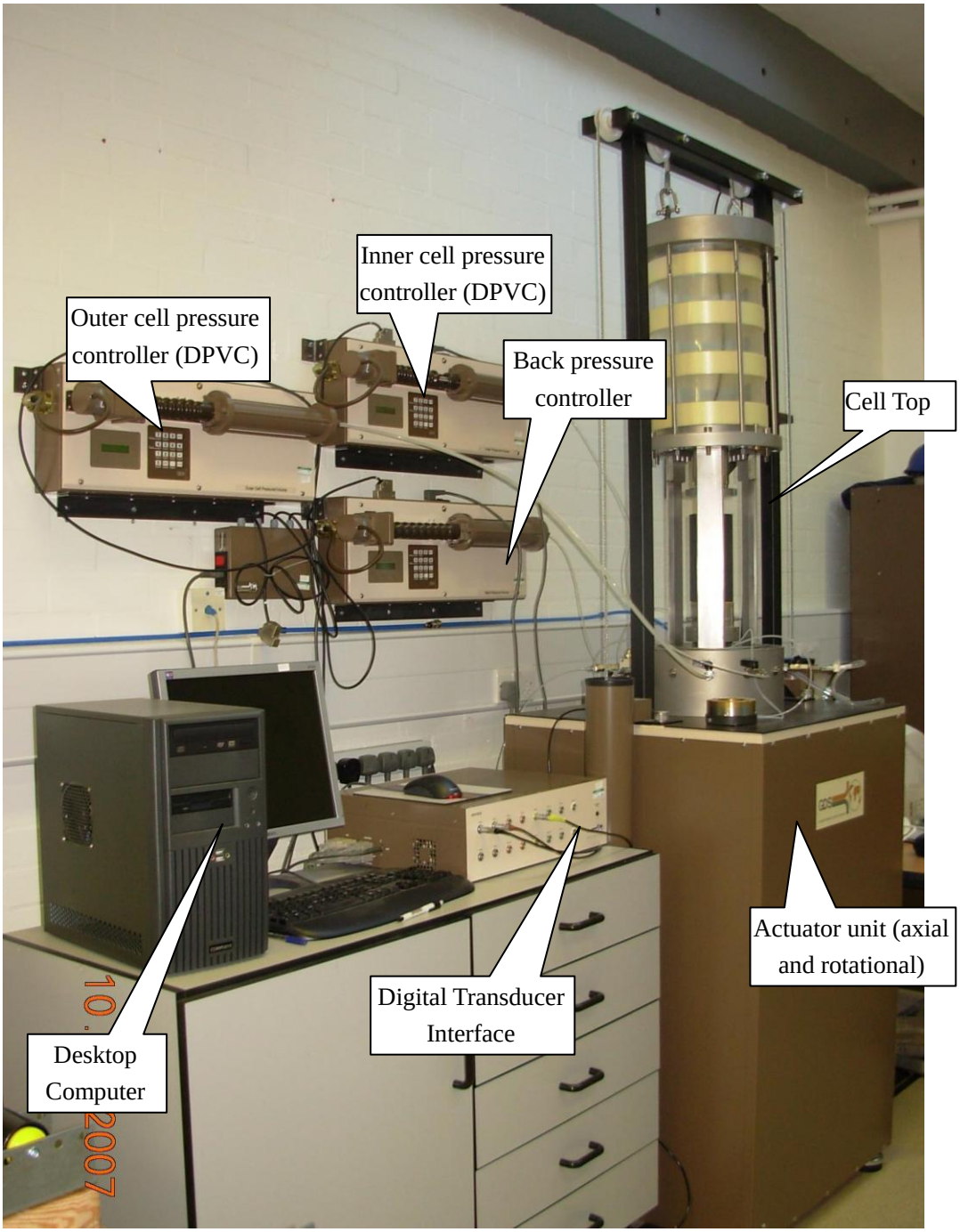

Figure 3-1 (a) Experimental setup

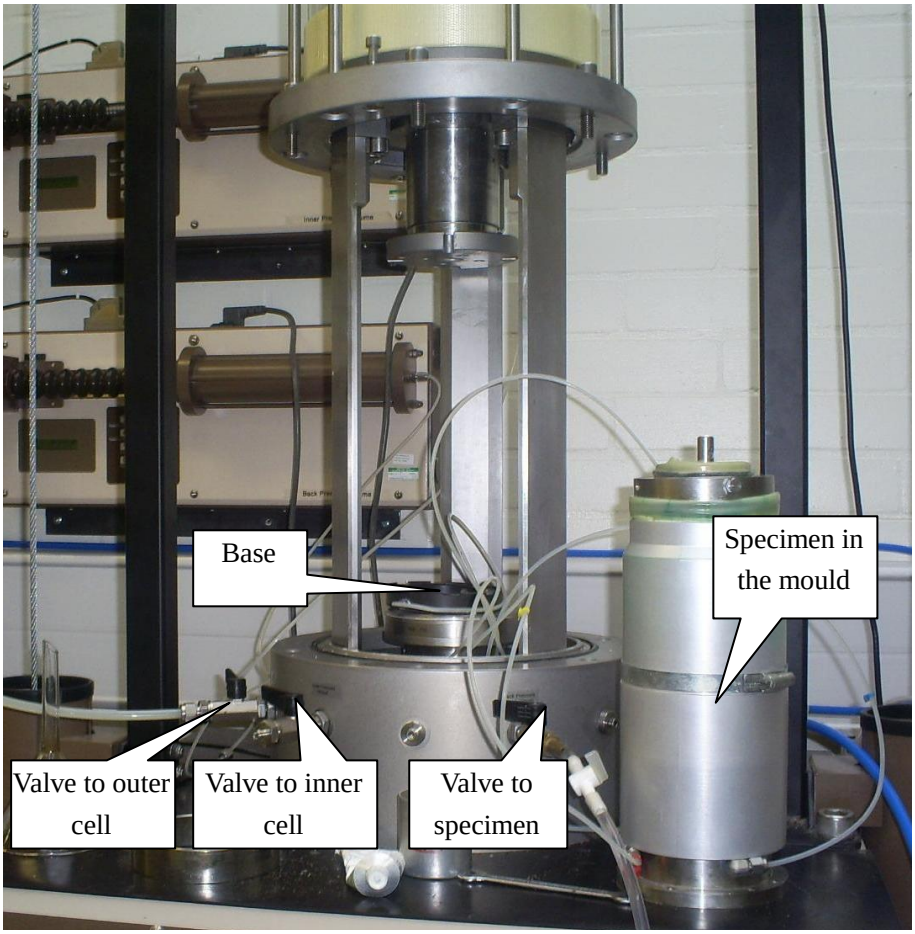

(b) The HCA cell

Figure 3-1 The Hollow Cylinder Apparatus used in this study: (a) experimental setup; (b) the HCA cell

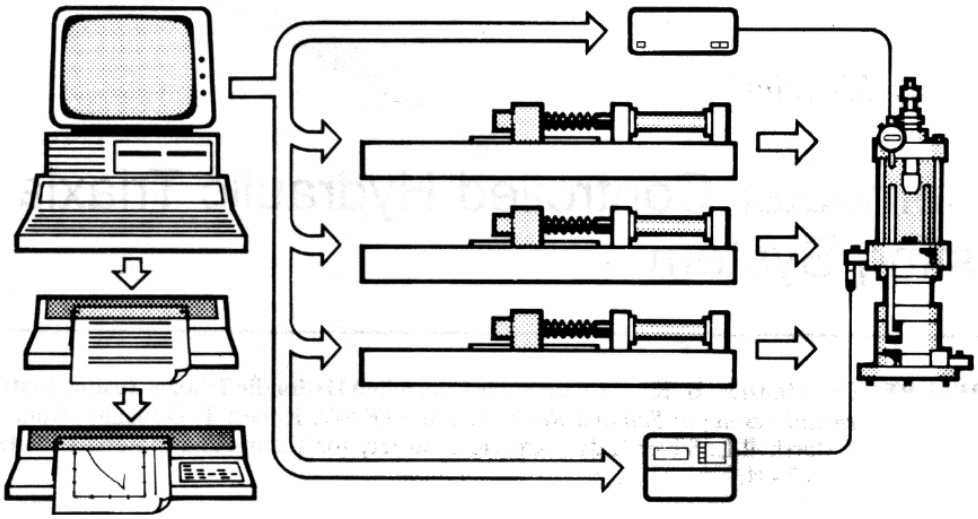

Figure 3-2 Diagrammatic layout of the testing system (after Menzies 1988)

3.2.3 Loading system and measuring instrumentation

The ‘heart’ of the HCA system is a 16 bit Digital Control System (DCS), shown in Figure 3-3, connected to the PC via a high speed USB connection, which is used to connect the DPVCs, pore pressure transducer and actuator units. The actuator unit (as shown in Figure 3-1(a)) is used for the control and measurement of torque, angular rotation, axial force and axial displacement of the specimen. The DCS gives a direct closed loop servo control of axial force and displacement as well as torque and angular rotation (GDS, 2005).

Figure 3-3 Digital control system

There are two servo motors in the HCA. One controls axial movement through an actuator in the base of the cell. The other one controls torsional movement. The torque is applied by the rotation of the same ram imposing the vertical force. Axial force and torque are measured by an internal submersible combined load and torque transducer. Axial displacement and rotation are measured using high resolution encoders read by the DCS. The transducer

resolutions for axial and rotational measurement are: axial load≤0.7N, axial displacement encoder ≤1μm, torque ≤0.008Nm, rotational encoder: ≤0.00011 degrees.

For dynamic testing, an additional encoder for rotational feedback is installed directly on the main ram to reduce backlash on the torque motor as the rotational load passes from positive to negative torque. This second rotational encoder ensures accuracy of the motor control and the reading for the rotational displacement.

Figure 3-4 shows the DPVC used to control the outer and inner cell pressures and the back pressure. The DPVC has a pressure capacity of 4MPa, and 200 cc volumetric. The resolution of pressure measurement is 1kPa on display and 0.1kPa via software, while the resolution of volume measurement is 1mm^3. The accuracy of measurement for the DPVC is shown as the follows: pressure ≤0.1% full range, volume ≤0.1% measured value with ±20mm^3 backlash.

The principles of DPVC operation are shown in the schematic diagram in Figure 3-4(b). De-aired water in a cylinder is pressurized and displaced by a piston moving in the cylinder. The piston is actuated by a ball screw turned in a captive ball nut by a stepping motor and gearbox that move rectilinearly on a ball slide (Menzies, 1988). The key features of the HCA are summarized in Table 3-1.

Table 3-1 Summary of key features of the HCA (GDS, 2005)

Transducer	Type of measurement	Capacity	Resolution	Maximum error* Accuracy
DPVC	Pore and cell pressures	2000kPa	0.1kPa	2kPa 0.1%
	Volume change	200cm^3	0.001cm^3	0.1% +0.02cm^3 back flash 0.1% of volume change
Pore Pressure	Pore pressure	2000kPa	0.1kPa	2kPa 0.1%
Axial	Axial load	12kN	0.0007kN	0.0012kNN 0.1%
	Axial displacement	40mm	0.001mm	0.062mm 0.15%
Rotational	Torque	200Nm	0.008Nm	0.220Nm 0.11%
	Rotational displacement	360 °	0.00011 °	0.206 ° 0.057%

* % errors are based on the full scale output

(a) DPVC

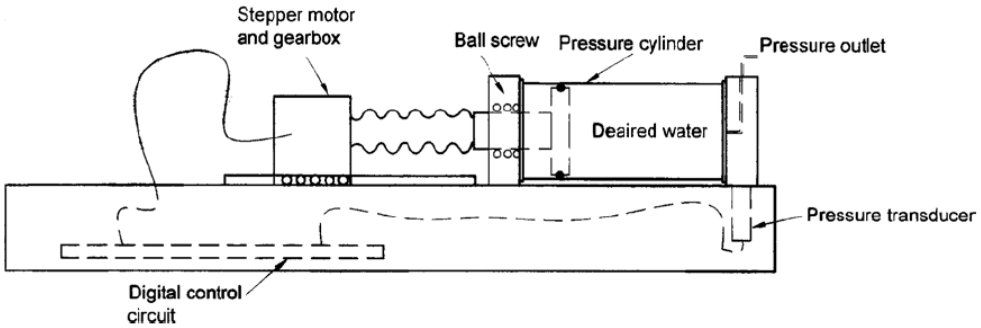

(b) Principles of operation of DPVC (after Menzies, 1984).

Figure 3-4 The Digital Pressure/Volume Controller: (a) DPVC; (b) principles of operation of DPVC

The back pressure controller applies back pressure and also measures volume change of the test specimen, while the inner cell pressure controller applies the inner cell pressure and measures volume change inside the hollow specimen. The outer pressure controller applies the outer cell pressure.

3.2.4 Control software

The software used for test control and data acquisition system is called GDSLAB and was supplied with the HCA. It can be used to perform not only a hollow cylinder test but also triaxial and direct shear tests. The transducers can easily be set up with the software. Figure 3-5 shows the object display of the HCA arrangement.

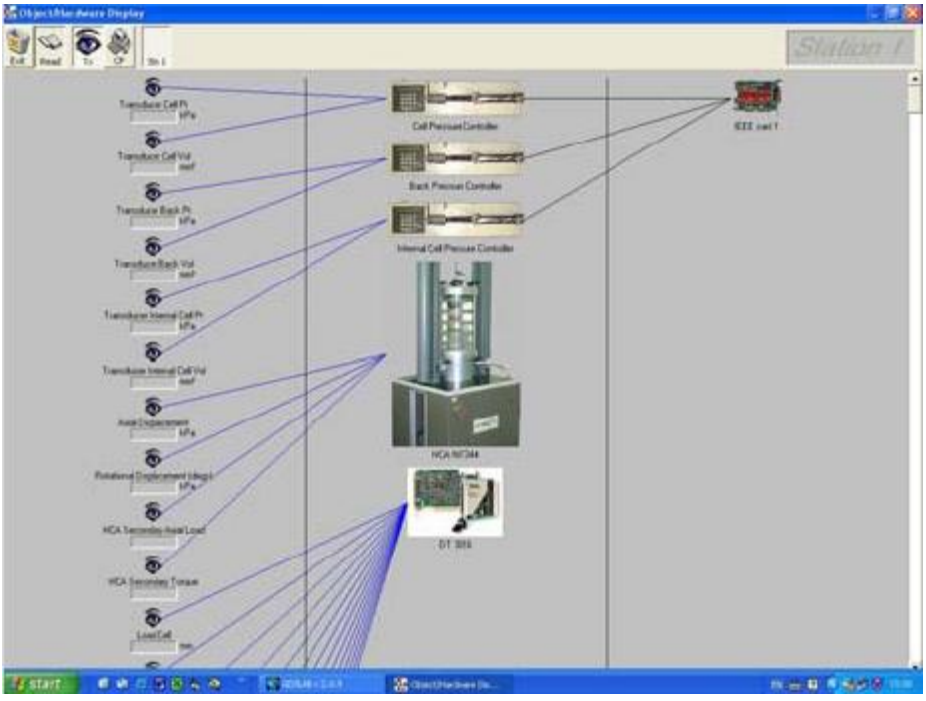

Figure 3-5 Object display showing a GDS SS-HCA arrangement

There are three default modules for HCA tests:

1. Advanced Loading. This module independently controls the five principal parameters, i.e. axial control, rotational control, outer cell pressure, inner cell pressure and back pressure. The axial control can be achieved by: axial stress (kPa), axial displacement (mm) or axial load (kN). Rotational control can be achieved by: rotational stress (kPa), rotational load (Nm) or rotational displacement (degs). This can be used for the saturation and consolidation stages.

2. HCA Stress Path Loading. This module controls the test by four parameters, P, q, b and α; an option for a drained test or an undrained test is also provided.

3. Dynamic Testing. Here sinusoidal cyclic control of axial displacement or axial force and rotational displacement/torque is provided. Dynamic cyclic loading tests can be performed at frequencies up to 5Hz.

The software records the values measured by all transducers and controllers connected to the system and uses these values to calculate all relevant stresses, strains and displacements. These values are then displayed on the screen. The user can choose what data is to be displayed before and during a test and change the displaying options at any time. All the data are saved to a data file in GDS format at any specified time interval. This time interval can be on a linear, square root or log scale. Both the raw data and all the calculated data can be saved. All measured and calculated data can be displayed graphically in real-time on up to three graphs. The user can choose what data to

display on the graph axes before and during a test and can change them at any time.

3.3 TESTED MATERIALS

In this research, Portaway sand was used for most of the tests. It was chosen because it has already been used in several other experimental projects at the NCG to study the stress-strain and strength characteristics of granular materials under axisymmetic conditions and to assess several critical state models for sand (Wang, 2005). Therefore, the strength and deformation characteristics of Portaway sand in triaxial compression and extension are well defined. Leighton Buzzard sand (Fraction B) was also used in two tests to study the effect of particle shape and particle size distribution.

3.3.1 Index properties

Portaway sand is a well-graded, medium quartz sand from Sheffield, England. The sand is passed through a 2mm sieve before the test and washed on a 0.063mm sieve under the running water to remove all the fines. In order to examine the physical characteristics of Portaway sand, a series of soil particle size distribution tests were carried out according to British Standard 1377-2 (1990). The Leighton Buzzard sand is quarried in and around Leighton Buzzard, Bedfordshire in the east of England. The maximum and minimum void ratios of the two sands were determined in accordance with the British Standard 1377-4 (1990). The index properties of these two sands are described

in Table 3-2, and the particle size distributions are shown in Figure 3-6. As it can be seen from the Figure 3-6, Leighton Buzzard sand has a more uniform particle size distribution than Portaway sand.

Table 3-2 Physical properties of Portaway sand and Leighton Buzzard sand (Fraction B)

Sand	Mean grain size D_{50}: mm	Effective grain size D_{10}: mm	Uniformity coefficient C_u: D_{60}/D_{10}	Specific gravity G_S	Minimum void ratio e_{min}	Maximum void ratio e_{max}
Portaway	0.35	0.16	2.50	2.65	0.45	0.66
Leighton Buzzard	0.62	0.45	1.56	2.65	0.52	0.79

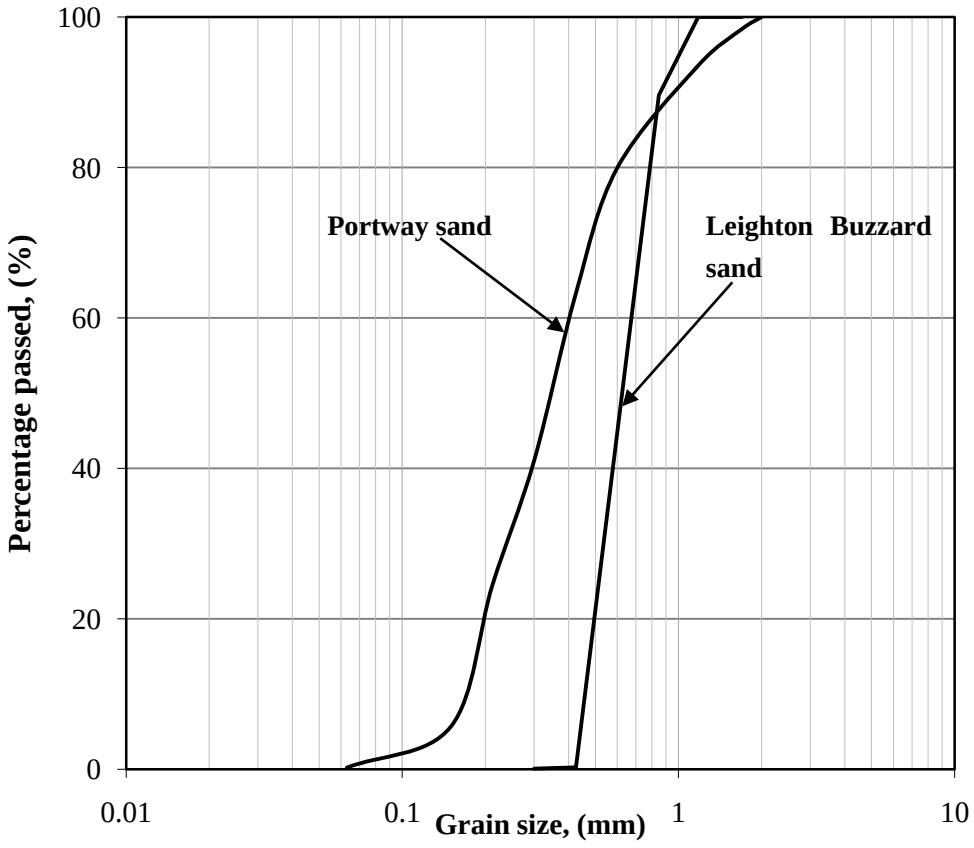

Figure 3-6 Particle size distribution of Portaway sand and Leighton Buzzard sand

3.3.2 Particle shapes

It is widely recognised that the mechanical behaviour of sand is directly related to its microstructure. The particle shape and size have significant effect on the inherent fabric anisotropy of sand. The particles of Portaway sand are subrounded to subangular in shape as illustrated in Figure 3-7. The particles are mainly composed of quartz with some carbonate materials. Leighton Buzzard sand particles are subrounded and contain mainly quartz, as shown in Figure 3-8.

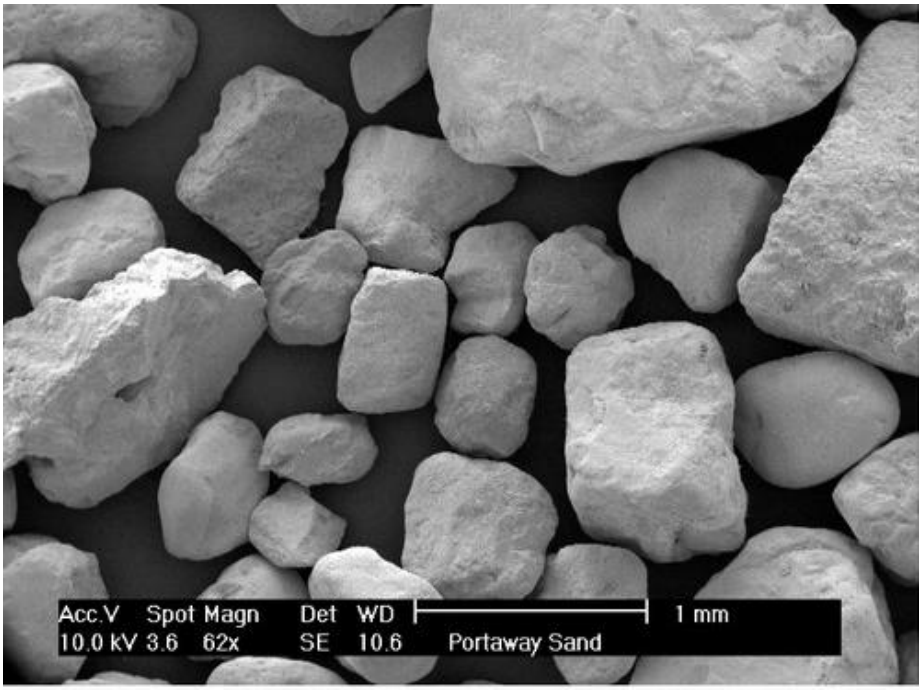

Figure 3-7 Scanning electron micrograph of Portaway sand

Figure 3-8 Scanning electron micrograph of Leighton Buzzard sand (fraction B)

3.4 TESTING PROCEDURES

3.4.1 Specimen preparation

All the components of the specimen preparation mould are shown in Figures 3-9. Three segments of the outer split mould (Figure 3-9(a)) and four of the inner split mould (Figure 3-9(b)), together with the base pedestal (Figure 3-9(c)), top cap (Figure 3-9(d)) and top cover (Figure 3-9(e)) are used for specimen preparation. To make it more convenient to put the specimen in position into the cell, the metal ring used to fix the outer mould (as shown in Figure 3-9(a)) was replaced by adjustable steel ring, as shown in Figure 3-1(b).

Latex membranes with diameters of 100mm and 60mm (Figure 3-10) are used to enclose the specimen with O-rings.

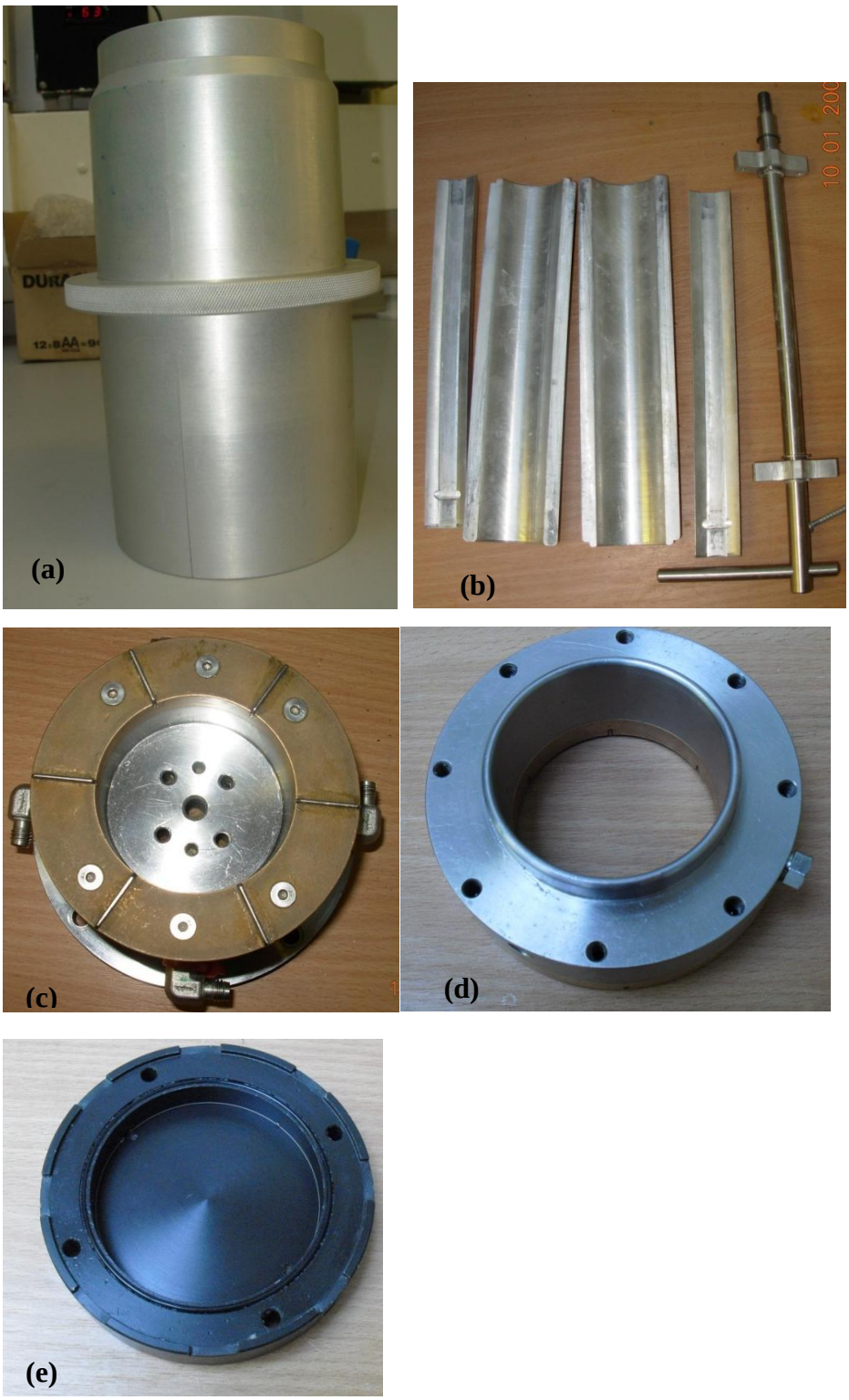

Figure 3-9 Specimen assembly components: (a) outer split mould; (b) inner split mould; (c) base pedestal; (d) top cap; (e) top cover

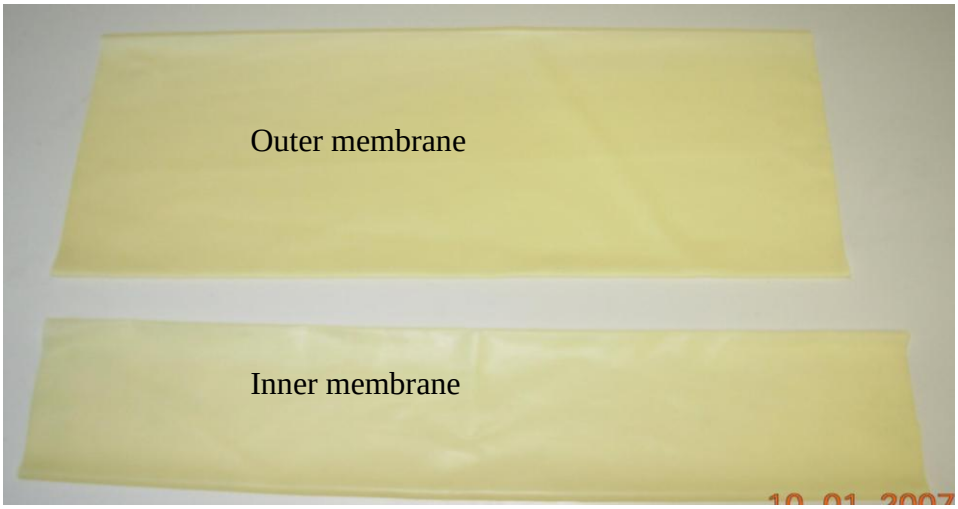

Figure 3-10 Outer and inner membranes

For repeatability of the tests and the accuracy of the results, it is important to prepare uniform and identical sand specimens. The following procedures were used in this study (the photos corresponding to each step are shown in Figure 3-11):

1. The inner membrane of 60mm in diameter and 350mm in length was put into the bottom of the base pedestal (Figure 3-9(c)) by the clamping ring. Four bolts were used for sealing the inner membrane.

2. The inner split mould (Figure 3-9(b)) was stood on the base supported by the steel bar which was scrolled into the base pedestal.

3. An outer membrane of 100mm in diameter and 300mm in length was put outside the base pedestal using two rubber O-rings.

4. Tubes from the base of the HCA for applying water and drainage to the inner cell and the specimen were connected to the base pedestal (Figure 3-9(c)).

5. The outer mould (Figure 3-9(a)) fixed by the iron ring was assembled on the base pedestal. The outer membrane was stretched against the mould.

6. A water sedimentation method was used to prepare all the specimens. Water was applied to the cavity between outer and inner membranes to remove the air bubbles from the base pedestal and the specimen. The weighted sand for the required relative density was then poured into the cavity through a funnel and distributed uniformly. For denser specimens, the assembly was tapped to compact the sand to a uniform relative density. Water was supplied throughout this step to push out the air from the sand.

7. The top cap shown in Figure 3-9(d) was gently seated on the top of the specimen. And then outer and inner membranes were rolled up around the top cap and sealed with O-rings, two for the outer membrane, one for the inner membrane.

8. The upper drainage tube was connected to the top cap. A suction of 20kPa was imposed to prevent the specimen from collapsing. The inner mould was pulled out by the steel bar shown in Figure 3-9(b). The top cover (Figure 3-9(e)) was positioned on the top cap and tightened using four bolts. The upper drainage tube for the inner cell was connected to the top cover. Then, the whole specimen with the outer mould was seated on the base of the equipment and screwed with four bolts. After this, the outer mould was removed. By adjusting the angle and axial displacement, the top cover was fixed to the machine with a very small axial load. After the specimen was set up, the final height and outer diameter of the specimen were measured.

9. The cell chamber was brought down and tightened. The outer and inner cells were filled with water. Then, cell pressures of 20kPa were applied and the suction was removed from the specimen.

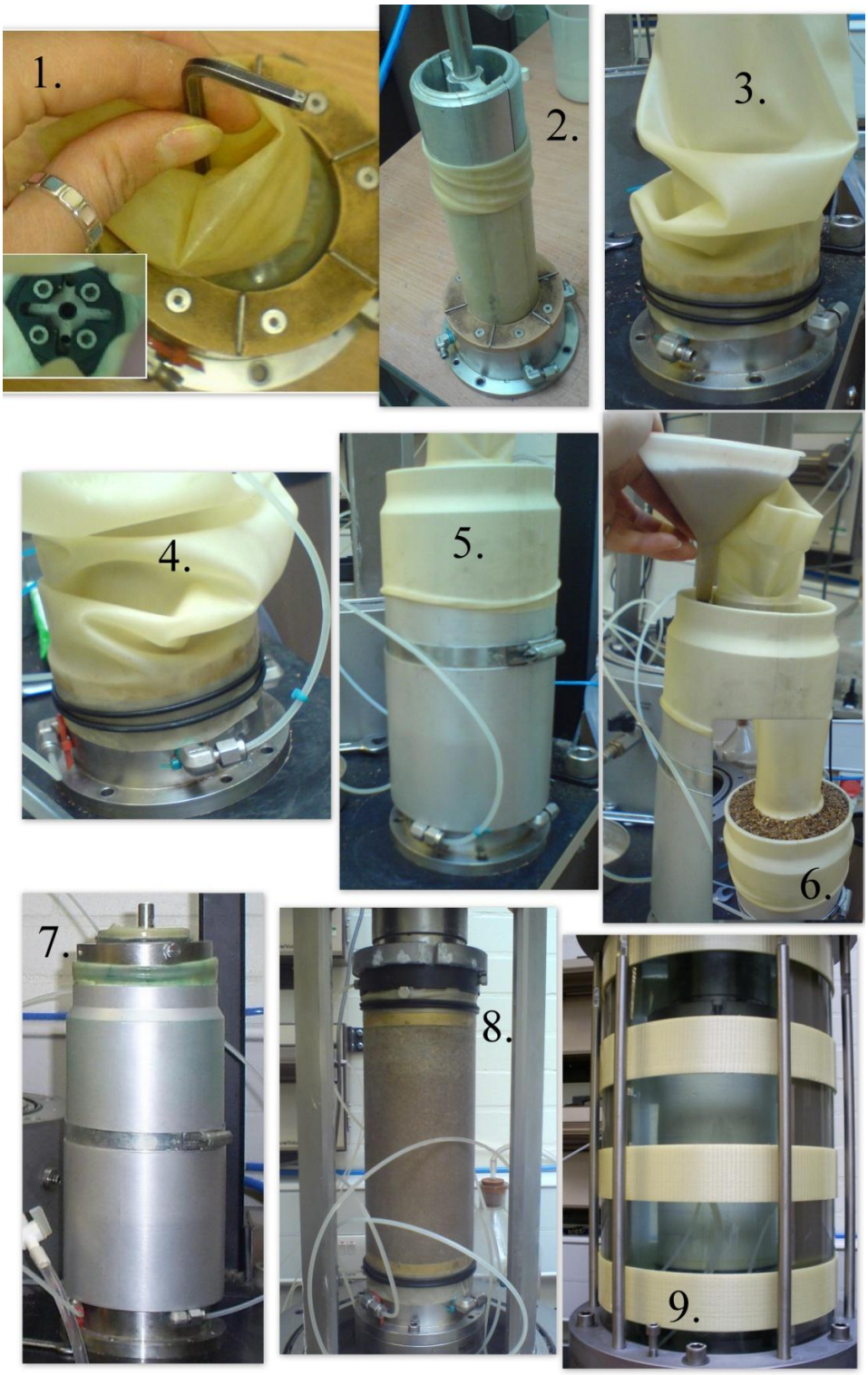

Figure 3-11 Specimen preparation procedures

3.4.2 Saturation and consolidation

In order to measure the volume change of specimen correctly, a fully saturated specimen is essential for all the tests. In this research, the following procedures were applied to ensure as high as possible degree of saturation:

- De-aired water was flushed through the specimen from the lower back pressure tube to the upper back pressure tube for about 90 minutes.

- The cell and back pressures were increased to 420 and 400kPa respectively while keeping the difference of 20kPa between them. In this study, the back pressure was kept constant at 400kPa in every test.

- Then, the specimen was left over night for saturation. The changes of pressures and volumes during saturation are shown in Figure 3-12 and Figure 3-13.

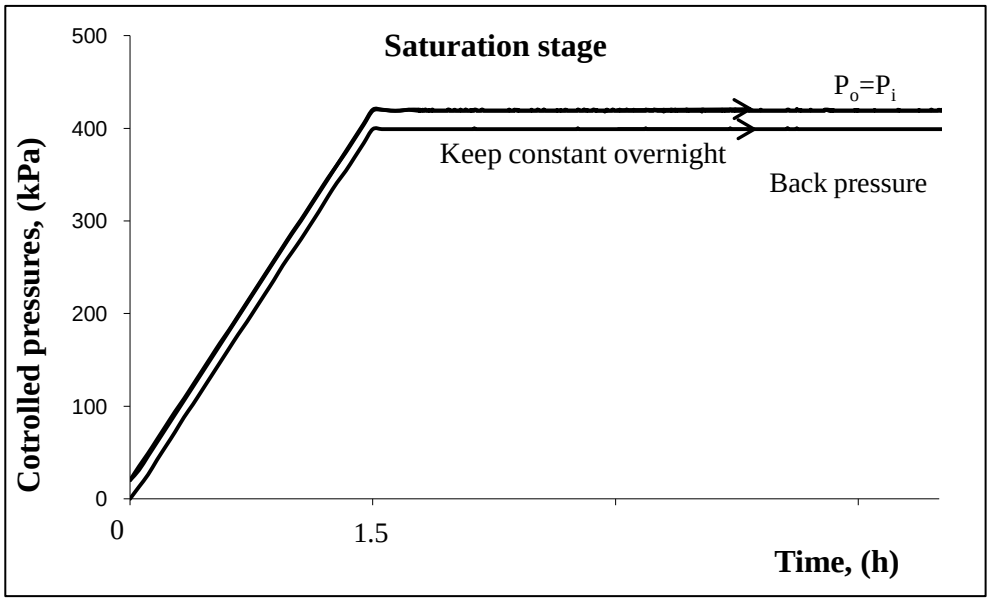

Figure 3-12 Pressure variations during saturation procedure

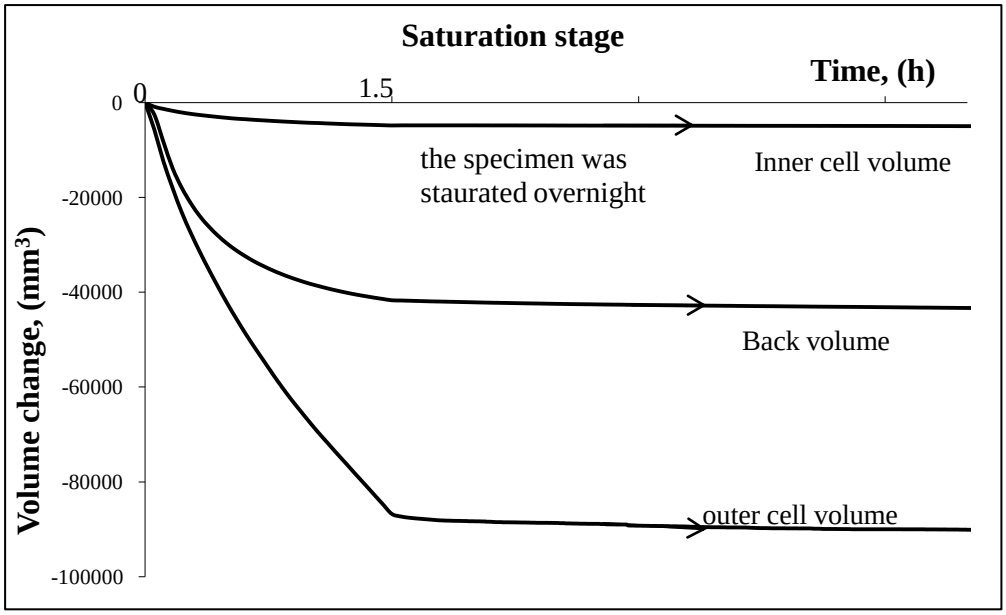

Figure 3-13 Volume variations of the controllers during saturation procedure

- After the sand was well saturated, the back pressure valve was closed to check the saturation degree. Then Skempton's *B*-value assessment was used. The outer and inner pressures were increased from 420kPa to 520kPa. As shown in Figure 3-14, the pore pressure was measured. If the magnitude of pore pressure increased by more than 96kPa, which meant the *B*-value was greater than 0.96, the specimen was considered to be 'fully' saturated.

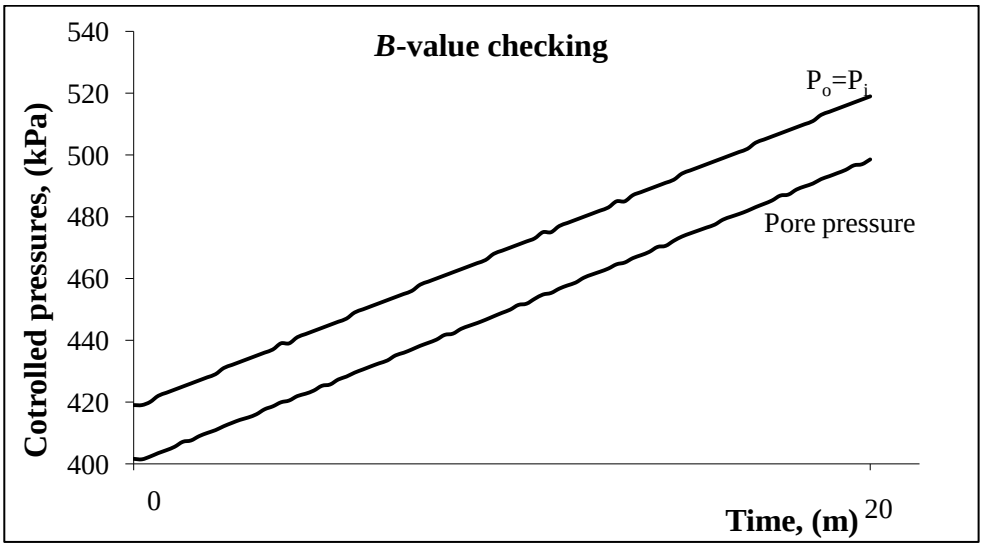

Figure 3-14 Checking saturation degree

- After checking *B*-value, the back pressure was decreased to 400kPa. And the cell pressures were increased to 600kPa, which made an effective confining pressure of 200kPa. The difference between vertical and horizontal stresses σ_z - σ_θ was kept equal to zero during consolidation, so the specimen was isotropically consolidated. The sand specimen was then left overnight to accomplish the consolidation process. Figures 3-15 and 3-16 show the pressures and volumes measured during consolidation.

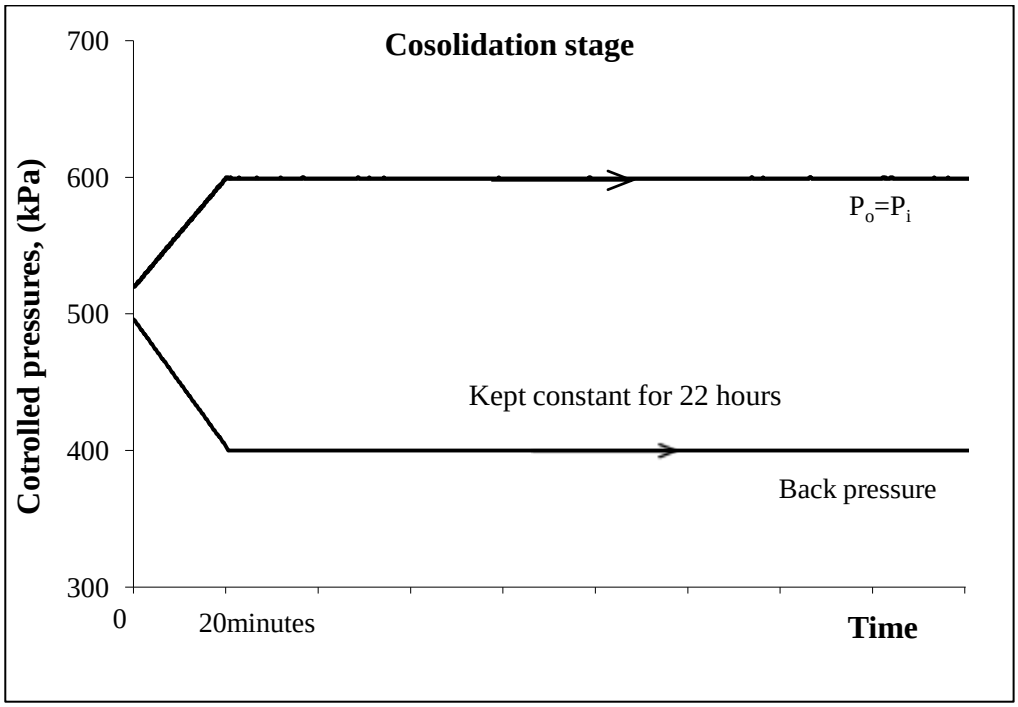

Figure 3-15 Pressures measured during specimen consolidation

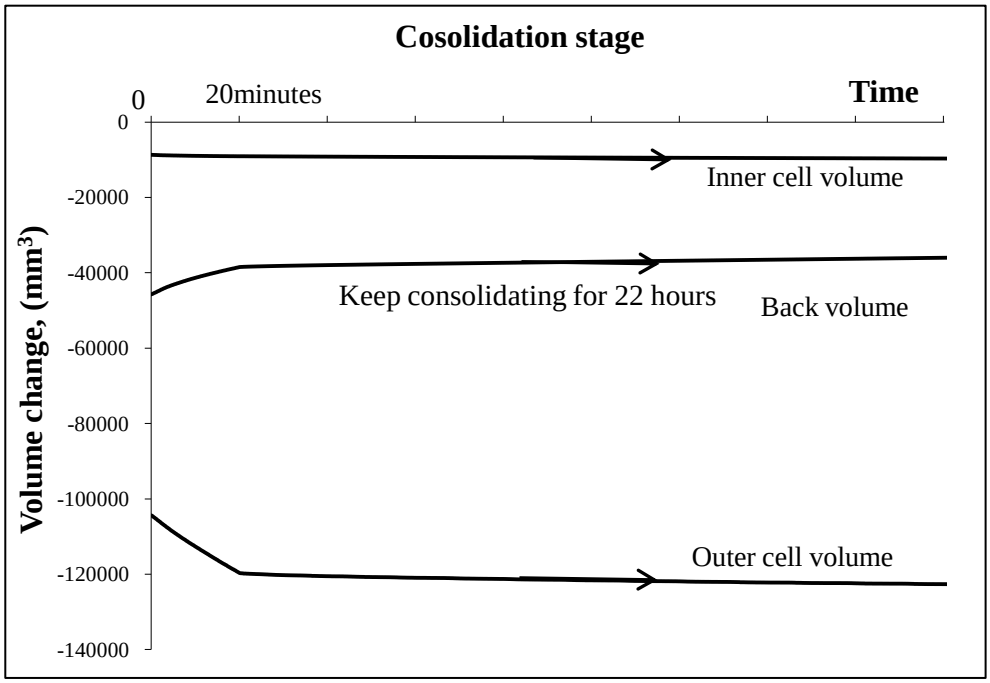

Figure 3-16 Typical volume changes measured during specimen consolidation

3.4.3 Test control

The control modes have been introduced in Section 3.2.4. For all the tests, the advanced loading control module was used for the saturation and consolidation stages. Then the HCA stress path control module was applied for the drained test. Due to the limitations of the control program, the HCA was not capable of performing a strain-controlled test.

3.4.4 Stress paths

Three types of stress paths were followed in this study. The first one was a monotonic loading test. The second one was a pure rotation test. The last one was a combined loading test.

Monotonic loading tests

All the monotonic loading tests were performed by increasing the deviator stress q monotonically until failure while the major principal stress direction α was fixed at the value of 0 °, 15 °, 30 °, 45 °, 60 °, 75 °, 90 °, as shown in Figures 3-17. Corresponding values of b were 0, 0.067, 0.25, 0.5, 0.75. 0.933 and 1, respectively. Due to the limitations of the testing equipment, it was not possible to rotate α to the prescribed value when q was 0kPa. Therefore, a deviator stress of 8kPa was applied before the rotation of the major principal stress direction was implemented.

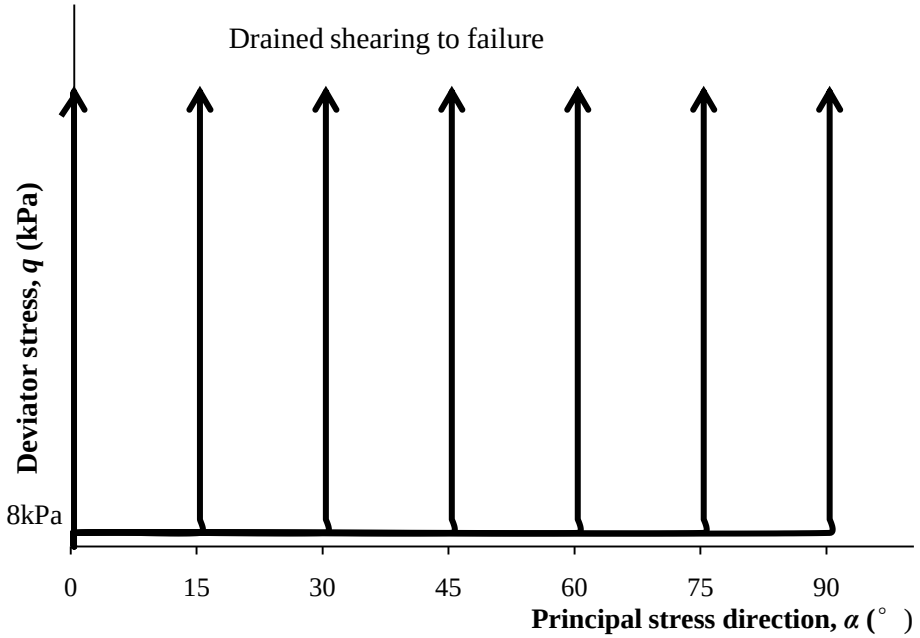

Figure 3-17 Stress paths of the monotonic loading tests

Pure rotation tests

This series of tests involved pure rotation of principal stress directions at constant deviator stress q. For Portaway sand, stress paths with q of 100kPa,

125kPa, 150kPa and 175kPa were applied. For Leighton Buzzard sand, only stress paths with q=125kPa and 150kPa were carried out. The stress paths in the X-Y stress space are shown in Figure 3-18. The X axis is defined as σ_z-σ_θ, and Y axis is defined as $2\tau_{\theta z}$. In this stress space, the vector from the origin has the length of deviator stress $q = \sigma_1 - \sigma_3 = \sqrt{(\sigma_z - \sigma_\theta)^2 + (2\tau)^2}$. The angle between the vector and the X-axis are twice of the major principal stress direction relative to the vetical axis: $\tan 2\alpha = \frac{2\tau_{\theta z}}{\sigma_z - \sigma_\theta}$.

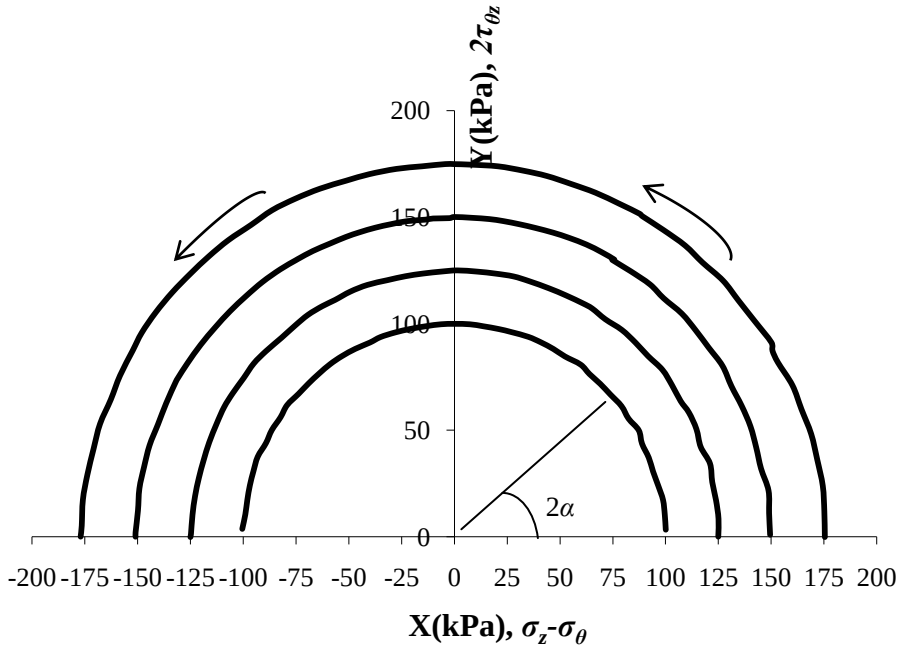

Figure 3-18 Stress paths of the pure rotation tests

Combined loading tests

In this series of tests the specimens were subjected to the rotation of principal stress axes as well as the increase of the deviator stress q, as shown in Figure 3-19. All the tests were carried out from a deviator stress of 75kPa.

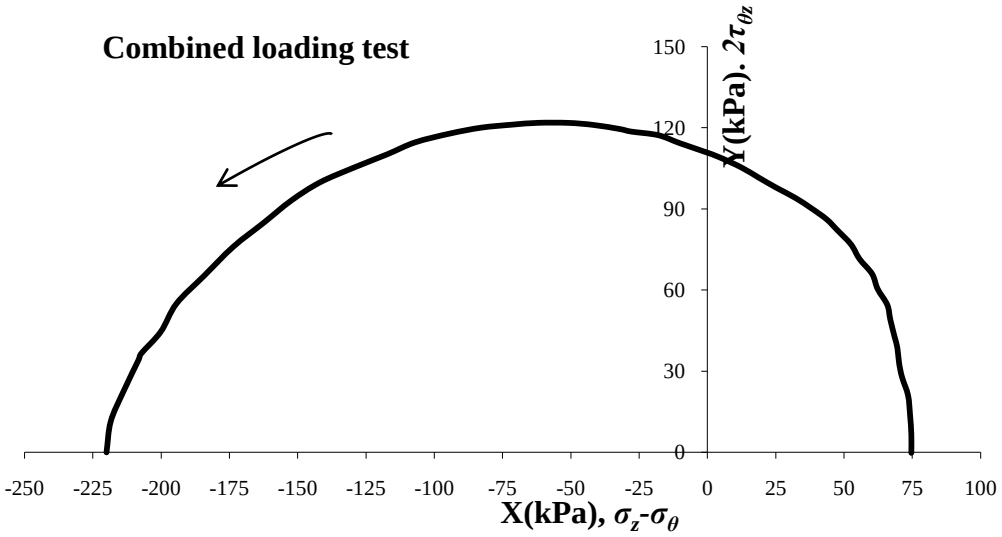

Figure 3-19 Stress paths of the combined loading test

3.5 EQUIPMENT EVALUATION

In order to verify the HCA control system for a selection of test conditions, i.e., suitable values of back pressure for full saturation, loading rates, etc, a series of four tests were carried out along three different stress paths. The results are analyzed and compared with the previous study of Hight *et al.* (1983). In additional, conventional compression triaxial tests were carried out using both the HCA and triaxial apparatus to validate the reliability of the HCA.

3.5.1 Preliminary experiments

Stress paths

All the specimens were prepared to an initial void ratio e=0.45 (D_r=95%), and consolidated isotropically to an effective mean pressure p' of 200kPa,

using a back pressure of 400kPa to ensure 'full' saturation. In all these tests p_o and p_i were kept equal. The effective mean stress was held at 200kPa throughout each test. Since the specimens were fully drained against a back pressure of 400kPa, the total mean stress was maintained constant at 600kPa. The stress paths followed are shown as plots of deviator stress q $(q=\sigma_1' - \sigma_3')$ against major principal stress direction, α (Figure 3-20). Tests L1, L2, L3 followed three different stress paths to reach the point C. Two specimens following stress path L1 were tested to determine the repeatability of test results. For tests L1, the deviator stress q was increased to 100kPa with the direction of the major principal stress α held constant at 0 °(path AB), and then followed by a continuous rotation of α from 0 °to 45 °(path BC). In test L2, the deviator stress q was increased to 100kPa while rotating the direction of the major principal stress direction α from 0 °to 45 °(path AC); For test L3, before increasing q, α was rotated from 0 ° to 45 °, and then deviator stress q was increased to 100kPa while α was maintained at 45 °(path DC). After reaching the point C (q=100kPa, α = 45 °), all tests followed the same path by keeping α = 45 °and increasing q until the specimens failed (path CF).

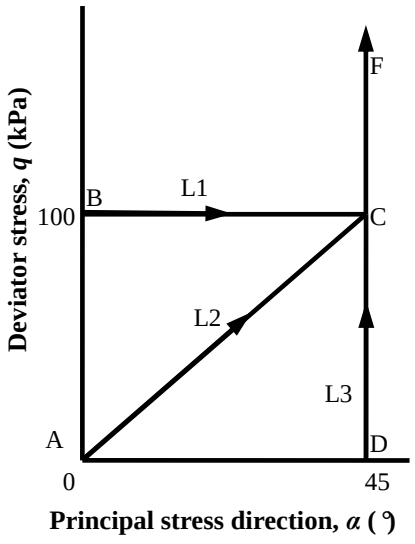

Figure 3-20 Prescribed stress paths

Stress path control

For the saturation, *B*-value check and consolidation stages, the advanced control module was employed to increase the pressures to the desired values and keep them constant. To achieve the stress paths for tests L1, L2 and L3, the stress path control module was used by keeping p constant at 600kPa, and changing q, α, and b in different stages. The shearing rate for q was 5kPa/min, for changing α it was 1 °/min.

As shown in Figure 3-21, a small deviator stress q about 8kPa had to be applied in test L2 and L3 before the rotation of major principal stress axes. This was because of the limitation of the control program, which did not allow an accurate control of α when q=0kPa. It can be observed from Figure 3-21 that a very good control of the q-α stress path was obtained in all three tests.

The combinations of σ'_z, σ'_θ, σ'_r and $\tau'_{\theta z}$ from the test results are plotted in Figure 3-22. For test L1, when q increased from 0 to 100kPa with no rotation of the principal stress axis, the axial stress (σ'_z) increased from 200kPa to 267kPa, while both the radial stress (σ'_r) and circumferential stress (σ'_θ) decreased from 200kPa to 167kPa. The shear stress ($\tau'_{\theta z}$) was kept zero. From point B to C, when the principal stress axis was rotated from vertical to 45 °, σ'_z decreased gradually to 200kPa, σ'_r=σ'_θ reduced back to 200kPa, and $\tau'_{\theta z}$ increased to 50kPa. In test L2, from point A to C, σ'_z rose to the maximum value then dropped back to 200kPa. σ'_r=σ'_θ acted in an opposite way. $\tau'_{\theta z}$ reached 50kPa at point C. For test L3, from point A to D, only a small deviator stress was applied, so σ'_z, σ'_θ and σ'_r were kept almost constant and equal to

each other. Small amounts of shear stresses were generated. Then, from point C to the failure point in tests L1 and L2, and from point D to failure in test L3, $\sigma'_z=\sigma'_r=\sigma'_\theta$ was observed to be constant. Shear stress ($\tau'_{\theta z}$) was built up with the increase of deviator stress. The results were consistent with results of proving tests conducted by Hight *et al.* (1983), as shown in Figure 3-23.

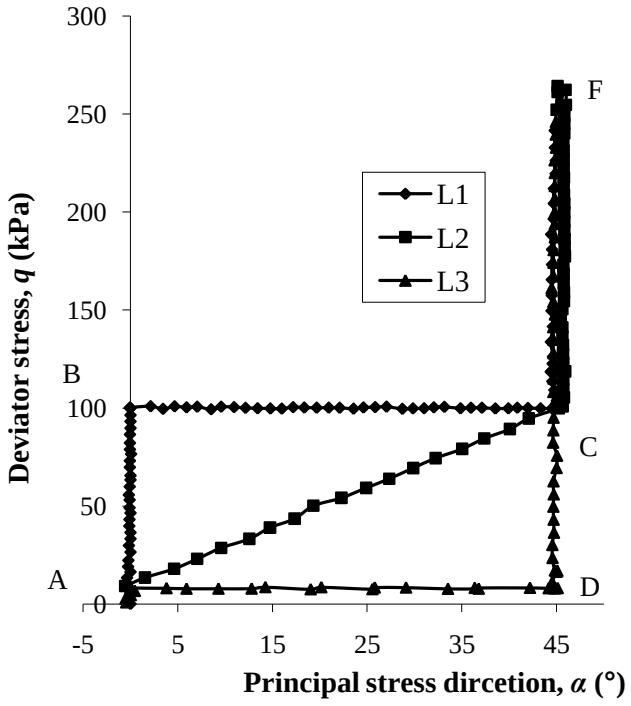

Figure 3-21 Actual stress paths followed

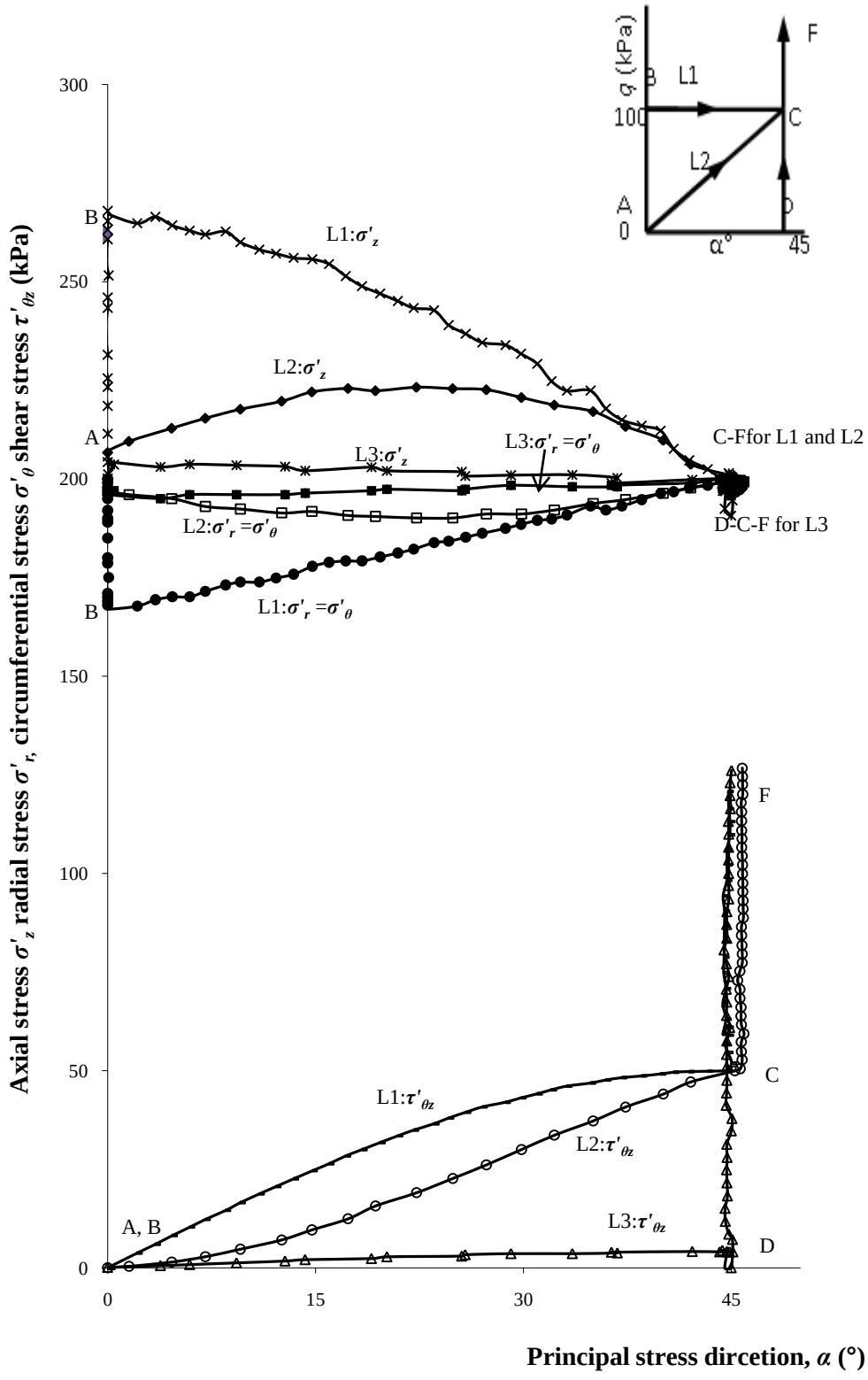

Figure 3-22 Variations in σ'_z, σ'_r, σ'_θ and $\tau'_{\theta z}$ in test L1, L2, and L3 (e=0.46, D_r=95%)

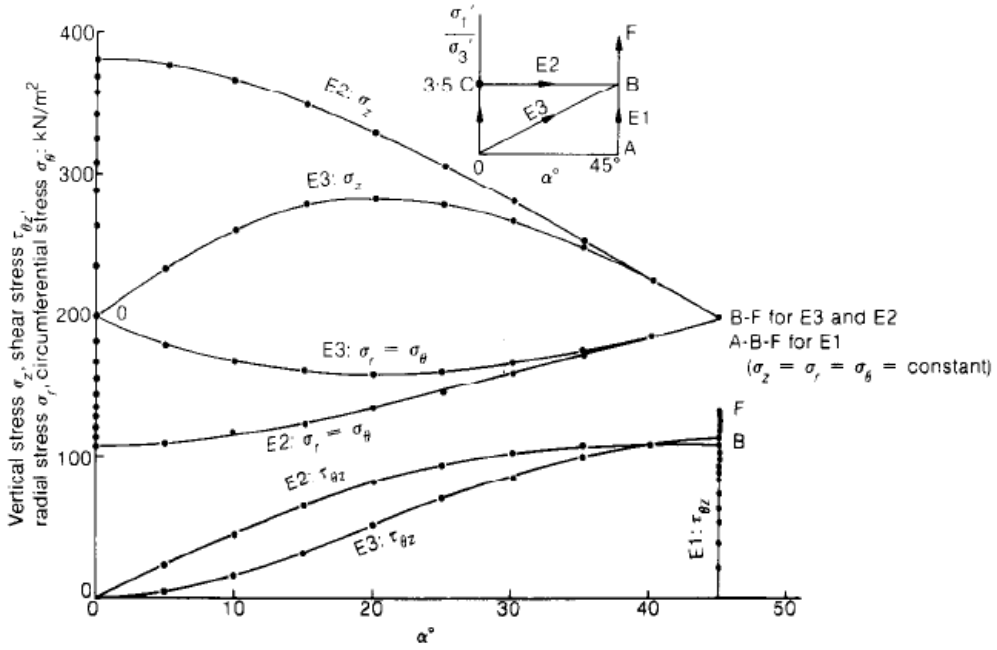

Figure 3-23 Combinations of σ_z, σ_r, σ_θ and $\tau_{\theta z}$ to followed the stress paths (after Hight *et al.*, 1983)

3.5.2 Repeatability of test results

To verify the repeatability of test results of HCA, two sand specimens with the same void ratio e=0.46 were consolidated isotropically to an effective mean stress of 200kPa using a back pressure of 400kPa. Two tests were carried out following the stress path L1 described earlier and shown in Figure 3-20.

The stress paths obtained from two tests on the q-α plane are shown in Figure 3-24. It can be seen that the failure strengths of the two specimens were very close to each other. In test L1(a) the specimen failed when q=241kPa, and in test L1(b) the failure strength was 247kPa, which means the difference between failure strength of two specimens were around 2.5%.

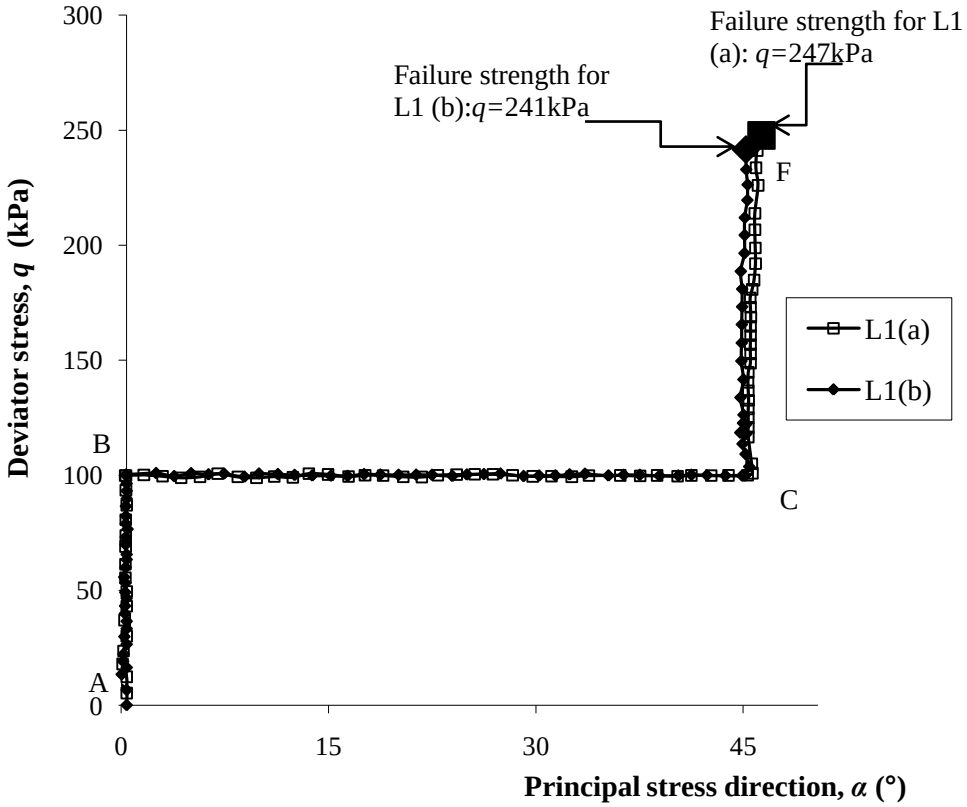

Figure 3-24 Stress paths followed in tests L1(a) and L1(b)

Figure 3-25 shows the stress-strain responses of these test specimens under the same stress. From points A-B, which was a triaxial compression stage (i.e. α=0 °, b=0), the axial strain and the shear strain increased linearly with q, while the shear stress was kept constant at 0kPa. At B-C stage, q was kept constant, and α varied from 0 ° to 45 °, (i.e. torque was applied while axial load became zero), so the axial strain and the shear strain decreased to zero, and shear stress increased linearly to 0.15%. At stage C-F, the axial strain developed in the negative direction, and the shear strain kept increasing.

It can be seen from Figure 3-25 that all stress-strain curves changed linearly firstly, then became non-linearly until failure was reached (point F). Similar values of deviator stresses for failure were obtained. It can also be

observed that the stress-strain curves for the two tests matched each other very well. The good agreement of stress-strain curves indicates that the results from this HCA were repeatable. When same strain was induced, the maximum deviation of the deviator stress was less than 3.5%.

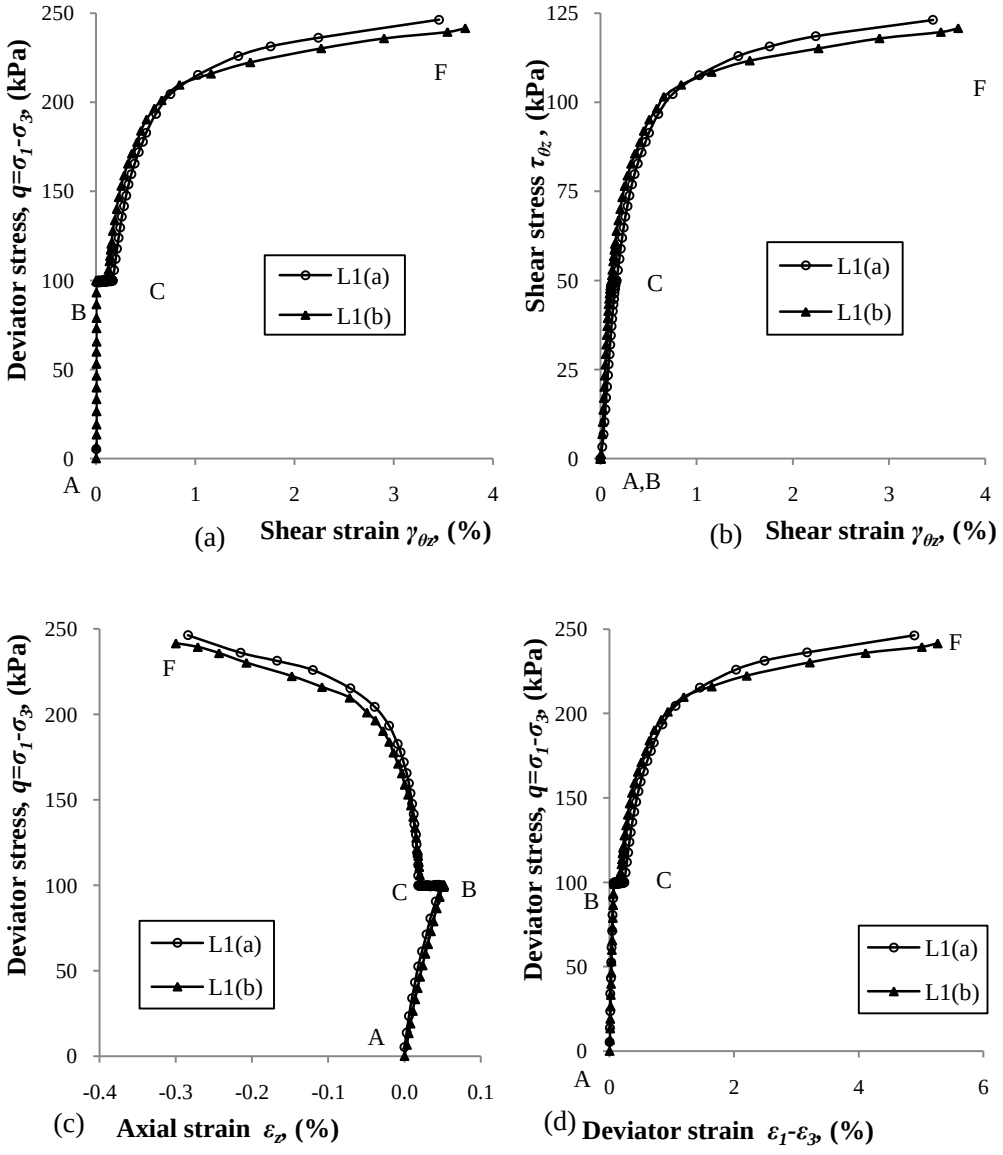

Figure 3-25 Repeatability of test results: (a) deviator stress vs. shear strain; (b) shear stress vs. shear strain; (c) deviator stress vs. axial strain; (d) deviator stress vs. deviator strain

3.5.3 Hollow cylinder test versus triaxial test

A series of drained triaxial compression tests were carried out in the HCA and a conventional triaxial apparatus to validate the testing result of the HCA. Two tests were performed using the HCA and one with the triaxial apparatus. All specimens were prepared to a relative density D_r≈90% using Portaway sand using the procedures mentioned in Section 3.4. After an isotropic consolidation, all the specimens were sheared monotonically under constant cell and back pressures, so that a constant σ'_3 was maintained. The purpose of this series of tests was to verify the measurement of strength parameters in HCA. Therefore, the comparison was focused on stress paths and friction angles. A summary of all the triaxial compression tests is given in Table 3-3.

Table 3-3 Summary of triaxial compression tests on Portaway sand

Test No.	e	D_r (%)	σ'_3 (kPa)	P'_f (kPa)	q_f (kPa)	$(q/P')_f$	φ_f (°)
HCA-150	0.464	93	150	359.8	613.4	1.70	41.5
HCA-200	0.466	92	200	438.87	720.5	1.64	40.1
TC-200	0.461	94	200	430.5	694.5	1.61	39.4
F-D00*	0.467	92	200	203	345	1.70	41.4

* In this test, p' was kept constant, so σ'_3 varied during the test, the value in table is the initial value. The value of $(q/p')_f$ is1.65 (Marri, 2010)

The stress paths of triaxial tests obtained from the HCA are shown in Figure 3-26. The advanced loading mode was employed using the displacement-controlled method. A loading rate of 0.1 mm/min was applied.

The broken line in the figure is the failure line obtained from triaxial compression tests (Marri, 2010). The data observed from HCA tests matched with the failure line very well.

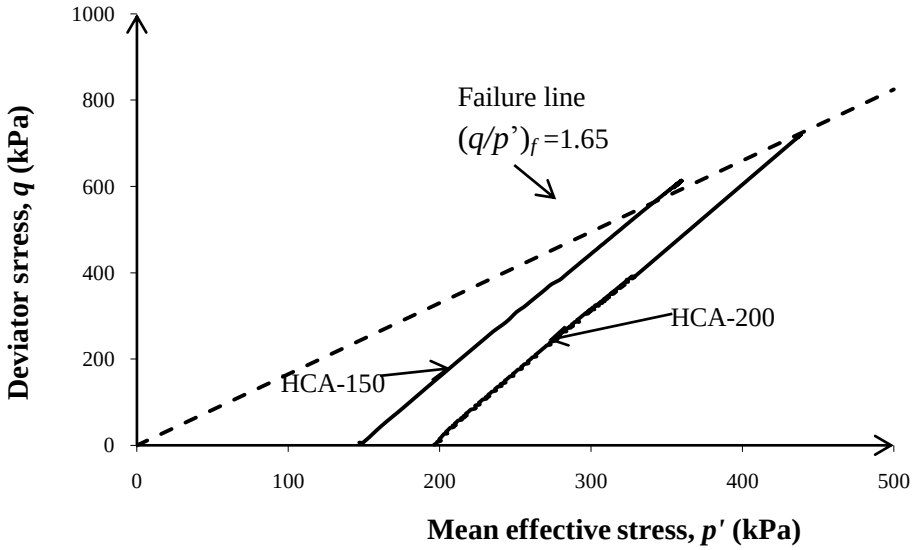

Figure 3-26 The stress paths of triaxial compression tests obtained from the HCA

In Figure 3-27, two tests are presented. Test TC-200 was conducted using a triaxial apparatus with a dimension of 50mm×100mm ($\Phi \times H$). The specimen was sheared monotonically under a constant effective confining pressure σ'_3=200kPa. Due to the different boundary conditions between the hollow cylinder apparatus and triaxial apparatus, the value of $(q/p')_f$ obtained from test TC-200 was slightly lower than those from HCA tests. However the results still can be considered to be consistent.

Another test shown in Figure 3-27 is test F-D00 carried out in the HCA. In this test, the mean effective stress p' was kept constant while the deviator stress was increased until specimen failed. The HCA stress path loading mode was used to control test F-D00. It can be seen from Figure 3-27 that the result

obtained from the HCA tests followed a stress path which was different from that in the triaxial cell. Nevertheless, the failure point agreed with the failure line shown in the figure.

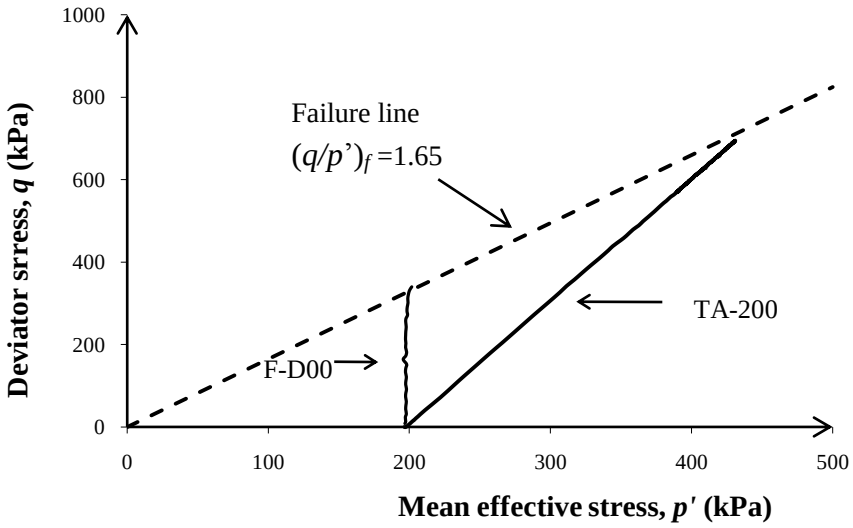

Figure 3-27 Validation of HCA testing results

3.5.4 Membrane penetration error correction

The membrane penetration (MP) correction was determined in accordance with the equation introduced by Sivathayalan and Vaid (1998) (see Eq. (2.32) in Chapter 2)

Figure 3-28 shows the effect of MP on changes of the back and inner cell volumes. From the figures, the corrected volumes were slightly different from the values recorded in test. However, the MP did not affect the volume changes significantly, especially when the specimen was approaching failure.

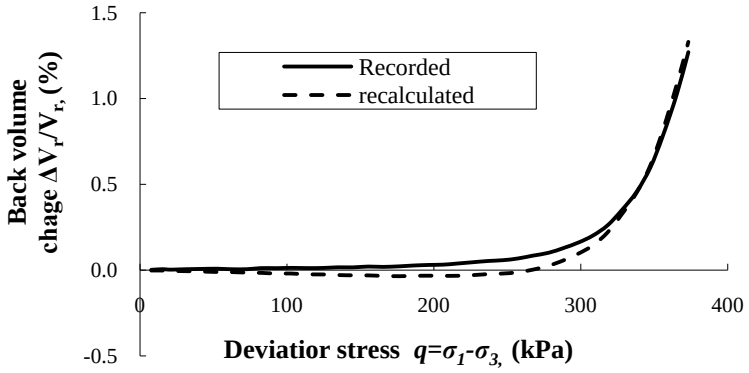

(a) Back volume change

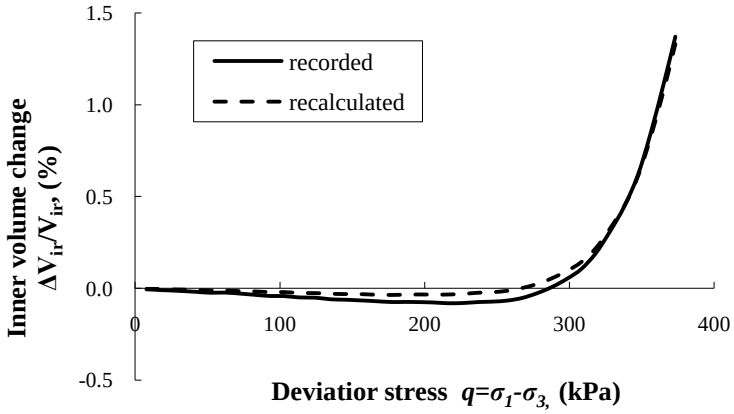

(b) Inner volume change

Figure 3-28 Volume changes of MP correction (a) back volume change; (b) inner volume change

The effects of MP on stress-strain curves are shown in Figure 3-29 when the radial strain (ε_r), volumetric strain (ε_v) and circumferential strain (ε_θ) are plotted against the deviator stress (q). As shown in Figures 3-29(b) and (c), there were small differences between the recorded values and recalculated values of radial strain and volumetric strain. However, the differences were very small, with the maximum difference being only 0.06%. In Figure 3-29(c), the circumferential deformation was not affected by the MP. As the research

was focused on the non-coaxial soil behaviour, the small difference in radial strain or volumetric strain will not materially affect the calculation of strain increment direction. Therefore, no MP correction has been made in the subsequent analyses.

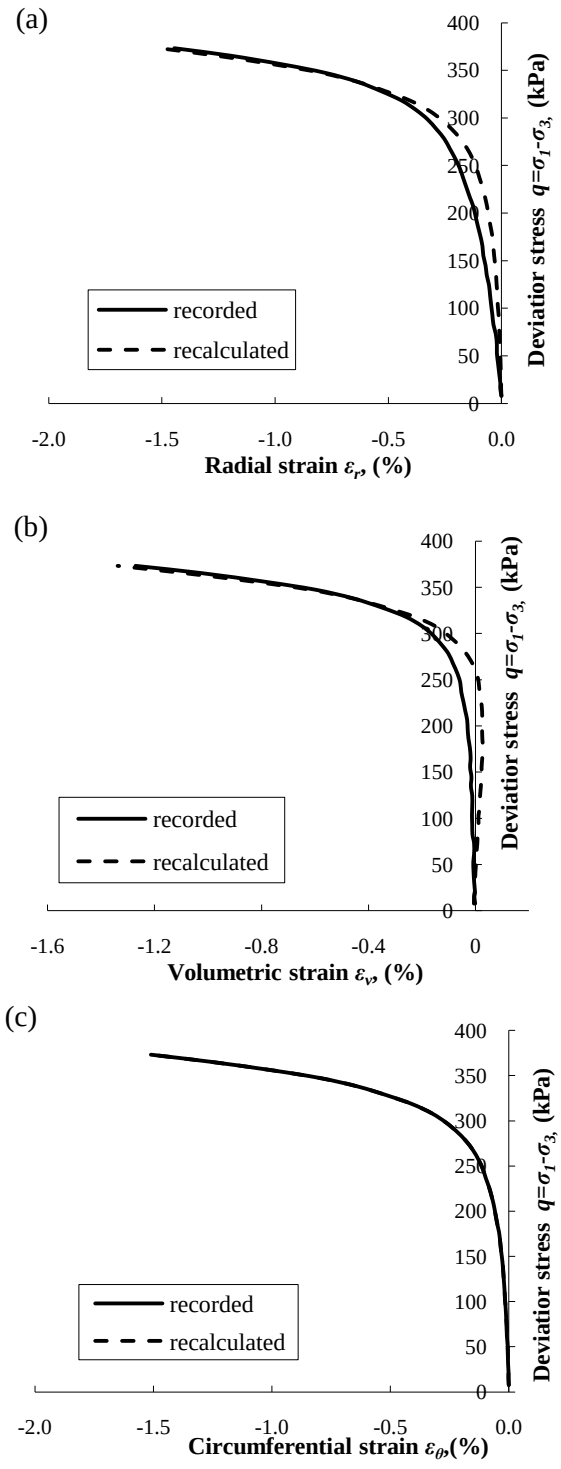

Figure 3-29 Effect of MP on stress-strain behaviours: (a) radial strain; (b) volumetric strain; (c) circumferential strain

3.6 SUMMARY

This chapter has introduced the HCA testing system employed in this study, including the hardware, such as loading cell, loading system and measuring instruments, and the control software. A 16 bit Digital Control System (DCS) was used to control and measure the axial load, torque, rotation and displacement. The outer and inner cell pressures and back pressure were controlled by Digital Pressure/Volume Controllers (DPVC). These controllers measured the volume change of the specimen, outer and inner cells by the water moved. A solid-state pressure transducer was plumbed directly to record the pore water pressure in the specimen. The

The physical characteristics of tested materials – Portaway and Leighton Buzzard sands, were presented with the particle size distributions and particle shapes. Furthermore, the specimen preparation techniques and routine test procedures involving consolidation and saturation have been described.

This chapter also deals with the verification of experimental tests and results. Four tests, following three different stress paths, were carried out to check the repeatability of test results and the control of the new testing equipment. All specimens were prepared with the same void ratio and consolidated isotropically under the same condition. According to the results, reasonable control of the different stress paths could be achieved, and good repeatability was obtained. Triaxial compression tests using HCA and

conventional triaxial apparatus were conducted and compared. Good agreement of the test data was observed, which illustrated that the results obtained from the HCA were reliable. This means that conventional triaxial tests can also be carried out using the HCA.

Chapter 4

Monotonic Loading Tests

4.1 INTRODUCTION

In this chapter, a series of tests on dense and medium dense Portaway sand will be presented to study the effect of initial anisotropy on non-coaxial behaviour of granular material. The dense specimens had a relative density of $D_r \approx 90\%$, and medium dense specimens had a relative density of $D_r \approx 50\%$. All the tests followed monotonic loading stress paths, in which specimens were sheared until failure with principal stress direction fixed at selected values. The experimental testing information will be introduced in Section 4.2. Then general soil behaviour under monotonic loading will be presented firstly in Section 4.3, followed by the discussion of non-coaxiality in Section 4.4. Finally summary of this chapter will be given in Section 4.5.

4.2 TEST DETAILS

4.2.1 Initial conditions

All the specimens in this series of tests were prepared using Portaway sand. There were fourteen tests in total, with seven tests performed on dense sand and another seven tests performed on medium dense sand. The specimen preparation, saturation, consolidation and data correction method have been described in Chapter 3.4. All specimens were isotropically consolidated to an initial effective confining pressure of 200kPa. Table 4-1 contains the initial test conditions for monotonic loading tests.

Table 4-1 Summary of initial testing conditions of monotonic loading tests (series F)

Test No.	α (°)	Stress-density state			
		e	D_r (%)	P(kPa)	P' (kPa)
F-D00	0	0.467	92	600	200
F-D15	15	0.475	88	600	200
F-D30	30	0.477	87	600	200
F-D45	45	0.479	86	600	200
F-D60	60	0.469	91	600	200
F-D75	75	0.479	86	600	200
F-D90	90	0.470	90	600	200
F-M00	0	0.551	52	600	200
F-M15	15	0.563	46	600	200
F-M30	30	0.565	45	600	200
F-M45	45	0.561	47	600	200
F-M60	60	0.552	51	600	200
F-M75	75	0.551	52	600	200
F-M90	90	0.549	53	600	200

4.2.2 Stress paths

All the monotonic loading tests were performed by increasing the deviator stress q monotonically until failure along the prescribed stress paths, which has been described in Chapter 3 and shown in Figure 3-17. Figures 4-1 (a) and (b) present the results obtained from tests for dense specimens and medium dense specimens. As displacement-control was not enabled with this apparatus, the stress control method was used for all the tests. So the figures only show the data before the specimens failed. In this study, the failure state was defined as the loading point when significant rate of strain was observed. The data was recorded in every 15 seconds. If the strain rate was about 10 times of the previous point, and the back pressure was not able to be kept constant, then the specimen was considered as failing. The accurate control of principal stress direction α is important to determine the accuracy of stress paths. Figure 4-1 shows small fluctuation of α when q is smaller than 20kPa. However the unstable deviation had been minimized with the loading rate. In the whole procedure α was controlled sufficiently well so as to be consistent with the prescribed value.

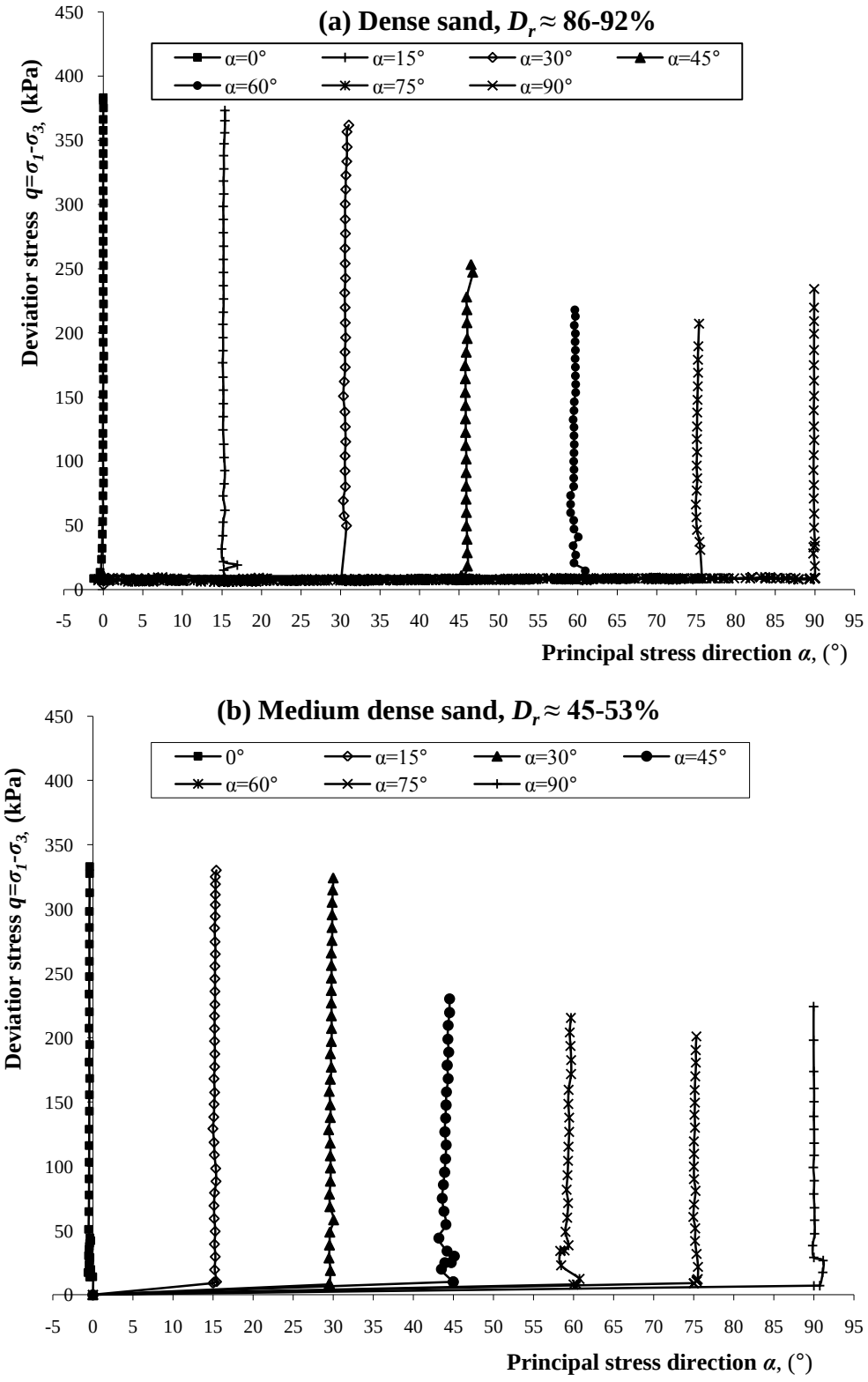

Figure 4-1 Actual stress paths followed in monotonic loading tests: (a) dense sand; (b) medium dense sand

4.3 GENERAL SOIL BEHAVIOUR

This section presents the general stress-strain behaviour of Portaway sand in the series of monotonic loading tests. The stress-strain behaviour along various shearing directions will be described for each single test, followed by the comparison and discussion.

4.3.1 Series F-D: dense sand

The results obtained from tests F-D00 to F-D90 are plotted in Figure 4-2 to Figure 4-8, and will be described in this section. There are 4 small figures for each test.

Variations of stresses

Figures 4-2(a) to 4-8(a) show the variations of the stress components, axial stress (σ_z), radial stress (σ_r), circumferential stress (σ_θ) and shear stress ($\tau_{\theta z}$), during the tests whilst shearing in fixed principal stress directions. In the figures, if the axial stress (σ_z) increased with the development of strain, the specimen was undergoing compressive loading, e.g. in Figure 4-2(a), when α=0 °, it was a compression test. In contrast, a decrease of σ_z indicates an extension loading imposed on the specimen, e.g. test F-D90 shown in Figure 4-8(a). The principal stress direction α is determined by the combination of axial and torsional load. For tests F-D00 and F-D90, when α=0 ° and 90 °, the specimen was subjected to pure compression and pure extension loading state. Under these conditions, there was no shear stress ($\tau_{\theta z}$) applied on the specimens,

as shown in Figures 4-2(a) and 4-8(a). For test F-D45, when α=45°, the specimen was subjected to cell pressures and torque only, no axial load (W) was imposed. The stress components ($\sigma_r=\sigma_\theta=\sigma_z$) were equal to the cell pressures (Figure 4-5(a)). Tests F-D15 and F-D30 were performed by combining compression loading mode with shear stresses. Similarly, tests F-D60 and F-D75 were accomplished by implementing extension load as well as the shear stresses. Table 4-2 gives a summary of all the stresses at their failure state.

Table 4-2 Summary of failure states of dense sand

Test No.	α (°)	Stresses (kPa)				Remarks at end of tests
		q	σ_z	$\sigma_r \approx \sigma_\theta$	$\tau_{\theta z}$	
F-D00	0	383	866	482	0	Bulging
F-D15	15	373	826	505	95	Bulging
F-D30	30	361	733	560	160	Shear band
F-D45	45	247	603	617	123	Twist
F-D60	60	217	527	634	95	Shear band
F-D75	75	207	492	667	49	Shear band
F-D90	90	234	446	680	0	Necking

As for all the tests, outer and inner cell pressures P_o and P_i were kept equal to each other. The radial stress (σ_z) and circumferential stress (σ_θ) were equal as well. The magnitude of σ_z and σ_θ were same as the cell pressures. Figures 4-2(a) to 4-8(a) show steady control of the outer and inner cell pressures to achieve the prescribed stress paths.

Stress-strain behaviour

The relationships between strain components and deviator stress (q) for dense specimens are presented in Figures 4-2(b) to 4-8 (b). The strain development was dependent on the inclination of principal stress axes during shearing. The strain components, axial strain (ε_z), circumferential strain (ε_θ), radial strain (ε_r) and shear strain ($\gamma_{\theta z}$) varied along with the stress components shown in Figures 4-2(a) to 4-8(a). The radial strains (ε_r) and circumferential strains (ε_θ) were found to be coincident in this series of tests. At the same deviator stress level q, axial strain (ε_z) abated with the increase of principal stress axis angle, and the radial strain (ε_r) and circumferential strain (ε_θ) followed the opposite trend. From Figures 4-2(b) to 4-4(b), α=0 ° to 30 °, axial strains (ε_z) developed in the positive direction. The specimens were compressed along the vertical axis and expanded along the radial direction, so circumferential strain (ε_θ) and radial strain (ε_r) increased in the negative direction. When α=45 °, as shown in Figure 4-5(b), ε_r and ε_θ followed the axis of zero, and only a small amount of axial strain (ε_z) was produced when the specimen approached failure. It should be noted that there was no shear strain ($\gamma_{\theta z}$) generated in test F-D00, when α=0 °, as the specimen was not subjected to torsional load, see Figure 4-2(b). Then from α=15 ° to 45 °, at the same deviator stress level, $\gamma_{\theta z}$ increased with the increase of α. From α=60 ° to 90 ° (Figure 4-6(b) to Figure 4-8(b)), axial strain (ε_z) developed in the negative direction, while ε_θ and ε_r were on the positive side. When α=90 °, there was no shear strain observed (Figure 4-8(b)).

Figures 4-2(c) to 4-8(c) illustrate the principal strains vs. deviator stress relationships. The intermediate strain (ε_2) was equal to radial strain (ε_r), so ε_2 varied in the same way as ε_r and ε_θ. In the tests sheared in compression mode, F-D00, F-D15 and F-D30 (Figures 4-2(c) to 4-4(c)), ε_2 developed towards the negative direction. While in the tests carried out in extension mode, F-D60, F-D75 and F-D90 (Figures 4-6(c) to 4-8(c)), the strain curves were located on the posstive side. No intermediate strain was generated in test F-D45 as shown in Figure 4-5(c).

The volumetric strains (ε_v) versus deviator strain (ε_1-ε_3) obtained from experiments are presented in Figures 4-2(d) to 4-8 (d). Due to the high density of specimens (D_r≈90%), only a very small amount of volumetric contraction was obtained at the beginnning stage of shearing. It was then followed by dilation, especially when the specimens were approaching failure.

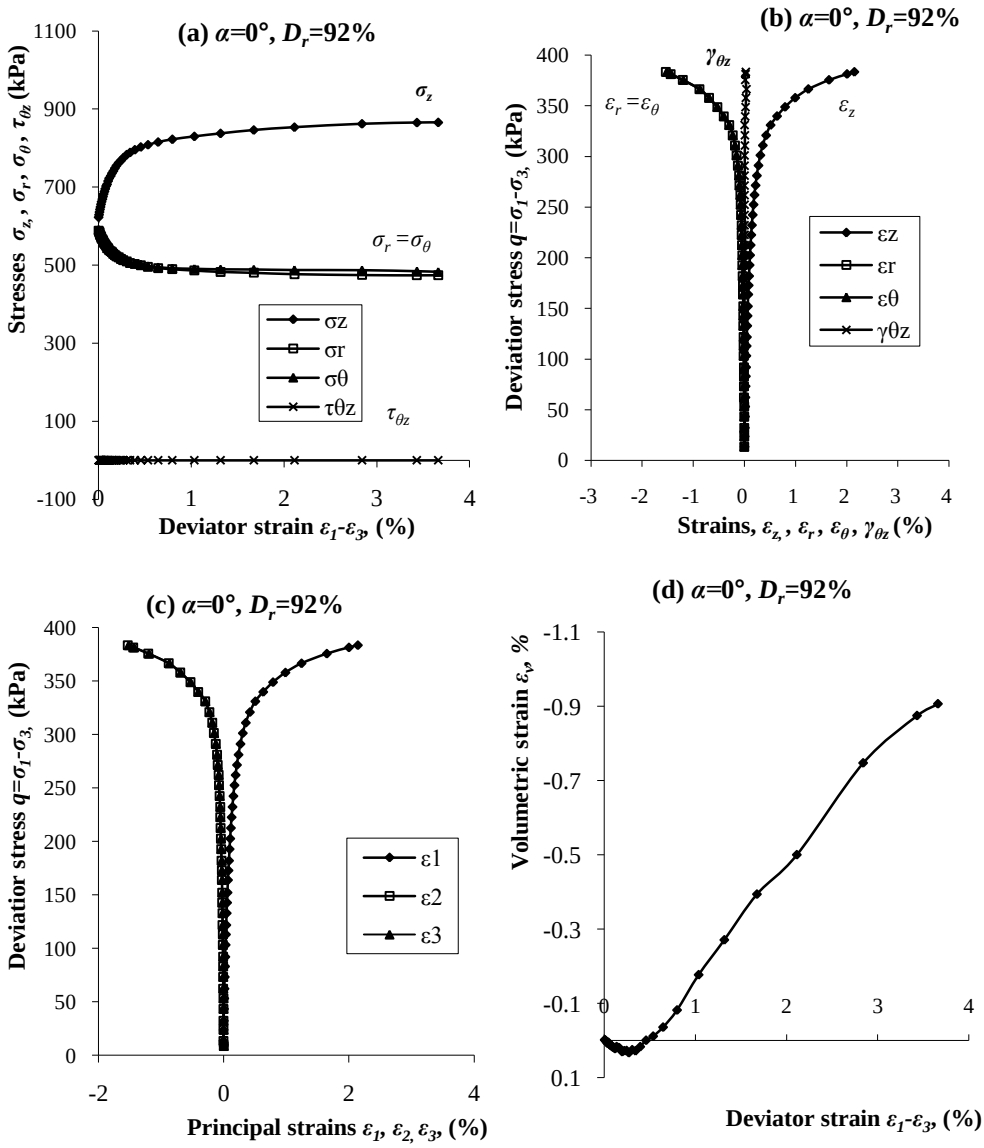

Figure 4-2 Results of test F-D00 with α=0°: (a) stress components vs. deviator strain; (b) deviator stress vs. strain components; (c) deviator stress vs. principal strains; (d) volumetric strain vs. deviator strain.

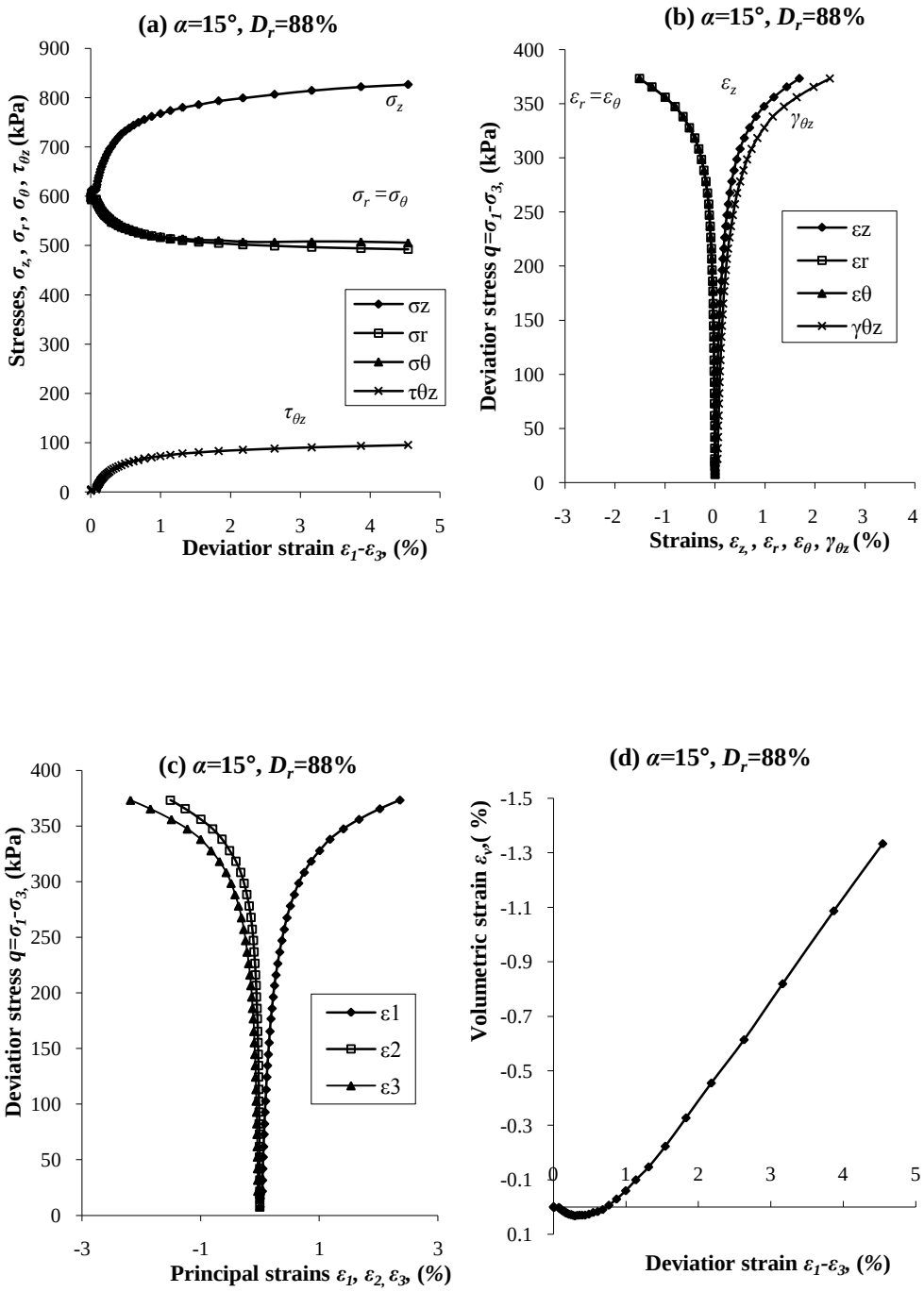

Figure 4-3 Results of test F-D15 with α=15°: (a) stress components vs. deviator strain; (b) deviator stress vs. strain components; (c) deviator stress vs. principal strains; (d) volumetric strain vs. deviator strain.

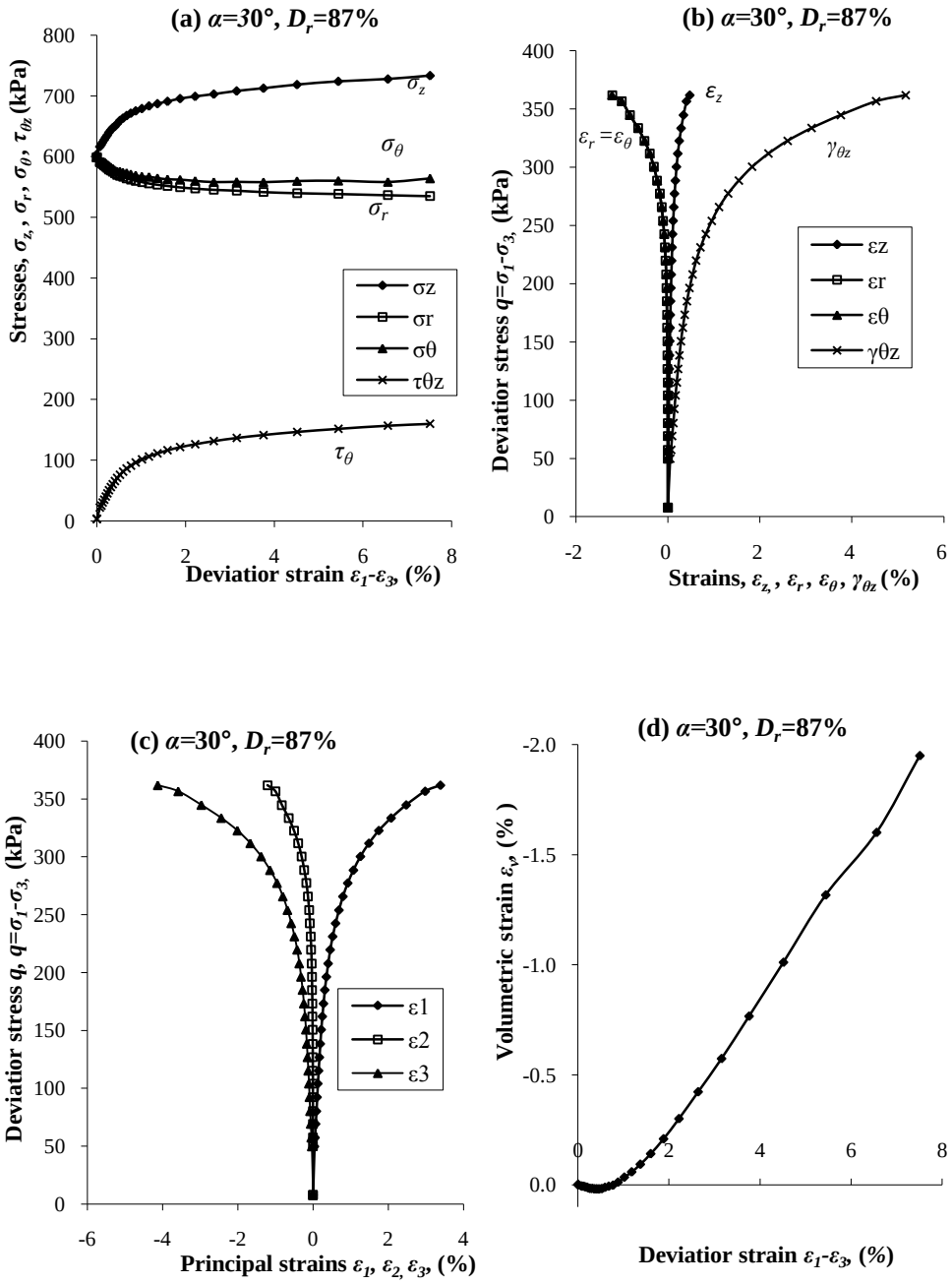

Figure 4-4 Results of test F-D30 with α=30°: (a) stress components vs. deviator strain; (b) deviator stress vs. strain components; (c) deviator stress vs. principal strains; (d) volumetric strain vs. deviator strain.

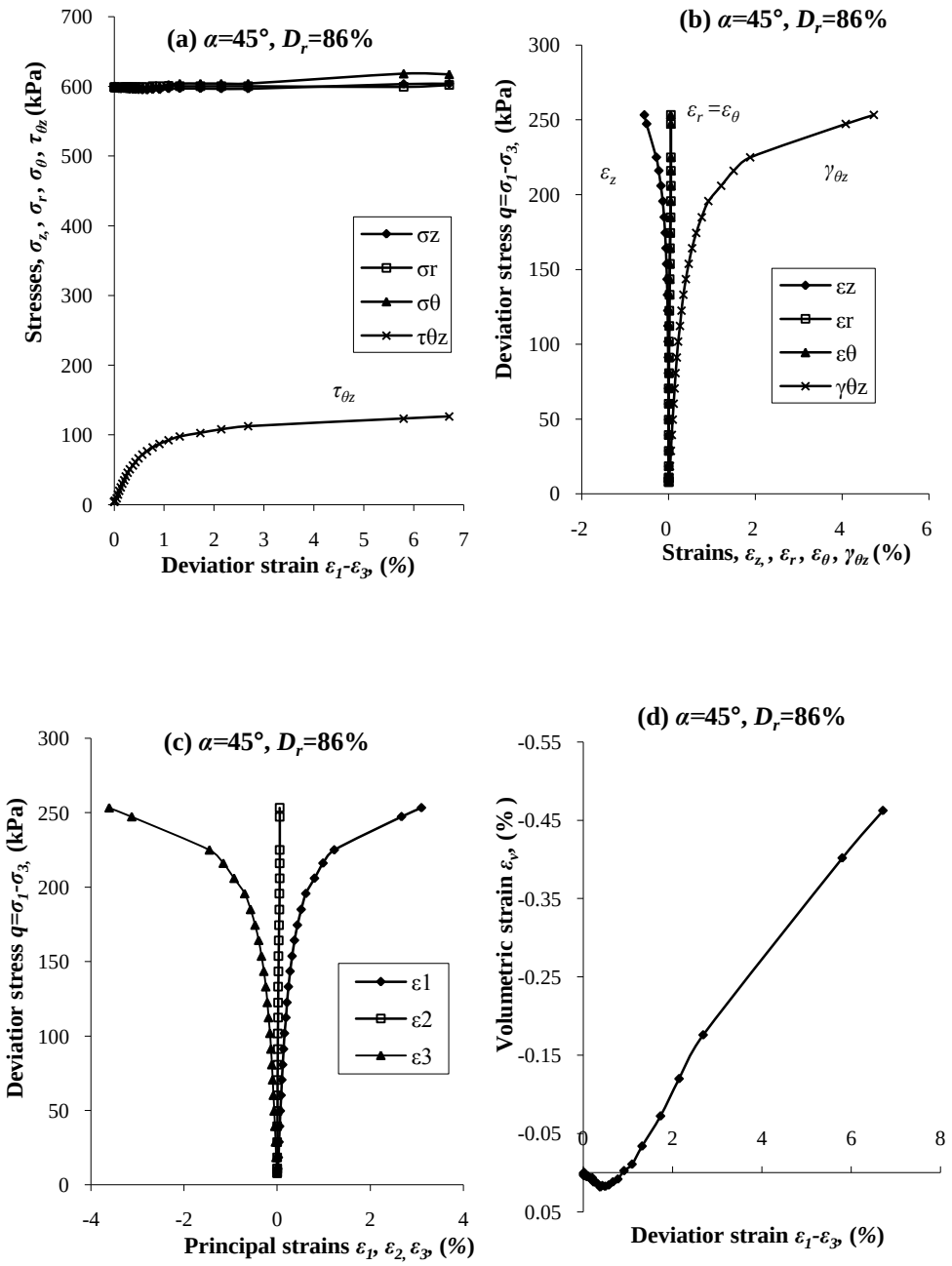

Figure 4-5 Results of test F-D45 with α=45°: (a) stress components vs. deviator strain; (b) deviator stress vs. strain components; (c) deviator stress vs. principal strains; (d) volumetric strain vs. deviator strain.

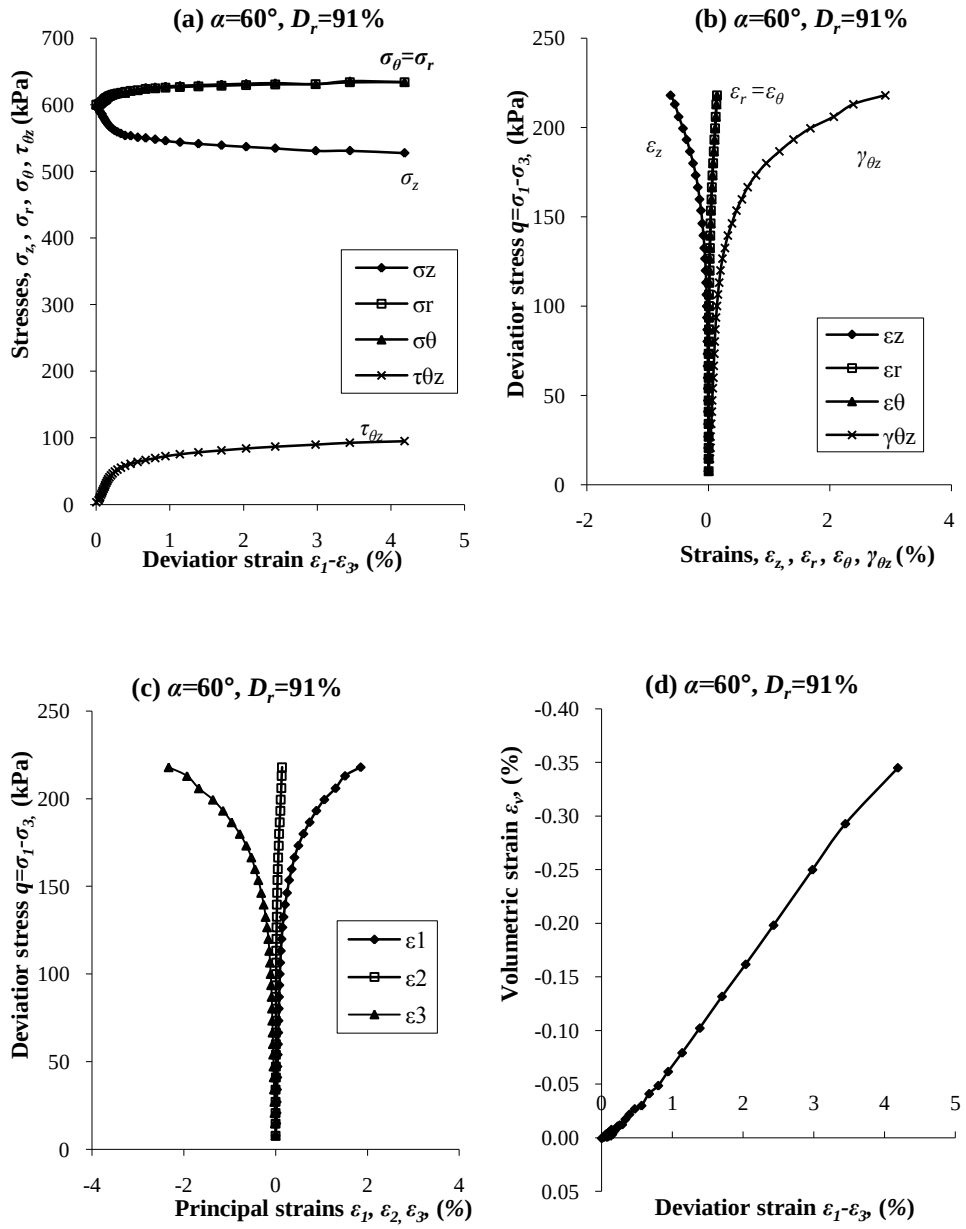

Figure 4-6 Results of test F-D60 with α=60°: (a) stress components vs. deviator strain; (b) deviator stress vs. strain components; (c) deviator stress vs. principal strains; (d) volumetric strain vs. deviator strain.

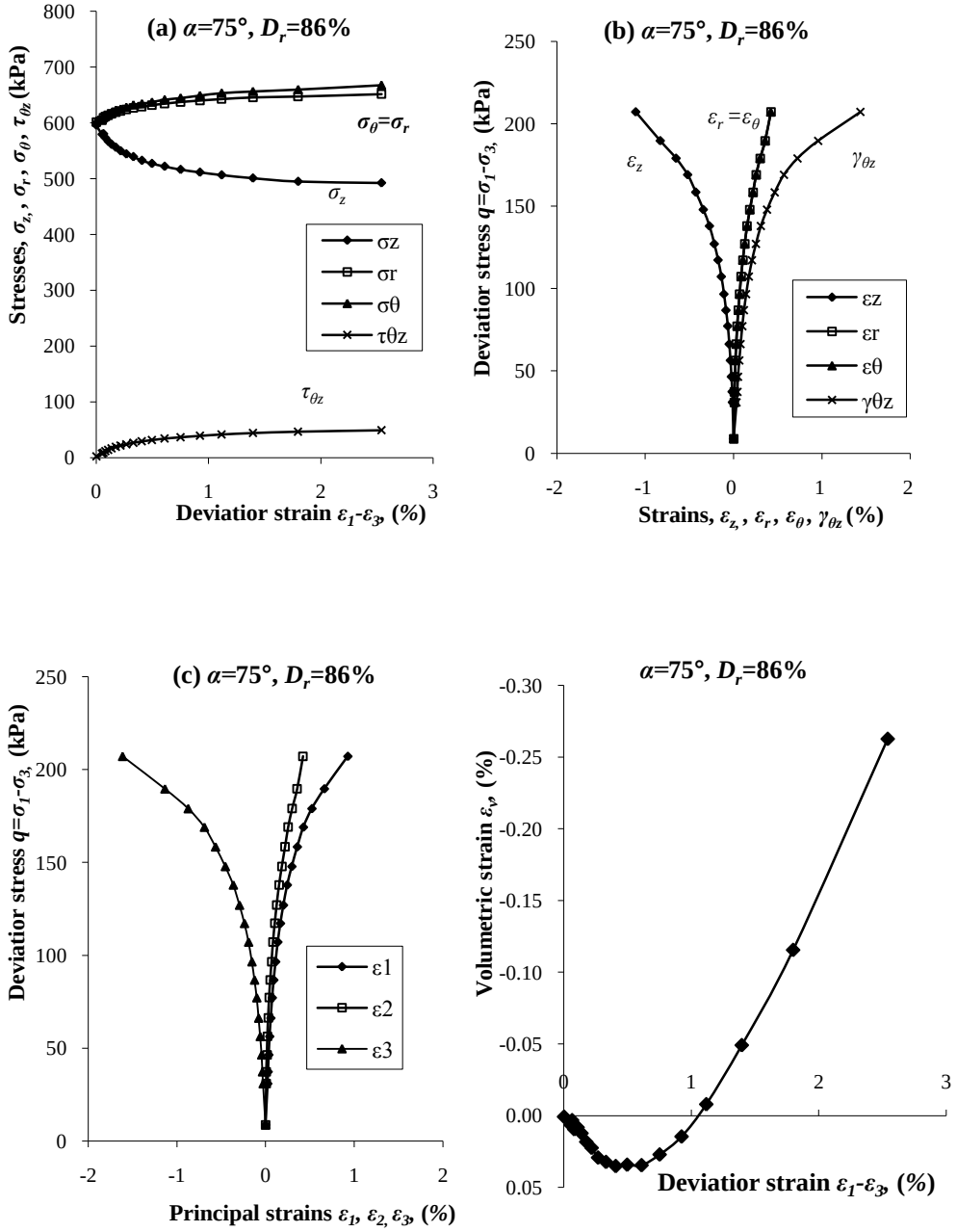

Figure 4-7 Results of test F-D75 with α=75°: (a) stress components vs. deviator strain; (b) deviator stress vs. strain components; (c) deviator stress vs. principal strains; (d) volumetric strain vs. deviator strain.

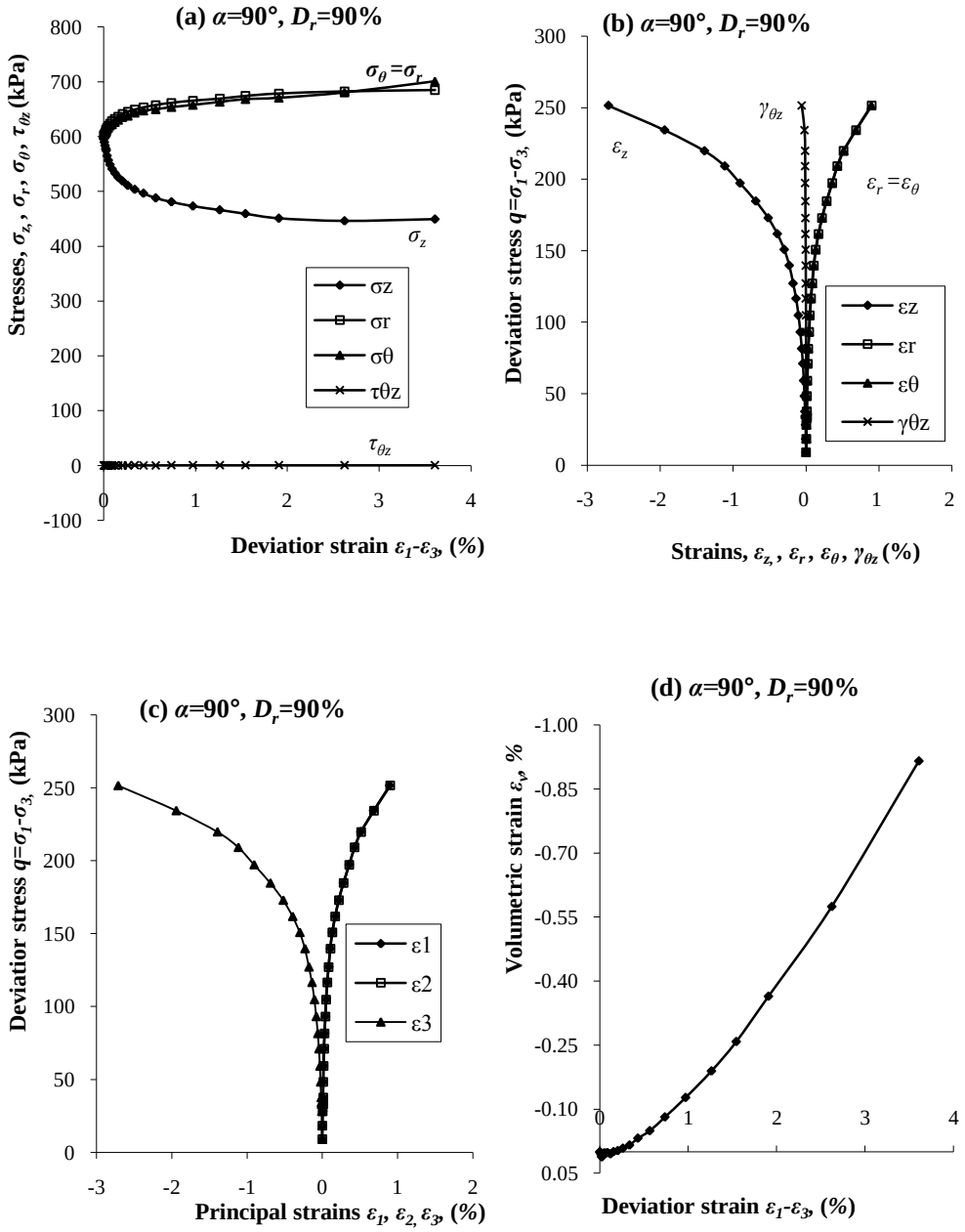

Figure 4-8 Results of test F-D90 with α=90°: (a) stress components vs. deviator strain; (b) deviator stress vs. strain components; (c) deviator stress vs. principal strains; (d) volumetric strain vs. deviator strain.

4.3.2 Series F-M: medium dense sand

Figures 4-9 to 4-15 present the results of tests F-M00 to F-M90 carried out on the medium dense specimens. The same stress paths as on the dense sand

were implemented. The actual stress paths have been shown in Figure 4-1(b). Table 4-3 summarizes the stresses states when specimens failed.

Table 4-3 Summary of failure states of medium dense sand

Test No.	α (°)	Stresses (kPa)				Remarks at end of test
		q	σ_z	$\sigma_r \approx \sigma_\theta$	$\tau_{\theta z}$	
F-M00	0	333	824	490	0	Bulging
F-M15	15	330	808	516	87	Bulging
F-M30	30	324	714	552	140	Shear band
F-M45	45	230	600	598	115	Twist
F-M60	60	215	527	634	94	Shear band
F-M75	75	201	486	661	49	Necking
F-M90	90	220	446	686	0	Necking

Variations of stresses

In Figures 4-9(a) to 4-15(a), the stress components are plotted against the deviator strain (ε_1-ε_3). As can be seen in Figure 4-9(a), in the compression test of medium dense sand, the radial stress (σ_r) diverged from the circumferential stress (σ_θ) by about 10kPa. This was due to the instability of the controller. However, as shown in Figures 4-9(b) and (c), the effect of this divergence on the strains was very small and can be neglected. From tests F-M00 to F-M30, the specimens were subjected to compression loading. With the developing of deformation, axial stress (σ_z) increased, radial strain (σ_r) and circumferential stress (σ_θ) decreased, as shown in Figures 4-9(a) to 4-11(a). Tests F-M00 with α=0 ° was a pure compression test, so there was no shear stress generated (Figure 4-9(a)). Test F-M45 with α=45 ° was a torsional test with no axial load (W) applied on the specimen. During the shearing, σ_z, σ_r and σ_θ were kept

constant and equal to each other and shear stress increased with the strain, as shown in Figure 4-12(a). Figures 4-13(a) to 4-15(a) are results of the tests involving extension loading, which are tests F-M60 to F-M90. As shown in the figures, during the shearing progress, radial strain (σ_r) and circumferential stress (σ_θ) increased while axial stress (σ_z) decreased. Test F-M90 was a pure extension test.

Stress-strain behaviour

Figures 4-9(b) to 4-15(b) aim to present the strain components developing with the loading was imposed. In Figure 4-9(b), the radial strain (ε_r) and circumferential strain (ε_θ) measured in the pure compression test on medium dense sand were slightly different. The reason for this difference was the deviation between the radial stress (σ_r) and circumferential stress (σ_θ) as mentioned. For the other tests, ε_r was equal to ε_θ. In the pure compression and extension tests, Figures 4-9(b) and 4-15(b), the shear strains were nearly zero. From Figures 4-9(b) to 4-11(b), specimens were compressed, so ε_z increased in the positive direction. For tests F-M60 to F-M90 (Figures 4-13(b) to 4-15(b)), specimens were extended, so ε_z developed in the negative direction. ε_r and ε_θ increased in the opposite way to the axial strain ε_z. In test F-M45 (Figure 4-12(b)), the specimen were under torsional loading, there was no axial strain and the specimen expanded slightly in the radial direction.

Figures 4-9(c) to 4-15(c) show the variations of principal strain with $\varepsilon_2 = \varepsilon_r$ for all the tests. In Figure 4-9(c), $\varepsilon_1 = \varepsilon_z$ and ε_3 was same as ε_θ. While in Figure 4-15(c), $\varepsilon_1=\varepsilon_\theta$ and $\varepsilon_3 = \varepsilon_z$. For test F-M45 in Figure 4-12(c), ε_2 was nearly zero, and ε_1 was symmetrical with ε_3 along the axis of zero. The volumetric strains

are plotted in Figures 4-9(d) to 4-15(d). The specimens contracted slightly at the beging of shearing then dilated until failure was reached.

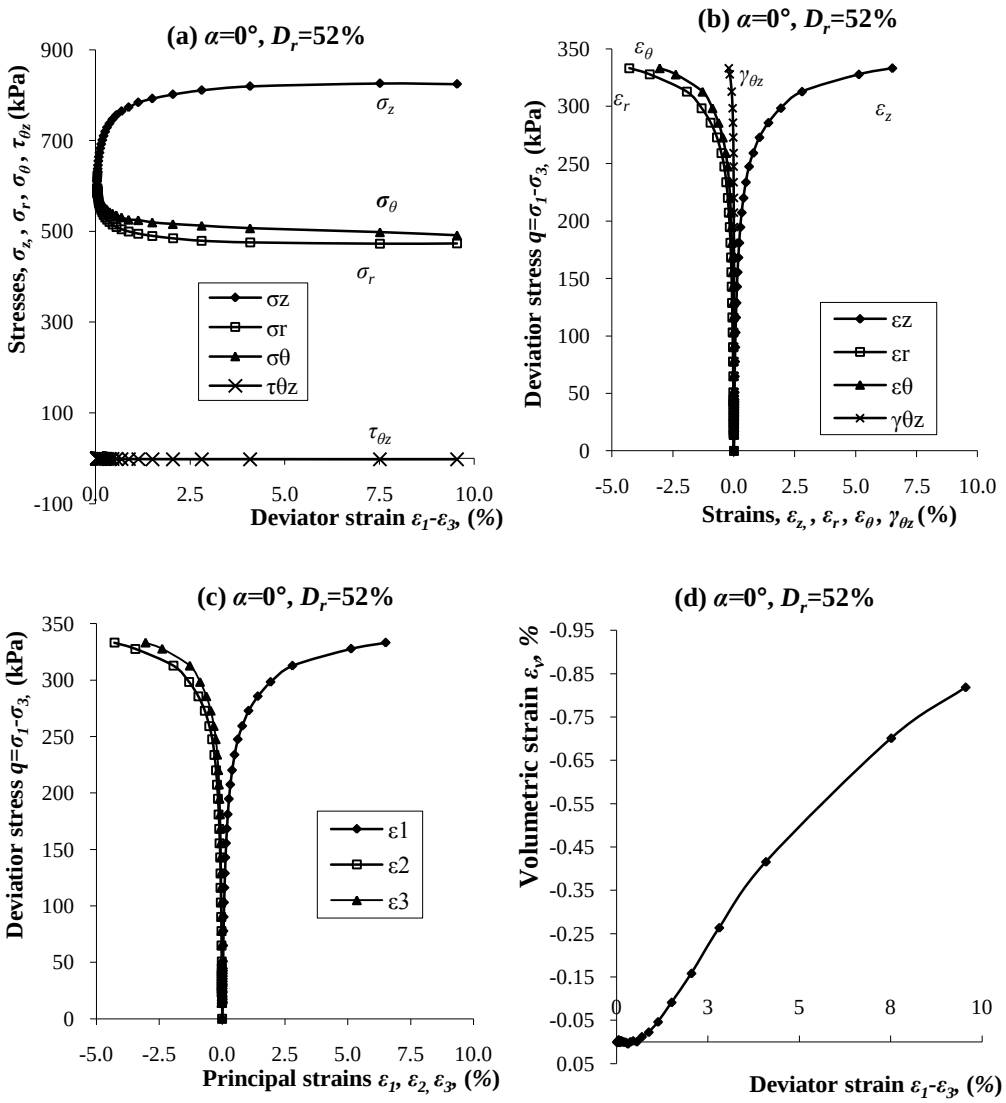

Figure 4-9 Results of test F-M00 with α=0°: (a) stress components vs. deviator strain; (b) deviator stress vs. strain components; (c) deviator stress vs. principal strains; (d) volumetric strain vs. deviator strain.

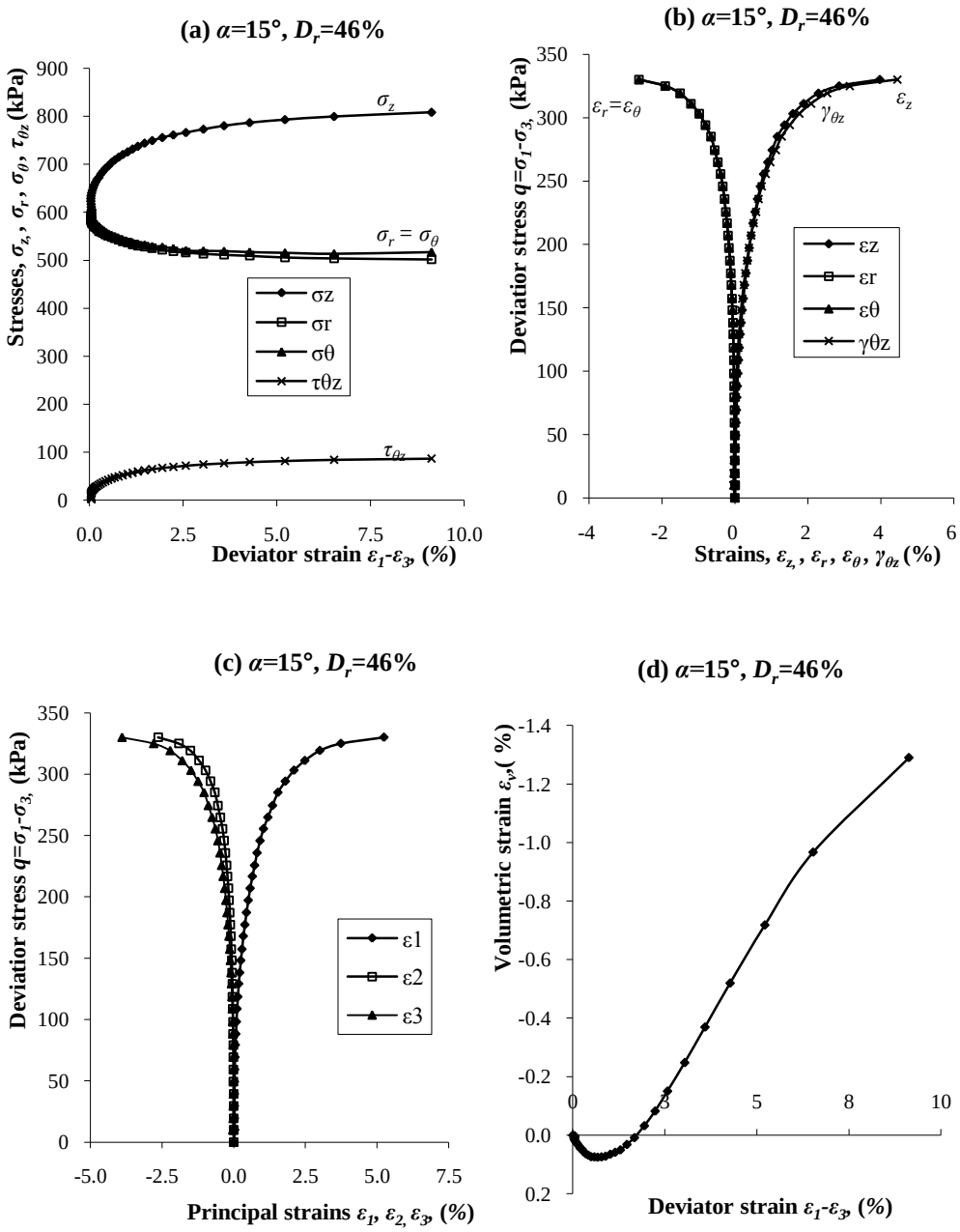

Figure 4-10 Results of test F-M15 with α=15°: (a) stress components vs. deviator strain; (b) deviator stress vs. strain components; (c) deviator stress vs. principal strains; (d) volumetric strain vs. deviator strain.

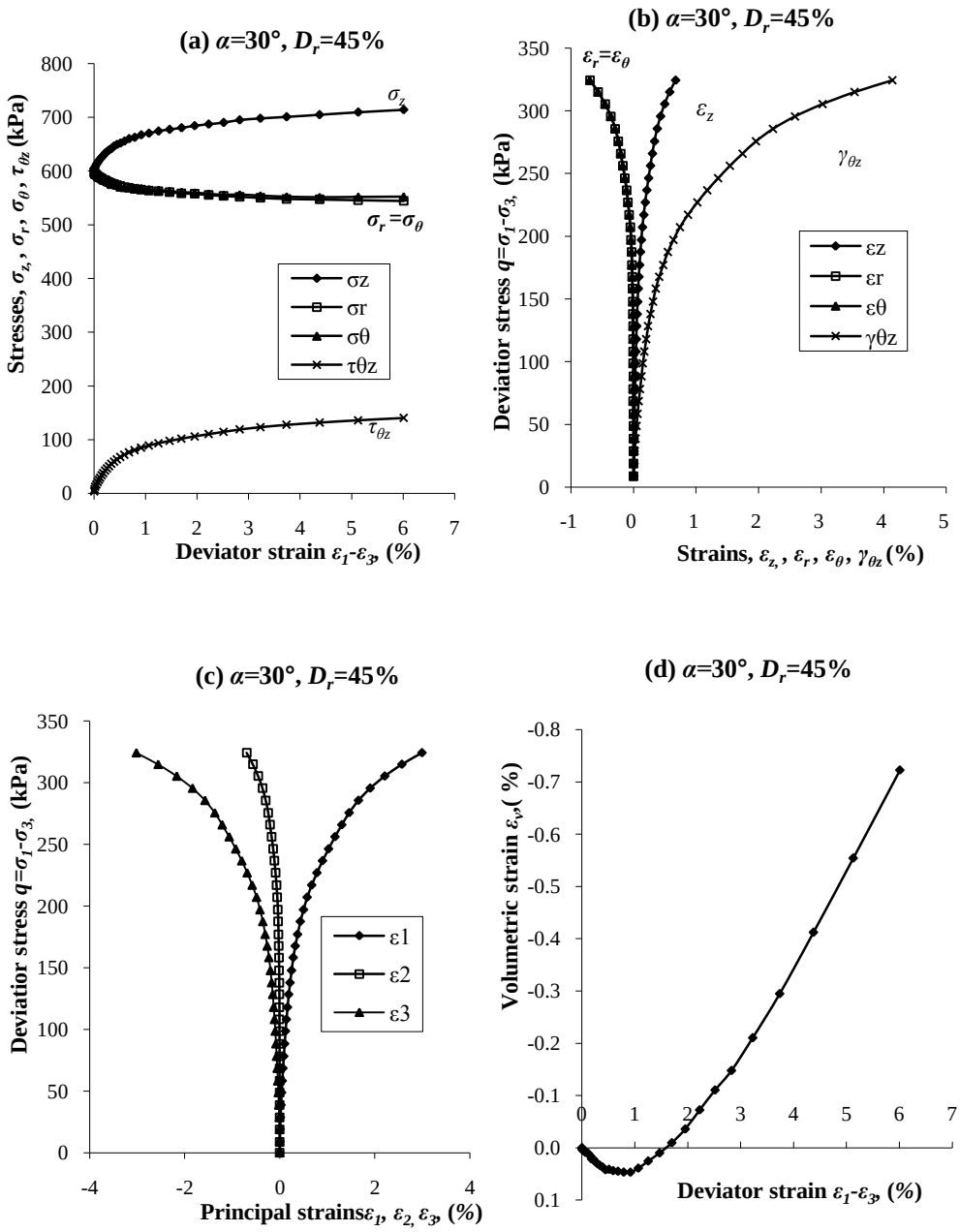

Figure 4-11 Results of test F-M30 with α=30°: (a) stress components vs. deviator strain; (b) deviator stress vs. strain components; (c) deviator stress vs. principal strains; (d) volumetric strain vs. deviator strain.

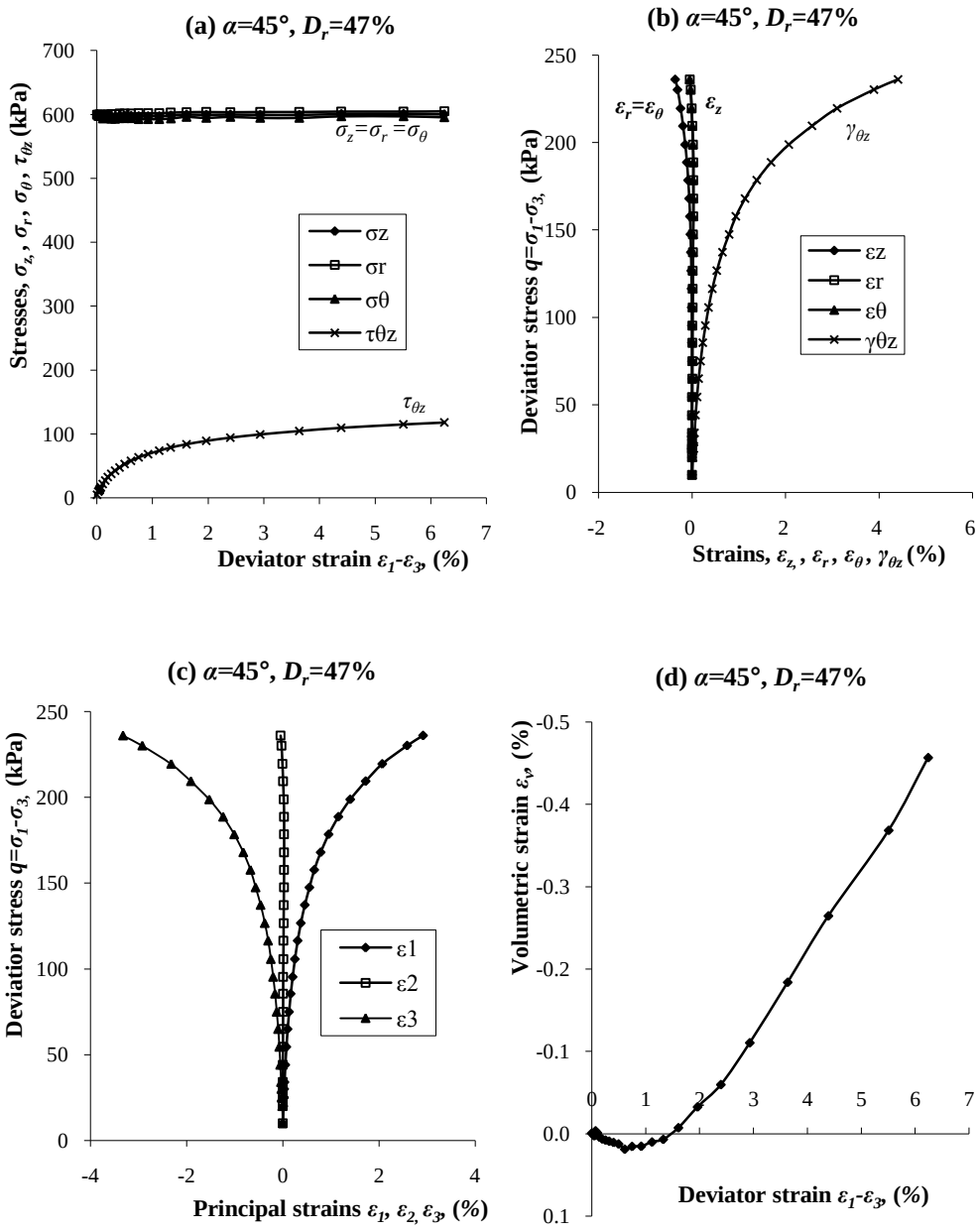

Figure 4-12 Results of test F-M45 with α=45°: (a) stress components vs. deviator strain; (b) deviator stress vs. strain components; (c) deviator stress vs. principal strains; (d) volumetric strain vs. deviator strain.

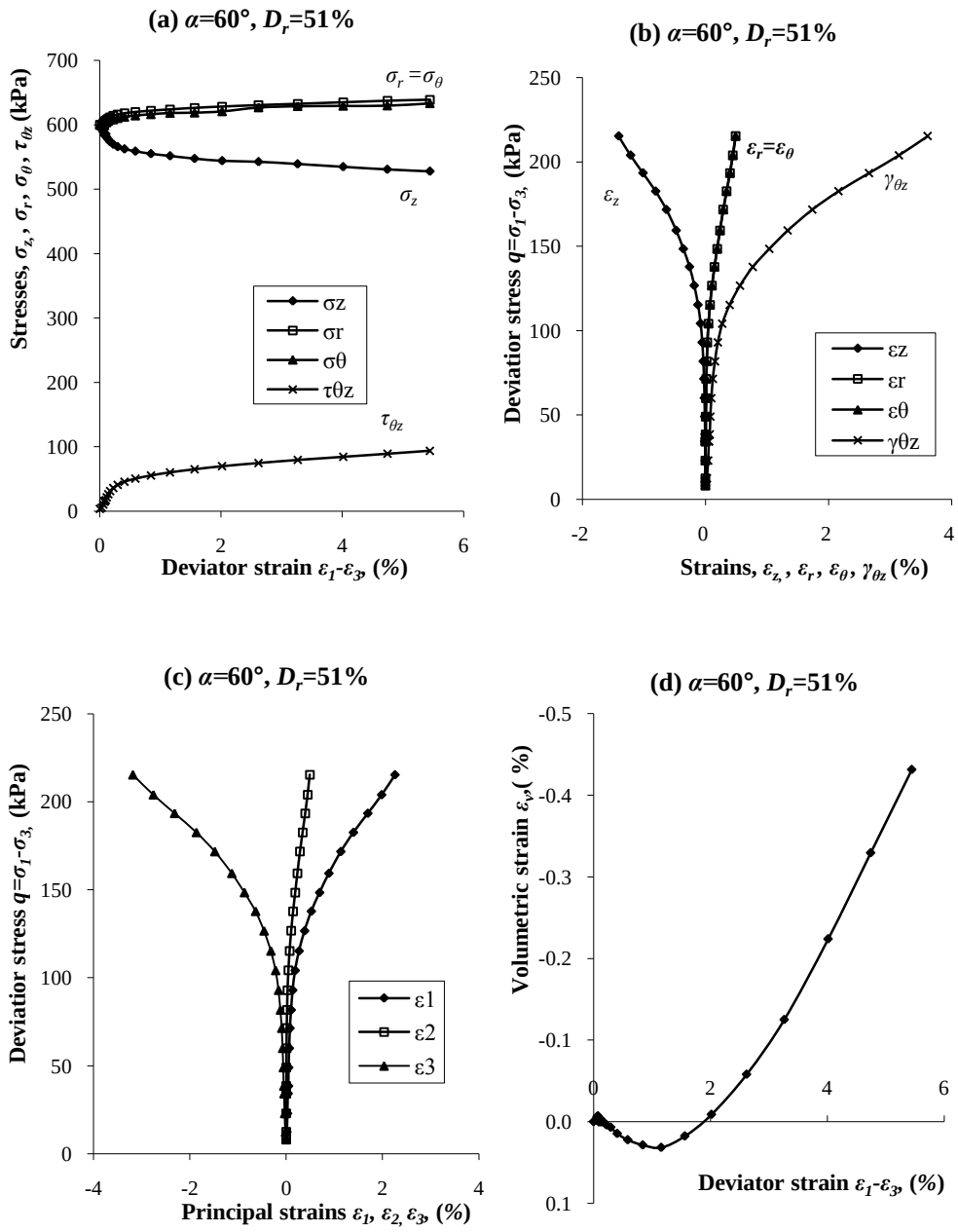

Figure 4-13 Results of test F-M60 with α=60°: (a) stress components vs. deviator strain; (b) deviator stress vs. strain components; (c) deviator stress vs. principal strains; (d) volumetric strain vs. deviator strain.

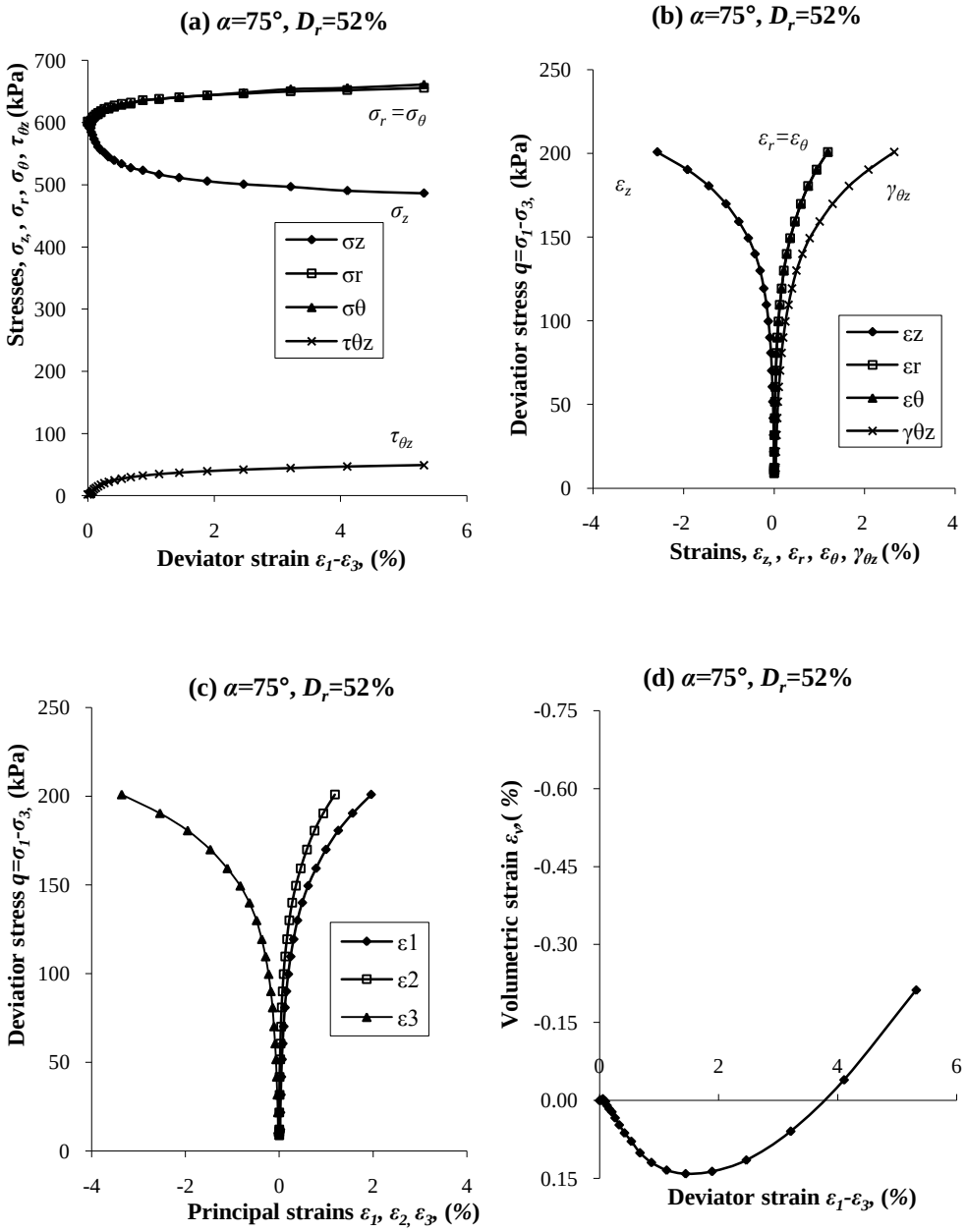

Figure 4-14 Results of test F-M75 with α=75°: (a) stress components vs. deviator strain; (b) deviator stress vs. strain components; (c) deviator stress vs. principal strains; (d) volumetric strain vs. deviator strain.

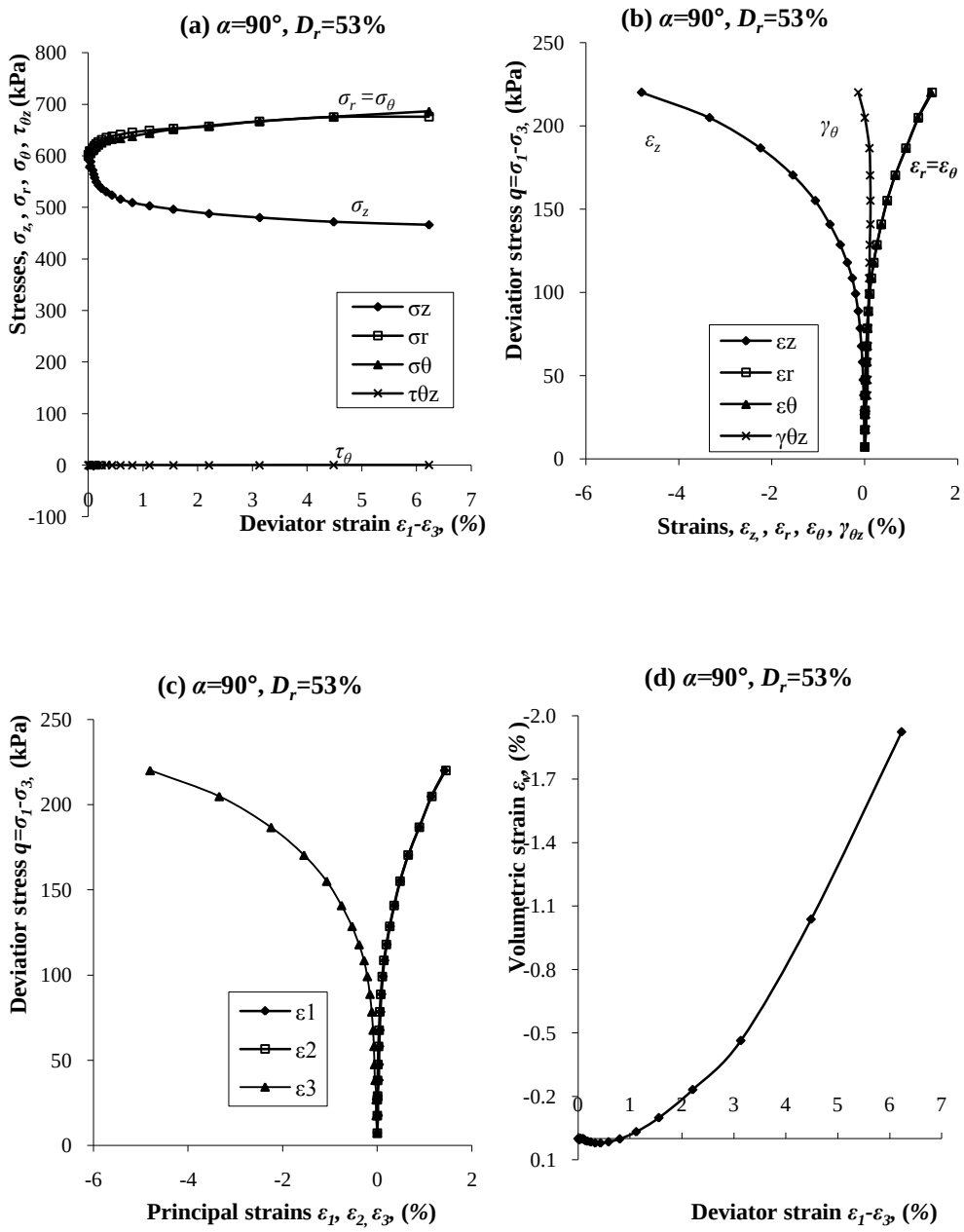

Figure 4-15 Results of test F-M90 with α=90°: (a) stress components vs. deviator strain; (b) deviator stress vs. strain components; (c) deviator stress vs. principal strains; (d) volumetric strain vs. deviator strain.

4.3.3 Discussion and comparison

Four tests for each density were chosen to analyze the influence of loading direction on soil behaviour. They are tests F-D00, F-D45, F-D75, F-D90, and F-M00, F-M45, F-M75, F-M90. These tests were selected because of their particularities, pure compression and extension, pure torsion, and lowest shear resistance.

Effect of loading direction

Figures 4-16 and 17 show the relationships between shear stress ($\tau_{\theta z}$)/ axial stress (σ_z) and deviator strains (ε_1-ε_3) of Portaway sand under monotonic loading, respectively. As shown in Figures 4-16(a) and 4-17(a), maximum shear stresses ($\tau_{\theta z}$) existed in the tests with α kept constant at 45 °. When there was the same deformation generated, the tests with the largest axial stress (σ_z) were the pure compression tests with α=0 °, as σ_z decreased with the increase of principal stress axis inclination, as shown in Figures 4-16(b) and 4-17(b).

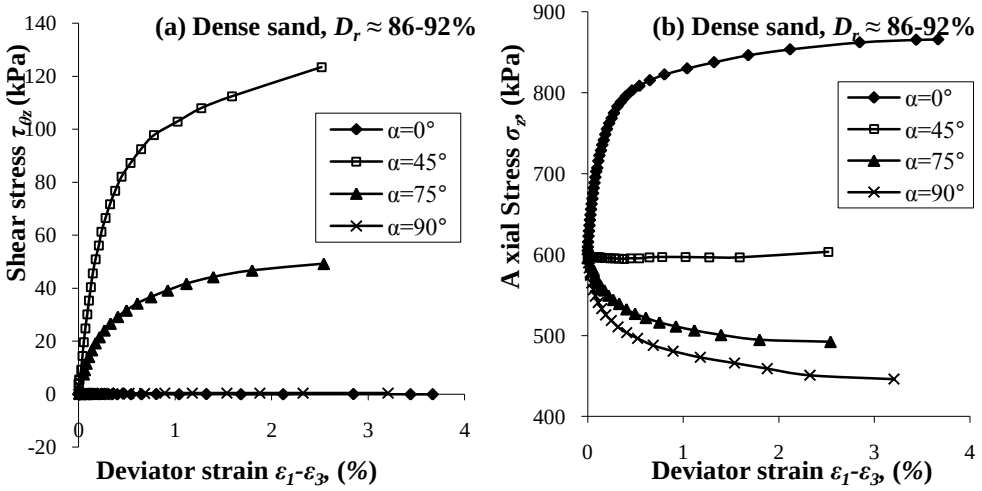

Figure 4-16 Relationships between the stress components and deviator strain on dense sand: (a) shear stress vs. deviator strain; (b) axial stress vs. deviator strain.

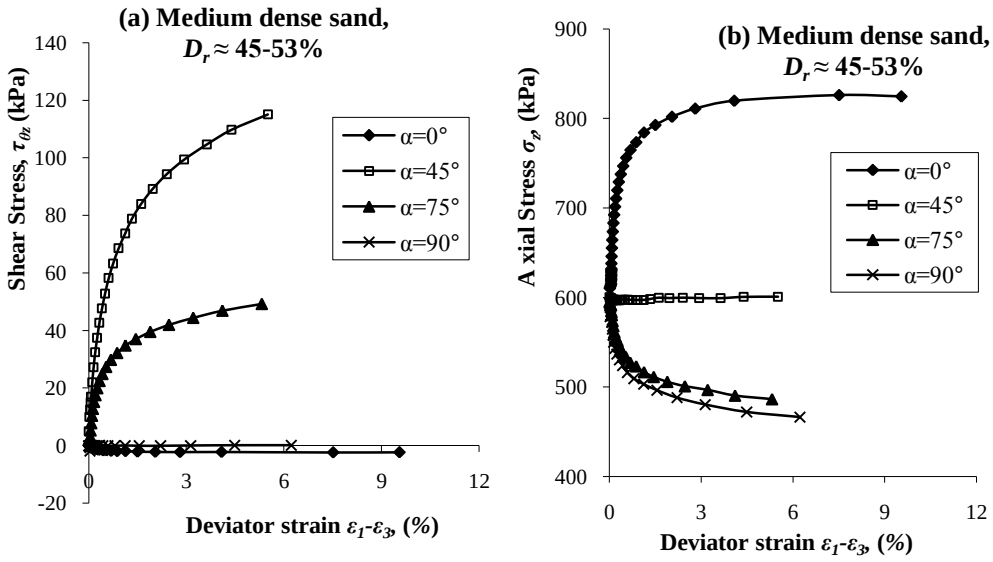

Figure 4-17 Relationships between the stress components and deviator strain on medium dense sand: (a) shear stress vs. deviator strain; (b) axial stress vs. deviator strain.

Figure 4-18 shows the relationships between deviator stresses (q) and the deviator strains for dense and medium dense specimens. For both dense and medium dense sand, the specimen strength and deformation behaviour was varied with the variation of principal stress direction. Specimens were stronger when the shearing direction, α, was 0°. In contrast, when α=75°, the lowest resistance was obtained. Less deformation was observed at higher stress in the test with α=0°. The relationships between volumetric strains and shear strains are presented in Figure 4-19. As the dense specimens were prepared with a high relative density, only slight contraction occurred in the early stages of the test. More contraction occurred in the medium dense sand. The volumetric strain was related to the failure strength. For the pure extension test, when α=90°, the specimens dilated when shearing along the fixed principal stress direction was enforced. An isotropic specimen means that the mechanical properties are isotropic, so the failure strength and deformation behaviour is

independent of the principal stress direction. The difference in soil behaviour caused by the change of loading direction provides a significant evidence to show the initial anisotropic fabric of the specimen. The inherent fabric anisotropy is a dominant factor that influences the soil behaviour including strain and strain increments in monotonic loading tests without pre-loading history.

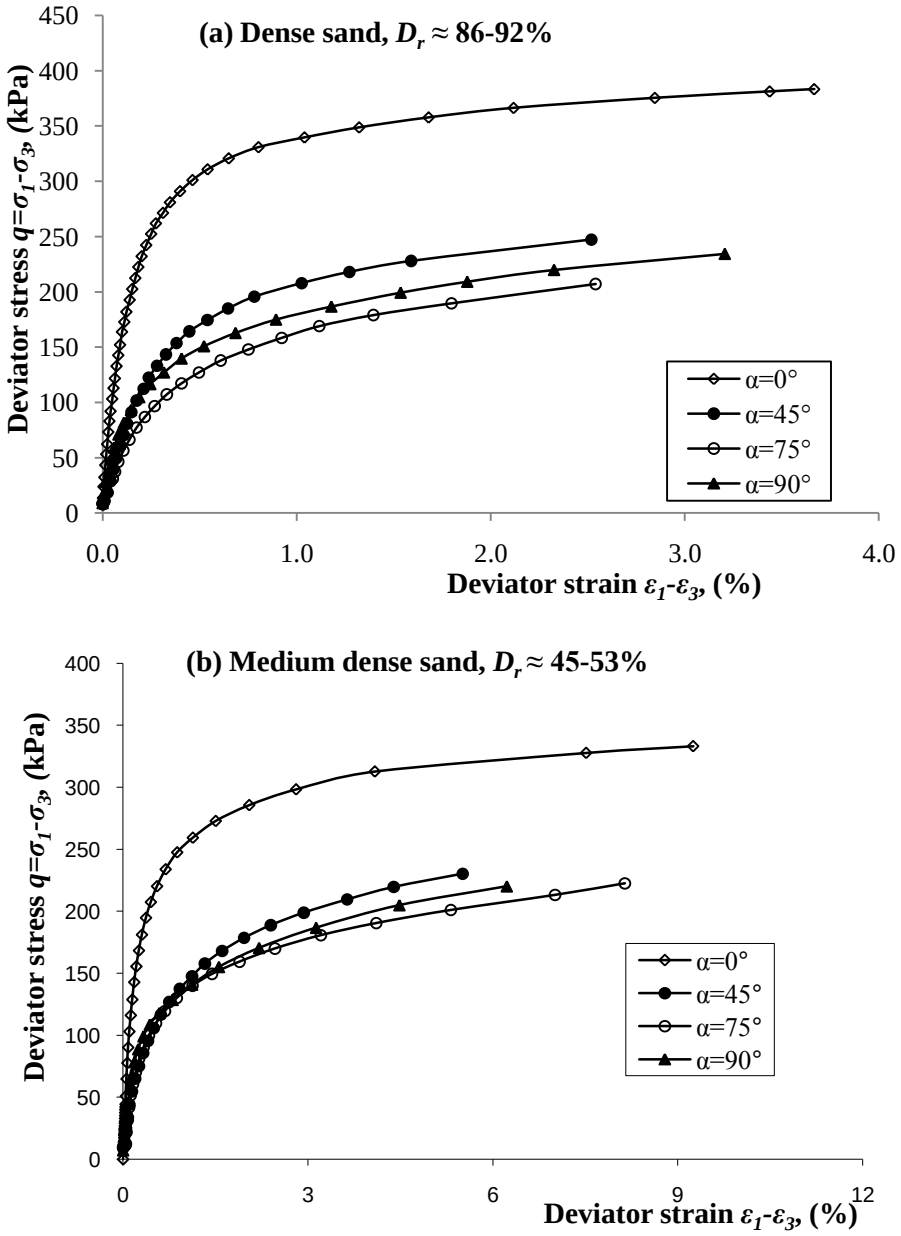

Figure 4-18 Stress-strain relationships: (a) dense sand; (b) medium dense sand.

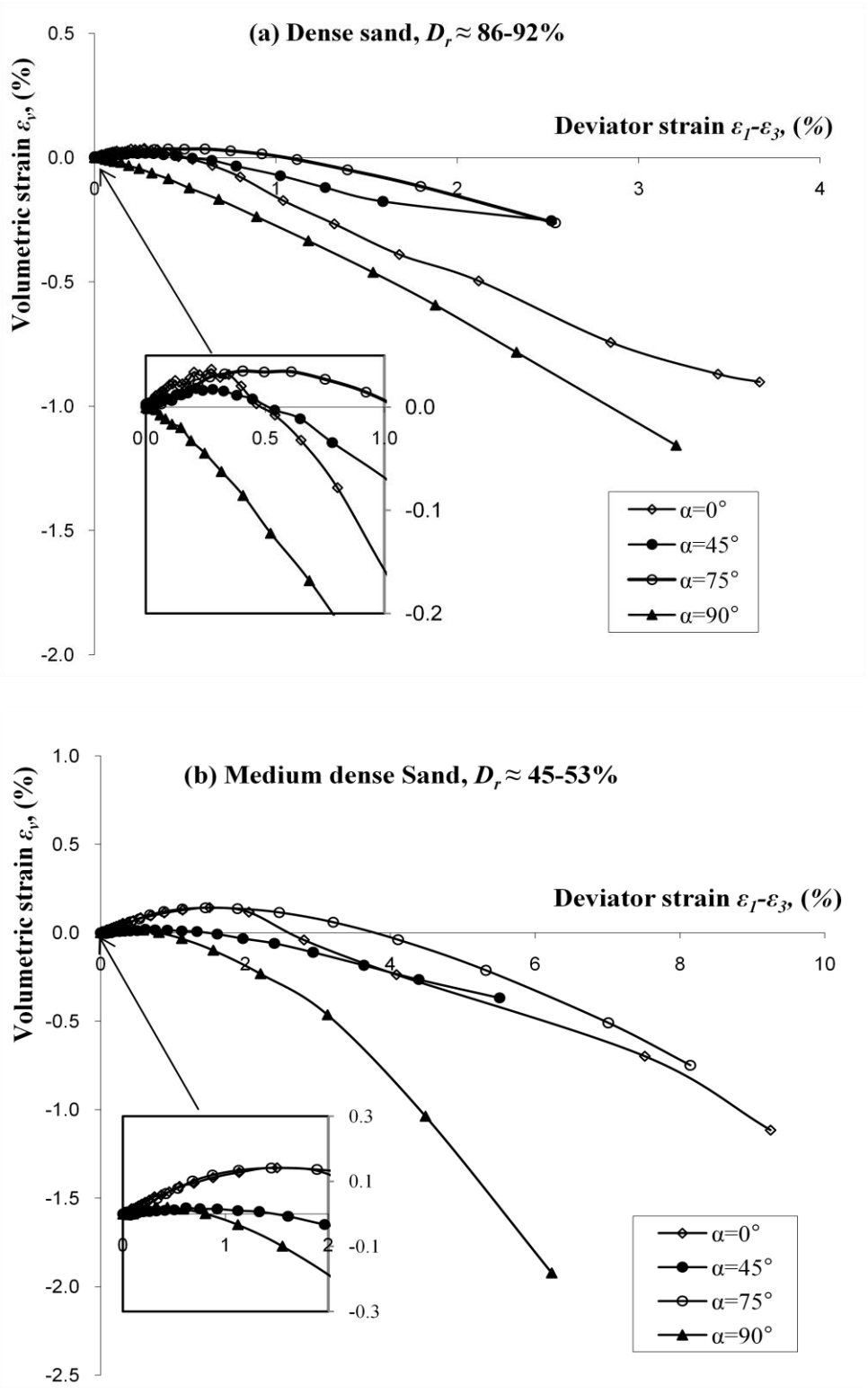

Figure 4-19 Volumetric strain vs. deviator strain: (a) dense sand; (b) medium dense sand

Effect of relative density

The soil behaviour is affected not only by the stress paths but also by the void ratio. A comparison of the soil stress-strain behaviours for dense and medium dense sand is presented in Figures 4-20 to 4-22. In Figure 4-20(a), for the pure compression tests, a lower axial stress was obtained in the medium dense sand. The dense specimen failed at higher axial stress of 866kPa, while the failure axial stress for medium dense sand was 824kPa. In Figure 4-20(b) are results of the pure extension tests, in which axial stresses decreased with the development of strain. At the same strain level, the axial stress for the medium dense specimen was higher. The situation for the shear stress ($\tau_{\theta z}$) shown in Figures 4-20(c) and (d) was similar with that of axial strain. A smaller shear stress was observed for medium dense sand.

Figure 4-21 contains the comparisons of stress-strain behaviour on tests with α=0° and α=45°. Medium dense specimens yielded and failed at lower stresses. In dense specimen, smaller strains were generated.

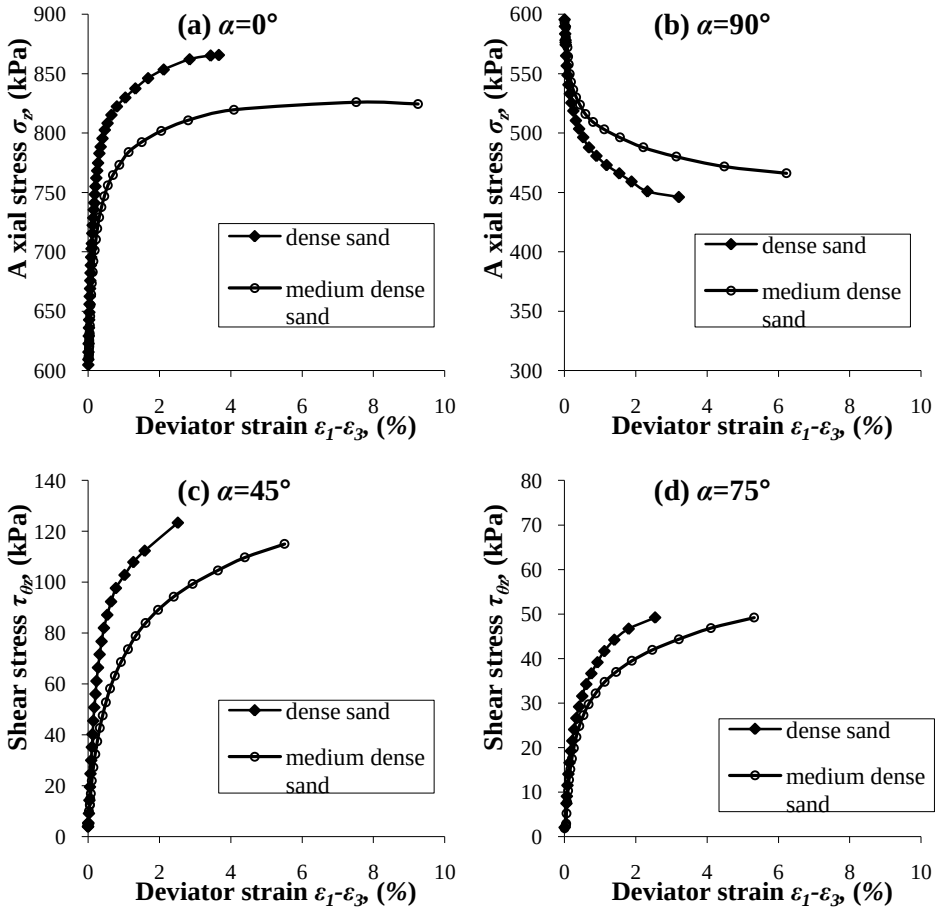

Figure 4-20 Effect of relative density on strain components: (a) axial stress vs. deviator strain, α=0°; (b) axial stress vs. deviator strain, α=90°; (c) shear stress vs. deviator strain, α=45°; (d) shear stress vs. deviator strain, α=75°.

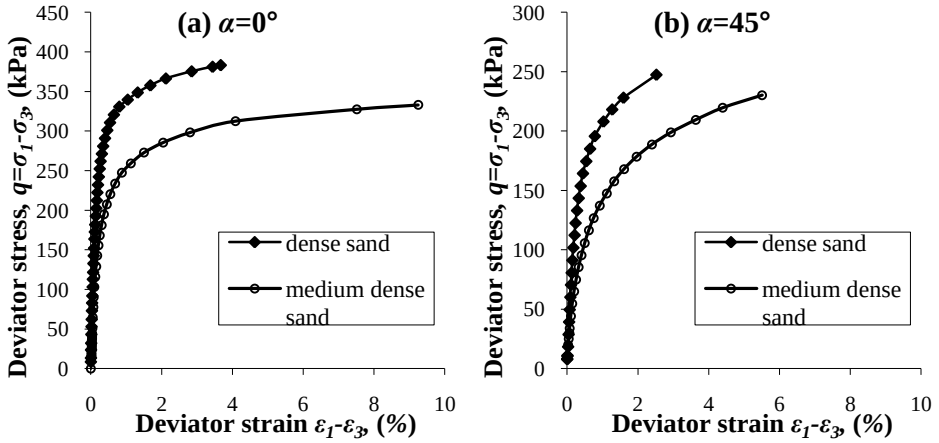

Figure 4-21 Stress-strain behaviour of: (a) q α=0°; (b) α=45°.

The results of volumetric strains vs. deviator strains are plotted in Figure

4-22 for tests with α=75 ° and α=90. In Figure 4-22(a), when α=75 °, volumetric contraction in both speimens was found before the dilation. When α=90 °, only dilation phenomena was found. It is clear to see that more contraction and less dilation of specimen volume was observed in medium dense sand .

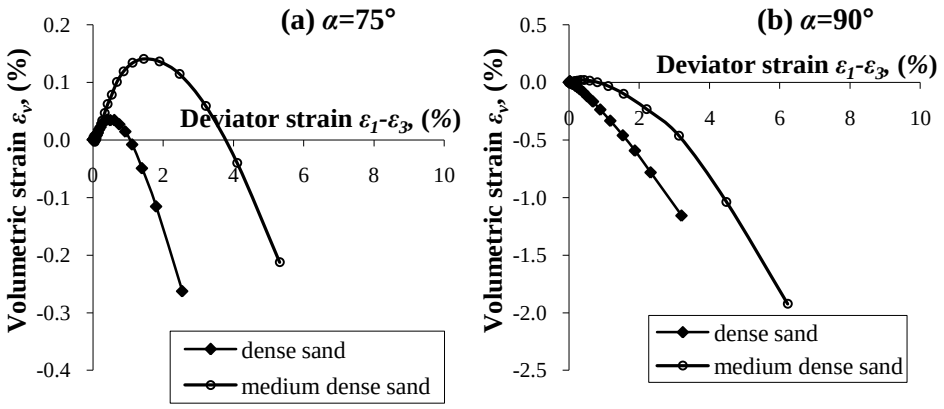

Figure 4-22 Effect of relative density on volumetric strains: (a) α=75 °; (b) α=90 °.

The failure deviator stresses vs. associated major principal stress directions for different stress paths are plotted in Figure 4-23. In the figure it is apparent that the specimen resistance had strong dependence on the loading direction. Between the ranges of α =0 ° to 30° and α =60° to 90°, the change of the failure deviator stress was not very significant, while a clear change occurred between α =30 ° to 60 °, especially from α =30 ° to 45 °. The maximum failure deviator stress existed at α =0 ° and kept dropping until the minimum value was achieved at α =75 °, then the specimen strength reverted slightly for the pure extension tests when α =90 °. This tendency agrees well with the numerical studies carried out by Li and Yu (2009), when they used a two dimensional DEM model to simulate the soil behaviour under monotonic loading. In their simulation, strain increment directions were fixed during shearing instead of

the stress directions. Figure 4-24 presents the observation on stress ratio under various fixed principal strain increment direction (Li and Yu, 2009). Miura *et al.* (1986) also reported similar results in their study of deformation behaviour of Toyoura sand. In their study, the tests were conducted by the HCA with b=0.5 and p'=98kPa. Similar results were also observed by Oda *et al.* (1978) and Symes *et al.* (1982). Comparison of the specimen strengths between specimen densities is also presented in Figure 4-23. Denser specimens provided higher resistance when the same loading direction was applied. However, for $\alpha = 60° \sim 90°$, the differences were very small. The result indicates that between $\alpha = 60° \sim 90°$, the effect of void ratio on the specimen resistance becomes insignificant and the specimen strength was influenced mainly by the loading direction.

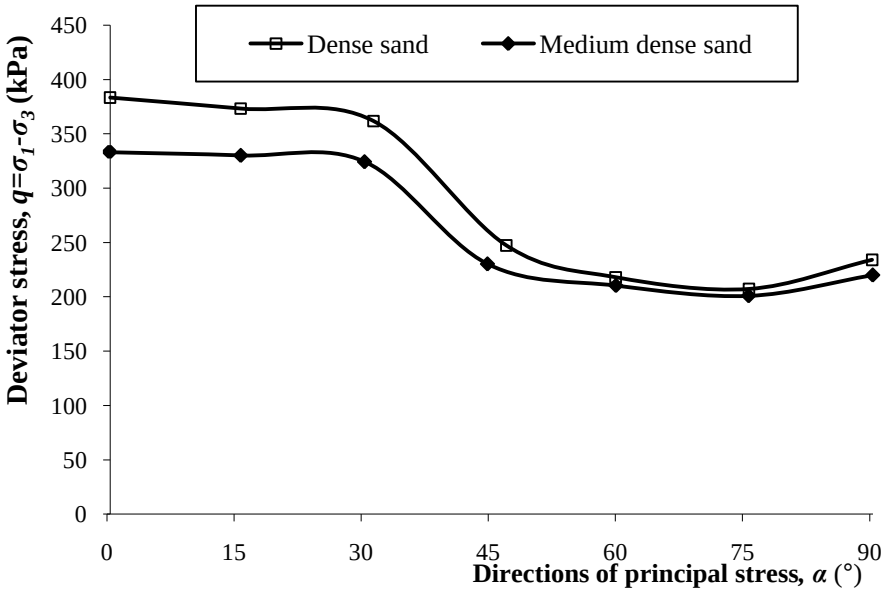

Figure 4-23 Dependence of failure strength on the loading direction (F tests).

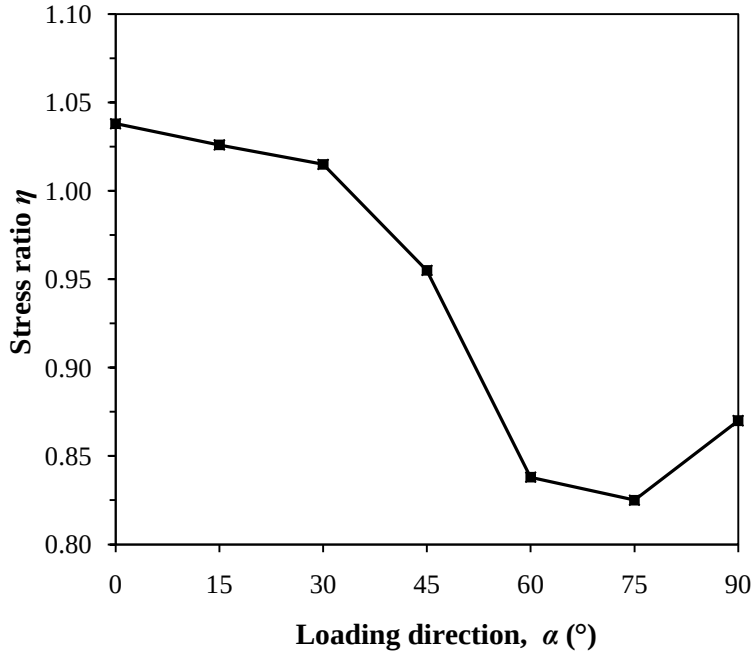

Figure 4-24 Variation in stress ratio on the initially anisotropic sample (after Li and Yu, 2009).

4.4 NON-COAXIAL SOIL BEHAVIOUR

The main purpose of this project has been stated in the title, which is to study the non-coaxiality between the principal stress direction and the strain increment direction of sand under different stress paths. In this section, the results related to this topic, as observed from the monotonic loading tests, will be presented for each test and will be compared between different densities.

4.4.1 Series F-D: dense sand

The deviations between the directions of major principal stress axes and principal strain increment axes for dense sand are plotted in Figure 4-21 in terms of the directions versus deviator stress, where α represents the principal

stress direction and $\alpha_{d\varepsilon}$ represents the principal strain increment direction. For tests of α=0 ° and α=90 °, specimens were subjected to pure compression and extension loading mode, respectively. The major principal strain ε_1 developed along the horizontal (for α=90 °) or vertical direction (α=0 °), Therefore, the strain increment axis should be on the horizontal or vertical line as well. In Figure 4-25(a), for α=0 °, the direction of strain increment fluctuated slightly around the stress direction, but the deviations were very small. In Figure 4-25(g), for α=90 °, $\alpha_{d\varepsilon}$ was almost coincident with α, which means that the soil behaviour was coaxial. These experimental results agreed with the analysis that directions of the principal stress and principal strain increment should be coaxial in pure compression or extension tests as mentioned above. When α=15 °, 30 ° and 45 °, the magnitude of strain increment directions were larger than the principal stress directions. In Figure 4-25(b), α=15 °, the curve of strain increment direction was almost parallel with that of stress direction from starting of shearing to the point of q around 275kPa. The deviation was about 6 °. After this point, $\alpha_{d\varepsilon}$ was close to α where the specimens was reaching the failure. The deviation was found to be less than 1 ° when the specimen failed. For the other tests, the non-coaxial degree varied. The maximum non-coaxial degree for monotonic loading tests was observed in the test with α=30 ° (Figure 4-25(c)), being about 10 ° at the initial stage of shearing. Then the strain increment axis slowly approached the principal stress axis. Finally, a deviation of 5 ° was obtained. When α=45 °, the specimen was subjected to torsional loading mode. In this test, a coincidence between the principal strain increment and the principal stress axis was found when the specimen was just sheared or nearly failed. Non-coaxiality was found during shearing with a maximum value

of 8 °, as shown in Figure 4-25(d). When the principal stress axes were inclined to 60 ° and 75 °, the magnitude of principal strain increment direction was found to be smaller than the magnitude of principal stress direction. The comparison is plotted in Figures 4-25(e) and (f). The degree of non-coaxiality decreased when the specimens approached failure.

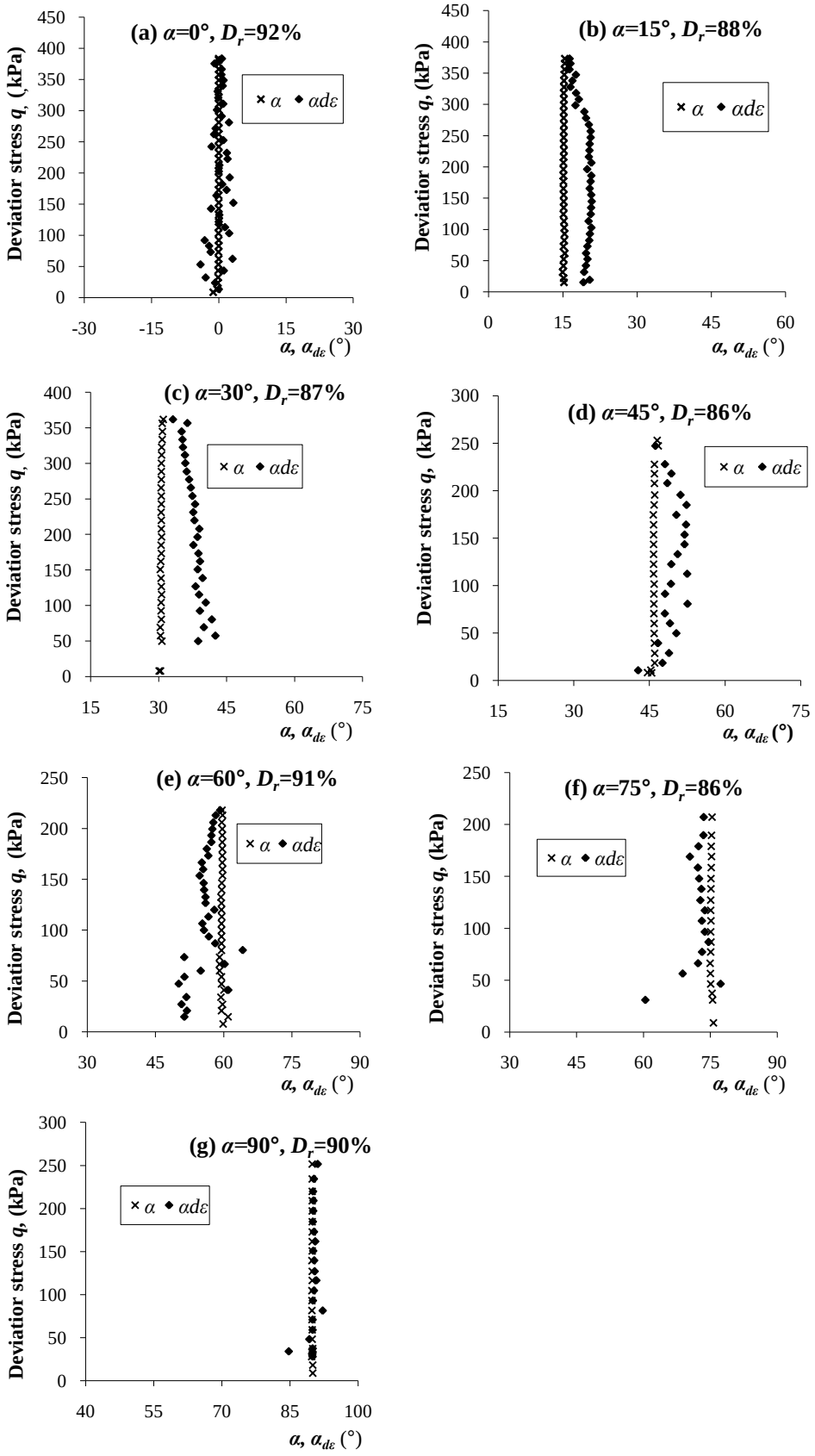

Figure 4-25 Directions of principal stress and principal strain increments for dense sand: (a)F-D00; (b)F-D15; (c)F-D30; (d)F-D45; (e)F-D60; (f)F-D75; (g)F-D90.

4.4.2 Series F-D: medium dense sand

Figure 4-26 shows the measurements of non-coaxiality for medium dense Portaway sand when specimens were sheared along fixed principal stress directions. The following observations can be made:

Figure 4-26(a): When α=0°, a fluctuation of principal strain increment direction happened at the lowest levels of q. However, consistent with Figure 4-25(b), the trend line of $\alpha_{d\varepsilon}$ was almost coaxial with the line of principal stress direction α.

Figure 4-26(b): The principal strain increment axis deviated from the principal stress axis towards horizontal before when α=15°. The deviation started at about 5° and reduced gradually with the increase of deviator stress. The behaviour was nearly coaxial when the specimen failed.

Figure 4-26(c): In this figure α was fixed at 30°. Similar to the results of tests on dense sand, the largest non-coaxiality for medium dense sand was found in this test. The non-coaxial degree trailed off with progress of loading.

Figure 4-26(d): The inclination of principal stress axis was 45° in this test. The curve of $\alpha_{d\varepsilon}$ was approximately parallel with the curve of α with $\alpha_{d\varepsilon} > \alpha$. The difference between the two angles was about 3°.

Figure 4-26(e): The soil behaved coaxially in this test (α=60°), except for during the early stage of shearing when q＜30kPa.

Figure 4-26(f): When the medium dense specimen was sheared with the principal stress direction fixed at 75 °, the inclination of principal strain increment was smaller than that of principal stress. As in the other tests in Figure 4-26, the soil behaviour was near to coaxial.

Figure 4-26(g): When α=90 °, the principal stress axis rotated to horizontal direction, and the specimen was subjected to pure extension. From the figure it can be seen that the non-coaxiality was very small. The soil behaviour can be considered as coaxial.

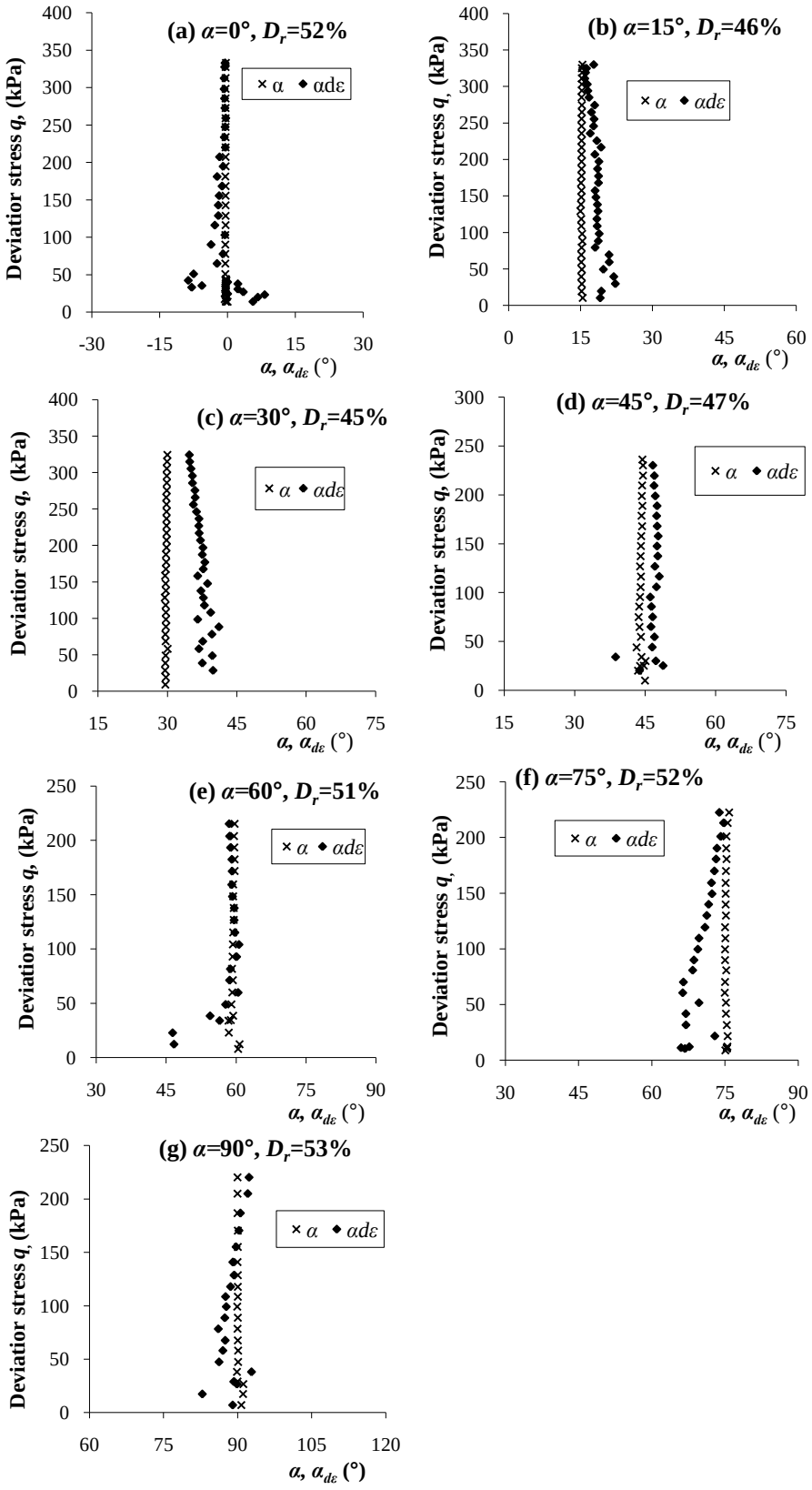

Figure 4-26 Directions of principal stress and principal strain increments for medium dense sand: (a)F-M00; (b)F-M15; (c)F-M30; (d)F-M45; (e)F-M60; (f)F-M75; (g)F-M90.

4.4.3 Discussion and comparison

Figures 4-25 and 4-26 have shown that in the monotonic loading tests, the non-coaxiality between the axes of principal stress and principal strain increment was rather small. The largest deviation angle between the principal stress direction and the principal strain increment direction was only 10 ° and ocurred in dense sand when α=30 °. However, in the same test, the maximum average deviation value was only about 7 °. In the pure compression and pure extension loading tests (i.e. α=0 ° and α=90 °), the soil behaved in a coaxial manner. In the other tests, the specimens became more coaxial with increasing deviator stress q and were nearly coaxial when the specimens failed. For tests with α=15 °, 30 ° and 45 °, values of directions of principal strain increments were larger than the values of principal stress directions, while for α=60 ° and 75 °, the directions developed in an opposite way. These results agree well with the laboratory tests results reported by Miura *et al.* (1986) and Gutierrez *et al.* (1991), which confirmed that the deviation was towards $\alpha_{d\varepsilon}$ =45 °, However different results were obtained by Symes *et al.* (1982). When they sheared the HCA specimens with the principal stress directions fixed at α=45 ° and 67.5 °, they found that the strain increment axis deviated towards the direction of $\alpha_{d\varepsilon}$ =90 °. The results were also different from the 2D DEM numerical simulations by Li and Yu (2009), as shown in Figure 2-3 in Chapter 2. In their simulations, $\alpha_{d\varepsilon}$ was always larger than α. The authors attributed this to the lack of intermediate stress component in the 2D simulation (Li and Yu, 2009).

It should be pointed out that although the non-coaxiality has been widely

investigated in the past (e.g. Miura *et al.*, 1986; Gutierrez *et al.*,1991; Symes *et al.*, 1984, 1986; Li and Yu, 2009), the effect of density on the non-coaxial behaviour was not been studied before. In this study, the same stress paths were applied to specimens with different densities to study the effect of density on the behaviour of Portaway sand. Figure 4-27 compares the results of four tests with α =15 °, α =30 °, α =45 ° and α =60 °. The straight dashed lines in the figures represent the principal stress directions. In Figures 4-27(a) and (b), the data obtained for the two densities were very similar when the same loading direction was applied to the specimens. It can be seen that the degree of non-coaxiality between axes of principal stress and principal strain increment was slightly larger in the dense specimens. However, the margin by which the dense sand non-coaxiality exceeded that for the medium sand was limited to 2 °. In Figure 4-27(c) and (d), although there was more fluctuation, larger non-coaxial degree was shown in the dense specimens. From all of the figures in Figure 4-27, the difference of non-coaxial degree between dense and medium dense sand is seen not to be very pronounced. The largest difference was less than 2 °, and the average value was less than 1 °. In a conclusion, the effect of the relative density on the non-coaxial behaviour of Portaway sand under monotonic loading was not significant.

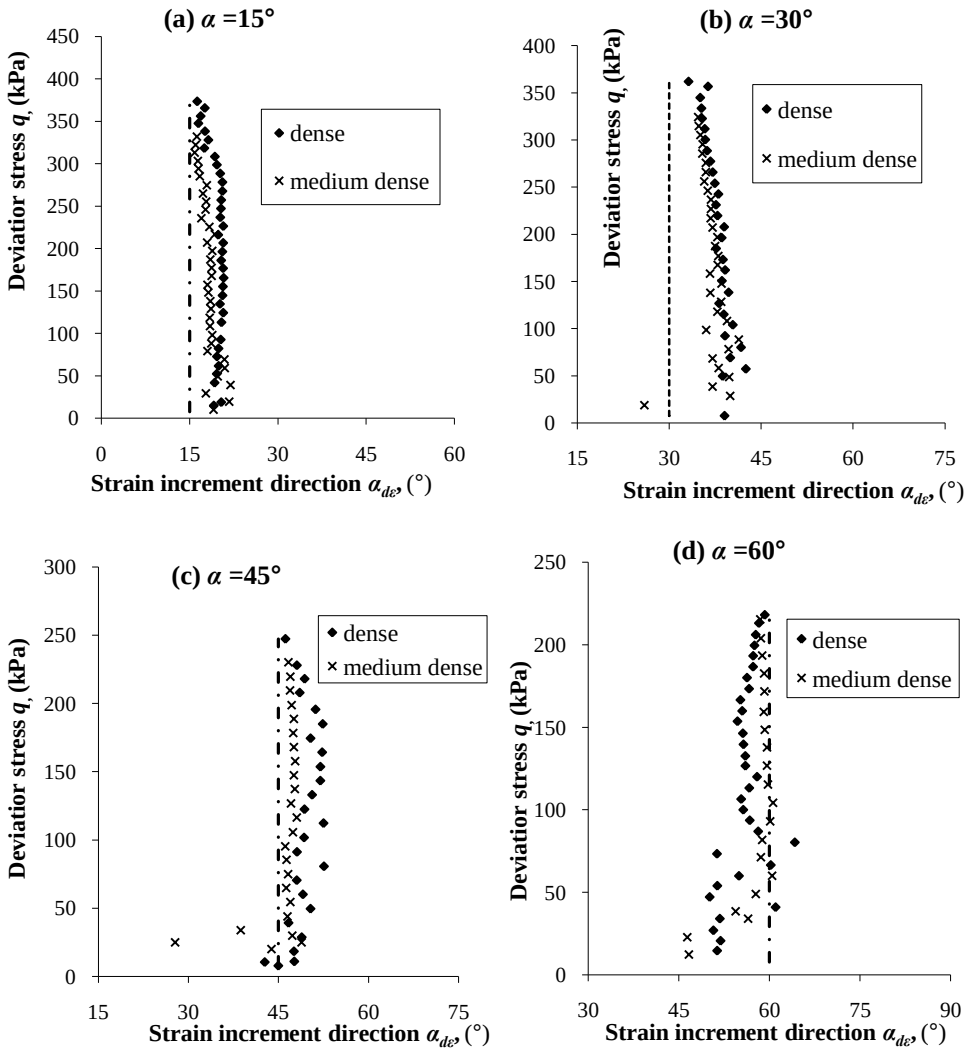

Figure 4-27 Comparisons of stress and strain increment directions for dense and medium dense specimens: (a) α =15°; (b) α =30°; (c) α =45°; (d) α =60°.

4.5 SUMMARY

This chapter describes results of the series of monotonic loading tests on dense and medium dense Portaway sand.

Seven specimens for each density were isotropically consolidated with an effective mean pressure *p'* of 200kPa and tested by application of shearing along the fixed inclination of principal stress axis relative to the vertical. The

actual stress paths show good control to prescribed stress paths. The general soil deformation behaviour is presented for each test. Then the results are discussed and compared in terms of shearing direction and void ratio. The failure deviator stress was found to vary with the loading direction, with the weakest response when the principal stress direction was 75°, and the strongest response when specimens were subjected to pure compression loading mode (α =0°). Strong dependence of the deformations on the direction of principal stress during shearing was observed. This observation implies that the inherent anisotropic fabric of a specimen has a vital effect on the soil behaviour.

Evidence for non-coaxiality between directions of principal stress and principal strain increments was obtained in some of the tests. However the degree of non-coaxiality was limited to 10°, when the principal stress axis was inclined to 30° from the vertical axis. The behaviour was coaxial when subjected to pure compression or extension loading. The strain increment direction tends to deviate towards the direction of 45°. The effect of specimen void ratio on the non-coaxiality was studied. The results show that denser specimen would induce slightly greater non-coaxial degree. However, the non-coaxiality between principal stress direction and principal strain increment direction was very small in both dense and medium dense sand for monotonic loading tests. Therefore the soil behaviour can be considered as coaxial when specimens are sheared along fixed principal stress direction.

Chapter 5

Pure Rotation Tests

5.1 INTRODUCTION

This chapter aims to study the non-coaxial behaviour of Portaway sand and Leighton Buzzard sand under a pure rotation of the principal stress direction. A series of tests (R-series) was carried out in which the deviator stress was fixed and the principal stress axes were continuously rotated. Portaway sand specimens were prepared with two different densities to investigate the influence of void ratio on the non-coaxial behaviour. Dense specimens of Leighton Buzzard sand were also prepared to study the effect of particle shape and grain size distribution on the non-coaxiality.

This chapter is arranged with the following sections: Section 5.2 will introduce the testing procedures including the test conditions, actual stress

paths obtained from tests and the control of stress paths. Then, test results on Portaway sand will be presented in Section 5.3, followed by test results on Leighton Buzzard sand described in Section 5.4. The results will then be discussed in Section 5.5. Finally, Section 5.6 will summarize this chapter.

5.2 TESTING PROCEDURES

In this series of tests, two granular materials, Portaway sand and Leighton Buzzard sand were used to investigate the non-coaxial behaviour of granular materials with different properties and the effect of density on sand behaviour. The specimen preparation procedures have been introduced earlier in Chapter 3.

5.2.1 Testing conditions

There were ten tests in total carried out in the R-series. Eight tests were carried out on Portaway sand, with four on dense specimens with relative density D_r≈90%, and four on medium dense specimens with relative density D_r≈50%. The other two tests were carried out on the Leighton Buzzard sand with a high relative density, D_r≈90%. The initial testing conditions are summarized in Table 5-1.

Table 5-1 Summary of initial testing conditions for pure rotation tests (Series R)

Test No.	Sand	q, (kPa)	Stress-density state			
			e_c	D_{rc} (%)	p_c (kPa)	p_c' (kPa)
R-D01	Portaway	100	0.469	91	600	200
R-D02	Portaway	125	0.477	87	600	200
R-D03	Portaway	150	0.479	86	600	200
R-D04	Portaway	175	0.477	87	600	200
R-M01	Portaway	100	0.561	47	600	200
R-M02	Portaway	125	0.551	52	600	200
R-M03	Portaway	150	0.559	48	600	200
R-M04	Portaway	175	0.561	47	600	200
R-L01	Leighton Buzzard	125	0.547	92	600	200
R-L02	Leighton Buzzard	150	0.560	88	600	200

5.2.2 Stress paths followed

The prescribed stress paths have already been described in section 3.4.4 in the X-Y stress space as shown in Figure 3-18. Figure 5-1 shows the stress paths obtained from the experiments. Only the stress paths for dense Portaway sand specimens are presented to verify the control of the testing program. By comparing the results with the prediction in Figure 3-18, it can be seen that the stress paths were controlled very well. As shown from the figure, the specimens in this series of tests did not reach failure for both dense and medium dense Portaway sand.

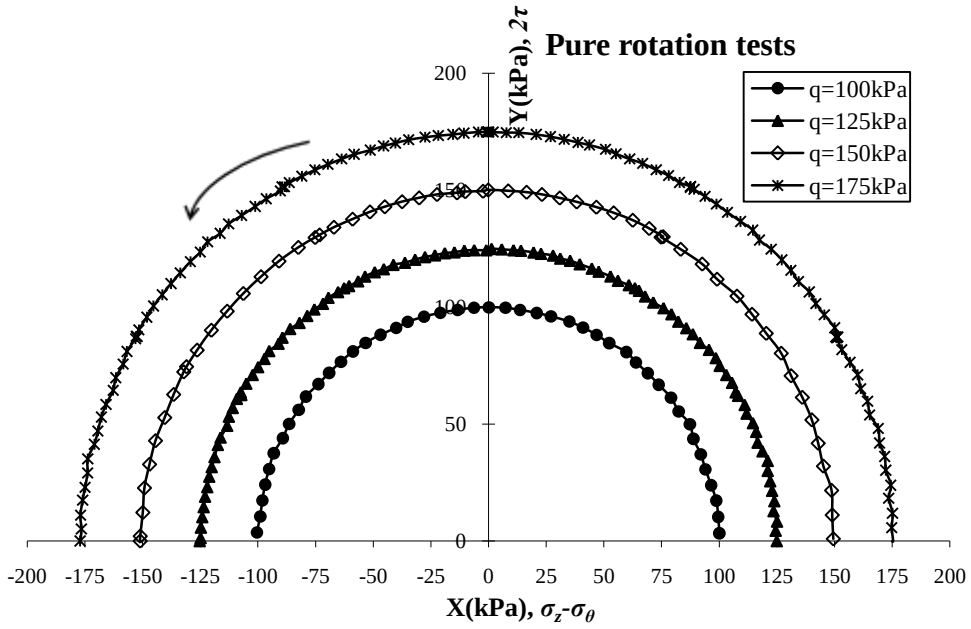

Figure 5-1 Actual stress paths obtained from the tests of dense Portaway sand.

In the stress path control mode, the controlled parameters were deviator stress (q), mean stress (p), major principal stress direction relative to vertical (α) and b. At the beginning, q was increased to 8kPa while α was set to be 0 ° and b=0. Then before rotation, the specimens were shearing monotonically to the expected q with α and b both kept at 0. In this study, as the outer and inner cell pressures were kept equal, b was relative to α as shown in Eq. (2.25b), which means that the relationship between b and α was not linear. When α changed from 0 ° to 90 °, the value of b changed from 0 to 1. To keep the relationship $b=sin^2\alpha$ between α= 0 ° - 90 °, the rotation was divided into six stages in every 15 ° of α, i.e. α was controlled as 0 °- 15 °, 15 °- 30 °, 30 ° - 45 °, 45 °- 60 °, 60 °- 75 °, 75 °- 90 °. Respectively, b varied from 0 - 0.067, 0.067 - 0.25, 0.25 - 0.5, 0.5 - 0.75, 0.75 - 0.933, 0.933 - 1. The α-b curves shown in Figure 5-2 present the control of pure rotation tests. It can be seen that the relationships between b and α obtained from tests agreed well with the theoretical prediction.

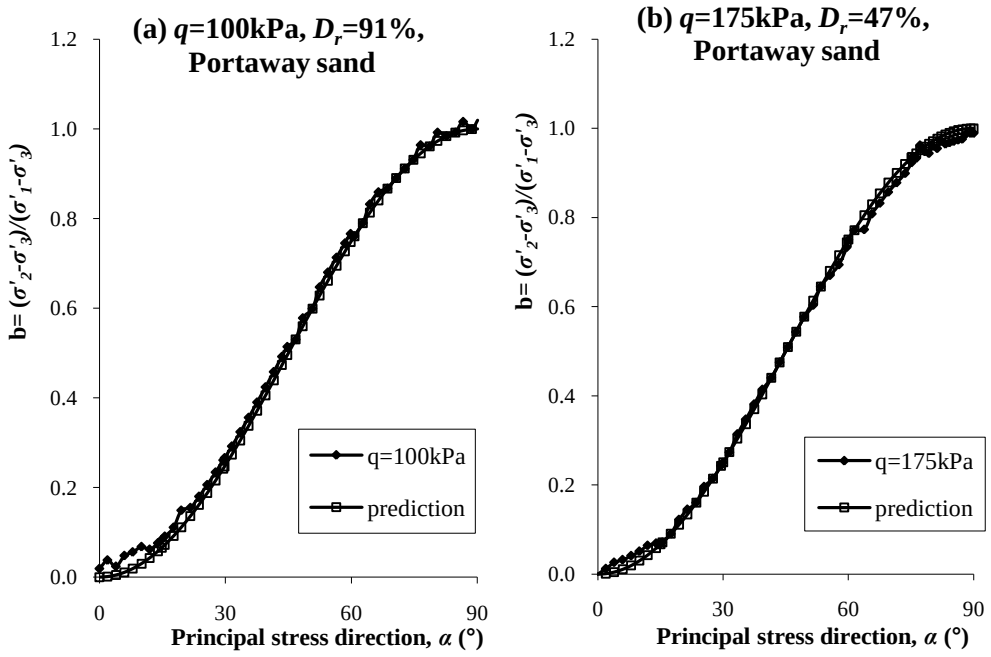

Figure 5-2 Control of parameter *b*: (a) dense Portaway sand, *q*=100kPa; (b) medium dense Portaway sand, *q*=175kPa.

It should also be pointed out that due to the limitation of the testing equipment and software, 2α could only be controlled between -180 ° and 180 °, and a full rotation of 2α from 0 ° to 360 ° could not be implemented.

5.2.3 Variation of stresses

The variation of effective stress components with the rotation of principal stress axes are shown in Figure 5-3. At the beginning of rotation, when α=0 °, the axial stress (σ'_z) had a maximum value, σ'_r and σ'_θ had minimum values, and shear stress ($\tau_{\theta z}$) was zero. Radial stress (σ'_r) was equal to circumferential stress (σ'_θ), and increased with the rotation of principal stress axis from 0 ° to 90 °. In contrast, σ'_z started from a maximum value and decreased with the rotation of principal stress axes. Furthermore, with the increasing value of α.

σ'_z-σ'_θ=q when the major principal stress axis was acting in the vertical and horizontal directions. With the further rotation, the shear stress ($\tau_{\theta z}$) increased firstly then reduced to zero when α=90°. The peak value of shear stress ($\tau_{\theta z}$) existed at the point of α=45°, and the value was $\tau_{\theta z}$=q/2. Besides, σ'_z=σ'_r =σ'_θ=200kPa when α=45°.

The effective principal stresses measured in the R-series are presented versus α in Figure 5-4. As shown in the figures, the curves of σ'_1 were parallel with the curves of σ'_3. When α=0°, σ'_1=σ'_z and σ'_3=σ'_θ, and when α=90°, σ'_1=σ'_θ and σ'_3=σ'_z. The intermediate stress σ'_2 (σ'_2=σ'_r) was same as σ'_3 at the beginning then rose to be same as σ'_1 when α reached 90°. In other words, a compression test (b=0) was changed to an extension test (b=1). The difference between the major principal stress and the minor principal stress (σ'_1 -σ'_3) was kept constant at the value of prescribed q, and σ'_1+σ'_1+σ'_3 was kept constant at 600kPa all through the rotation.

Both Figures 5-3 and 5-4 indicate a good control of the stress paths in the pure rotation tests.

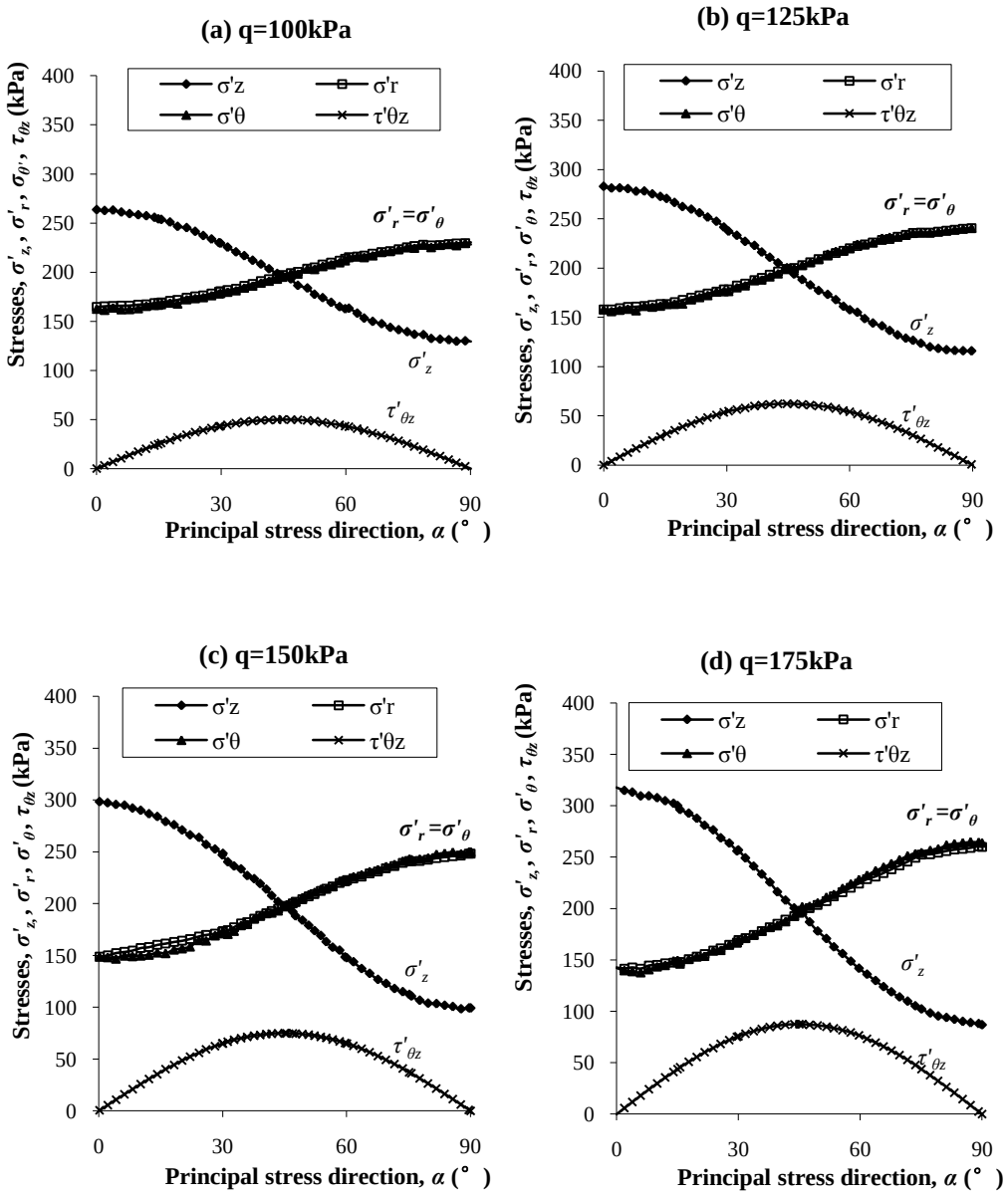

Figure 5-3 Variations of stress components in the R-series: (a) *q*=100kPa; (b) *q*=125kPa; (c) *q*=150kPa; (d) *q*=175kPa.

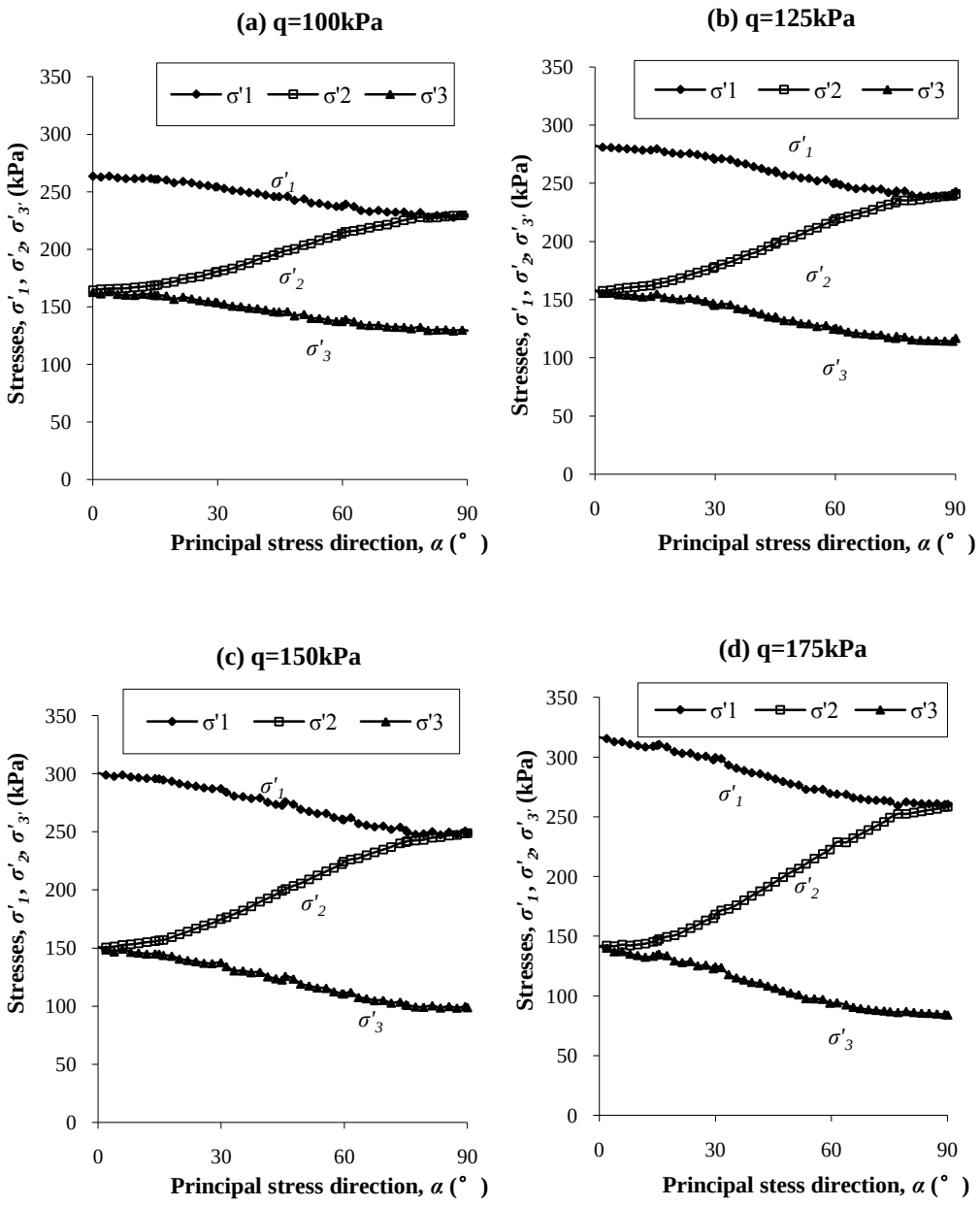

Figure 5-4 Variation of principal stresses in R-series: (a) *q*=100kPa; (b) *q*=125kPa; (c) *q*=150kPa; (d) *q*=175kPa.

5.3 TESTS ON PORTAWAY SAND

The results of pure rotation tests on dense and medium dense Portaway sand will be introduced in this section, including the general stress-strain behaviour and discussion of the non-coaxial behaviour.

5.3.1 General soil behaviour

The general stress-strain and strain-strain behaviour of the R-series tests is presented in this section.

The relationship between strain components and the directions of major principal stress axes for tests R-D01 and R-M01 are shown in Figure 5-5. It can be seen that when q was kept constant at 100kPa, there was not much strain generated for both dense and medium dense sand. The strain components followed similar trends as did the stress components shown in Figure 5-3. Axial strains (ε_z) increased in the negative direction as the axial stresses (σ'_z) decreased during the rotation of principal stress directions. Radial strains (ε_r) and circumferential strains (ε_θ) developed in the positive direction with the increase of σ_r and σ_θ. Shear strains ($\gamma_{\theta z}$) increased first then decreased with the rotation of the principal stress axes. As shown in Figure 5-5(a), for dense sand, the shear strain reached a peak value when α was around 45°, and reverted to almost zero when 90° rotation was accomplished. However, for medium dense sand, (Figure 5-5(b)), the maximum shear strain occurred when α=60°. When

the major principal strain axes were rotated to the horizontal direction, the shear strain was much larger than that in the dense specimen, which suggested that more plastic deformation was produced in the medium sand when the same deviator stress was applied.

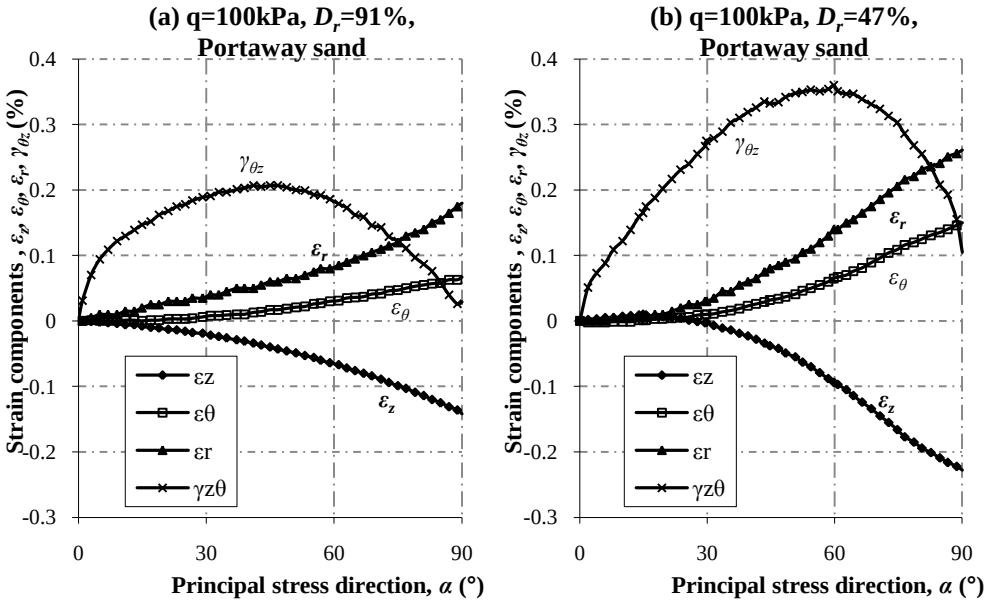

Figure 5-5 Relationships between strain components and the direction of principal stress axes for test R-D01 and R-M01, *q*=100kPa: (a) dense sand; (b) medium dense sand.

In Figure 5-6 are shown the results of tests R-D02 and R-M02, in which the deviator stresses were fixed at 125kPa while the principal stress axes were inclined. More strains were produced in these tests than in those tests with q=100kPa. At the beginning of rotation, shear strains ($\gamma_{\theta z}$) were the main deformation, while the other strain components, axial strains (ε_z), radial strains (ε_r) and circumferential strains (ε_θ) were very small. With the increase of magnitude of the principal stress direction (α), $\gamma_{\theta z}$ reached the greatest value then dropped down, and ε_z, ε_r and ε_θ were increasing with the rotation,

especially after $\alpha > 40°$. The maximum shear strain occurred when α was around 55° for dense sand, as shown in Figure 5-6(a). For medium dense sand, the maximum shear strain was observed when α=75° (Figure 5-6(b)). It can also be seen that much greater deformations were generated in the medium than in the dense specimen.

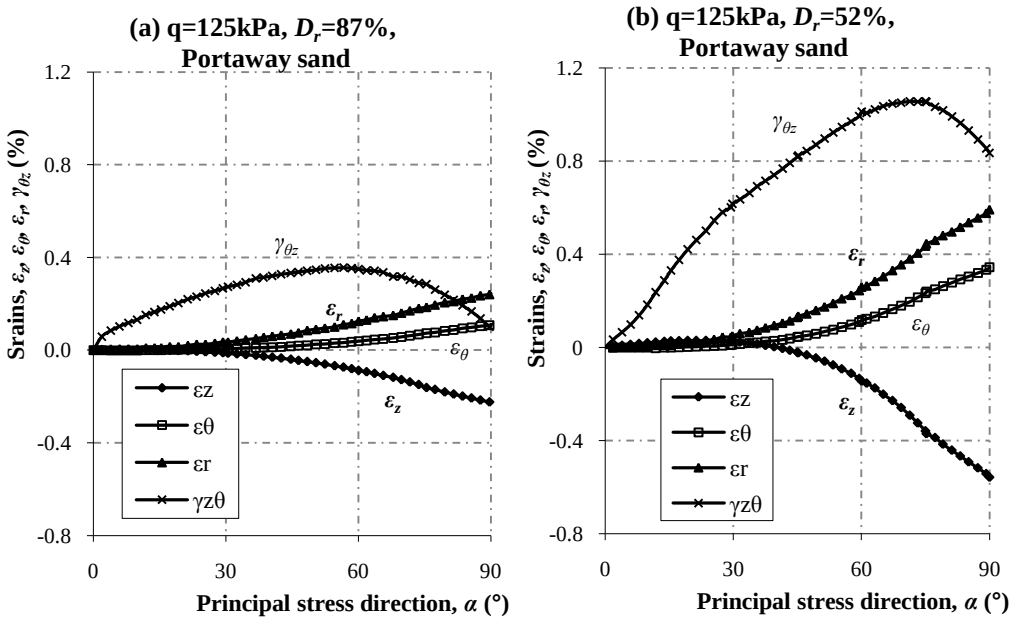

Figure 5-6 Relationships between strain components and the direction of principal stress axes α for test R-D02 and R-M02, q=125kPa: (a) dense sand; (b) medium dense sand.

Figure 5-7 shows the strain components vs. principal stress directions of tests R-D03 and R-M03. In these tests, the specimens were sheared by rotating the principal stress axes with deviator stress q fixed at 150kPa. As in tests R-D02 and R-M02, only small amount of axial strains (ε_z), radial strain (ε_r) and circumferential strain (ε_θ) were generated at the beginning of tests. Shear strains mounted up gradually with increase of principal stress direction relative to the vertical until α=75° for both dense and medium dense specimens, then

reduced as α approached 90 °. As with the development of stress components in Figure 5-3, ε_z developed in the negative direction and ε_r and ε_θ grew on the positive side. The strains increased to a much higher value once α was more than 40 °.

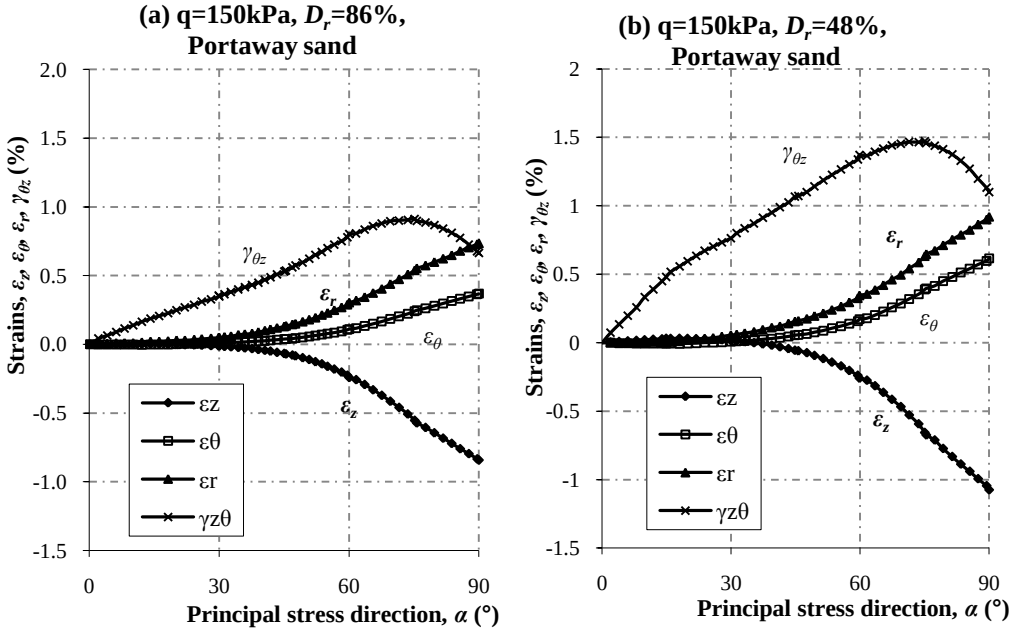

Figure 5-7 Relationships between strain components and the direction of principal stress axes α for test R-D03 and R-M03, q=150kPa: (a) dense sand; (b) medium dense sand.

The strain components of tests R-D04 and R-M04 are plotted against principal stress direction in Figure 5-8. The last two tests on Portaway sand were performed with a constant q=175kPa. The largest deformations were generated. Similar with the other three pairs of tests, there was only a small amount of axial strain (ε_z), radial strain (ε_r) or circumferential strain (ε_θ) observed between α = 0 ° and α = 40 °. Then the strains developed quickly after α = 40 °, with ε_z in the negative direction and ε_r and ε_θ in the positive direction. The shear strain ($\gamma_{\theta z}$) varied with the rotation of principal stress axes. For both

dense and medium dense specimens, $\gamma_{\theta z}$ started from zero when α=0 °, then reached the maximum value at α=75 °. After that, $\gamma_{\theta z}$ decreased. However, when α=90 °, the shear strains remaining were much larger in these two tests than in those performed at lower values of q.

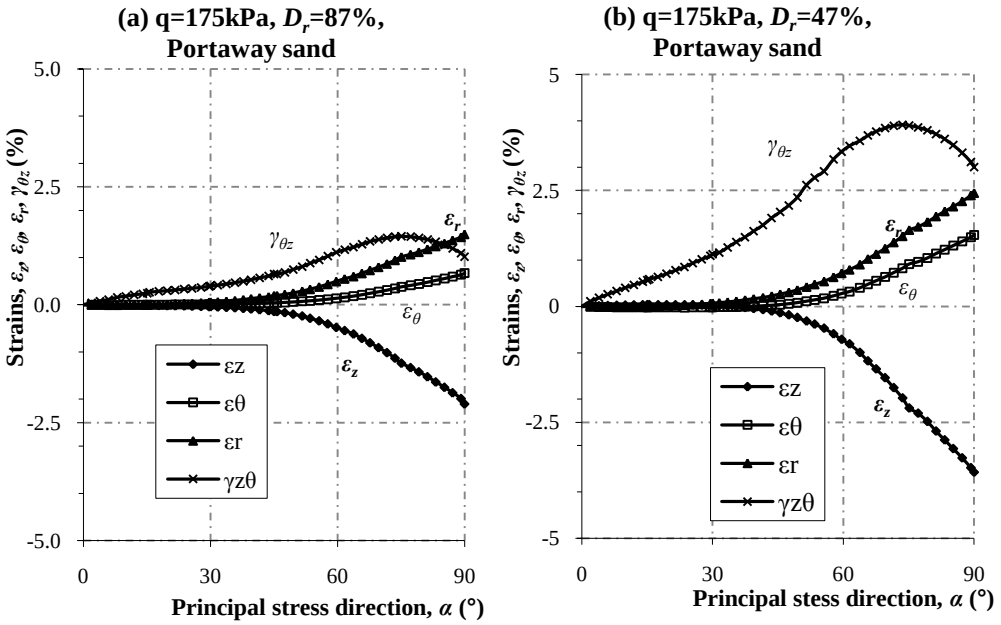

Figure 5-8 Relationships between strain components and the direction of principal stress axes α for test R-D04 and R-M04, q=175kPa: (a) dense sand; (b) medium dense sand.

Based on the data shown in Figures 5-5 to 5-8, it can be concluded that the deformation depends on the deviator stress and on the specimen density. Smaller strains were generated at a lower q level. For the same q level, smaller strains were obtained in dense sand than that in medium dense sand.

The shear strains ($\gamma_{\theta z}$) were plotted against principal stress direction (α) in Figure 5-9. When the principal stress axes inclined from 0 °to 90 °, shear strains ($\gamma_{\theta z}$) increased from 0 to the maximum values then decreased, following similar

trends as for the shear stress components ($\tau_{\theta z}$) shown in Figure 5-3. When the rotation was completed, at a lower deviator stress level, e.g. q=100kPa, shear strain ($\gamma_{\theta z}$) almost reverted to zero, while at a higher stress level, e.g. q=175kPa, more significant shear was observed. These results suggested that the deformation changed from elastic deformation dominant to plastic component dominant with the increase of deviator stress.

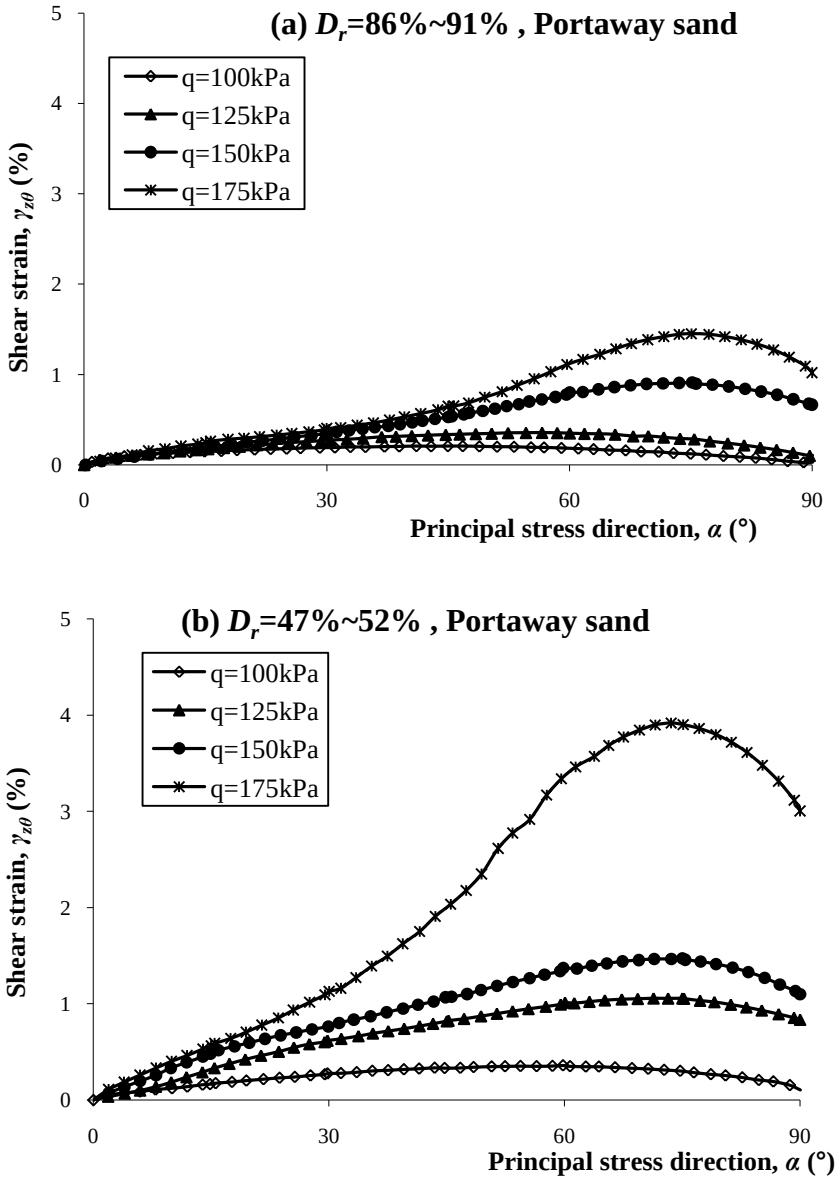

Figure 5-9 Shear strains vs. the direction of principal stress axes: (a) dense sand; (b) medium dense sand.

Figure 5-10 presents the relationship between shear strain ($\gamma_{\theta z}$) and shear stress ($\tau_{\theta z}$). In the dense specimens, as shown in Figure 5-10(a), before shear stress ($\tau_{\theta z}$) reached the peak value, the stress-strain behaviour in all the tests were similar. Then during the reduction of shear stresses ($\tau_{\theta z}$), more shear strains were observed in the specimens subjected to higher deviator stress (q), especially when q=150kPa and 175kPa. From Figure 5-10(b), for the stress path with same value of q, more strains were obtained from the medium dense specimens than that from the dense specimens shown in Figure 5-10(a), particularly with the higher deviator stress q. In the medium dense sand, during loading, the highest shear stiffness was obtained for the stress path with lowest deviator stress as shown in Figure 5-10(b). In test R-M04, when q=175kPa was applied to the medium dense specimen, the unloading stiffness was much lower. When $\gamma_{\theta z}$ reached the maximum value, $\tau_{\theta z}$ had reduced from peak value to 50kPa. The significant development of shear strain indicates that the specimen was approaching failure.

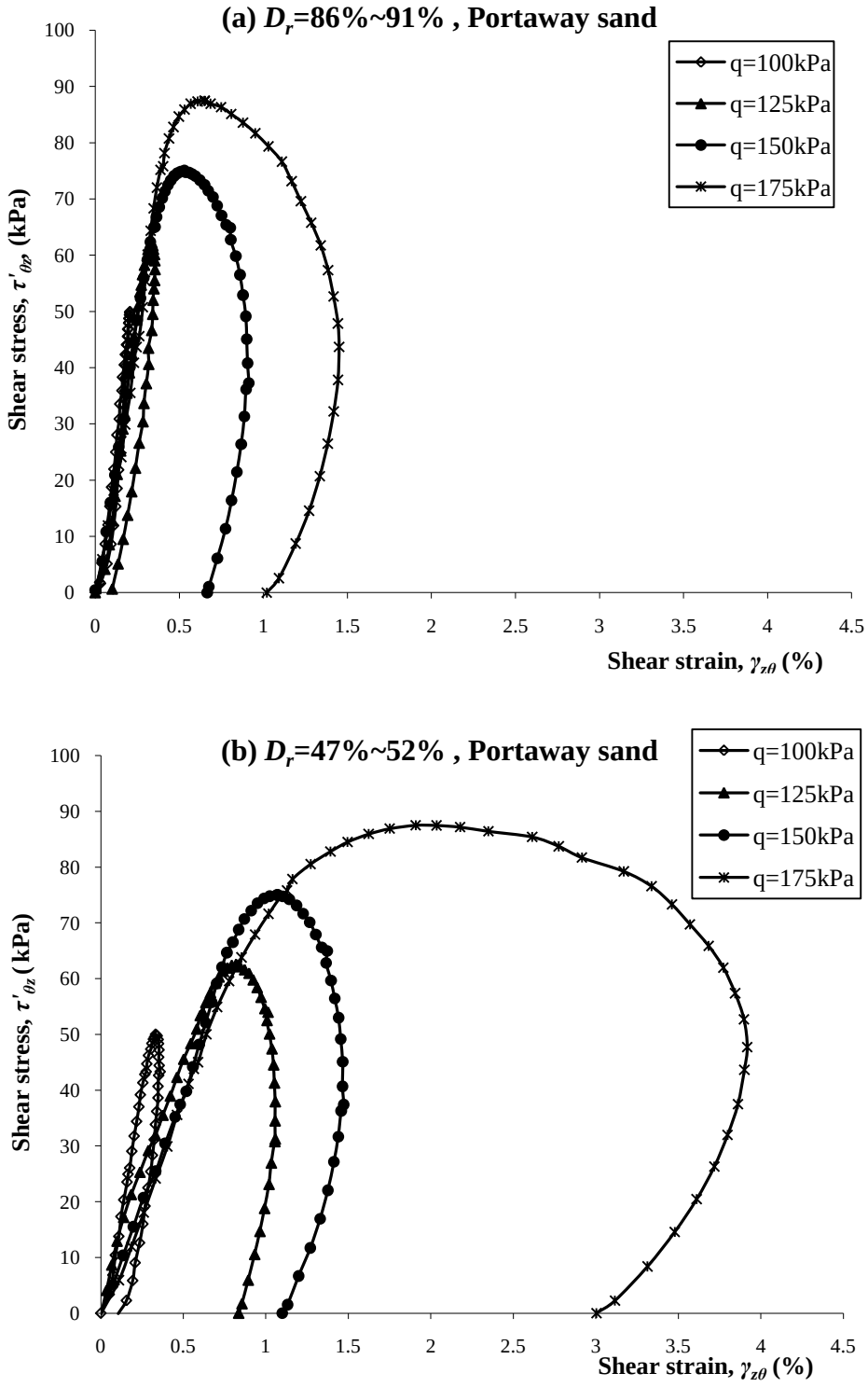

Figure 5-10 Shear strains vs. shear stresses: (a) dense sand; (b) medium dense sand.

The deviator strains vs. principal stress direction (α) are displayed in Figure 5-11. Generally speaking, the strains were influenced by the void ratio and the loads applied on the specimen. More strain was produced in the looser sand shown in Figure 5-11(b) compared to the dense specimens in Figure 5-11(a). Higher deviator stresses brought about more strain. The deviator strains built up with the rotation of the principal stress axis in the first instance then dropped down slightly except at q=175kPa.

The volumetric strains due to the principal stress axis rotation for Portaway sand are shown in Figures 5-12(a) and (b). When q was between 100kPa and 150kPa, (tests R-D01, R-D02, R-D03 and R-M01, R-M02, R-M03), the specimen volumes contracted when the direction of principal stress axes were rotated from 0 ° to 90 °. The medium dense sand exhibited more contractive volume changes. However, when the specimens were subjected to a higher deviator stress, (q=175kPa), a dilative volume change was obtained at the early stage of rotation, which was followed by a contractive volume change. This phenomenon was more obvious in the dense sand as shown in Figure 5-12(a). It can also be observed from Figure 5-12 that from α=65 ° to 90 °, the dense specimen started to dilate again, and the medium dense sand experienced less contractive volume change. Such dilative response of the specimen volumes can be explained using Figure 4-23 about the failure strength when specimens were under monotonic loading. The specimen has lowest resistance when α=60 ° to 75 °, with the failure deviator stress about 200kPa, which indicates that in the pure rotation tests, the specimens were close to failure when the principal stress axes were rotated to α larger than 60 °

with q=175kPa.

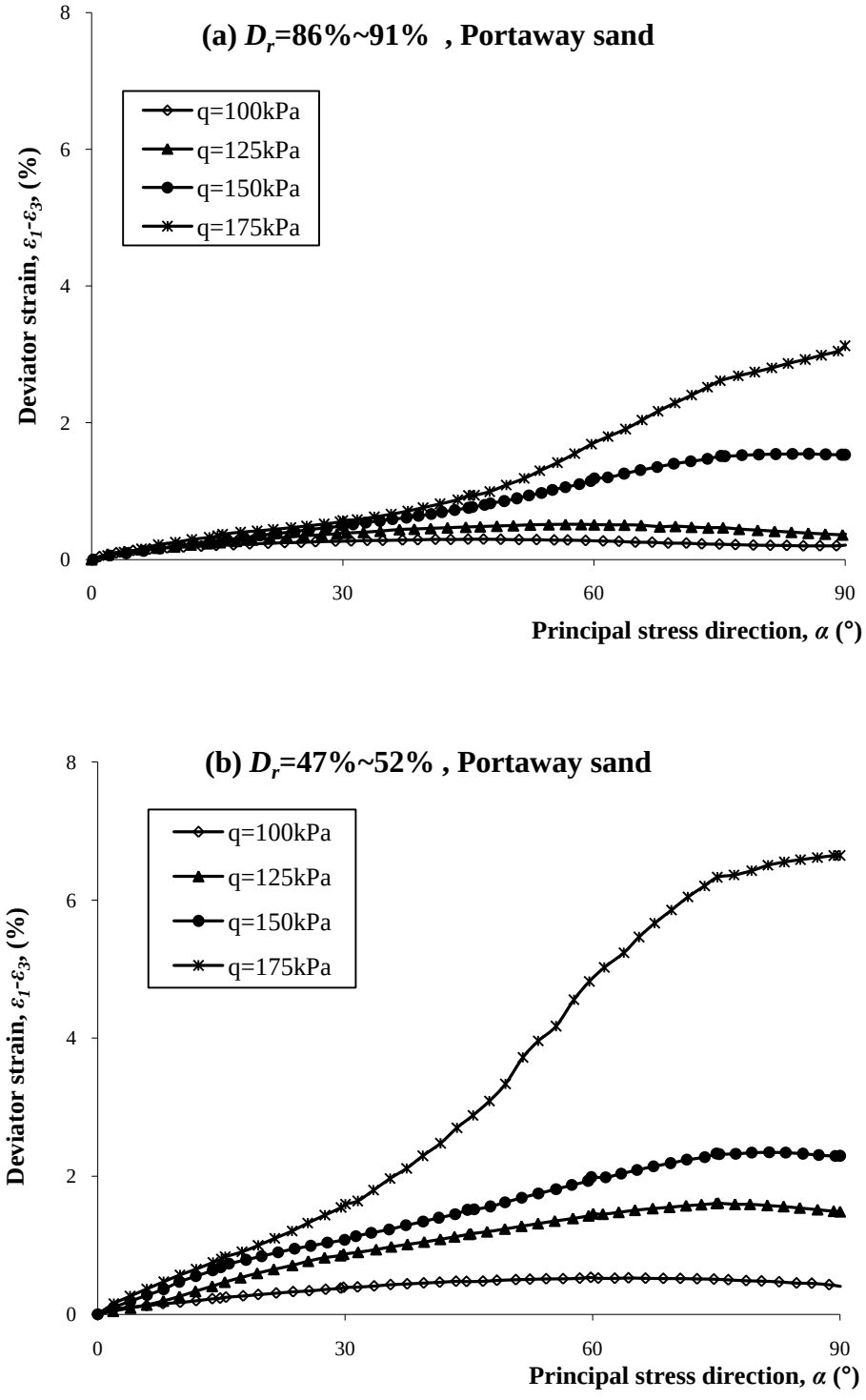

Figure 5-11 Deviator strains vs. the direction of principal stress: (a) dense sand; (b) medium dense sand.

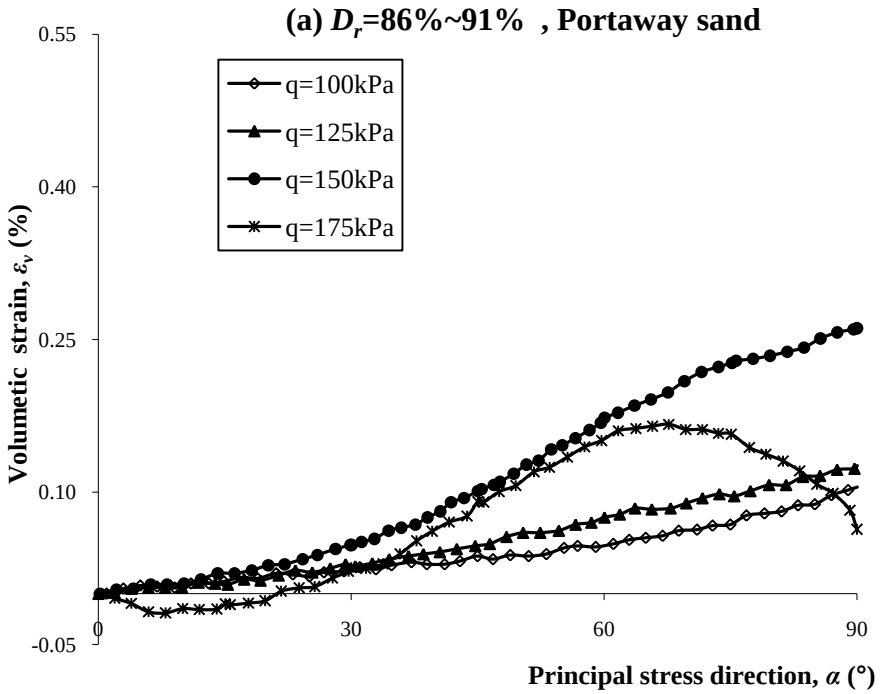

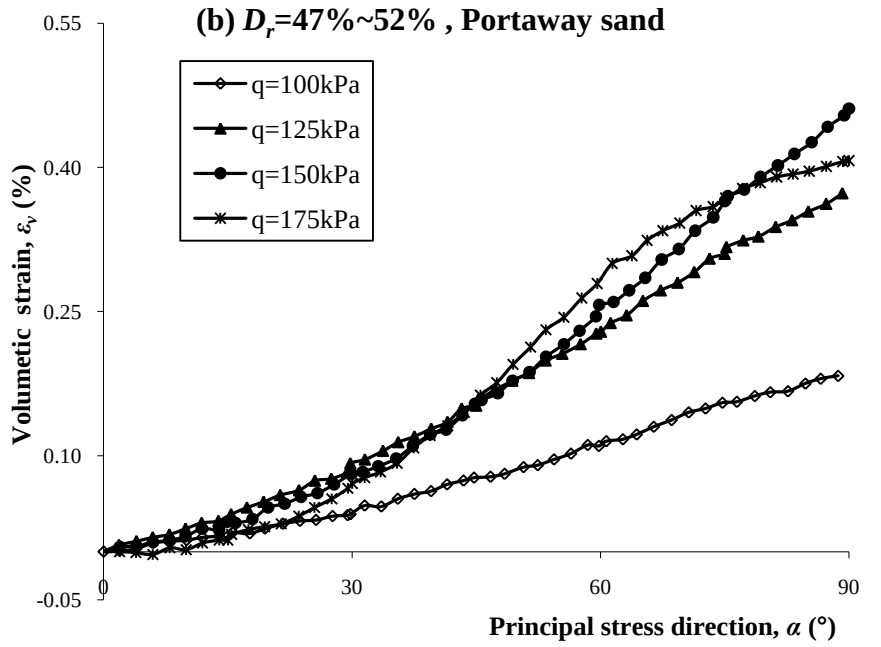

Figure 5-12 Volumetric strains vs. the direction of principal stress: (a) dense sand; (b) medium dense sand.

The strain paths for the R-D tests and R-M tests, with strain component ε_z-ε_θ plotted against shear strain $\gamma_{z\theta}$, are shown in Figure 5-13. The strain paths were dependent on the stress paths followed and the specimen density. For dense sand, when q = 100kPa, the peak shear strain was only 0.25%, and was 1.5% when q = 175kPa. In medium dense sand, the largest deformation was about 3.8% when q = 175kPa.

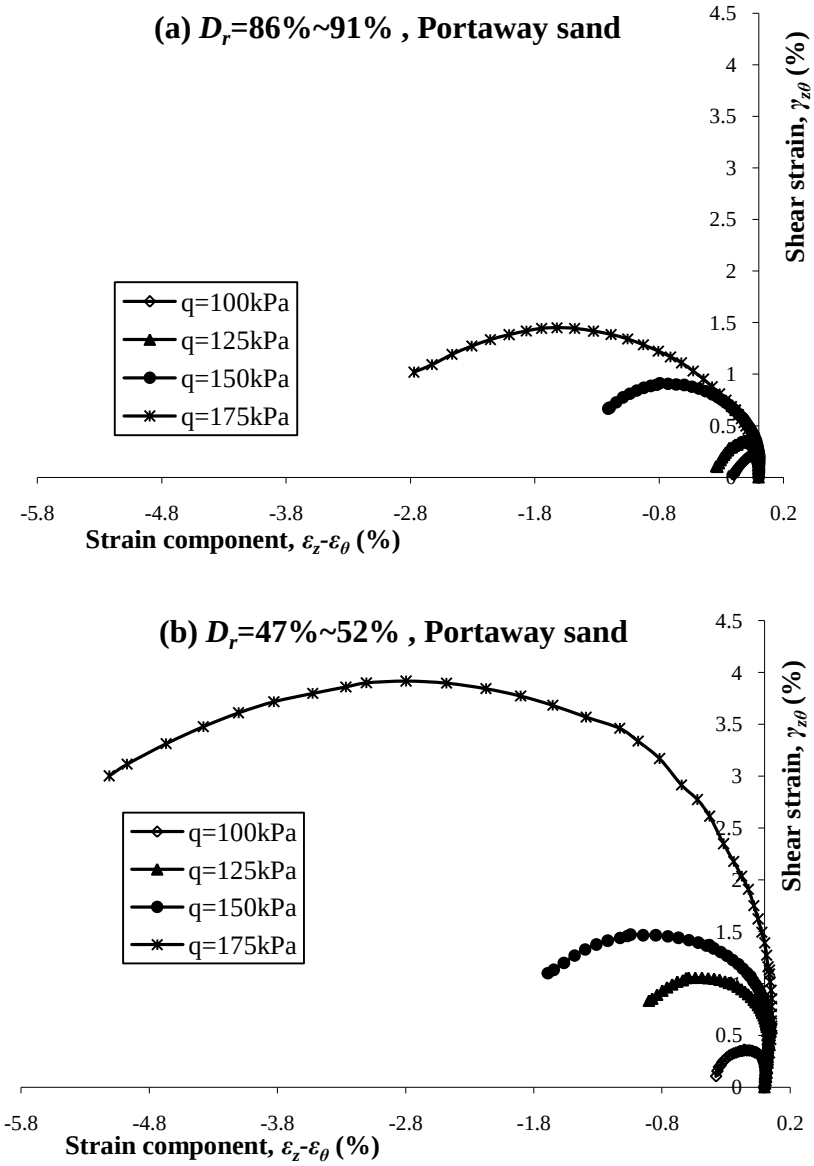

Figure 5-13 Strain paths: (a) dense sand; (b) medium dense sand.

5.3.2 Non-coaxial behaviour

The principal strain increment directions $\alpha_{d\varepsilon}$ are plotted against the major principal stress directions α in Figures 5-14 to 5-17. If the axes of principal strain increment and principal stress are coaxial, the data points should be coincident with the solid line given in the figures. According to the experimental results, the deviation of the principal strain increment direction from the direction of principal stress is prominent in the pure rotation tests. A detailed analysis is presented below.

Effect of deviator stress level

It can be seen from Figures 5-14 to 5-17 that at the beginning of shearing, the degree of deviation between the axes of principal stress and principal strain increment were similar when different deviator stresses were applied, about 42 °. The degree of non-coaxiality was higher at lower deviator stress level. The average deviation was about 40 ° for dense sand and about 32 ° for medium dense sand when q=100kPa (Figure 5-14). In Figure 5-15, with the deviator stress level raised to 125kPa, the average non-coaxial degree was about 33 ° for dense sand and 20 ° for medium dense sand. Figure 5-16, when the deviator stress q=150kPa, the curves of principal strain increment directions for the two densities are similar. The average degree of non-coaxiality was about 17 °. Then when q=175kPa, the average non-coaxial degree was less than 16 ° for both dense and medium dense sand as shown in Figure 5-17.

When the deviator stress was increased, the stress path approached the failure surface and the principal strain increment axis becomes more coaxial with the principal stress direction. From Figures 5-14 to 5-17. the degree of non-coaxiality decreased with the rotation of principal stress direction before α = 60°, then kept nearly constant during α = 60°~90°, or increased slightly. According to the previous studies (Miura *et al.*, 1986; Li and Yu, 2009) and experimental data obtained in the monotonic loading shown in Figure 4-23, the specimen was weakest in the range of α = 60°~75°. So the results indicate that the degree of non-coaxiality is dependent on the shear stress level with respect to the soil strength. It decreases with increasing deviator stress.

Effect of material density

Specimens of Portaway sand with different densities were prepared to study the effect of density on the non-coaxiality between axes of principal strain increment and principal stress. To the author's knowledge, there was no related result reported by previous researchers. The specimens were tested with the same stress paths and with the same testing condition. The results are compared in Figures 5-14 to 5-17. In Figures 5-14 and 5-15, when q=100kPa and 125kPa, the differences in degree of non-coaxiality between dense sand and medium sand are clear to see. The degree of non-coaxiality was more pronounced in the dense specimen than that in the medium dense specimen when both of them were subjected to the same stress path. The difference could be as much as 18°. However, in Figures 5-16 and 5-17, when q = 150kPa and 175kPa, the data points from the two tests almost match. The results indicate

that the effect of specimen density on the non-coaxial behaviour was more significant at lower deviator stress level during the rotation of principal stress direction. Dense sand performed more non-coaxial than medium dense sand. However, when specimens were subjected to higher stress levels that approached failure, the effect of density became inconsiderable, while the deviator stress level and direction of principal stress were the main factors.

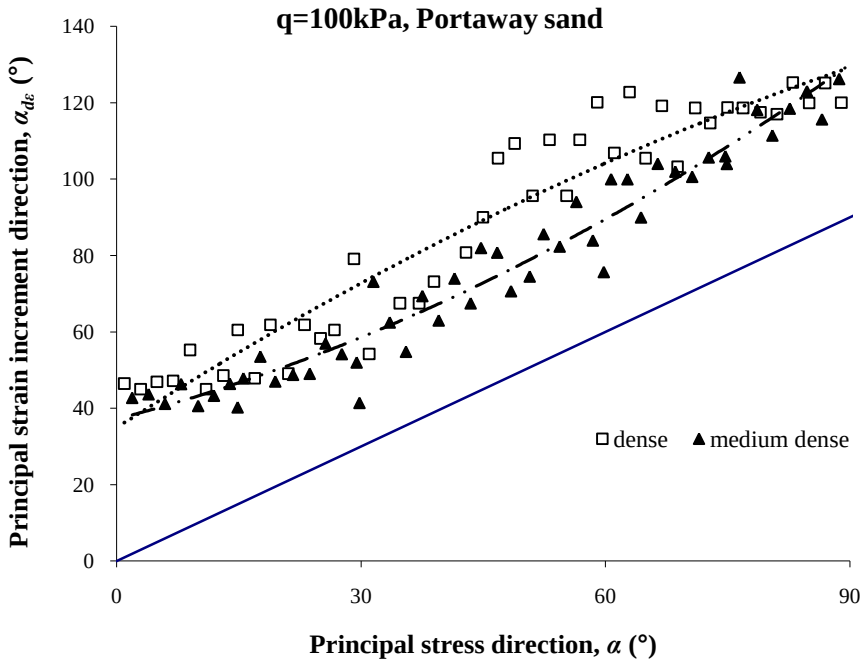

Figure 5-14 Directions of principals stress and principal strain increments of tests R-D01 and R-M01, *q*=100kPa.

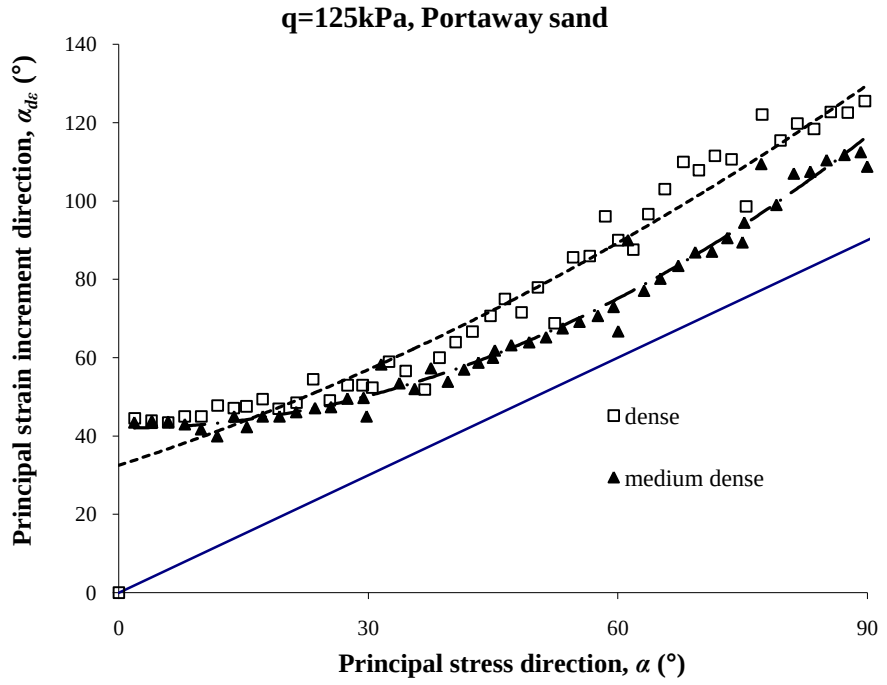

Figure 5-15 Directions of principals stress and principal strain increments of tests R-D02 and R-M02, *q*=125kPa.

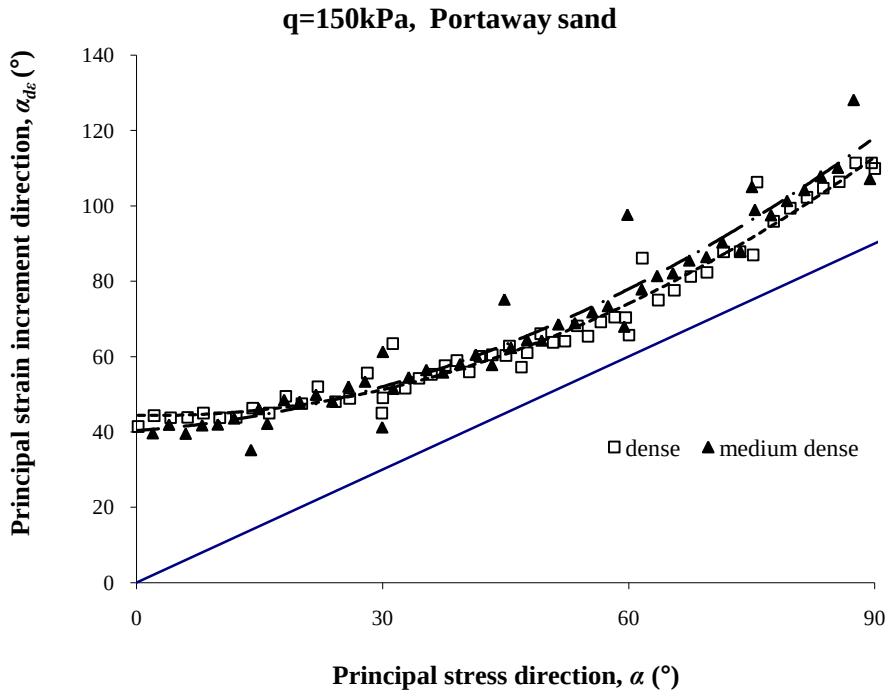

Figure 5-16 Directions of principals stress and principal strain increments of tests R-D03 and R-M03, *q*=150kPa.

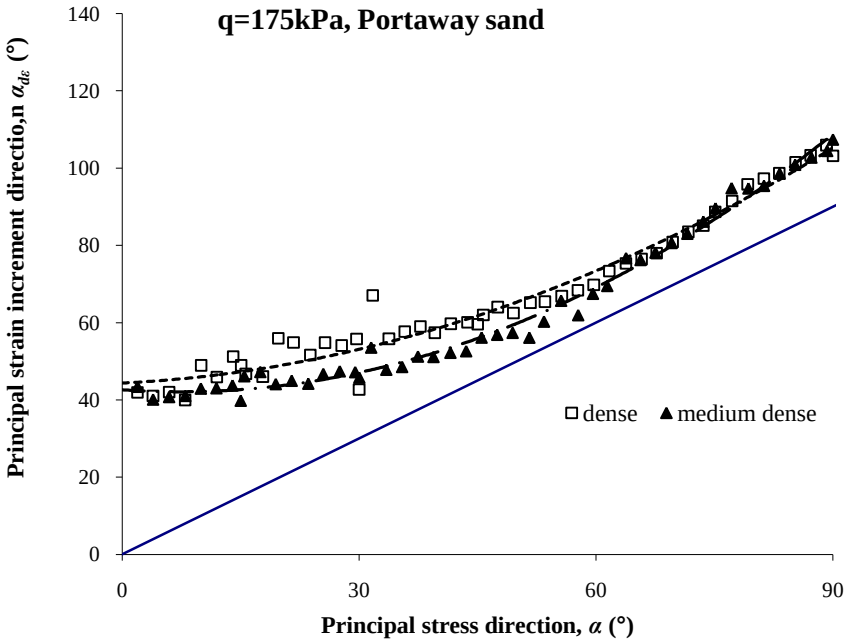

Figure 5-17 Directions of principals stress and principal strain increments of tests R-D04 and R-M04, *q*=175kPa.

5.4 TESTS ON LEIGHTON BUZZARD SAND

It is considered that the non-coaxial degree was related to the magnitude of fabric anisotropy (Miura et al., 1986; Li and Yu, 2009). Material anisotropy is associated with particle shape and size distribution as well as the specimen preparation. To investigate this possibility, two tests were carried out on dense Leighton Buzzard sand with a relative density (D_r) around 90% using the same specimen preparation procedures with tests on Portaway sand. Detailed results are presented in this section.

5.4.1 General soil behaviour

The general behaviour of Leighton Buzzard sand, (tests L-D01 and L-D02), are plotted in Figure 5-18. Figure 5-18(b) does not show a 90 ° α-rotation test because when test L-D02 was conducted, the specimen failed when α reached 75 °. The specimen was considered as failure when the deviator stress q was not able to maintain constant at 150kPa and the back pressure started to deviated from 400kPa. As with the results of Portaway sand shown in Figures 5-5 to 5-8, Figure 5-18(a) shows that before α reached 45 °, shear strain ($\gamma_{\theta z}$) was the largest strain component and increased with α. Significant axial strains (ε_z), circumferential strain (ε_θ) and radial strain (ε_r) started to build up from α= 45 °. And $\gamma_{\theta z}$ kept increasing until the principal stress axis inclined oat 65 ° before reducing. In Figure 5-18(b), as the failure occurred, shear strain only increased with a faster incremental rate between α= 45 ° and 75 °.

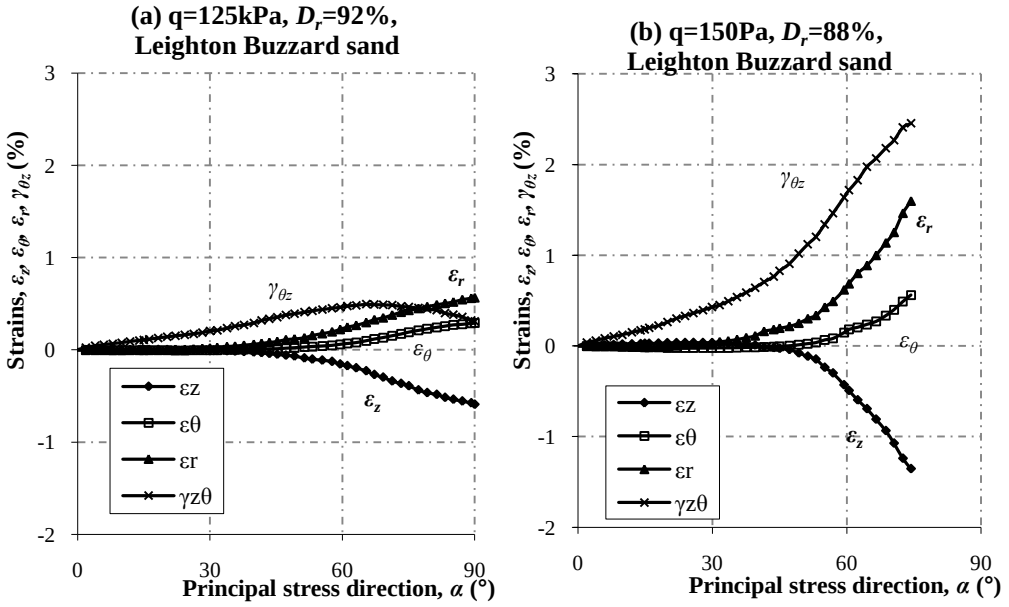

Figure 5-18 Relationships between strain components and the direction of principal

stress axes for test R-L01 and R-L02: (a) *q*=125kPa; (b) *q*=150kPa.

The relationships between shear stress ($\tau_{\theta z}$) and shear strain ($\gamma_{\theta z}$) from tests on dense Leighton Buzzard sand are presented in Figure 5-19. In test R-L01, higher shear stress was observed than that of test R-L02 with smaller shear strains during the stress increasing progress. Figures 5-20 and 5-21 present the results of the deviator strain and volumetric strain vs. principal stress direction respectively. Disproportionately greater strains were produced when higher deviator stress was imposed on the specimen. A volumetric contraction occurred during the rotation of principal stress axis. The strain paths for tests R-L01 and R-L02 are shown in Figure 5-22. Much larger deformation for test R-L02, when q was 150kPa, was obtained than that for test R-L01, when q=125kpa.

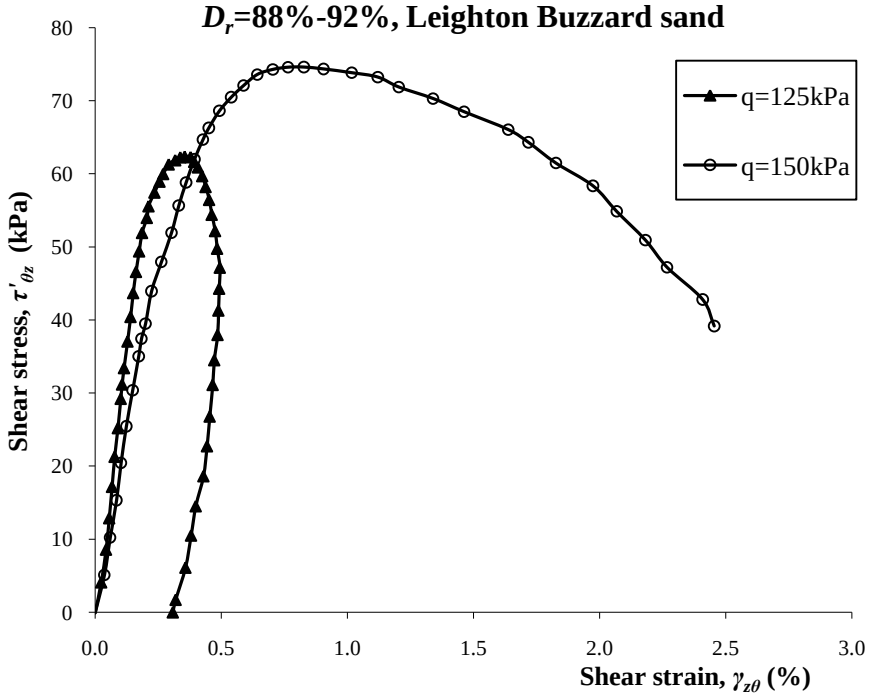

Figure 5-19 Shear strains vs. shear stresses for test R-L01 and R-L02.

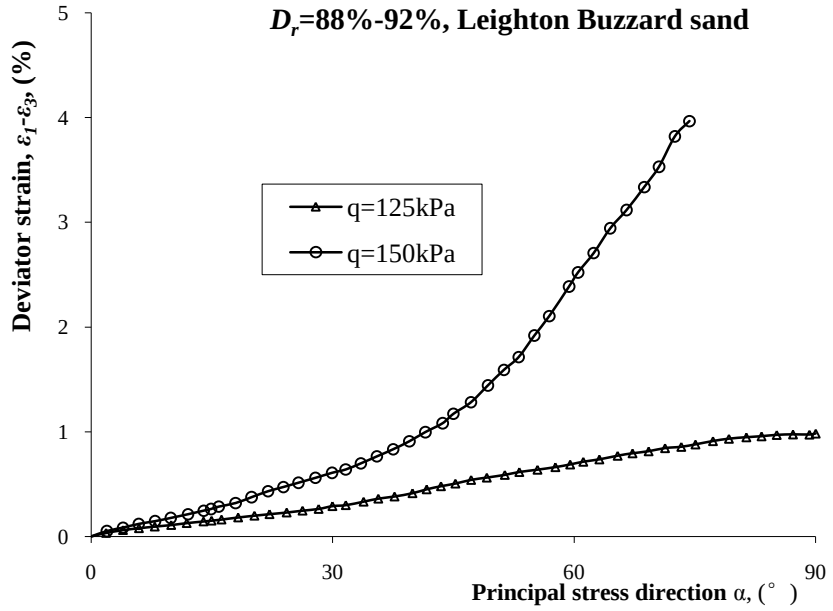

Figure 5-20 Deviator strains vs. shear stresses for test R-L01 and R-L02.

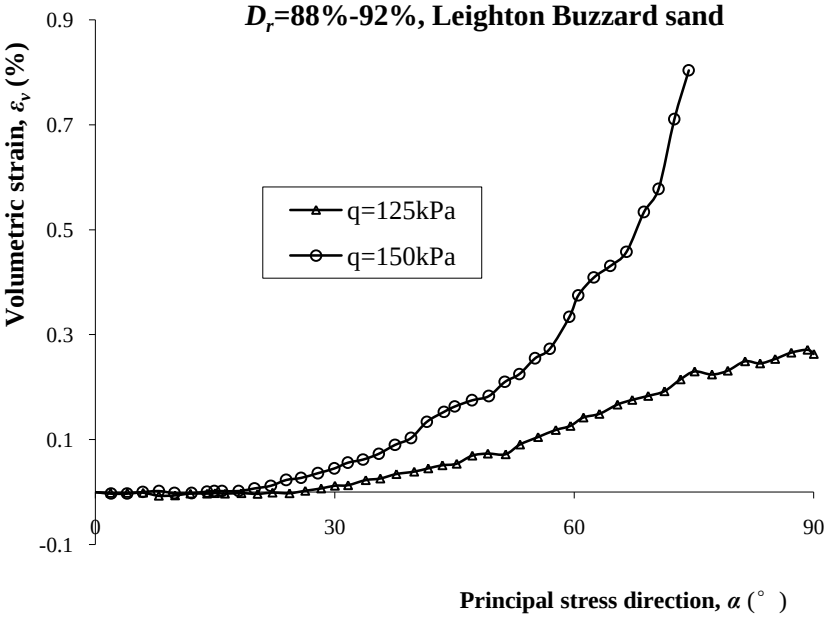

Figure 5-21 Volumetric strains vs. shear stresses for test R-L01 and R-L02.

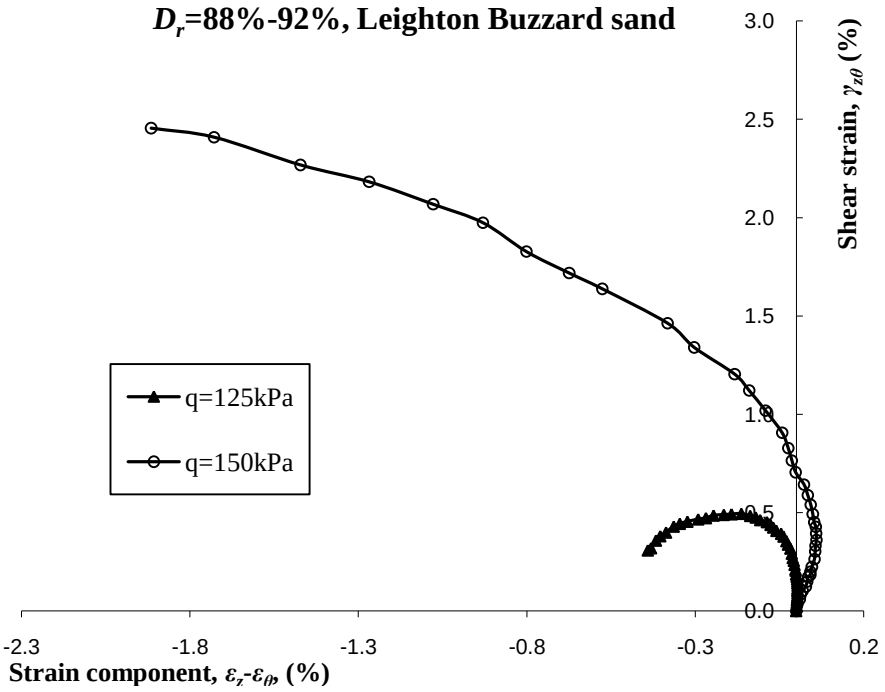

Figure 5-22 Strain paths for test R-L01 and R-L02.

5.4.2 Non-coaxial behaviour

The results of non-coaxiality between the principal stress direction (α) and principal strain increment direction ($\alpha_{d\varepsilon}$) for tests on Leighton Buzzard sand are plotted in Figure 5-23 in the same way as for the Portaway sand. In the figures, the solid diagonal is representative of the coaxial line. Stronger evidence for non-coaxiality can be found because the principal strain increment angles were clearly larger than the angles of principal stress direction. The largest deviation between the axes of principal stress and principal strain increment existed at the beginning of rotation, which was about 40 ° for both tests. The minimum deviations existed around α=60 ° in test R-L01, and occurred when the specimen failed in test R-L02. The trends were consistent with the results of Portaway sand (Figure 5-14 to 5-17), which indicated that the smallest degree

of non-coaxiality happened between α=60 ° to 75 °. At the higher shear stress level, i.e. q=150kPa, the principal strain increment axis was more coaxial with the principal stress axe, which also agrees with the conclusion from tests on Portaway sand. The sand behaviour was more coaxial when specimen approached failure. The average degree of non-coaxiality for test R-L01 (q=125kPa) was about 20 °, and about 12 ° for test R-L02 (q=150kPa).

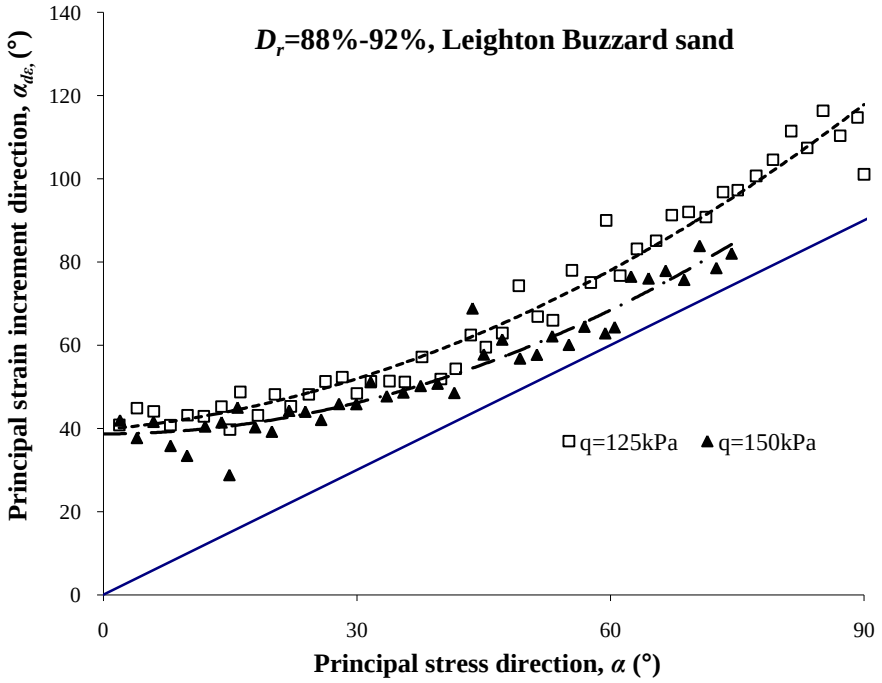

Figure 5-23 Directions of principal stress and principal strain increments of tests R-L01 and R-L02, Leighton Buzzard sand.

5.5 COMPARISON AND DISCUSSION

Laboratory results based on Portaway sand and Leighton Buzzard sand were compared to study the influence of material anisotropy associated with

particle characteristics on material non-coaxial behaviour. From the particle size distribution curves for Portaway sand and Leighton Buzzard sand given in Figure 3-6, and the SEM pictures given in Figures 3-7 and 3-8, Leighton Buzzard sand has much more isotropic particle shapes and more uniform particle size distribution. Due to the different particle characteristics, Leighton Buzzard sand should possess different fabric anisotropy for that of the Portaway sand. As the specimens were prepared using the same methods and following the same procedures, Leighton Buzzard sand specimens should induce a more isotropic fabric than Portaway sand specimens.

Figures 5-24 and 5-25 show the non-coincidence of principal stress direction and principal strain increment direction for both sands at q =125kPa and 150kPa. The differences in the degree of non-coaxiality between the two different materials are obvious. Portaway sand exhibits a more pronounced non-coaxial behaviour than does the Leighton Buzzard sand. In Figure 5-24, when q=125kPa, the largest difference between the result of the two sands was about 20 ° and occurred between α =45 ° to 60 °. In Figure 5-25, when q=150kPa, the Leighton Buzzard sand specimen could not sustain a 90 ° α-rotation due to the lower resistance. The curves in Figure 5-25 also show that the soil behaviour of Leighton Buzzard sand was more coaxial than that of Portaway sand. But the disparity between results of two materials is about 5 °, which is smaller than that in Figure 5-24.

The results compared in Figures 5-24 and 5-25 confirm that the initial fabric anisotropy of the specimen has a significant influence on the

non-coaxiality between the directions of principal stress and principal strain increments. The effect will be impaired by increasing the shearing stress level.

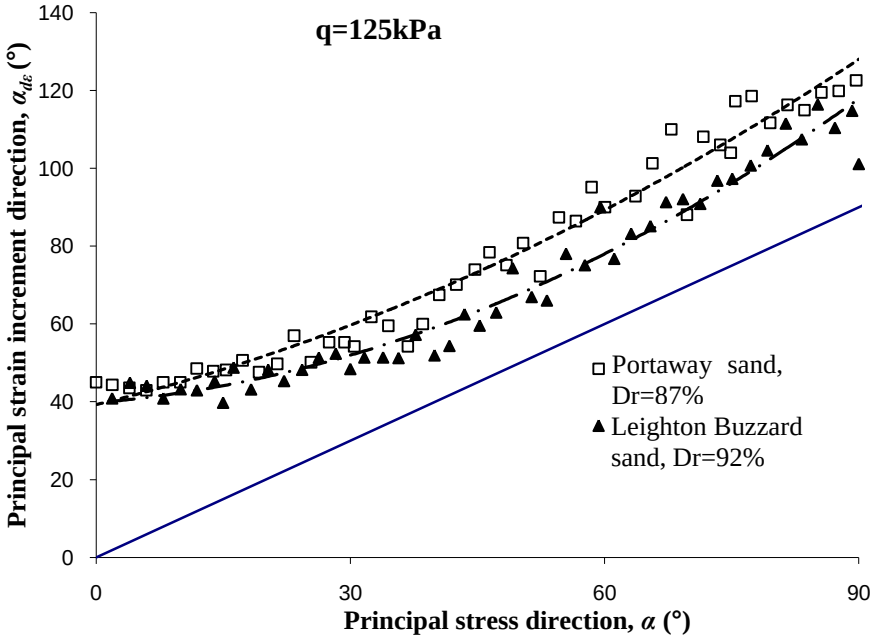

Figure 5-24 Directions of principals stress and principal strain increments of tests R-D02 and R-M01, *q*=125kPa.

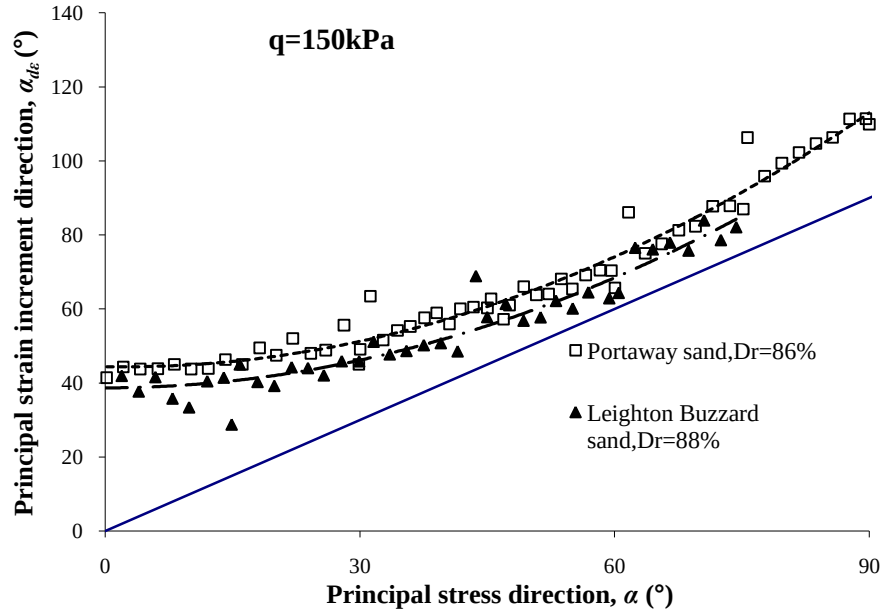

Figure 5-25 Directions of principals stress and principal strain increments of tests R-D03 and R-M02, *q*=150kPa.

5.6 SUMMARY

This chapter presents the results of tests under pure rotational loading, in which the principal stress axes were rotated with deviator stress q kept constant. Two types of sand were used in this series of tests, Portaway sand and Leighton Buzzard sand.

Four drained dense (D_r≈90%) specimens and another four medium dense (D_r≈50%) specimens of Portaway sand were prepared. Two drained tests were conducted using Leighton Buzzard sand with a relative density of 90%. Four stress paths with a rotating major principal stress axis from vertical to horizontal under different deviator stress levels were applied, q=100kPa, 125kPa, 150kPa and 175kPa. Only the stress paths with q=125kPa and 150kPa were employed on the Leighton Buzzard sand so as to study the effect of initial fabric anisotropy of different materials.

The results obtained from the tests showed a good control to the prescribed stress paths. The general stress-strain soil behaviour was described firstly followed by the discussion on the non-coaxial soil behaviour. Both Portaway sand and Leighton Buzzard sand provide strong evidence for non-coaxiality between the axes of principal stress and principal strain increment. The degree of non-coaxiality was dependent on the stress path, the stress level and the density. The maximum deviation occurred at the beginning of rotation, and the minimum value was obtained when α=60°-75°. With the increase of deviator

stress q, the specimen behaved in a more coaxial manner. More non-coaxiality was found in the dense sand than in the medium dense sand. However, at the higher stress level, the effect of density was eliminated.

By comparing the results of Portaway sand and Leighton Buzzard sand, the soil behaviour was seen to be affected by the material's initial anisotropy. The results indicate that specimen with a more isotropic fabric will generate more coaxial soil behaviour. However, a further experimental study on the non-coaxiality using an artificial isotropic material is required to fully understand the effects of soil anisotropy on the non-coaxiality of geomaterials.

Chapter 6

Combined Loading Tests

6.1 INTRODUCTION

This chapter describes the combined loading tests carried out on Portaway sand specimens. In these tests, the principal stress axes were rotated with increase of deviator stress q. Specimens with different densities were tested following the same stress path so as to study the effect of void ratio on soil behaviour. The next section will introduce the test procedures. Then, in Section 6.3, the stress-strain behaviour will be described, followed by the investigation of non-coaxiality in Section 6.4. A discussion on the effect of stress path including the monotonic loading, pure rotation loading and combined loading will be presented in Section 6.5. Finally, Section 6.6 will summarise this chapter.

6.2 TESTING PROCEDURES

Two drained tests on Portaway sand were conducted in this series, one on dense sand and the other one on medium dense sand. The properties of Portaway sand have been introduced in Chapter 3, together with the specimen preparation procedures and experimental setup. The testing conditions including the stress path followed in the tests and the test control is introduced in this section.

Table 6-1 summarises the initial conditions and failure states of the tests. The prescribed stress paths for the two tests were the same, as shown in Figure 3-19 in Chapter 3. The actual stress paths obtained from the tests are presented in Figure 6-1 for both dense and medium dense sand. Before the rotation of principal stress direction, the specimens were sheared monotonically in the vertical direction to the state of q=75kPa and α=0°. Then, the deviator stress q was increased with the simultaneous rotation of principal stress axis as shown in Figure 6-1. The deviator stress q was increased at an average rate of 1.5kPa/min, and α was rotated at the rate of 1°/min. It can be seen from the figure that the stress path agreed well with the prescribed path in Figure 3-19 in Chapter 3 but rotation stopped before α reached 90° due to the failure of specimens. In these two tests, the specimens were considered as failing when the back pressure was not able to keep constant, and the difference between out and inner cell pressures was larger than 4kPa.

Table 6-1 Summary of initial testing conditions of combined loading tests

Test No.	Stress-density state					Failure state	
	q (kPa)	e_c	D_{rc} (%)	p_c (kPa)	P'_c (kPa)	q (kPa)	α (°)
C-D	75	0.469	91	600	200	205	84
C-M	75	0.552	51	600	200	192	79

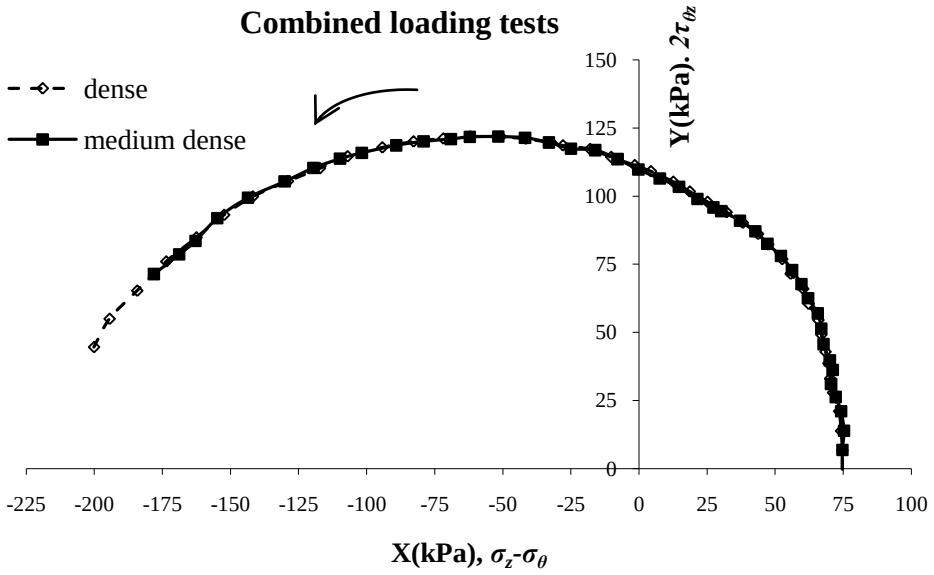

Figure 6-1 Actual stress paths for combined loading tests

The control of parameters b and α is shown in Figure 6-2. The rotation was carried out in 15° steps to keep $b=sin^2\alpha$ when the principal stress axes rotated from vertical to horizontal. In Figure 6-2, the relationships between b and α obtained from both tests were very close to the calculated ones, which reflects a good control of the test.

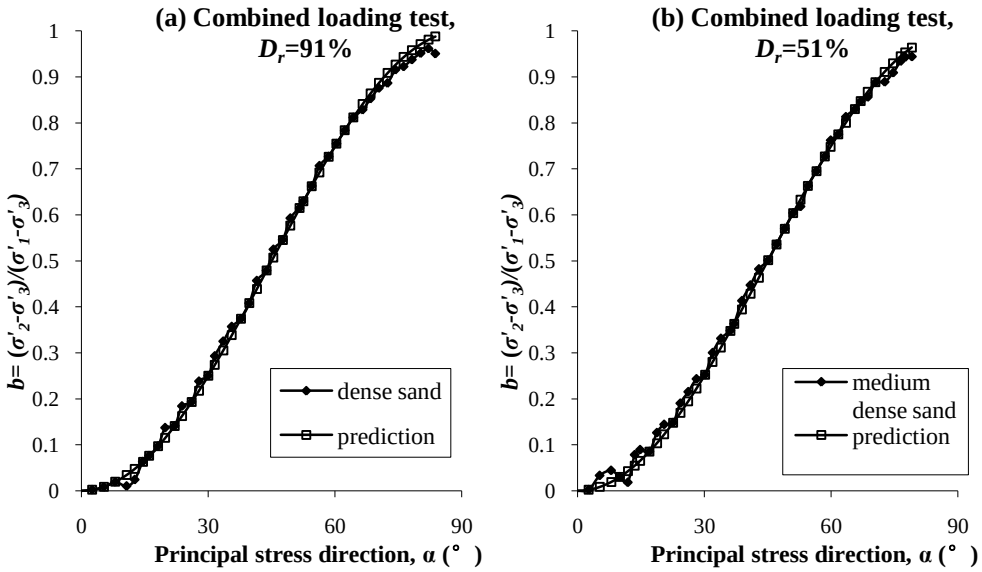

Figure 6-2 Control of the parameter *b*: (a) dense sand; (b) medium dense sand

6.3 GENERAL SOIL BEHAVIOUR

6.3.1 Stress variation

Figure 6-3 shows the relationship between the stresses and principal stress direction. As the variation of stresses was related to the stress path but not the density, only the results of dense sand are plotted in Figure 6-3. In Figure 6-3(a), the effective axial stress (σ'_z) started from 250kPa then reduced with the rotation of principal stress axis and reached the minimum value of 72kPa, where the specimen failed. The effective radial stress (σ'_r) and circumferential stress (σ'_θ) ($\sigma'_r = \sigma'_\theta$) increased from the value of 175kPa to the maximum value of 272kPa. The developments of σ'_z, σ'_r and σ'_θ, were affected by the increase of q. The variations of the curves were amplified compared with that in pure rotation tests (Figure 5-3 in Chapter 5). Shear stress ($\tau_{\theta z}$) increased with α until 57 °, then started to decrease. The greatest magnitude of shear stress was 61kPa.

The curves of principal stresses vs. principal stress direction are shown in Figure 6-3(b). The effective major principal stress (σ'_1) was equal to the axial stress (σ'_z) at the beginning of test then increased to 275kPa, while the minor principal stress (σ'_3) was the same with the radial stress (σ'_r) when rotation started then decreased to 70kPa when the specimen failed.

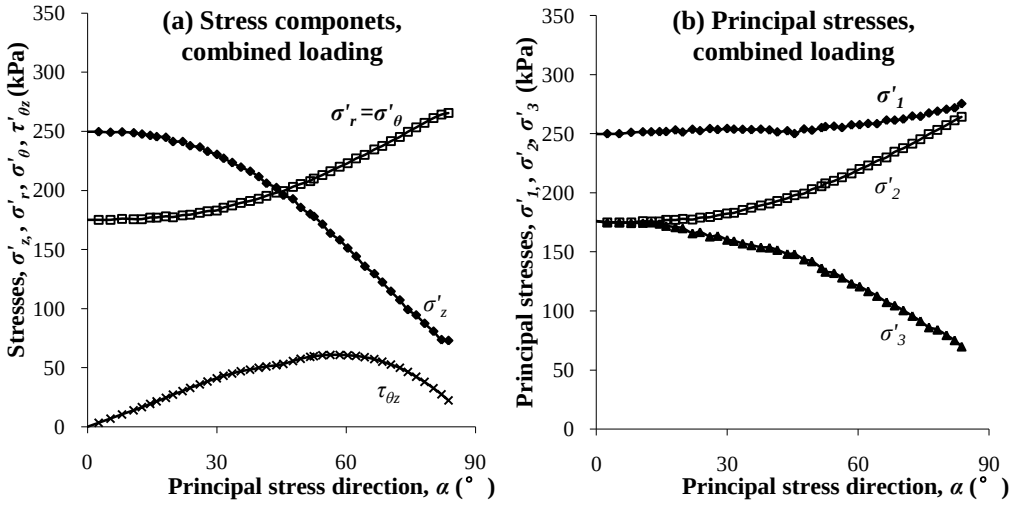

Figure 6-3 Variation of stresses vs. principal stress direction for dense sand: (a) stress components vs. α; (b) principal stresses vs. α

6.3.2 Strain variation

The strain components are plotted vs. the principal stress direction, α, in Figure 6-4. In the range of α=0 ° to 60 °, the axial strain (ε_z), circumferential stain (ε_θ) and radial strain (ε_r) were very small, and the shear strain ($\gamma_{\theta z}$) increased gradually with the increase of α. Then after α=60 °, the strain components increased significantly, especially in the medium dense sand, as shown in Figure 6-4(b). The strain variations are different from those of the pure rotation tests shown in Figures 5-5 to 5-8 in Chapter 5 due to the change of deviator stress q. Figure 6-5 presents plots of the deviator stress q vs. strain

components ε_z, ε_θ, ε_r and $\gamma_{\theta z}$. For medium dense sand in Figure 6-5(b), the strains developed more significantly than for the dense sand in Figure 6-5(a), which illustrates the effect of relative density on the stress-strain behaviour of granular soil.

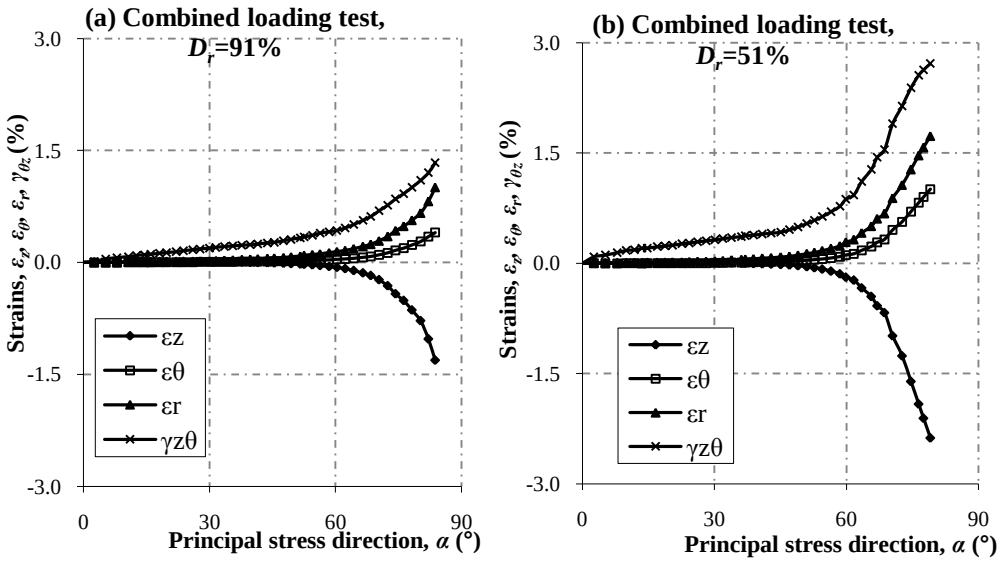

Figure 6-4 Strain components vs. principal stress direction: (a) dense sand; (b) medium dense sand

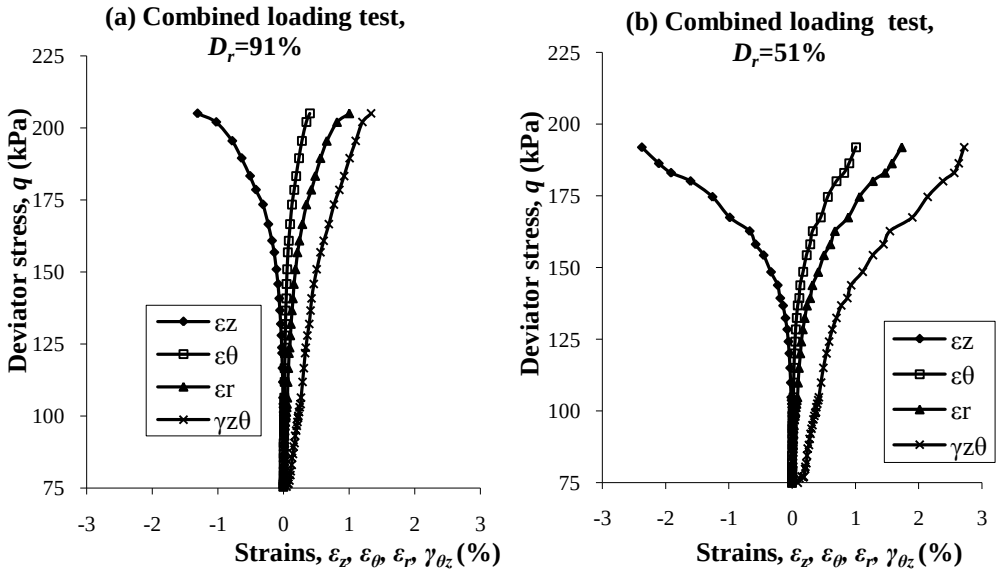

Figure 6-5 Deviator stress vs. strain components: (a) dense sand; (b) medium dense sand

6.3.3 Effect of density

The effective shear stress vs. shear strain curves obtained from the combined loading tests on dense and medium dense sand are compared in Figure 6-6. As shown in the figure, before the shear stress reached the peak value, the curve for dense sand is slightly stiffer than that of medium dense sand. Larger strain was obtained in medium dense sand at the maximum value of q. Then when $\tau_{\theta z}$ started to decrease, the shear strain softening in medium dense sand was much more significant than that in the dense sand. The maximum shear strain for dense sand was less than 1.5% when specimen failed, while the shear strain for medium dense sand at the end of test was about 2.8%.

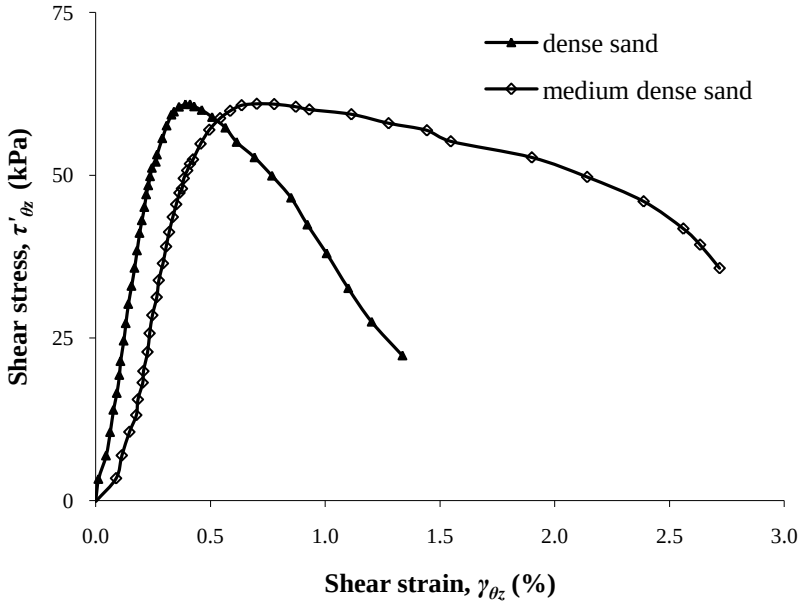

Figure 6-6 Shear stress vs. shear strain curves for combined loading tests on Portaway sand.

Figure 6-7 shows the variation of deviator strain with the rotation of principal stress axis. The developing trends of deviator strains were similar to

those of shear strains ($\gamma_{\theta z}$) shown in Figure 6-4. In the medium dense specimen, a larger deviator strain was obtained at any particular value of α than was obtained for the dense specimen. The disparity is much larger after α=60 °. At the end of test, the deviator strains of dense and medium dense sand were 2.5% and 5.2%, respectively.

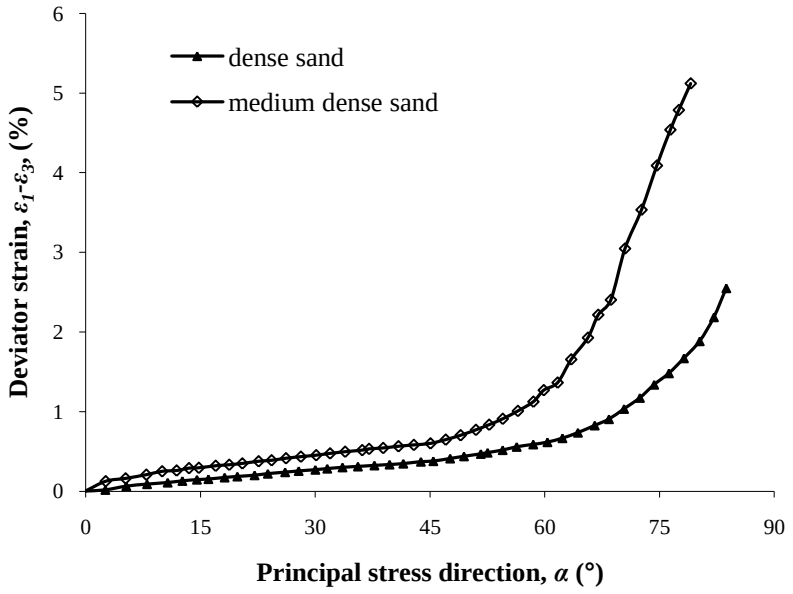

Figure 6-7 Deviator strain vs. principal stress direction in combined loading tests

The volumetric stains vs. principal stress directions are presented in Figure 6-8. Both of the specimens performed a contractive volume change from α=0 ° to around 75 °. When the specimen approached to failure, a volumetric dilation started to develop. It is also clear to see from the figure that the contraction of volume in the medium dense sand was larger than that in the dense sand, and less dilation was observed in the medium dense sand when the specimen failed.

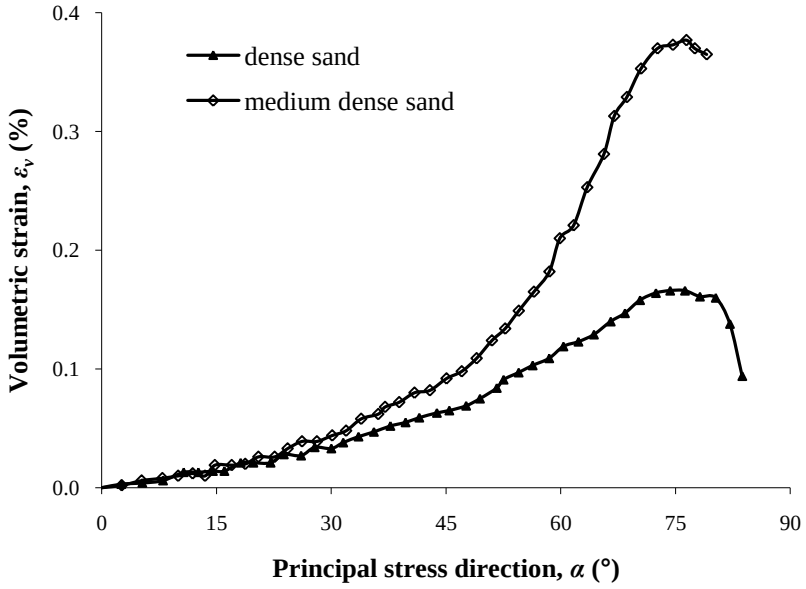

Figure 6-8 Volumetric strains vs. principal stress directions in combined loading tests for both dense and medium dense sand

6.4 NON-COAXIAL SOIL BEHAVIOUR

The curves in Figures 6-9 and 6-10 display the principal strain increment direction $\alpha_{d\varepsilon}$ against the principal stress direction α obtained from combined loading tests on dense and medium dense sand, respectively. In the figures, the solid straight lines represent the coaxial state of principal strain increment and principal stress directions. Again, the deviations of the principal strain increment directions from the coaxial line provide clear evidence for non-coaxiality.

It can be seen from Figures 6-9 and 6-10 that the degree of non-coaxiality was dependent on the principal stress direction α. The largest deviation was observed at the beginning of shearing with a value of approximately 45 °. Then the degree of non-coaxiality reduced with the increasing principal stress axis

inclination. As the deviator stress q increased with α, the degree of non-coaxiality reduced with the increase of q as well. After α=60 °, referring to Figure 6-4, the strains started to increase significantly. The axes of principal stress and principal strain increment became coaxial when α = 60 ° and kept until the specimens failed, as shown in Figures 6-9 and 6-10.

By comparing the two figures of different densities, it can be noticed that the strain increment directions measured for both the dense and medium dense sand were very close to each other. Therefore, the effect of density can be considered to negligible in this series of tests.

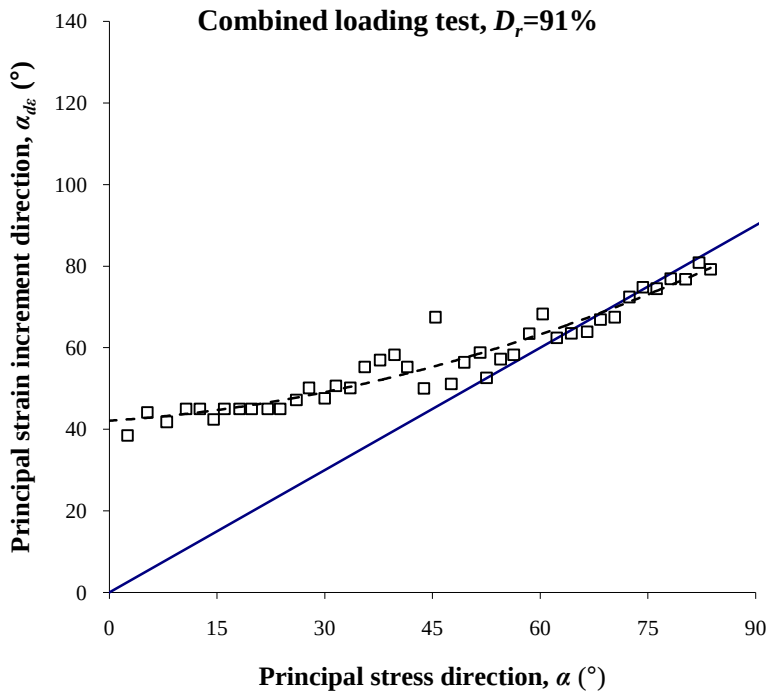

Figure 6-9 Non-coaxiality for combined loading tests on dense sand

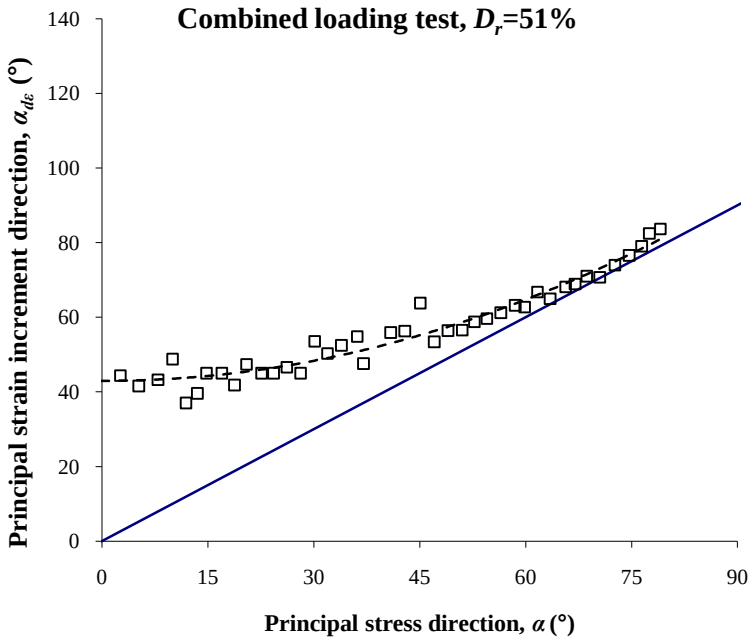

Figure 6-10 Non-coaxiality for combined loading tests on medium dense sand

6.5 COMPARISON AND DISCUSSION

In order to compare the non-coaxiality between axes of principal stress and principal strain increment obtained from the different stress path tests, the unit strain increment are displayed in the form of vectors plotted on X-Y stress space on Figures 6-11 to 6-13. When plotted in this space, the strain increment vector makes an angle of twice the angle of strain increment axis relative to the vertical direction as shown by Eq. (2.26) in Chapter 2 and indicated in Figure 6-11.

In Figure 6-11, the arrows represent the unit of strain increment vectors for the monotonic loading tests and combined loading tests on dense Portaway sand. As all the specimens were prepared using the same procedures and were tested under the same condition with no pre-shearing history, the sand

behaviour was affected by the stress path. In Figure 6-11, there are six common states with the same stresses and loading directions for the two series of tests (points A, B…F). The discrepancy in the degree of non-coaxiality was observed when different stress paths were applied. Especially at points A, B, C and D, the magnitude of strain increment direction was much higher when the specimen was subjected to the combined loading. At point E, when α=60 °and q=140kPa, $\alpha_{d\varepsilon}$ was smaller than α for monotonic loading tests, but $\alpha_{d\varepsilon}$ was larger for combined loading tests. In both tests, the degree of deviation between axes of principal stress and principal strain increment was very small. At point F, when α=75 °and q=180kPa, and the specimen was approaching failure in the combined loading test, a coaxial behaviour between the principal stress and principal strain increment directions was obtained. The magnitude of strain increment direction for monotonic loading tests was smaller than the stress direction and the strain increment direction of the combined loading test.

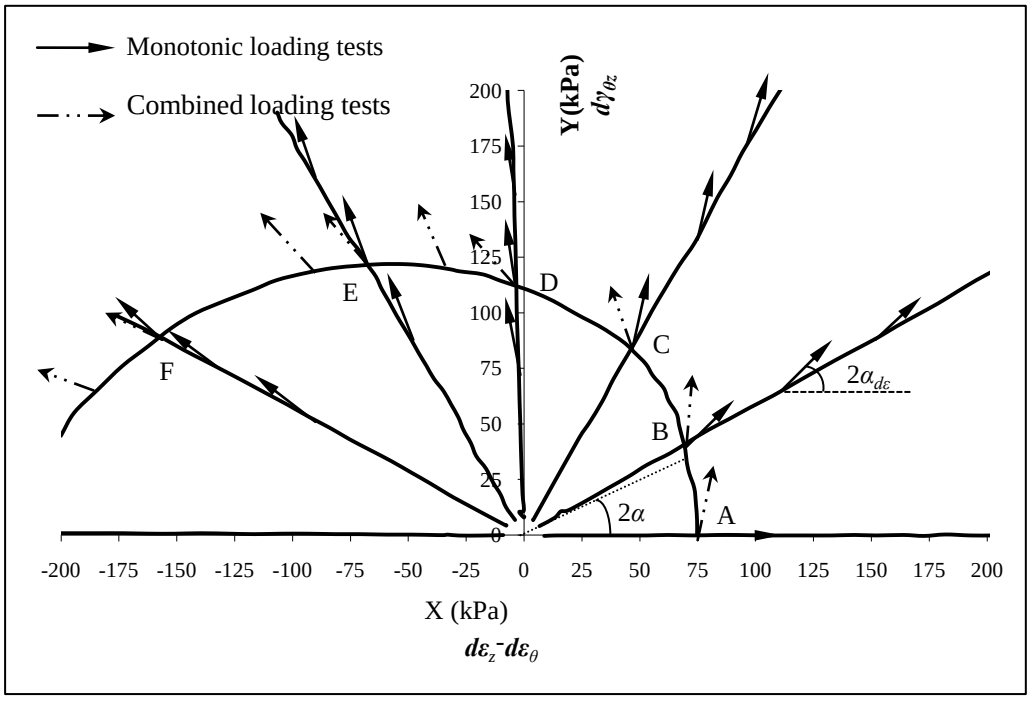

Figure 6-11 Unit strain increment vectors on the stress paths for monotonic loading and combined loading

Figure 6-12 compares the results of the pure rotation tests with that of the combined loading test on dense Portaway sand. It can be seen from the figure, at the beginning of rotation, when α =0°, the directions of principal strain increments were similar for all of the pure rotation tests and the combined loading test. For the two types of stress paths, there were four common states (point A, B, C and D), when q was 100kPa, 125kPa, 150kPa and 175kPa; with the value of α being 37.5°, 53.5°, 64° and 73°, respectively. A clear difference in the degree of non-coaxiality was observed in the pure rotation tests and the combined loading test. The angles of the strain increment axes relative to the vertical direction in the combined loading test were much smaller than those in the pure rotation tests.

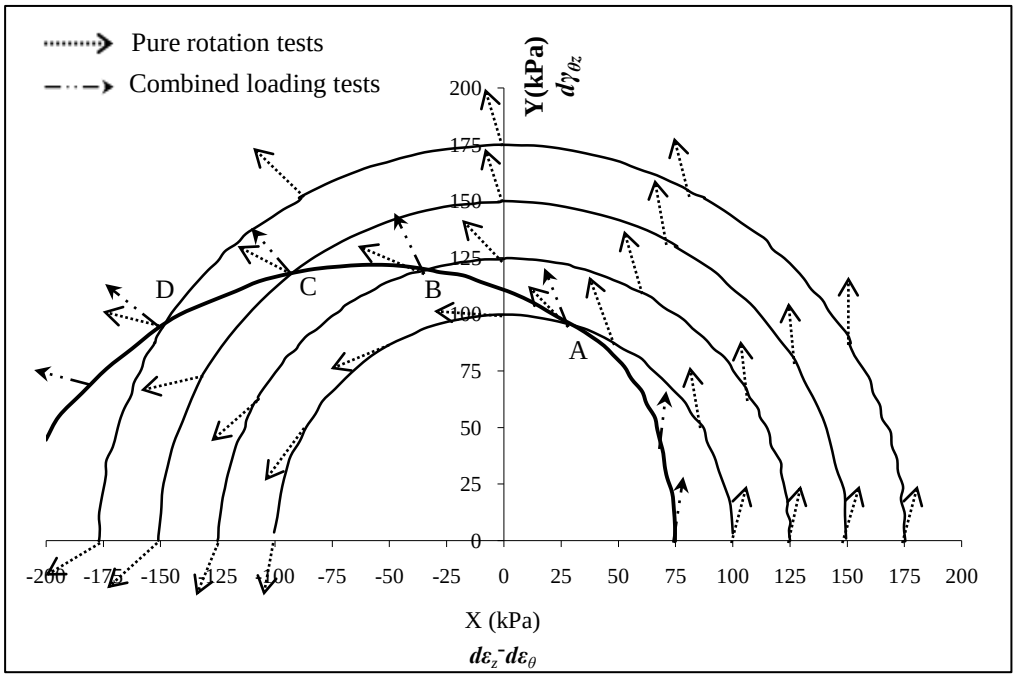

Figure 6-12 Unit strain increment vectors on the stress paths for pure rotation and combined loading

The results for all three types of stress paths are compared in Figure 6-13. As there were no common stress states for all three types of stress paths, similar states are pointed out for the discussion between the three series of tests, they are points A and B, C and D, and E and F. Points A and C are the common states of the monotonic loading and the combined loading tests, and points B and D are the common states of the monotonic loading test and the pure rotation test. Point A has same stress direction with B and similar deviator stress, while point C and D have same stress direction and very similar deviator stress. By comparing the degree of non-coaxiality of point A with B, and C with D, it clear to see that the degree of non-coaxiality observed from monotonic loading tests was lowest and could be neglected. The degree of non-coaxiality in specimen subjected to combined loading took lay in the middle for the three types of stress paths. The pure rotation tests provided the most pronounced evidence for non-coaxiality. Point E is the common state of the pure rotation test and the combined loading test, and point F is the common state of the pure rotation test and the monotonic loading test. These two states have the same stress paths with very similar principal stress directions. It can be seen from the figure that the stain increment directions of the three types of tests were in the order: pure rotation test >combined loading test >monotonic loading test. The results indicate that the non-coaxiality is not only dependent on the principal stress direction, but also on the stress path with most being observed when pure rotation was applied.

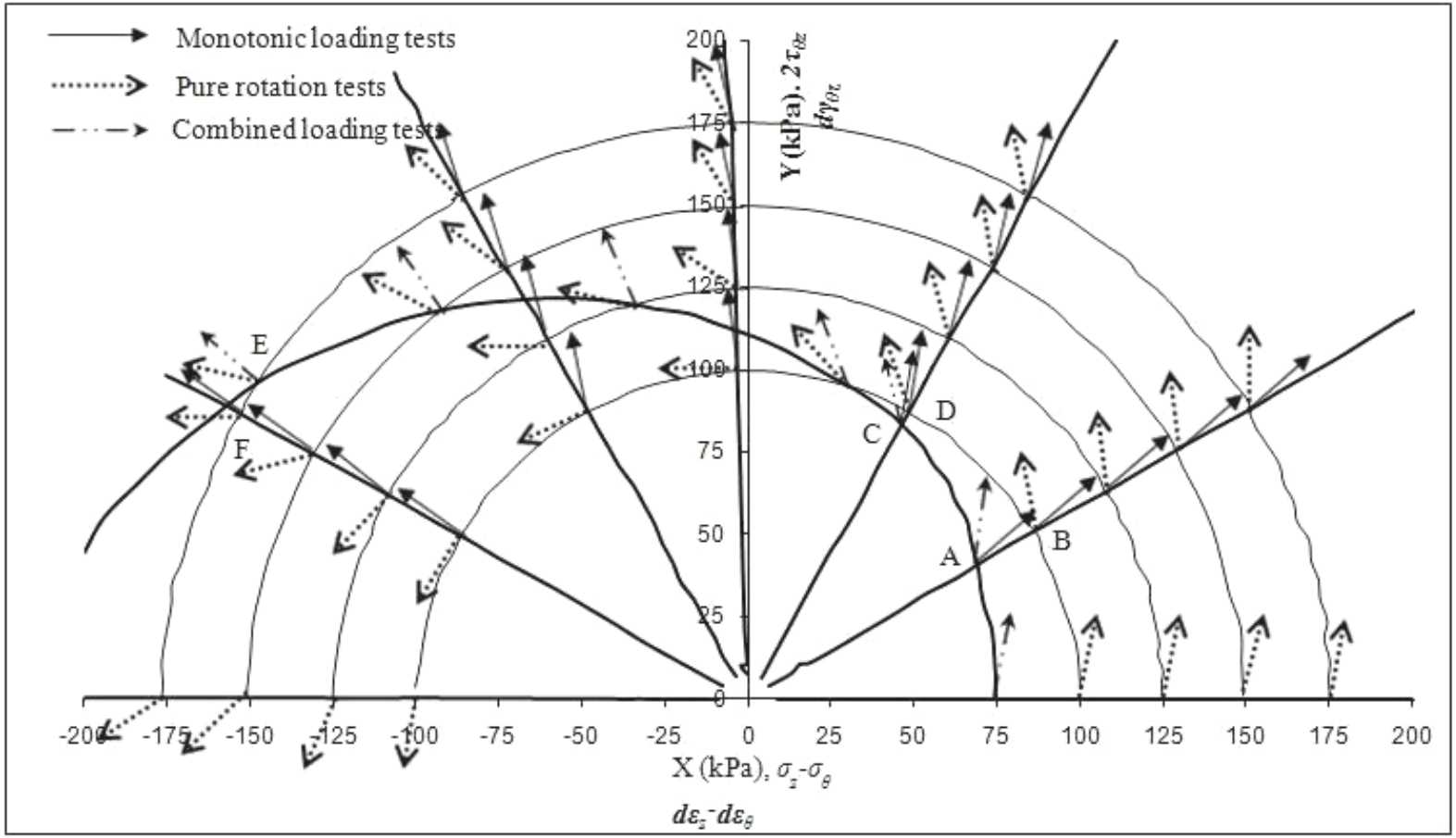

Figure 6-13 Unit strain increment vectors on the stress paths for monotonic loading, pure rotation and combined loading

6.6 SUMMARY

This chapter can be divided into two major parts. The first part deals with the series of tests carried out under the combined loading stress path. In this series, drained tests on specimens with different densities were carried out by rotating the principal stress axes and increasing the deviator stress at the same time. The stress path and relationship curves between b and α obtained from the tests show a good control of the paths. Furthermore, it was observed that the medium dense specimen failed at a lower deviator stress level than the dense specimen. Larger strains also developed in the medium dense sand. Non-coaxiality between the axes of principal stress and principal strain increment was obtained for both dense and medium dense sand. The density showed no effect on the degree of non-coaxiality in the combined loading test. The degree of non-coaxiality varied with the rotation of principal stress axes and the deviator stress level. The largest deviation occurred at the beginning of rotation, and decreased with the rotation of α. From $\alpha > 60°$, the soil behaviour became and remained coaxial until the specimens failed.

In the second part of this chapter, the effect of stress paths on the non-coaxiality is investigated by comparing the results of three series of tests followed different stress paths on dense Portaway sand. It was demonstrated that at similar stress states, the directions of principal strain increment in specimen subjected to the monotonic loading path were smallest, and those in

sand subjected to the pure rotation of principal stress axes were largest. The comparison shows that the degree of non-coaxiality was affected not only by the magnitude and direction of principal stress, but also by the stress path followed.

Chapter 7

Summary and Conclusions

7.1 SUMMARY

7.1.1 Background on non-coaxiality

Non-coincidence of the principal stress axis and the principal strain increment axis is called non-coaxiality. It has been observed and recognized in element soil testing using both simple shear and hollow cylinder apparatus. Non-coaxiality is an important feature of numerous plasticity models describing “fully developed” plane plastic flow of granular materials by means of kinematic theories. Rudnicki and Rice (1975) reported that non-coaxiality plays an important role in shear band formation in sands and needs to be introduced into the constitutive relations in order to obtain a better estimate of the onset of strain localization. In some pre-failure plasticity models that have

been proposed for granular materials, such as hypoplastic models (Wang *et al*., 1990; Kolymbas, 1991), non-coaxiality is given a shows its theoretical basis.

From the experimental perspective, Roscoe *et al.* (1967) and Roscoe (1970) found that the principal axes of strain rates and stresses are not coincident during the early stage of shearing in simple shear tests on sand. Drescher and De Josselin De Jong (1972) reported the evidence for non-coaxiality on the experimental micro-mechanical study of a photoelastic disc assembly as a two-dimensional analogue of granular media. Experimental evidence of non-coincidence of the principal stress direction and the principal strain increment direction has also been shown by Wong and Arthur (1986) in both dense and loose sands during cyclic rotation of principal stresses using the directional shear cell apparatus. The HCA has been a valuable equipment to investigation of the non-coaxial behaviour of granular soils since the 1980's. For example, Symes *et al.* (1984) conducted a series of undrained tests in a HCA to investigate the anisotropy and the effects of principal stress rotation on the behaviour of medium-loose Ham River sand. In their tests, with α fixed at 24.5 ° and 45 °, the maximum deviation between the principal stress and strain increment directions was as large as 20 °. Miura *et al.* (1986) investigated the anisotropy of dense Toyoura sand using a HCA test. Non-coaxiality was observed in both monotonic loading tests and rotational shear tests. However, the degree of non-coaxiality was rather small in monotonic loading tests. The soil behaviour became more coaxial at larger strain levels. The authors concluded that the deviation of strain increment direction from the stress direction was caused by the initial anisotropy of sand and, in rotational shear

tests, the effect continues even after 7 or 8 cycles of rotation of the major principal stress (Miura *et al.*, 1986). A HCA was also used by Ishihara and Towhata (1983), Pradel *et al.* (1990) and Gutierrez *et al.* (1991, 1993) to further analyze the non-coaxial behaviour of Toyoura sand. Their studies all give evidences of the non-coaxiality. For example, Pradel *et al.* (1990) found that the direction of principal plastic strain increment was strongly dependent on the direction of stress increment applied to specimens. Gutierrez *et al.* (1991) further reported that the plastic strain increment direction depends on the stress magnitude and direction, as well as the direction of stress increment. Their results were used to build an elastoplastic constitutive model to simulate the behaviour of sand in rotational shear tests (Gutierrez *et al*., 1993).

7.1.2 Reason to study the non-coaxial soil behaviour

A precise prediction of the magnitude and direction of deformation in soil when a new soil structure is planned is of the first importance. The essentiality of considering the non-coaxiality between axes of principal stress and principal stain increment in modelling soil structure has been emphasized by Yu and Yuan (2005). It is necessary to introduce the non-coaxial flow rules into the development of advanced plasticity models. Without accounting for the non-coaxiality, the design might be unreliable.

Although there have been several experimental studies showing evidences of non-coaxiality between the principal stress directions and principal strain increment directions, most of the studies have focused on other issues (e.g. stress-strain behaviour, effect of anisotropy). Only Gutierrez and Ishihara

(2000) carried out a study focused particularly on the non-coaxiality and energy dissipation in a granular material. The purpose of this study is to provide a better understanding of the non-coaxial soil behaviour by experiments using HCA. Also, the factors that may affect the degree of non-coaxiality are focused to provide valuable information for verifying numerical results obtained from non-coaxial FEM and DEM models.

7.1.3 Experimental techniques

A HCA which allows independent control of magnitudes and directions of the principal stresses was used in this study. The HCA specimens with height of 200mm, outer diameter of 100mm and inner diameter of 60mm were prepared. The HCA is capable of applying the loads up to 12kN/ 200Nm of axial force and torque respectively.

Portaway and Leighton Buzzard sands were used in this study. Portaway sand is a well–graded medium sand composed of quartz with some carbonate materials. Leighton Buzzard sand is a uniform sand composed mainly of quartz. The former sand consists of subangular particles, while the latter consists of subrounded particles. The particle size distribution curves show that Leighton Buzzard sand is more uniform than Portaway sand.

Water sedimentation method was applied to prepare all of the specimens to two different density states, medium dense and dense. For dense samples (Portaway sand and Leighton Buzzard sand), the relative density, D_r, was about 90%, and for the medium dense samples (Portaway sand), D_r was about 50%.

After isotropic consolidation, tests were carried out under drained condition using stress path control. In all the tests, the mean stress *p* was kept constant at 600kPa and the back pressure at 400kPa, thus the effective mean stress was held at 200kPa. The outer pressure was kept equal to the inner cell pressure, P_i=$P_{o,}$ which made $b = \sin^2 \alpha$.

Three series of tests were carried out. The first series was monotonic loading tests performed on Portaway sand. In these tests, the axes of principal stress were fixed while the deviator stress, *q*, was applied at a constant rate until the specimen failed. The second series of tests, named pure rotation test, included both Portaway and Leighton Buzzard sands were tested by continuous rotation of the major principal stress axis from vertical to horizontal at a constant deviator stresses *q*. The last series of tests followed a combined stress path, and were performed on the Portaway sand. The specimens were subjected to the rotation of principal stress axes as well as the increase of the deviator stress.

7.2 CONCLUSIONS

7.2.1 Behaviour under monotonic loading

- The deformation of specimens was affected by the void ratio. More deformation was obtained in the medium dense sand when specimens were subjected to the same stress conditions. More dilation and less

contraction of the specimen volume was obtained in the dense specimens.

- The failure strength was affected by specimen density. Denser sand has a higher shearing resistance. However when α=60 °~ 90 °, the influence of density became less significant.

- The stress-strain behaviour of sand was dependent on the loading direction. The specimen strength was determined by the loading direction. The largest failure deviator stress occurred when α=0 °, and the lowest value was found when the specimen was sheared at α=75 °. The results provide clear evidence for the initial fabric anisotropy of Portaway sand specimens.

- Slight deviation between the axes of principal stress and principal strain increments was obtained in these tests. The strain increment direction tends to deviate towards the direction of 45 °. The greatest degree of non-coaxiality was found in the dense specimen when α=30 ° with a largest value of 10 °. However, in all the tests, the average deviation was limited to 7 °.

- The degree of non-coaxiality was sufficiently small in both dense and medium dense sand so that the behaviour is considered coaxial in this series of tests. Even though, the degree of non-coaxiality was slightly larger in the dense specimens than in the medium dense specimens.

7.2.2 Behaviour under pure rotation of α

- Pronounced non-coincidence between the principal stress and principal strain increment directions was found for both Portaway sand and Leighton Buzzard sand.

- The degree of non-coaxiality was similar at the beginning of rotation for various deviator stress levels, and was about 42°. However, the average non-coaxial degree was related to the deviator stress level. The soil behaviour became more coaxial when the deviator stress was higher and the specimen was closer to failure.

- For each test, the greatest deviation occurred at the beginning of the test, and the most coaxial soil behaviour was observed between α=60°~ 75°. From the results of monotonic loading tests, when α=60° ~ 75°, specimens possess lowest strength. These results indicate a consistent conclusion with the above, which is that the soil behaviour became more coaxial when the specimen was getting close to failure.

- The void ratio had a much clearer effect in this series of tests, especially when specimens were subjected to a lower deviator stress. The degree of non-coaxiality obtained from medium dense sand was smaller than that from dense sand. However, with the increase of q, the influence of density became negligible.

- From the particle size distribution and particle shapes of two sands,

Leighton Buzzard sand specimens were expected to be more isotropic than Portaway sand specimens. The soil behaviour of Leighton Buzzard sand was more coaxial than that of Portaway sand when the same stress path was employed. The results support the hypothesis that the non-coaxiality between axes of principal stress and principal strain increment was induced by the initial anisotropy when no preloading was applied.

7.2.3 Behaviour under combined loading

- A significant deviation of strain increment axis from the principal stress axis was obtained in the combined loading tests.

- At the beginning of the tests, the maximum value of the degree of non-coaxiality (about 45°) was obtained. Then the soil behaviour was getting more coaxial with the rotation of α and the increase of q. When α was larger than 60°, the specimens were approaching failure, and the soil behaviour became coaxial.

- Effect of density was also studied in this series of tests. The density did not have a clear effect on the degree of non-coaxiality.

- The degree of non-coaxiality was strongly affected by the applied stress path. With the same stress state, the soil behaviour was almost coaxial when the monotonic loading stress path was applied. The degree of non-coaxiality was larger when the principal stress axes were rotated at

constant q, and was smaller when both α and q were increased at the same time.

7.3 RECOMMENDATIONS FOR FUTURE RESEARCH

Further experimental evidences for non-coaxiality between principal stress and principal strain increment directions in granular materials have been obtained from the current study. The results have provided a better understanding of the non-coaxiality and some factors that affect the non-coaxial soil behaviour. To the author's knowledge, the effect of density on the non-coaxiality was studied for the first time. It was shown that the degree of non-coaxiality was related to the void ratio, especially at a lower deviator stress level. A clearer non-coaxiality was observed in denser sand. The effect of density became less significant when specimens approached failure. However, there are still some aspects of non-coaxiality that have not been analysed in the present study. As a result, some suggestions for future research are listed below.

7.3.1 Update of the experimental techniques

Firstly, a new control module, strain path control, is required for the current testing system. The stress path control module that was used in present study allows controlling the parameters of p, q, b and α independently. However, it does not allow investigating the soil behaviour after failure. A new

strain path module capable to control of p, b, α, axial displacement, and rotational displacement would help study the post-failure behaviour of soil.

Secondly, the current HCA is only capable of applying the rotation of α from -90 ° to 90 °, and rotation of α from 0 ° to 180 ° cannot be imposed. In this case, the cyclic tests with continuous rotation of α cannot be conducted. Thus, a modification of the software code is necessary to study non-coaxiality of granular materials under a wide-range of stress /strain path.

7.3.2 Experimental work

There are still a wide range of experimental tests that will be helpful in the investigation of non-coaxiality.

First of all, similar tests to those in the current study but with different parameters can be carried out. The soil behaviour may be affected by different effective mean pressure, P', and different b. Loose specimens can be prepared to complete the study on the effects of specimen density.

The current tests were carried out with no pre-loading history. However, the DEM simulation has shown that the pre-loading would affect the soil behaviour, including the non-coaxiality of a granular soil. Experimental tests involved pre-shearing followed by the same stress paths in this study are recommended to investigate the influence of stress induced anisotropy. However, a test with the pre-loading to the peak or post-peak state will require an update of the control programme to enable strain path control, which has

been mentioned in the previous section.

More experiments on the combined loading tests will provide more information on the effects of deviator stress and principal stress direction. The tests can be conducted with various rates of q relative to α, or tests involving reducing deviator stress q with the increase of α.

The author also suggests that the cyclic tests involving continuous rotation of the principal stress axes with constant deviator stress with various numbers of cycles. However, these tests would need a upgrade of the testing system.

The effect of particle size distribution and shape on non-coaxiality has been discussed for Portaway sand and Leighton Buzzard sand. Although the Leighton Buzzard sand specimens were more isotropic than Portaway sand specimens, it was still anisotropic in fabric mechanism. Tests on artificial isotropic materials, such as small plastic (or metal) balls, can help in understanding the effects of initial and induced anisotropy on the non-coaxiality of granular materials.

References

Alonso-Marroquin, F. Luding, S., Herrmann, H.J., (2005). Role of Anisotropy in the Elastoplastic Response of a Polygonal Packing. *Physical Review*; **E71**:051304.

Anand, L., (1983). Plane Deformations of Ideal Granular Materials. *Journal of the Mechanics and Physics Solids*, Vol. **31**, pp. 105-122.

Arthur, J.R.F., Chua, K.S. and Dunstan, T. (1977). Induced Anisotropy in a Sand. *Geotechnique*, Vol. **27**, No. 1, pp. 13-30.

Baldi, G. and Nova, R. (1984). Membrane Penetration Effects in Triaxial Ttesting. *Journal of Geotechnical Engineering, ASCE*, Vol. **110**, No. 3, pp. 403-420.

British Standards (1990). BS 1377-2: Classification Tests, Determination of Particle Size Distribution. B.S.I, London.

British Standards (1990). BS 1377-4: Compaction-Related Tests. Determination of Maximum and Minimum Dry Densities for Granular Material. B.S.I, London.

British Standards (1990). BS 1377-8: Shear Strength Tests (Effective Stress), Consolidated Drained and Undrained Triaxial Compression Tests. B.S.I, London.

Cundall, P. A. (1971). A Computer Model for Simulating Progressive Large Scale Movements of Blocky Rock Systems. *Proceedings of the Symposium of the International Society of Rock Mechanics*, Nancy, France. Vol. **1**, paper no. II-8.

de Josselin de Jong, G., (1958). The Undefiniteness in Kinematics for Friction Materials. *Proceeding Conference on Earth Pressure Problem, Brussels,* Vol. **1**, pp. 55–70.

de Josselin de Jong, D. (1988). Elasto-plastic Version of the Double Sliding Model in Undrained Simple Shear Test. *Geotechnique,* Vol. **38**, No. 34, pp. 533-555.

de Saint Venant, B. (1870). Memoire sur l'etablissement des equations differentielles des mouvements interieurs operes dans les corps ductiles au dela des limites ou le elasticite portrait les ramener a leur premier etat. *Comptes Rendus de l'Academie des Sciences Paris*, Vol. **70**, pp. 473-480

Drescher, A. and de Josselin de Jong G., (1972). Photoelastic Verification of a Mechanical Model for the Flow of a Granular Material. *Journal of the Mechanics and Physics Solids,* Vol. **20**, 337–351.

Frydman, S., Zeithlen, J.G. and Alpan, I. (1973). The Membrane Effect in Triaxial Testing of Granular Soils. *Journal of Testing and Evaluation, JTEVA*. Vol. **1**, No. 1, pp. 37-41.

GDS, (2005). Geotechnical Digital Systems Instruments,. *http://www.gdsinstruments.com/hollow_cylinder.htm*

Gutierrez, M., Ishihara, K. and Towhata, I., (1991). Flow Theory for Sand During Rotation of Principal Stress Direction. *Soils and Foundations.* Vol. **31**, pp. 121–132.

Gutierrez, M. and Ishihara, K., (2000). Non-coaxiality and Energy Dissipation in Granular Material. *Soils and Foundations*. Vol. **40**, pp. 49–59.

Harris, D., (1993). Constitutive Equations for Planner Deformations of Rigid-plastic Materials. *Journal of the Mechanics and Physics of Solids*, Vol. **41**, No. 9, pp. 1515-1531.

Hight, D.W., Gens, A. and Symes, M.J. (1983). The Development of a New Hollow Cylinder Apparatus for Investigating the effects of principal rotation in Soils. *Geotechnique***,** Vol. **33**, No. 4, pp. 355-383.

Iai, S., Matsunaga, Y. and Kameoka, T. (1992). Strain Space Plasticity Model for Cyclic Mobility. *Soils and Foundations*, Vol. **32**, No. 2, pp. 1-15.

Ishihara, K. and Towhata, I. (1983). Sand Response to Cyclic Rotation of Principal Stress Directions as Induced by Wave Loads. *Soils and Foundations*, Vol. **23**, No. 4, pp. 11-26.

Jiang, M. J., Harris, D. and Yu, H. S. (2005a). Kinematic Models for Non-coaxial Granular Materials. Part Ⅰ: Theory. *International Journal for Numerical and Analytical Methods in Geomechanics*, Vol. **29**, pp. 643-661

Jiang, M. J., Harris, D. and Yu, H. S. (2005b). Kinematic Models for Non-coaxial Granular Materials. Part Ⅱ: Evaluation. *International Journal for Numerical and Analytical Methods in Geomechanics*, Vol. **29**, pp. 663-689

Joer, H.A., Lanier, J. and Fahey, M., (1998). Deformation of Granular Materials Due to Rotation of Principal Axes. *Geotechnique*, Vol. **48**, No.5, pp.:605–619.

Kramer, S.L. and Sivaneswaran, N. (1989). A Non-destructive, Specimen-specific Method for Measurement of Membrane Penetration in

the Triaxial Test. *Geotechnical Testing Journal*, Vol. **12**, No.1, pp. 50-59.

Kolymbas, D. (1991). An Outline of Hypoplasticity. *Archive of Applied Mechanics*, Vol. **61**, pp. 143-151.

Kuwano, R. (1999). The Stiffness and Yielding Anisotropy of Sand. PhD. Thesis, Imperial College of Science, Technology and Medicine, University of London

Lade, P.V., Namb, J., and Hong, W.P. (2009). Interpretation of Strains in Torsion Shear Tests. *Computers and Geotechnics*, Vol. **36**, pp. 211 – 225'

Lambe, T.W. (1967). Stress Path Method. *Journal of Geotechnical Engineering, ASCE*, Vol. **93**, No. SM6, pp. 309-331.

Lashkari, A. and Latifi, M. (2007), A Non-coaxial Constitutive Model for Sand Deformation Under Rotation of Principal Stress Axes. *International Journal for Numerical and Analytical Methods in Geomechanics*, Vol. **32**, No. 9, pp. 1051-1086.

Li, X.S., Dafalias, Y.F. (2004). A Constitutive Framework for Anisotropic Sand Including Non-proportional Loading. *Geotechnique.* Vol. **54**, No. 1, pp. 41–55.

Li, X. and Yu, H.S. 2009. Influence of Loading Direction on the Behaviour of Anisotropic Granular Materials. *International Journal of Engineering Science.* Vol. **47**, No. 11-12, pp. 1284-1296.

Mandel, J. (1966). Sur les lignes de glissement et le calcul de deplacements dans la deformation plane et le concept du doble glissement. *Journal of the Mechanics and Physics Solids,* Vol. **14**, pp. 303-308.

Mandel, G. and Fernandez Luque, R. (1970). Fully Developed Plastic Shear Flow of Granular Materials. *Geotechnique*, Vol. **20**, No. 3, pp. 277-307.

Marri, A. (2010). Behaviour of Cemented Sand at High Pressure, *PhD. Thesis, Nottingham Centre for Geomechanics, School of Civil Engineering, University of Nottingham* (In preparation).

Mehrabadi, M.M. and Cowin, S.C. (1978). Initial Planar Deformation of Dilatant Granular Materials. *Journal of the Mechanics and Physics Solids*, Vol. **26**, pp. 269-284.

Menkiti, C.O. (1995). Behaviour of Clay and Clayey-Sand, with Particular Reference to Principal Stress Rotation. *Msc. Dissertation, Imperial College of Science, Technology and Medicine, University of London.*

Menzies, B. K. (1984). Soil Testing Systems. *Geotechnical News*, Vol. **1**, No. 3, pp. 38–39.

Menzies, B. K. (1988). Computer Controlled Hydraulic Triaxial System. *Proceedings, Advanced Triaxial Testing of Soil and Rock, ASTM STP 977*, R. T. Donaghe, R. C. Chaney, and M. L. Silver, Eds., ASTM International, West Conshohocken, PA, pp. 82–94.

Miura, K., Miura, S. and Toki, S. (1986). Deformation Behaviour of Anisotropic Dense Sand under Principal Stress Axis Rotation. *Soils and Foundations*, Vol. **26**, No.1, pp. 36-52.

Molenkamp, F. and Luger, H.J. (1981). Modelling and Minimization of Membrane Penetration Effects in Tests on Granular Soils. *Geotechnique*, Vol. **31**, No. 4, pp. 471-486.

Naughton, P. J. and O'Kelly, B. C. (2007), Stress Non-uniformity in a Hollow Cylinder Torsional Sand Specimen. *Geomechanics and Geoengineering*, Vol. **2**, No. 2, pp. 117-122.

Nishimura, S., Minh, N.A. and Jardine, R.J. (2007), Shear Strength Anisotropy

of Natural London Clay. *Geotechnique*, Vol. **57**, No. 1, pp. 49-62.

O'Kelly, B. C. and Naughton, P. J. (2005), Development of a New Hollow Cylinder Apparatus for Stress Path Measurements over a Wide Strain Range. *Geptechnical Testing Journal.* Vol. **28**. No. **4**, pp. 1-10.

Porovic, E., (1995). Investigations of Soil Behaviour Using a Resonant Column Torsional Shear Hollow Cylinder Apparatus. *PhD. Thesis, Imperial College of Science, Technology and Medicine, University of London*

Pradel, D., Ishihara, K. and Gutizrrez, M. (1990), Yielding and Flow of Sand Under Principal Stress Axes Rotation. *Soils and Foundations*, Vol. **30**, No. 1, pp. 87-99.

Rolo, R. (2003). The Anisotropic Stress-Strain-Strength Behaviour of Brittle Sediments. *PhD. Thesis, Imperial College of Science, Technology and Medicine, University of London*

Roscoe, K. H., Bassett, R. H., and Cole, E. R. L., (1967). Principal Axes Observed During Simple Shear of a Sand," *4th European Conference on Soil Mechanics and Foundation Engineering*, *Oslo,* pp. 231–237.

Roscoe, K.H., (1970). The Influence of Strains in Soil Mechanics. *Geotechnique,* Vol. **20**, pp. 129–170.

Rudnicki, J.W. and Rice, J.R., (1975). Conditions for the Localisation of Deformation in Pressure-Sensitive Dilatant Materials. *Journal of the Mechanics and Physics Solids,* Vol. **23**, pp. 371–394.

Saada, A.S. (1988). Hollow Cylinder Devices: Their Advantages and Limitations. *Advanced triaxial testing of soils and rocks. ASTM* STP **977**, pp. 766-795.

Saada, A.S. and Townsend, F.C. (1981). State of the Art: Laboratory Strength

Testing of Soils. *Laboratory Shear Strength of Soil. ASTM* STP **740**, pp. 7-77.

Sayão, A. and Vaid, Y.P. (1991). A Critical Assessment of Stress Non-uniformities in Hollow Cylinder Test Specimens. *Soils and Foundations*, Vol. **31**, No. 1, pp. 61-72.

Sayão, A. and Vaid, Y.P. (1996). Effect of Intermediate Principal Stress on the Deformation Response of Sand. *Canadian Geotechnical Journal*, Vol. **33**, pp. 822-828.

Silvestri, V., Diab, R. and Ducharme, A. (2005). Development of New Hollow Cylinder Triaxial Apparatus for the Study of Expansion Tests in Clay. *Geotechnical Testing Journal*. Vol. **28**, No. 3, pp. 1-9

Sivathayalan, S. and Vaid, Y. P. (1998). Truly Undrained Response of Granular Soils with no Membrane Penetration Effects. *Canadian Geotechnical Journal*, Vol. **35**, pp. 730–739.

Spencer, A.J.M. (1964). A Theory of the Kinematics of Ideal Soils under Plane Strain Conditions. *Journal of the Mechanics and Physics Solids*, Vol. **12**, pp. 337-351

Symes, M.J., Hight, D.W and Gens, A. (1982). Investigation Anisotropy and the Effects of Principal Stress Rotation and of the Intermediate Principal Stress Using a Hollow Cylinder Apparatus. *IUTAM Conference on deformation and failure of granular materials. Delft,* pp. 441-449.

Symes, M.J., Gens, A. and Hight, D.W. (1984). Undrained Anisotropy and Principal Stress Rotation in Saturated Sand. *Géotechnique,* Vol. **34,** No. 1, pp. 11-27.

Symes, M.J., Gens, A. and Hight, D.W. (1988). Drained Principal Stress

Rotation in Saturated Sand. *Geotechnique,* Vol. **38**, No. 1, pp. 59-81

Teunissen, J.A.M and Vermeer, P.A. (1988). Analysis of Double Shearing in Frictional Materials. *International Journal for Numerical and Analytical Methods in Geomechanics*, Vol. **12**, pp. 323-340.

Thornton, C. and Zhang, L. (2006). A Numerical Examination of Shear Banding and Simple Shear Non-coaxial Flow Rule. *Philosophical Magazine*, Vol. **86**, pp. 3425-3452.

Vaid, Y.P., Sayao, A., Hou, E. and Neussey, D. (1990), Generalized Stress-Path-Dependent Soil Behaviour with a New Hollow Cylinder Torsional Apparatus, *Canadian Geotechnical Journal,* Vol. **27**, No. 5, pp. 601-616.

Vardoulakis, I. (1980). Shear Band Inclination and Shear Modulus of Sand in Biaxial Tests. *International Journal for Numerical and Analytical Methods in Geomechanics.* Vol. **4**, pp. 103-119

Wang, J. (2005). The Stress-Strain and Strength Characteristics of Portaway Sand. *PhD. Thesis, Nottingham Centre for Geomechanics, School of Civil Engineering, University of Nottingham*

Wang, Z.L., Dafalias, Y.F. and Shen, C.K. (1990). Bounding Surface Hypoplasticity Model for Sand. *Journal of Engineering Mechanics, ASCE,* Vol. **116,** No. 5, pp. 983-1001.

Wijewickreme, D. and Vaid, Y.P. (1991). Stress Nonuniformities in Hollow Cylinder Torsional Specimens, *Geotechnical Testing Journal*, Vol. **14**, No. 4, pp. 349-362.

Wong, R.K.S and Arthur, J.R.F. (1986). Sand Sheared by Stresses with Cyclic Variations in Directions. *Geotechnique,* Vol. **36,** No. 2, pp. 215-226

Yang, Y. and Yu, H.S. (2006a). Numerical Simulations of Simple Shear with Non-coaxial Soil Models. *International Journal for Numerical and Analytical Methods in Geomechanics*. Vol. **30**, pp. 1-19

Yang, Y. and Yu, H.S. (2006b). Application of a Non-coaxial Soil Model in Shallow Foundation. *Geomechanics and Geoengineering*, Vol. **1**, No.2, pp. 139-150)

Yatomi, C., Yashima, A., Iizuka, A. and Sano, I. (1989). General Theory of Shear Bands Formation by a Non-coaxial Cam-Clay Model. *Soils and Foundations*, Vol. **29**, No. 3, pp. 41-53.

Yu, H.S and Yuan, X. (2005). The Importance of Accounting for Non-coaxial Behaviour in Modeling Soil-structure Interaction. In *Prediction, Analysis and Design in Geomechnical Applications*, Barla G, Barla M (eds). Patron Editore: Bolognia, pp. 385-382.

Yu, H.S and Yuan, X. (2006). On a Class of Non-coaxial Plasticity Models for Granular Soils. *The Proceedings of Royal Society A*, Vol. **462**, pp. 725-748

Yu, H.S. (2006). *Plasticity and Geotechnics*, Springer, New York.

Zdravkovic, L. and Jardine, R.J. (2001). The Effect on Anisotropy of Rotating the Principal Stress Axes during Consolidation. *Geotechnique*. Vol. **51**, No. 1, pp. 69-83.